Process Engineering and Chemical Plant Design 2011

Editors:
Günter Wozny and Łukasz Hady

Universitätsverlag der TU Berlin
Berlin 2011

Editors: Günter Wozny and Łukasz Hady
Fachgebiet Dynamik und Betrieb
Technischer Anlagen
Technische Universität Berlin
Sekretariat KWT 9
Straße des 17. Juni 135
D-10623 Berlin
http://www.dbta.tu-berlin.de

Umschlaggestaltung: Łukasz Hady
Umschlagfoto: Gasbehandlungsanlage zur Kokerei-gasentschwefelung, Uhde GmbH

ISBN 978-3-7983-2361-2 (Druckausgabe)
ISBN 978-3-7983-2362-9 (Online-Version)

Berlin 2011

* Gedruckt auf säurefreiem alterungsbeständigem Papier

Druck/ Printing: Endformat, Ges. für gute Druckerzeugnisse mbH
Köpenicker Str. 187-188, 10997 Berlin

Vertrieb/ Publisher: Universitätsverlag der TU Berlin
Universitätsbibliothek
Fasanenstr. 88 (im VOLKSWAGEN-Haus)
D-10623 Berlin
Tel.: (030)314-76131;
Fax.: (030)314-76133
E-Mail: publikationen@ub.tu-berlin.de
http://www.univerlag.tu-berlin.de

18th International Conference Process Engineering and Chemical Plant Design
Günter Wozny and Łukasz Hady, Editors

P R E A M B L E

The 18th International conference in "Process Engineering and Chemical Plant Design" is taking place in Berlin from september 19th to september 23rd 2011. We are pleased with the successful collaboration which is the result of a meanwhile 30 years continual international cooperation between the Cracow University of Technology and the Berlin Institute of Technology. This relationship has also been intensified by student exchange programs and international transfer of knowledge between the participating universities during the last years.

This book contains the abstracts of all contributions and lectures which are presented by the miscellaneous participants within the scope of the conference. Different topics are addressed, concerning industrial problems as well as forward-looking questions and fundamental investigation of special phenomena for the chemical and the power generation industry. Thereby special attention is paid to fundamental research of complex correlations, modelling and simulation, process control and operation, sustainable and efficient energy generation as well as troubleshooting and problems within the operation and control of chemical processes.

We want to appreciate all participants individually, especially our partners from Cracow University of Technology and also from the Warsaw and the West Pomeranian University of Technology. Special thanks go to the office for foreign relations (ABZ) and the DAAD for their financial support.

All contributions have been peer-reviewed. Therefore we also want to thank the reviewers for their work.

The authors are responsible for the contents of their articles.

18th International Conference Process Engineering and Chemical Plant Design
Günter Wozny and Łukasz Hady, Editors

BARBARA TAL-FIGIEL*

SOLID-LIQUID EXTRACTION FROM PLANTS WITH A BIDISPERSE POROUS STRUCTURE – EXPERIMENTAL KINETICS AND MODELLING

Abstract

This paper deals with the mathematical model of extraction from a capillary porous particle with bidisperse structure. Capillary porous particles with bidisperse structure, possessing capillaries of two, strongly different sizes, occur frequently in nature and technology. Neglecting the polydispersity of capillary sizes in capillary porous particles makes the obtained results less accurate and prevents elucidation of some physical mechanisms of substance transfer inside the particles. The bidisperse model of a capillary porous particle is analytically the simplest variant of the polydisperse model, which makes it possible to reveal fundamental aspects of mass transfer in real polydisperse particles. The mathematical planar model of extraction process from the particle can be described by the following set of equations: the diffusion equation for the porous body and the convective diffusion equation for the transport channel, with initial and boundary conditions for these equations, and the velocity profile in the transport channel.

To solve the set of equations the grid and finite element methods were used. A numerical analysis of the model demonstrates that, for liquid extraction of a desired substance from the particle, there exists an optimum range of oscillation frequencies of the liquid in large pores. Results of numerical simulations are presented together with the criterial equation for calculating the effective diffusion coefficient, obtained in the course of processing these results.

The experiments consisted of different types of liquid-solid extraction of active ingredients from plants.

Keywords: solid-liquid extraction, bidisperse porous model.

*Institute of Chemical and Process Engineering, Cracow University of Technology, Warszawska 24, 31-155 Kraków, Poland.

1. Introduction

Mathematical models of extraction processes, that are different from conventional diffusion models [1-4], were proposed recently. The reason for this is the need to make the description of the process more realistic, in particular, to improve the way in which the structure of a porous solid, from which the target component has to be extracted, is taken into account. New models take into consideration the bidispersed structure of a porous material and the presence of convective motion in large pores [5-9].

Convective mass transfer is taken into account within the diffusion models both by introducing coefficients of effective diffusion and by directly introducing the convective term [5,6].

The model is proposed for the process of extraction from a semi-infinite solid containing two types of pores: large pores that extend to the surface and small pores that are connected to large pores. Effective transport coefficients in two types of pores are assumed to be different. Theoretical results are compared with experimental data related to the kinetics of the extraction of the target components from plant materials obtained in apparatuses with an intensive hydrodynamic mode (mixing, ultrasounds). In this model, it is shown that the mass flux at the boundary of a semi-infinite solid with the branched system of pores at each time point $t>0$ is greater than that for a system, in which there are no branches from the main channel. The processing of experimental data on the kinetics of the extraction of active substances from plants has shown that the process is equally well described by both the model of extraction from a porous solid with semi-infinite transport pores and the model of extraction from a solid with the pores of a finite length.

The problem of studying the regularities of solvent extraction from porous media is a matter of concern, because this process is widely used in the industry, especially in the extraction of medicinal components from plants. The pore space in actual media can have a very complicated structure (fig.1). There are pores with variable diameter, branched pores, isolated cavities, and the like. Therefore, the behavior of the diffusion process in such media can be much different from that in a single pore.

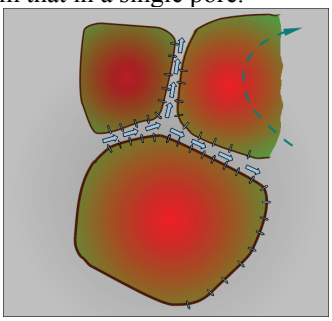

Fig. 1. Structure of plant material

Conventional methods for extracting active substances from plants are, as a rule, ineffective, since they do not ensure a sufficient degree of depletion of plants and are characterized by a long duration and nonproductive expenditures of input energy. At the same time, a constant increase in the volumes of production dictates a necessity for

development of new intensive extraction methods and apparatuses for their implementation.

2. Mass transfer model

The model of solid-liquid extraction [5], depicted on fig.2, was used. A solution of the desired component from the porous body, is largely transported through small capillaries which branch off in large pores, either dead-end or through. It is assumed, that there is no liquid motion in the capillaries and active substance is transported there by molecular diffusion. However external-pressure pulses of some amplitude can induce liquid oscillations in large pores because of compression of the gas contained in capillaries [9].

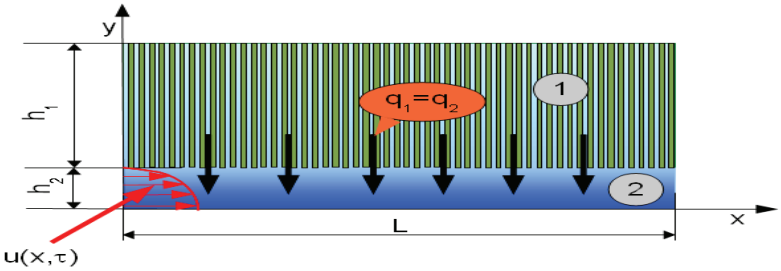

Figure 2. Planar model of a particle with bidisperse structure;
1) porous block, 2) transport channel

Thus, large pores can be regarded as transport channels where active substance is transferred by convection. Compared to molecular diffusion, convection can ensure a rate of solute extraction from particle, that is many times higher. Assuming, that the diffusion coefficient D_M is independent of the active substance concentration, this process can be described by the following set of equations:

diffusion equation for the porous body:

$$\frac{\partial C_1}{\partial \tau} = -D_M \frac{\partial^2 C_1}{\partial y^2}, \tag{1}$$

where:

C_1 is the active substance concentration in the porous block,
D_M – molecular diffusion coefficient [m^2s^{-1}],
τ – time [s],

and the convective diffusion equation for the transport channel

$$\frac{\partial C_2}{\partial \tau} + u\frac{\partial C_2}{\partial x} = -D_M\left(\frac{\partial^2 C_2}{\partial x^2} + \frac{\partial^2 C_2}{\partial y^2}\right), \tag{2}$$

where:

C_2 – the active substance concentration in the transport channel,
u – the longitudal (along the x-axis) fluid velocity.

The initial and boundary conditions for these equations are the following:

$$C_1\left(x, y, \tau = 0\right) = C_{10}\ , 0 \le x \le L\ , h_2 < y \le h_1 + h_2; \tag{3}$$

$$C_2\left(x,y,\tau=0\right)=C_{20}\ ,\ 0\le x\le L\ ,\ 0<y\le h_2; \tag{4}$$

$$C_2\left(x,y=h_2,\tau\right)=C_1\left(x,y=h_2,\tau\right); \tag{5}$$

$$q_1\left(x,y=h_2,\tau\right)=q_2\left(x,y=h_2,\tau\right); \tag{6}$$

$$C_2\left(x=0,y,\tau\right)=C_2\left(x=L,y,\tau\right)=C_{20},\quad 0<y<h_2; \tag{7}$$

$$q_1\left(x,y=h_1+h_2,\tau\right)=0; \tag{8}$$

$$q_2\left(x,y=0,\tau\right)=0\ , \tag{9}$$

where:

h_1 and h_2 are the half widths of the porous block and the transport channel, respectively

L – the particle length,

q_1, q_2 – the substance fluxes.

The velocity profile in the transport channel is given by equation:

$$u\left(x,\tau\right)=u_{max}\left[1-\left(\frac{y}{h_2}\right)^2\right]\sin\left(\omega\tau\right), \tag{10}$$

where:

ω – angular velocity of oscillation.

The substance fluxes through the porous body-channel boundary (at $y=h_2$) are expressed as:

$$q_1=-\varepsilon D_M\frac{\partial C_1}{\partial y}, \tag{11}$$

$$q_2=-D_M\frac{\partial C_2}{\partial y}, \tag{12}$$

where:

ε – specifies the fraction of the channel surface through which active substance is transferred from the porous body.

Since the liquid velocity in the channel is low and the channel diameter is small, the liquid flow can be assumed to be laminar and the liquid profile to be parabolic in space and harmonic in time.

To solve the set of equations (1)-(12) the finite element and finite difference methods were used. Equation (1) was approximated using the absolutely stable Crank-Nicholson method of second order accuracy and equation alternating direction implicit (ADI) method of first order accuracy, with the approximation error O [$\Delta\tau$, Δx^2, Δy^2], which is unconditionally stable in the linear case [6,7,10].

The boundary conditions were approximated by expressions of second-order accuracy. To ensure stability, the values of the Fourier number for the porous body and the Courant and Peclet numbers for the channel were checked.

The program enables to monitor the concentration fields at mesh points and the relative linear concentrations of the extractable substance in the porous body and the channel:

$$C_{L1}(x,\tau)=\frac{1}{h_1 C_{10}}\int_{h_2}^{h_1+h_2} C_1(x,\tau)\,dy\,, \tag{13}$$

$$C_{L2}(x,\tau)=\frac{1}{h_2 C_{10}}\int_{0}^{h_2} C_2(x,\tau)\,dy\,, \tag{14}$$

$$Pe=\frac{u_{max}L}{D}\gg 1\,. \tag{15}$$

At Peclet numbers

$$Pe=\frac{\bar{u}L}{D}\le 1, \tag{16}$$

where*:*

$\bar{u}=\omega\pi^{-1}\int_0^{\pi/\omega}\int_0^{h_2} u(y,\tau)\,dy\,d\tau=4u_{max}/3\pi$.–fluid motion velocity averaged over the half-period and the transport channel cross-section.

Since the convective transfer in the channel has virtually no effect on the extraction rate, the main calculations were done for

$$Pe=\frac{\bar{u}L}{D}>1. \tag{17}$$

As the extraction efficiency criterion, the time τ required to attain a specified value for the residual concentration of the extractable substance in the porous body, was used:

$$R=\frac{\int_{h_2}^{h_1+h_2}\int_0^{L} C_1\,dx\,dy}{h_1 L C_{10}}\,. \tag{18}$$

For the convective transfer of substance from a particle with a bidisperse capillary structure to occur at the highest rate, it is necessary that, at the maximum liquid velocity, the substance concentration at the channel outlet (x=L) also be maximum, because the convective flux of the substance is expressed as $q_{conv}=uC_2$. The velocity obtains its maximum in a time equal to a quarter of the oscillation period T: $\tau_0=T/4=\pi/2\omega$.

Within the suggested model, the instantaneous velocity of the liquid front is $u_{fr}=\frac{2}{3}u_{max}\sin(\omega t)$ and in time τ_0, the front will travel the distance:

$$x_{fr}=\int_0^{\tau_0} u_{fr}\,d\tau=\frac{2}{3}\frac{u_{max}}{\omega}=\frac{u_{av}}{\omega}\,, \tag{19}$$

which must be of the order of L. Therefore, the optimum oscillation frequency of the liquid can be found from the condition:

$$Sr=\frac{\omega L}{u_{av}}\approx 1. \tag{20}$$

In practice, it is important to know how the accelerating effect of oscillations on the extraction rate depends on the particle size. The bigger the particles, the weaker the effect of oscillations.

The fluid volume contained within the transport channel is described by the balance equation expressing the law of mass conservation with respect to the substance being extracted:

$$\frac{\partial M_1}{\partial \tau} = G_1 - G_0 , \tag{21}$$

where $\partial M_1/\partial\tau$ is the rate at which the mass of the substance being extracted grows in the transport channel, G_1 is the substance flux at the boundary between the porous block and the transport channel and G_0 is the outward flux from the transport channel:

$$\frac{\partial M_1}{\partial \tau} = \frac{\partial}{\partial \tau}\int_0^{h_2}\int_0^{L} C_2 dx dy , \tag{22}$$

$$G_1 = D_M \int_0^{L} \left.\frac{\partial C_2}{\partial y}\right|_{y=h_2} dx , \tag{23}$$

$$G_0 = D_M \int_0^{h_2} \left(\left.\frac{\partial C_2}{\partial x}\right|_{x=0} - \left.\frac{\partial C_2}{\partial x}\right|_{x=L} \right) dy . \tag{24}$$

3. Numerical simulations

Numerical simulations were conducted for the several parameter sets. One of them is shown below:

$h_1 = h_2 = 1\cdot 10^{-6}\text{m}$ $\qquad$ $\varepsilon = 0.29$

$u_{max} = 0,002\,\text{m/s}$ $\qquad$ $C_{10} = 10\ \text{kg/m}^3$

$L = 1\cdot 10^{-5}\ \text{m}$ $\qquad$ $\omega = 1, 100, 1000, 10000\ \text{rad/s}$

$D = 4.5\cdot 10^{-11}\ \text{m}^2/\text{s}$

Numerical experiments demonstrated that, all other conditions being the same, there exist the optimal frequency of fluid oscillations in the channel ω_{opt}, at which the minimum process duration can be achieved. Analysis of numerical calculations shows that two stages exist at any oscillation frequency (fig.3). The first is the attainment of regularity, with the substance content in the porous block falling fast because of high concentration gradients. In the process, one part of molecules of the substance being extracted goes from the transport channel outwards, and the other is accumulated in the transport channel. The second stage depends on the oscillation frequency. At low frequencies, the role played by convective substance transfer is insignificant. At higher frequencies, curve exhibits a weakly pronounced maximum. At the same time the intensity of substance transfer is still rather low. This is due to the fact that the molecules of the substance being extracted have to pass a longer way toward the opening at the transport channel virtually by means of diffusion only.

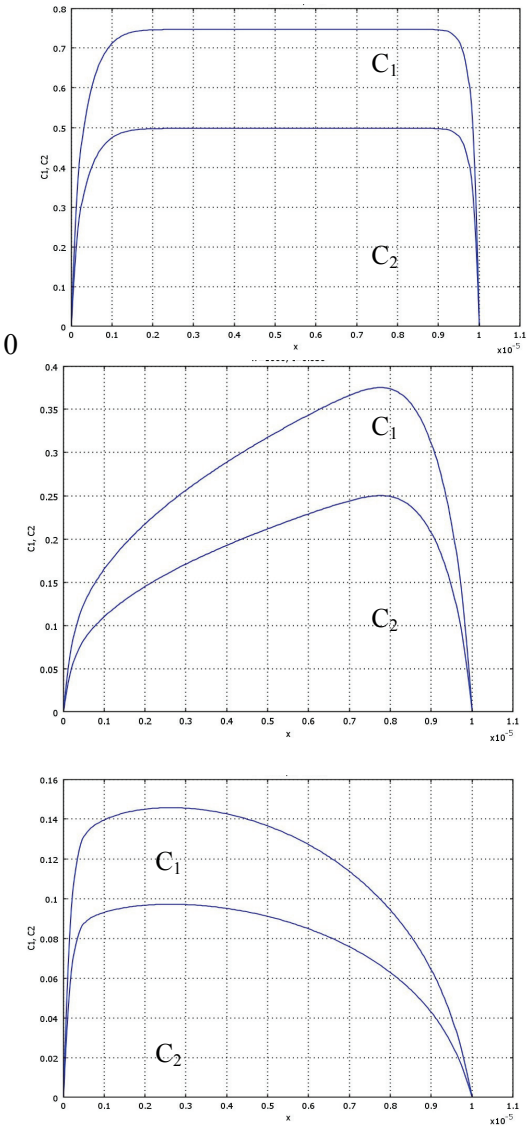

Figure 3. Plots of C_1 and C_2 vs length for the frequency 1000 [s^{-1}], and process times 0, 0.036, 0.056 [s].

At a nearly optimal frequency all curves show clearly pronounced extrema virtually coinciding in phase. The outflow of the substance to the transport channel is immediately followed by its transfer from the particle outwards, into the fluid surrounding the particle. The transfer from the porous block into the transport channel is enhanced, since the fluid in

the transport channel rapidly “releases” the substance outwards, with all lines having large amplitudes.

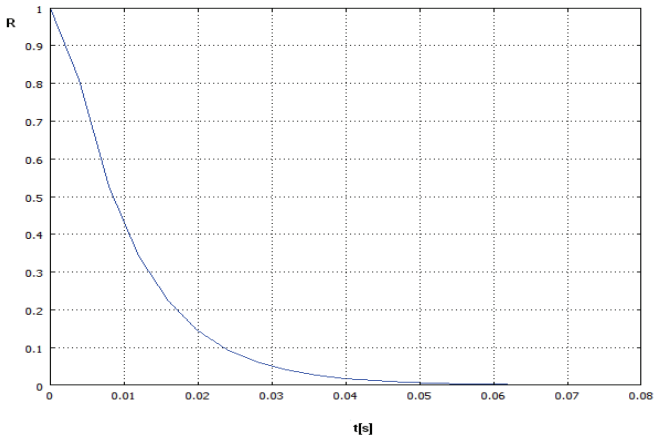

Figure 4. Function R, eq (18) at the ω=1000

This type of substance transfer resembles exchange of potential and kinetic energies in mechanical and ultrasound oscillatory systems and therefore quite deserves being termed the “resonance” in mass transfer.

Due to small particle size used for the simulation, the extraction progress is very fast what can be seen on fig.4. For longer channels the positive effect of oscillation gradually vanishes.

Experimental

The experimental part consisted of different types of liquid-solid extraction of active ingredients from plants (chlorophyll from stinging nettle leaves, menthol from peppermint leaves, inuline from dandelion root), obtained from Herbapol, Poland. These extraction methods included maceration, Soxhlet extraction, ultrasound-assisted extraction and microwave-assisted extraction. Solvents used in experiments were distilled water and 99,8% ethanol. Long time (48h) Soxhlet extraction was used to establish total amount of desired substance in plant material [11]. Obtained extracts were analyzed using 6715 UV/Vis Jenway Spectrophotometer. Theoretical results were compared with experimental data on the kinetics of the extraction of the target components from plant material in apparatuses with an intensive hydrodynamic mode (mixing, ultrasounds).

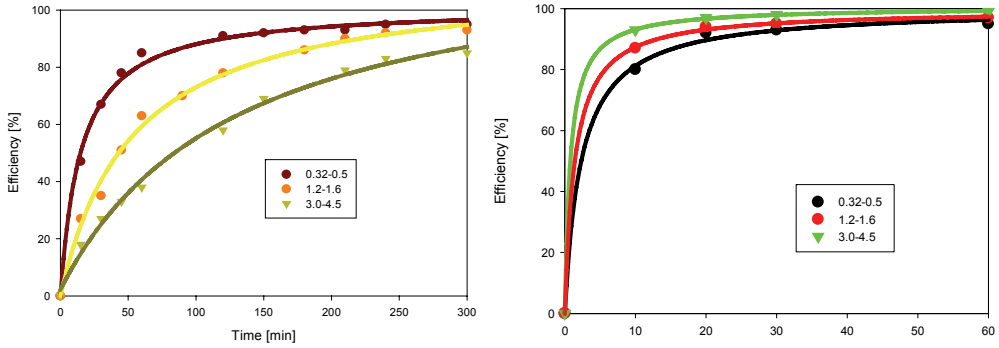

Figure 5. Comparison of water extraction efficiency of inulin from the dandelion root, with low speed mechanical mixing (6 s^{-1}) and an ultrasonic field (P=220 W) for various grain size.

The processing of experimental data on the kinetics of the extraction of active substances from plants has shown that the process can be qualitatively well described by presented model. However this description is applicable only for the very beginning of process, when the dimensions of the internal channels can be regarded constant. Since both ultrasounds and microwaves deteriorate internal structure of plant material, which leads to changes in the channel size and also another mechanisms, apart from diffusion convection may appear (cavitation).

Conclusions

Base on the results of the conducted experiments, the following conclusions can be derived:

- the obtained relations make possible to provide recommendations for determining the optimal extraction conditions, when the pore sizes in real particles are known;
- for each fluid oscillation amplitude there exists the optimal oscillation frequency, at which the extraction has the highest intensity;
- at a certain Strouchal number, approximately equal to unity, the extraction proceeds the most intensely;
- in particles with long transport channels practically no effect was observed on the optimal oscillation frequency;
- both in the case of ultrasound and microwaves the intensification of extraction process was observed. Greater efficiency was obtained with microwave extraction;

- Soxhlet extraction is a good method in the case of organic solvent with low boiling temperature, and small amount of material, but both microwave and ultrasonic extractions are more energetically economic.

Symbols

C – active substance concentration [kg m^{-3}]
C_L – relative active substance concentration, [--]
D_M – molecular diffusion coefficient, [m^2s^{-1}]
h_1 – half-thickness of the porous body, [m]
h_2 – half-width of the transport channel, [m]
L – particle length
q – active substance flux, [kg $m^{-2}s^{-1}$]
R – relative amount of the desired substance that remains in the porous body,
T – oscillation period, [s]
ε – porosity
τ – extraction time [s]
ω – angular oscillation frequency [rad s^{-1}]
Pe – Peclet number
Sr – Strouchal number

Literature

[1] Crank J.: The Mathematics of Diffusion, Clarendon Press, Oxford, 1975.
[2] Aksielrud G.A., Łysianski W.M.: Ekstrakcja w układzie stało ciałe ciecz (Extraction. Solid-Liquid System), WNT, Warszawa 1978.
[3] Aksielrud G.A., Altszuler M.A.: Ruch masy w ciałach porowatych (Mass Transport in Porous Media), WNT, Warszawa 1987.
[4] Shewmon P.: Diffusion in Solids, Wiley, New York, 1989.
[5] Abiev R.Sh.: Zh. Prikl. Khim. 74(5), (2000), 754-761.
[6] Abiev R.Sh., Ostrovski G.M.: Teor.Osn. Khim. Teknol., 35(3), (2001), 270-275.
[7] Malyshev R.M., et al.: Dokl. Akad. Nauk. 381(6) (2001), 800.
[8] Babenko Yu., Ivanov E.V.: Teor.Osn. Khim. Teknol., 39(6), (2005), 644.
[9] Ivanov E.V., Babenko Yu.I.: Zh. Prikl. Khim. 78(9), (2005), 1478.
[10] Fletcher C.A.J.: Computational Techniques for Fluid Dynamics Vol.1. Springer Verlag, Berlin, 1988.
[11] Quality control methods for medicinal plant materials, World Health Organization, Geneva, 1998.

18th International Conference Process Engineering and Chemical Plant Design
Günter Wozny and Łukasz Hady, Editors

Z. GUETTA[*], J. C. SCHÖNEBERGER[**], H. ARELLANO-GARCIA[*], H. THIELERT[**], G. WOZNY[*]

DEVELOPMENT OF A CLAUS PROCESS COMBUSTION CHAMBER MODEL

Abstract

Claus processes are widely used for the recovery of sulphur from hydrogen sulphide containing sour gas streams. The hydrogen sulphide is partially oxidized to sulphur, sulphur dioxide, and water in a combustion chamber. The hot gases coming from the furnace is cooled down and fed to the so called Claus reactors where the formation of sulphur from hydrogen sulphide and sulphur dioxide is supported by a catalyst. The scope of this work is the physical and chemical modelling of the reaction furnace in the combustion chamber. Due to the high number of microkinetic reactions and active species the numerical implementation of the mathematical model represented by a highly nonlinear algebraic equation system is a challenging task. Several numerical techniques are presented in order to reach high convergence qualities and robustness combined with a low computation time, thus enabling the use of process analysis and optimization tools.

Keywords: *Claus process, Combustion modeling, Sulphur, Model based control.*

1. Introduction

The original Claus process was developed by C.F. Claus in 1883 [11]. Currently there are plenty of different process implementations which have been developed in order to increase the rate of sulphur recovery or to reduce the capital and the operational expenditures. However, all these processes are based on the same principles, the partial oxidation of hydrogen sulphide at high temperatures (thermal region) and the formation of sulphur at low temperatures (catalytic region). The process can be characterized by the following main reactions:

[*] TU-Berlin, Institut für Prozess- und Verfahrenstechnik, Sekr. KWT 9, Straße des 17. Juni 135, 10623 Berlin
[**] Uhde GmbH Dortmund

Thermal region:

$$2H_2S + 3O_2 \rightarrow 2SO_2 + 2H_2O \quad (1)$$

$$2H_2S + SO_2 \leftrightarrow 1½S_2 + 2H_2O \quad (2)$$

Catalytic region:

$$2H_2S + SO_2 \leftrightarrow 1½S_2 + 2H_2O \quad (3)$$

The rate of sulphur recovery can be increased by adding intermediate condensation steps (multiple stage Claus processes, e.g. Superclaus) or by recycling the tail gas (e.g. SCOT process). In order to maximize the conversion of hydrogen sulphide to sulphur the concentration of hydrogen sulphide must be twice the concentration of sulphur dioxide in the gas stream leaving the reaction furnace as can be seen in equation (3). The difficulty in handling the process is attributed to the side reactions, which can take place in the reaction furnace. These reactions occur depending on the composition of the sour gas stream. Sour gas streams coming from a refinery have to be treated differently than those coming from a coal gasification or the by-product plant of a coking plant.

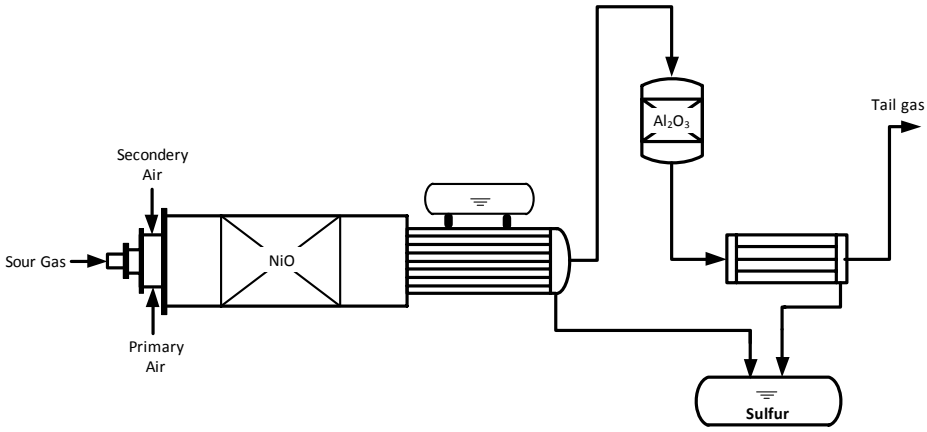

Fig. 1. MONOCLAUS process.

The MONOCLAUS process is an emission-free sulphur recovery process as the tail gas can be fed completely to the untreated coke oven gas, which is entering the by-product plant, see Fig. 2.

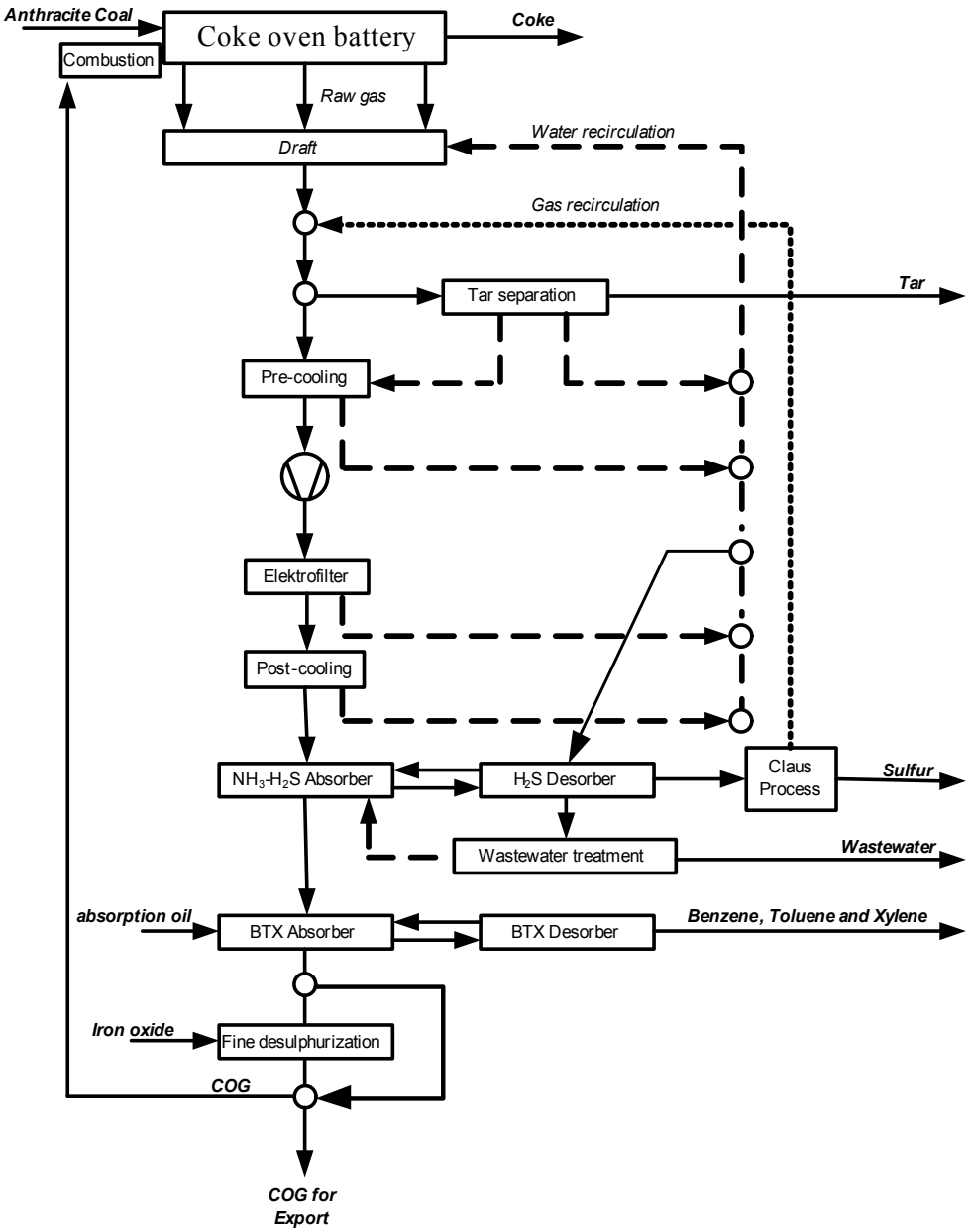

Fig. 2. By-product plant [13].

Sour gas coming from an amine based scrubbing process (e.g. CYCLASULF) commonly contain large amounts of ammonia, carbon dioxide, and hydrogen cyanide beside hydrogen

sulphide and water. The ammonia must be destroyed before the gas is fed to the Claus reactors as it leads to catalyst poisoning. Commonly, the decomposition to hydrogen and nitrogen in the furnace is not sufficient, so that a catalytic fixed bed for the decomposition is included in the combustion chamber. Due to the fact that the operation temperature of the catalyst is limited, it is important to control properly the furnace temperature. Furthermore, the minimum temperature of the furnace is also a safety relevant constraint of the operation conditions. At too low temperatures an explosive atmosphere can be created, as the combustion process is operated under oxygen deficiency conditions. Here, an accurate model is required during the process design phase in order to make arrangements e.g. for a feed charge of natural gas or quenching steam. During the operation phase of a Claus plant the model can be used for an online process optimization (e.g. GASCONTROL) or for the prediction of the concentration of undesired substances such as organic sulphur compounds in the tail gas.

2. Development of the Claus process combustion model

The Claus process combustion model is based on three combustion mechanisms, which were combined together to one. The sources in the open literature of those mechanisms are referred bellow under the main combusted components.

1) Combustion of NH_3 - J.A. Miller et al [7].
2) Combustion of CH_4, C_2H_6 and HCN - ‘‘GRI-Mech Version 3.0‘‘ [9].
3) Combustion of SO_2 and H_2S - P. Glarborg et al [2], [3], [5] & [6].

Changes in these mechanisms were done in order to make the combining feasible. Some reactions were eliminated so as to avoid duplication. In addition, some reaction rates were changed for fitting the simulated results to the measurements. The model art chosen to describe the combustion is a continuous stirred-tank reactor model. Moreover, in order to simulate the whole combustion chamber, small segments was defined where each of them is described by a continuous stirred-tank reactor model.

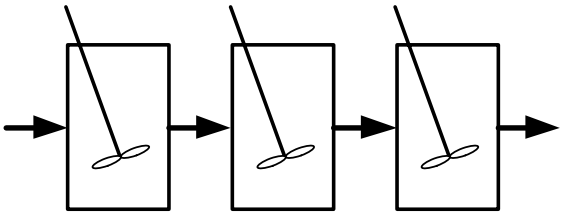

Fig. 3. PFR modeling by using a CSTR equations.

The mass balances in the model are formulated as follow:

$$0 = x_{j,in} F_{in} - x_{j,out} F_{out} + V_R \sum_{1}^{i=N_R} \nu_{j,i} \dot{r}_i \tag{4}$$

Where x_j and V_R are the mole fraction of component j and the reaction volume, respectively. The reactants are defined as ideally mixed. $\dot{r}_i$ represents the reaction rate of reaction i. The reaction rates ($\dot{r}_i$) is calculated as followed:

$$\dot{r}_i = K_{f,i} \cdot \prod_{j=1}^{N_C} C_j^{\nu'_{j,i}} - K_{b,i} \prod_{j=1}^{N_C} C_j^{\nu''_{j,i}} \tag{5}$$

Where, C_j denotes the concentration of component j. C_j is calculated under the assumption of an ideal gas behavior as followed:

$$C_j = \frac{P \cdot x_j}{R \cdot T} \tag{6}$$

$K_{f,i}, K_{b,i}$ represent the forward and backward reaction rate coefficients, respectively.
$K_{f,i}$ is calculated by the following Arrhenius equation:

$$K_{f,i} = A_i \cdot T^{\beta_i} e^{\frac{-Ea_i}{R \cdot T}} \tag{7}$$

$K_{b,i}$ is depended on the chemical equilibrium constant (K_{eq}) defined as followed:

$$K_{b,i} = \frac{K_{f,i}}{K_{eq}} \tag{8}$$

The chemical equilibrium constant is calculated from the Gibbs free energy for a chemical reaction (ΔG_i^0), which is calculated by using enthalpy and entropy polynomials taken from [1].

$$K_{eq,i} = \exp\left(\frac{-\Delta G_i^0}{RT}\right) = \exp\left(\frac{\Delta S_i^0}{R} - \frac{\Delta H_i^0}{RT}\right) \tag{9}$$

The standard-state molar enthalpy and entropy of the reaction i are obtained with the relationship:

$$\frac{\Delta S_i^0}{R} = \sum_{j=1}^{N_c} \nu_{j,i} \frac{S_j^0}{R} \tag{10}$$

$$\frac{\Delta H_i^0}{RT} = \sum_{j=1}^{N_c} \nu_{j,i} \frac{H_j^0}{RT} \tag{11}$$

The standard-state molar enthalpy and entropy for the component j are written as:

$$\frac{H_j^0}{RT} = a_{j,1} + \frac{a_{j,2}T}{2} + \frac{a_{j,3}T^2}{3} + \frac{a_{j,4}T^3}{4} + \frac{a_{j,5}T^4}{5} + \frac{a_{j,6}}{T} \tag{12}$$

$$\frac{S_j^0}{R} = a_{j,1}\ln T + a_{j,2}T + \frac{a_{j,3}T^2}{2} + \frac{a_{j,4}T^3}{3} + \frac{a_{j,5}T^4}{4} + a_{j,7} \tag{13}$$

3. The combustion model solver

In order to solve the equation system presented in section 2, a novel tailored solver has been proposed. The main challenge represents the development of a robust solver, which demands also low computation time. Commercial solvers were considered but they showed a low performance in solving this type of equation system. The model contains 78 material balances, which include 418 reaction rates, and one energy balance. Due to the high correlation between the reactor temperature and the material balances, the equations system had to be decoupled into to two tasks. The first one solves the reactor material balances for a given temperature and the second one represents an external loop function, which solves then the energy balance.

3.1 The material balance solver

The solver shown bellow is based on the Newton-Raphson approach, which was improved by adding additional functions so as to increase its performances. The proposed solver performs systematically. So for instance, the additional functions are described as followed:

1) Multiple sets of initial values - in case that no solution is found a new set of initial values is proposed and a new run starts.
2) Detect the validity of new iteration variables - the function checks whether the new iteration variables are within the boundaries defined, or if the computer memory has been exceeded (arithmetic overflow). In case of irregularity, a penalty function will be implemented.
3) Flexible convergence criteria - The convergence criteria is set to be a function of the iteration number.

4) Saving the best solution found - Corresponding to a flexible convergence criterion, if a previous convergence criterion is not fulfilled, still a previous solution set may fulfill the new convergence criteria.

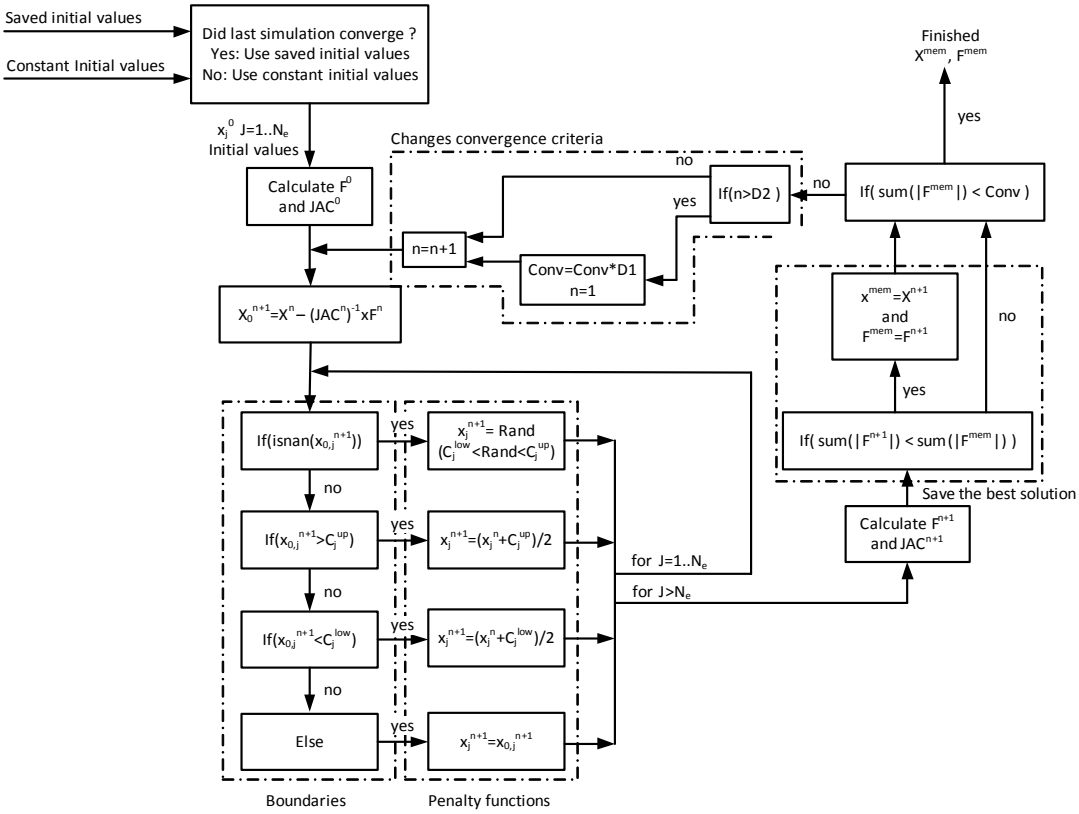

Fig. 4. The material balance solver algorithm

Further numerical methods, which are listed below, are significant so as to solve the linear equation system ($X_0^{n+1} = X^n - (JAC^n)^{-1} \times F^n$):

1) The Jacobi matrix (JAC) is calculated analytically. This operation is done by using an own-developed computer tool.
2) The LU factorization and the afterwards iterative refinement are computer functions, which are used to increase the condition number of the linear equation system.

3.2 The energy balance solver

A part of the energy balance solver corresponds to the material balance solver. The energy balance can be calculated sequentially. After that the material balance is solved for given values of X_{in}, P, F_{in} and T. The energy balance solver is based on the Newton method, where the reactor temperature (T) represents the only system variable.

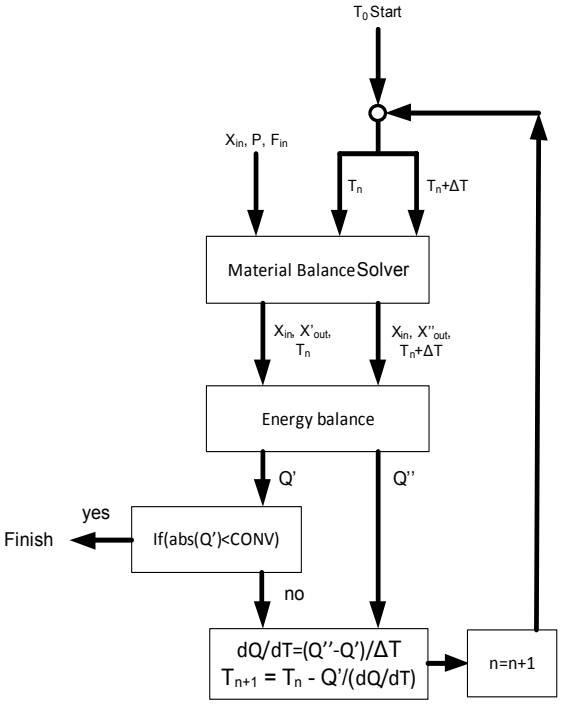

Fig. 5. The energy balance solver algorithm

4. Conclusions

The results obtained through the developed model show a good agreement with the measurements. Although, a comparison between model and the measurements is not introduced in this work, the fully model foundations is presented and can be used for Claus process combustion modeling or another combustion modeling cases. Moreover, the presented solver algorithm is highly robust. The computation time needed for solving a combustion modeling case is now estimated to be less than 3 sec. This advantage and others presented above make this model able to be used by an online simulation of a Claus process operation.

Equations symbols

F - Mole flow
x_i - Mole fraction
V_R - Reactor volume
$\nu_{j,i}$ - Stoichiometric coefficient
$\nu'_{j,i}$ - Forward stoichiometric coefficient
$\nu''_{j,i}$ - Reverse Stoichiometric coefficient
$\dot{r}_i$ - Reaction rate
N_R - Number of reactions
N_C - Number of components
$K_{f,i}$ - Forward rate constant
$K_{b,i}$ - reverse rate constant
K_{eq} - Equilibrium constant
C_j - Concentration
A_i - From the Arrhenius equation, pre-exponential factor
β - From the Arrhenius equation, temperature exponent
Ea_i - From the Arrhenius equation, activation energy
T - Temperature
P - Pressure
R - Gas Constant
H_j^0 - Standard-state molar enthalpy
S_j^0 - Standard-state molar entropy
G^0 - Standard-state molar free energy

Algorithm symbols

F^n - Vector of the zero function values
JAC^n - Jacobian matrix
X^n - Vector of the equation system variables
$x_{n,j}$ - Variable j
C_j^{up} - Upper boundary for variable j
C_j^{low} - Lower boundary for variable j

N_e - Number of equations

$CONV$ - Convergence criterion

$RAND$ - A random value

n - Iteration step

Q - The energy balance error

Literature

book:

[1] Burcat A., Ruscic B.: Third millennium ideal gas and condensed phase thermochemical database for combustion with updates from active thermochemical tables, The University of Chicago for the U. S. Department of Energy, September 2005.

Paper:

[2] Glarborg P.: Hidden interactions—Trace species governing combustion and emissions, Proceedings of the combustion institute, 31, (2007), 77–98.

[3] Rasmussen L. C.; Glarborg P.: Marshall P.: Mechanisms of radical removal by SO_2 , Proceedings of the combustion institute, 31, (2007), 339–347.

[4] Gargurevich A. I.: Hydrogen sulfide combustion: relevant issues under Claus furnace conditions, Ind. Eng. Chem. Res. (2005), 44, 7706-7729.

[5] Hindiyarti L.; Glarborg P.; Marshall P.: Reactions of SO_3 with the O/H radical pool under combustion conditions, J. Phys. Chem. A, (2007), 111, 3984-3991.

[6] Glarborg P.; Kubel D.; Dam-Johansen K.; Chiang H. M.; Bozzelli W. J.: Impact of SO_2 and NO on CO oxidation under post-flame conditions, International journal of chemical kinetics, vol. 28, 773-790 (1996).

[7] Miller A. J.; Smooke D. M.; Green M. R.; Kee J. R.: Kinetic modeling of the oxidation of ammonia in flames, AIChE Journal, November (1997) Vol. 43, No. 11.

[8] Jensen A.; Johnsson E. J.; Dam-Johansen K.: Catalytic and gas-solid reactions involving HCN over limestone, AIChE Journal, November (1997) Vol. 43, No. 11.

[9] GRI-Mech Version 3.0, http://www.gri.org, (7/30/1999).

[10] Claus F. C.: UK Patents No. 5958. 1883

[11] Elsner M. P.: Experimentelle und modellbasierte Studien zur Bewertung des adsorptiven Reaktorkonzeptes am Beispiel der CLAUS-Reaktion, Univ., Dissertation Dortmund, 2004, Logos, Berlin 2004. ISBN 3-8325-0565-2

[12] Brettschneider O.: Synthese und Optimierung der Kokereigasreinigung. Dissertation, TU-Berlin, FG DBtA, 2004.

18th International Conference Process Engineering and Chemical Plant Design
Günter Wozny and Łukasz Hady, Editors

MICHAL GULA[*], JÖRG STEINBACH[*], KAI HOLTAPPELS[**], AYDAN ACIKALIN[**], HANS-PETER SCHILDBERG[***], ARKADIUSZ KOBIERA[****]

SAFETY RELATED CHARACTERISTICS OF CHEMICALLY UNSTABLE GASES

Abstract

The explosive decomposition of chemically unstable gases in closed systems was examined. In order to analyse the experiments the pressure-time (p-t) histories were measured. In particular, this included the determination of the resulting explosion pressures and the rates of pressure rise at varied initial temperatures and pressures in five autoclaves with different geometries and sizes. The results of the experiments showed that not only the volume but also the form and orientation of the vessel strongly influence the flame propagation. In order to estimate the effect of an explosion of a pure chemically unstable gas the simulation model "FireBall" [1] was used. These calculations are based on the modeling of a laminar and a turbulent flame. By means of an implemented sub model the influence of built-in obstacles on the reaction dynamics can be predicted.

Keywords: explosion, decomposition, nitrous oxide

1. Introduction

Gas explosions are exothermic reactions with a rapid rise in temperature and pressure. Such chemical reactions can cause damage to chemical plants or personal life. In order to initiate an explosion usually a fuel gas and an oxidizing agent, e.g. oxygen, together with a sufficiently strong ignition source are required. Furthermore, the gas mixture must be within the explosion range. In contrast to combustion reactions, chemically unstable gases can explosively decompose without the presence of any reacting agent. Because of that, the handling of chemically unstable gases requires special preventive measures. Unfortunately, the knowledge about flame propagation of chemically unstable gases and about influencing

[*] Technische Universität Berlin, Straße des 17. Juni 135, 10623 Berlin, Germany
[**] BAM Bundesanstalt für Materialforschung und –prüfung, Unter den Eichen 87, 12205 Berlin, Germany
[***] BASF SE, 67056 Ludwigshafen, Germany
[****] Politechnika Warszawska, Pl. Politechnik 1, 00-661 Warszawa, Poland

parameters is rather poor. Using the example of the decomposition of nitrous oxide (N_2O) and nitrogen monoxide (NO) the explosion behavior in closed systems was investigated.

2. Experimental Setup

The influence of the initial pressure, the initial temperature, and, in particular, the influence of the reaction vessel itself like shape and orientation were investigated using five different autoclaves; three with a cylindrical volume (3.0 L, 6.5 L and 10 L) having a diameter-to-length ratio of 1/1, one cylindrical vessel with a volume of 100 L and a diameter-to-length ratio of 1/3, and one spherical vessel of 50 L (see Fig. 1). Furthermore, the 100 L vessel was placed in a rack in order to change its orientation.

Fig. 1. a) Cross-section of the 3.0 L vessel, b) cross-section of the 6.5 L vessel, c) 10 L vessel with a window, d) 100 L vessel placed in a rack in order to change orientation (horizontal or vertical), and e) 50 L spherical vessel.

3. Results

In all explosion tests the decomposition was initiated with the aid of an exploding wire (depicted in EN 13673). In general, decompositions –compared to fast oxidation reactions– can start very slowly when initiated by ignition. The typical evolution of slowly progressing reactions is strongly affected by free convection. Immediately after ignition, the flame speed is relatively slow compared to the free convection. That means the flame moves upwards by buoyancy effects. At the same time the reaction zone grows slowly. The flame can propagate undisturbed until the upper wall is reached. When this finally has happened heat loss will occur through heat transfer to the wall while the gas is still decomposing. Due to this heat loss the reaction will be quenched. The time when the quenching takes place for the first time is very crucial for the further evolution of the decomposition. Generally, the flame speed of decomposition reactions is by several orders of magnitude smaller than the flame speed of typical combustion reactions. In case of decomposition reactions the flame speed amounts to several centimeters per second, only.

In order to reduce the experimental effort that is associated with the investigation of safety related characteristics of chemically unstable gases the modified simulation model "FireBall" was used. Originally the model was developed for simulations of explosions of fuel/air mixtures that are close to their stoichiometric compositions. The flame propagation model contains different sub models that, for example, consider the heat transfer to the walls, free convection and the interaction between obstacles and the flame. Based on the simulated pressure curves the following important safety related characteristics can be determined: the explosion pressure, the rates of pressure rise and K_G-values, respectively.

Selected results of experiments and simulations are shown in Fig. 2. For both unstable gases, N_2O and NO, the modified simulation model „FireBall" yields results that are in good agreement to experimental data. More results are presented in [2].

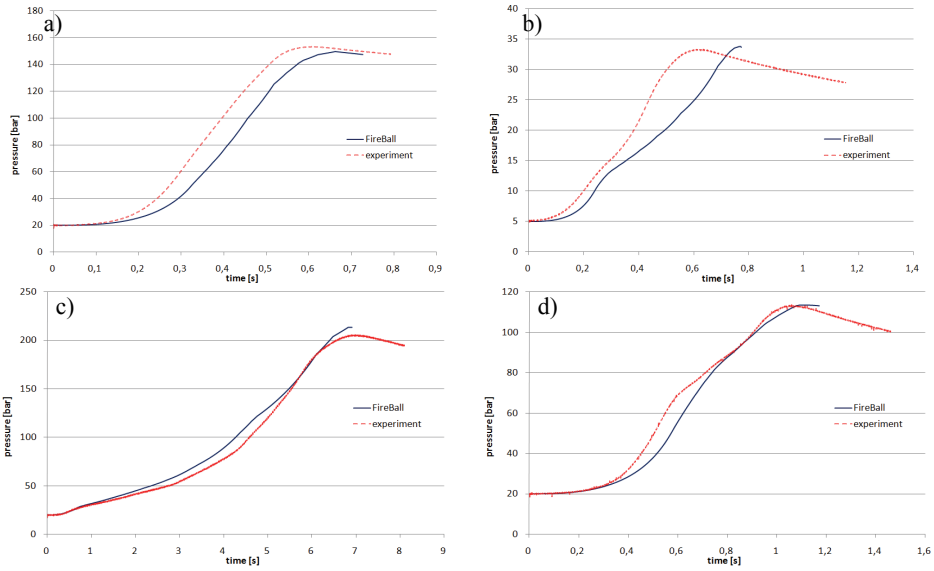

Fig. 2. Simulated and experimental pressure curves of the decomposition of nitrous oxide N_2O (a, b, c) and nitrogen monoxide NO (d) in different vessels: a) 6.5 L vessel, T_0 = 200 °C, b) 3 L vessel, T_0 = 200 °C, c) 100 L vessel (horizontal), T_0 = 50 °C, d) 6.5 L vessel, T_0 = 220 °C.

Using "FireBall" it is possible to obtain important information about the evolution of the decomposition depending on the reaction vessel. The results for N_2O, for example, show very clearly how strong the influence of shape and orientation is. Three different vessels with the same volume of 50 L were considered in the simulations: a cylindrical vessel with a diameter-to-length ratio of 1/7 (conventional gas cylinder), a cylindrical vessel with a diameter-to-length ratio of 1/1 and a spherical vessel. For the cylindrical vessels different orientations were used as simulation input. The results are shown in Fig. 3. The highest explosion pressures are similar for all vessels. However, the time at which the explosion pressures reach their maximum is significantly different in each case. Additionally, the rates of pressure rise and K_G-values, respectively, strongly depend on the reaction vessel where the decomposition takes place. In particular, the time at which the maximum value of the pressure rise is reached is being influenced. K_G-value is the maximum value of the pressure rise in relation to vessel volume:

$$K_G = \left(\frac{dp}{dt}\right)_{max} V^{\frac{1}{3}}$$

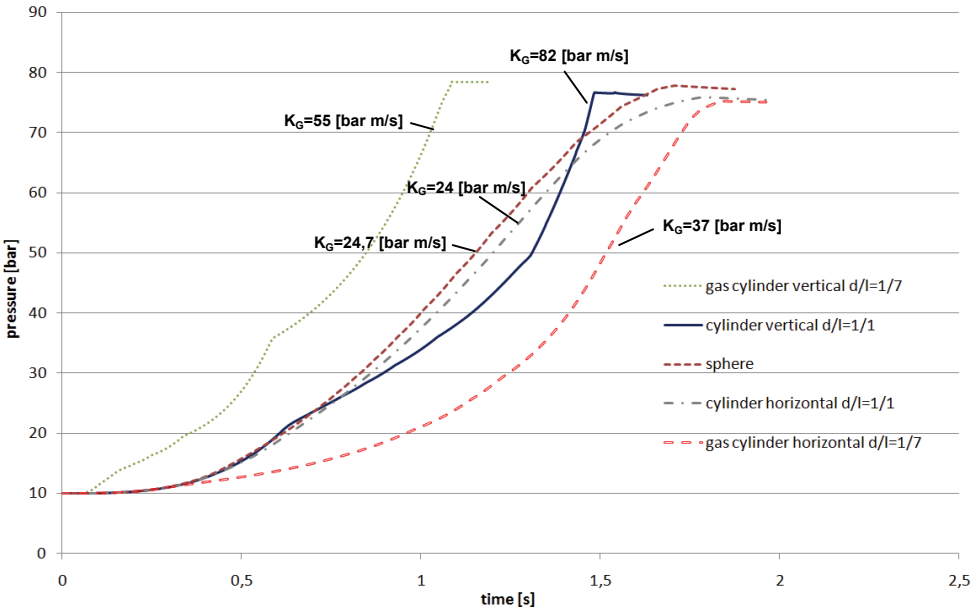

Fig. 3. Simulated pressure curves for N_2O decomposition in a cylindrical vessel: The curves are being influenced by the shape and the orientation of the explosion vessels (V = 50 L, T_0 = 200 °C, p_0 = 10 bar).

With the modified "FireBall" the influence of obstacles on the decomposition can be predicted. The sub model is based on turbulent energy that is generated when gas flows around the obstacles [3]. Because of the turbulent energy the flame propagation can be accelerated. A model validation was accomplished for a methane/air mixture in a 40 L vessel [3]. The results for the decomposition of nitrous oxide that depend on specific parameters of the obstacle are shown in Fig. 4. The decomposition was simulated for a spherical vessel with a volume of 50 L at an initial pressure of 5 bar and initial temperature of 200 °C.

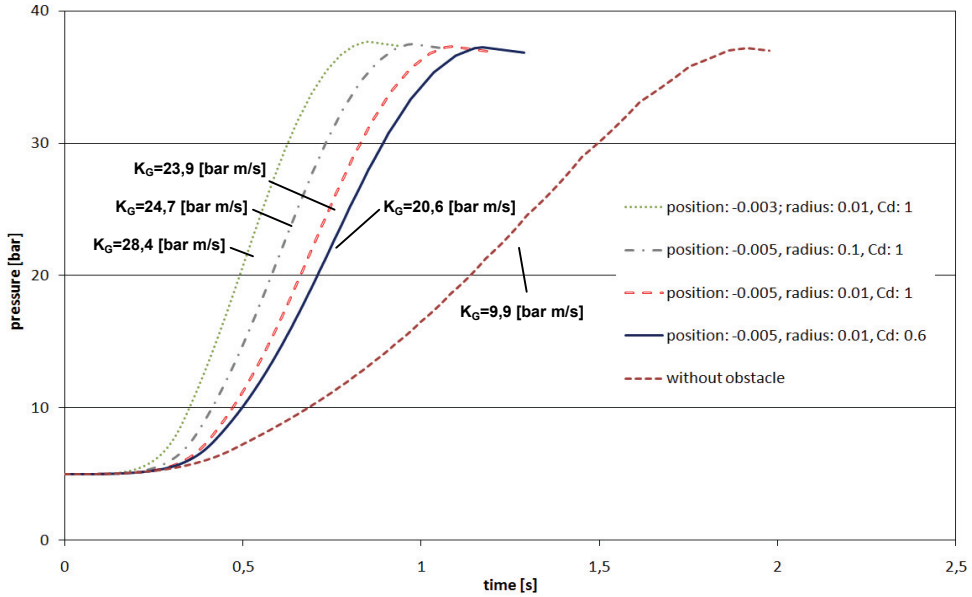

Fig. 4. Simulated pressure curves for N_2O decomposition in a spherical vessel: The curves are being influenced by different obstacles (V = 50 L, T_0 = 200 °C, p_0 = 5 bar).

4. Summary

Important safety related characteristics like explosion pressure and rate of pressure rise were determined for the decomposition of the two chemically unstable gases nitrous oxide and nitrogen monoxide. Five different explosion vessels were used for the experiments. It was shown that, in particular, shape and orientation have a strong influence on the evolution of the decomposition reactions. Additionally to the experiments simulations were carried out using the modified model "FireBall". The computational results demonstrate that the evolution of the decomposition reactions can be predicted. This is also true for reactions that take place in vessels with built-in obstacles that affect the way the gases decompose.

Literature

[1] Kobiera A., Kindracki J.: A new phenomenological model of gas explosion based on characteristics of flame surface, Journal of Loss Prevention in the Process Industries 20 (2007) 271–280.

[2] Gula M.: Explosionstechnische Charakterisierung chemisch instabiler Gase, Dissertation, Technische Universität Berlin, Berlin 2010.

[3] Kobiera A., Kindracki J.: Explosion propagation model, software development. Second report on influence of obstacles, turbulence and fuel concentration, elongated vessels and multi-channels, www.safekinex.org.

18th International Conference Process Engineering and Chemical Plant Design
Günter Wozny and Łukasz Hady, Editors

Niklas Paul, Matthias Kraume*

Influence of surfactants on fluid dynamics and mass transfer of single drops

Abstract

The understanding of the mechanisms influencing the fluid dynamics and the mass transfer in liquid/liquid systems is of great interest, due to its frequent use in the chemical industry. For some applications the use of surfactants is on purpose, but the exact mechanism of the influence of these amphiphilic molecules is not understood, yet. Especially in micellar Systems. In this work the fluid dynamics and the mass transfer of single droplets will be observed in surfactant solutions. The liquid/liquid system water/octanol will be used as a model system. The influence of surfactants will be tested with the ionic surfactant sodium dodecyl sulfate (SDS). Results show that the use of SDS causes a decrease of the interfacial tension as well as a decrease of the drop rise velocity. These phenomena were expected. But the increase of the mass transfer was not expected.

Keywords: Surfactant, mass transfer, fluid dynamics, micellar systems.

1. Introduction

One of the most important homogenous catalyzed reactions in the chemical industry is the hydroformylation [1]. Olefines will react to an aldehyde. The solubility of olefines in water decreases with an increase of the chain length. Renewable recourses such as vegetable oils consist of long-chain alkenes, activating these molecules by introducing a functional group should be of great interest [2]. On this way it is possible to produce basic chemicals for the chemical industry out of renewable recourses. The Ruhrchemie/Rhone-Poulenc Process fails due to the low solubility of long chain olefins. One possibility realizing this reaction is the use of surfactants [1]. Surfactants are so called amphiphilic molecules, which adsorb, because of their molecular structure at hydrophobic/hydrophilic interfaces. This adsorption of surfactant molecules at the interface influences the fluid dynamics and the mass transfer. Both influence the yield and the selectivity of the hydroformylation.

* Fachgebiet Verfahrenstechnik, TU Berlin, Ackerstraße 71-76, Berlin 13355, Germany

To understand the complex momentum- and mass transport processes the system needs to be simplified. Therefore the investigations in this work will be carried out in a model liquid/liquid system and single droplets will be observed.

While a single droplet is rising in a surfactant solution, the amphiphilic molecules will adsorb at the interface. Due to the shear stress, molecules will gather at the rear end of the droplet, thus an interfacial tension gradient occurs [3]. Additionally, the adsorbed molecules influence the internal circulations as well as the mobility of the interface [4]. For high surfactant concentrations, when the interface is completely covered with surfactant molecules and micelles are formed, the adsorption layer of the surfactant molecules creates an additional mass transport resistance and the micelles may solubilize the component, which should be transported. All of these effects are responsible for the influences of surfactants on fluid dynamics and mass transfer around single moving droplets. To understand the effects and the mechanisms experiments have to be carried out.

2. Experimental

The regarded system for the experiments consisted of the following components: The continuous phase has been water, the dispersed phase has been octan-1-ol, PADA (Pyridine-2-azo-dimethylaniline) was the transferred component and sodium dodecyl sulfate (SDS) was used as an ionic surfactant. All measurements carried out in this work are highly sensitive to impurities; hence all components used were at highest purity. Due to the expected low interfacial tension of the system water/octanol the spinning drop method was used for the determination of the interfacial tension. The experimental setup used for the determination of fluid dynamics and mass transport is described in Wegener (2007) [5].

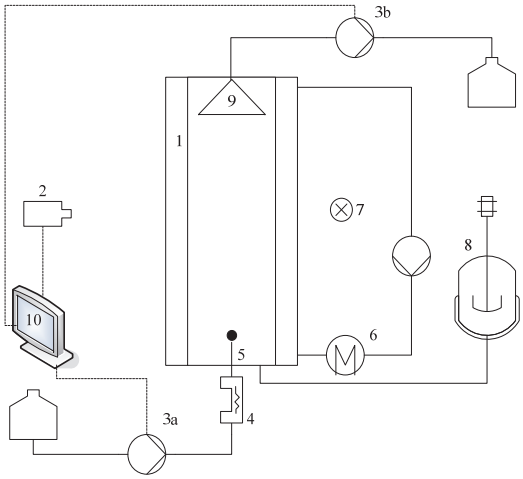

Fig. 1. Experimental setup: (1) Glass column, (2) camera, (3a, 3b) Hamilton PSD/2 module, (4) solenoid device, (5) nozzle, (6) thermostat, (7) illumination, (8) saturation tank, (9) glass funnel, (10) computer control

The glass column's height is 1000 mm and its diameter is 75 mm. A jacket surrounds the glass column, due to the similar refraction index to borosilicate glass it is filled with glycerol. Every experiment was carried out at 25°C; therefore the RK 20 thermostat by LAUDA® was used. Generating a specific drop volume at one of the used nozzles was realized by a Hamilton® PSD/2 module. The solenoid device was used to release the droplet at a specific volume respectively diameter. For realizing a wide range of droplet diameters five different nozzles (see table 1) have been used.

T a b l e 1

Used nozzles for realizing a wide range of droplet diameters

	N1	N2	N3	N4	N5
OD (mm)	0.5	1.0	3.0	4.0	6.0
ID (mm)	0.2	0.4	2.0	3.0	4.0
Material	Borosilicate	Borosilicate	Stainless Steel	Stainless Steel	Stainless Steel

For the determination of the drop rise velocity a high-speed camera (Photonfocus® MV-752-160) has been installed in a perpendicular position to the column. With a frame rate of 100 Hz up to 3000 pictures for one sequence could be stored on the computer (10). The analysis of one sequence has been carried out with Image-Pro Plus® 5.1 by Media Cybernetics. The vertical and horizontal position of the drop (mass center) is the result of this analysis. With this information the drop rise velocity can be calculated.

For the determination of the mass transfer the droplets must be collected with the glass funnel (9). At the funnel's neck a tiny dispersed phase is kept; thus the droplets can coalescence and can be taken out of the system by the second Hamilton® PSD/2 module. The funnel is moveable in its position; therefore different contact times can be realized. For every investigation of the mass transfer seven different positions (25, 50, 100, 175, 325, 500, 700 mm) respectively contact times were adjusted. At every position three samples are taken after exchanging the dispersed phase at the funnel's neck and in the tube. The samples were analysed with a Specord 210 photometer by Jena Analytik®.

3. Results and Discussion

In this work the influence of surfactants on the fluid dynamics and the mass transfer shall be obtained. The interfacial tension influences both the fluid dynamics as well as the mass transfer; thus it is necessary to measure the dependence of the surfactant concentration on the interfacial tension.

3.1. Interfacial tension

The exact knowledge of the interfacial tension is of great interest in this work. On one hand side the interfacial tension influences the drop formation. Furthermore the interfacial tension affects the stability of a droplet. With the use of surfactants the interfacial tension will be decreased. Figure 2 shows the interfacial tension at steady state in dependence of the SDS- concentration.

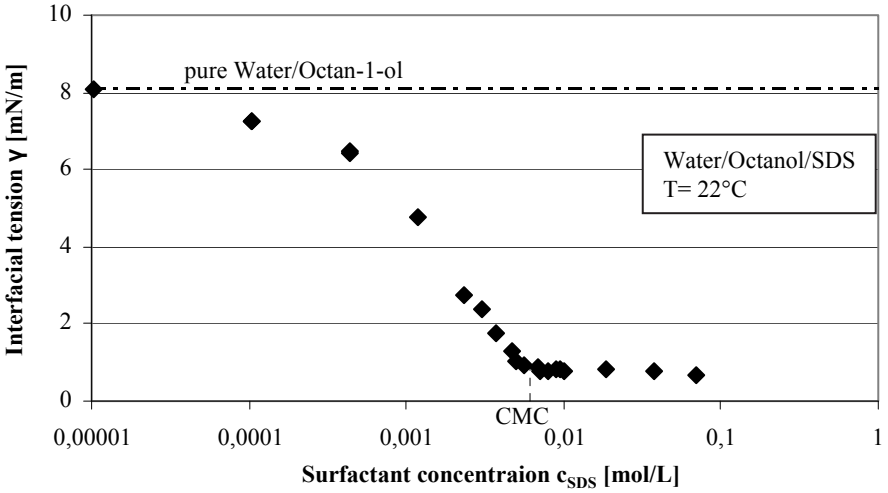

Fig. 2. interfacial tension in dependence of the logarithm of the surfactant concentration

With an increase of the SDS concentration the interfacial tension decreases. For low surfactant concentrations ($c_{SDS}<10^{-5}$ mol/L) there is only a small decrease of the interfacial tension. Due to the logarithmic scale of the surfactant concentration the interfacial tension decreases linearly with the increase of the surfactant concentration, at higher surfactant concentrations ($c_{SDS}>10^{-4}$ mol/L). After reaching the critical micelle concentration (6.5 mmol/L) the interfacial tension stays at a constant value of 0.7 mN/m.

The literature value of the interfacial tension of the pure system water/octan-1-ol could be reproduced very precisely as shown in table 2. The value for the critical micelle concentration (CMC) is smaller than the literature values. Table 2 shows the literature values of the CMC for the system water/air. For other liquid/liquid systems the critical micelle concentration of SDS could also be reduced [10].

T a b l e 2

The experimental values of the interfacial tension and the critical micelle concentration (CMC) in comparison with the literature values

Literature [7-9]		This work	
γ [mN/m]	**CMC [mmol/L]**	**γ [mN/m]**	**CMC [mmol/L]**
8.09≈ 8.1	7.8- 8.25	8.08 ≈ 8.1	6.5

The measured behavior of the interfacial tension in dependence of the surfactant concentration can be used to calculate the adsorption of the surfactant molecules at the interface. First the interfacial pressure has to be calculated:

$$\pi^{\gamma} = \gamma_0 - \gamma_{cs} \tag{1}$$

After plotting the interfacial pressure against the logarithm of the surfactant concentration, the Szyskowski-Equation [11]:

$$\pi^{\gamma} = nRT\,\Gamma_{\max}(\ln c - \ln b)\,, \tag{2}$$

can be used for low surfactant concentrations to determine the maximal surfactant concentration at the interface $\Gamma_{\max}$ as well as the Langmuir-constant *b*. This constant represents the relationship between the desorption-rate and the adsorption-rate. For small values of *b* the adsorption-rate is high and the surfactant's interfacial activity is high [11]. The determined values for $\Gamma_{\max}$ and *b* can be used to calculate the coverage of the interface with surfactant molecules at a certain surfactant concentration [11]:

$$\Gamma = \frac{\Gamma_{\max}\, c_S}{b + c_S} \tag{3}$$

Although, all criteria are not fulfilled this adsorption-isotherm gives a good first impression of the coverage of interfacial active substances at the interface. For the used system a value of $4.97 \cdot 10^{-7}\, mol/L$ had been calculated for the maximal surfactant concentration at the interface. The value for *b* was $4.6 \cdot 10^{-4}[-]$. Due to the small value of b the used surfactant is highly interfacial active in the system of water/octan-1-ol. Both values can be used to calculate the surfactant concentration at the interface; thus the coverage of the interface can be calculated. The knowledge of the interface's coverage is of great interest for discussion of influences on the fluid dynamics and the mass transfer.

3.2. Fluid dynamics

Figure 3 shows the transient drop rise velocities for different droplet diameters. For a clearer representation only one representative sequence out of fifteen is shown in this diagram.

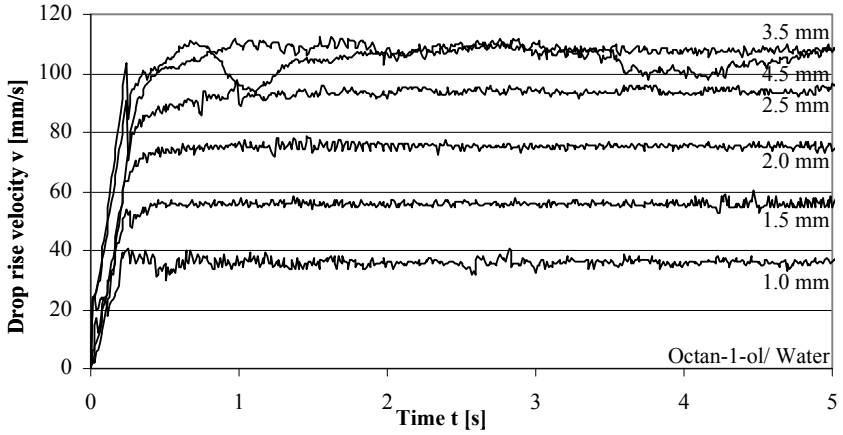

Fig. 3. transient drop rise velocities for different droplet diameters (1.0 mm, 1.5 mm, 2.0 mm, 2.5 mm , 3.5 mm and 4.5mm)

After releasing, the droplets accelerate to their terminal rise velocity. For droplets with a diameter smaller than 2.5 mm the rise velocity stays after the acceleration constant. For

droplets bigger than 2.5 mm a velocity oscillation occurs. The occurring oscillations are not as distinctive as in the observed system by Wegener et al [6], in this work the system water/toluene was observed. The main differences in the physical properties between the systems water/octan-1-ol and water/toluene are the interfacial tension and the ratio of the viscosities. Due to the lower interfacial tension of the system water/octan-1-ol the Weber-, Morton- and Eötvös numbers of the water/octan-1-ol system are higher than the corresponding numbers in the system water/toluene. Therefore a deformation of the droplets should occur for smaller drop diameters in the system water/octan-1-ol than in the system water/toluene. But due to the high viscosity ratio of the water/octan-1-ol system the droplets behave almost like rigid spheres. In figure 4 the drag coefficient is shown as a function of the Reynolds number.

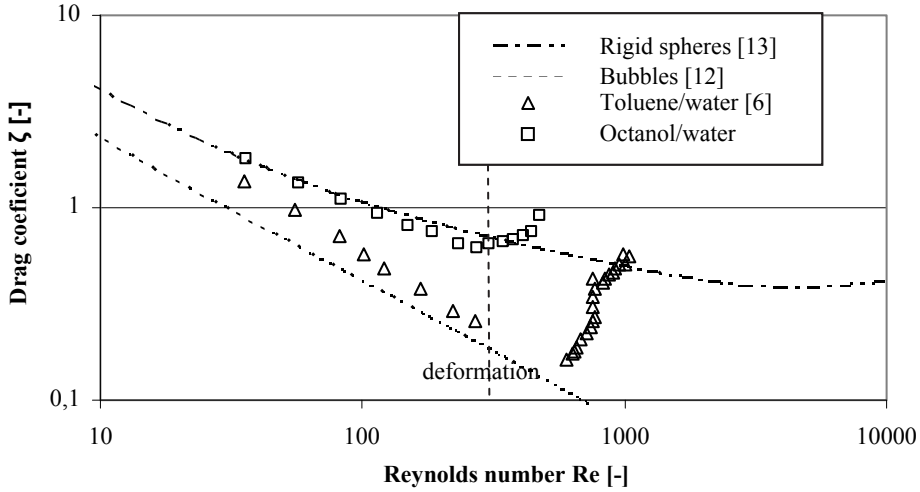

Fig. 4. drag coefficients; comparison between the experimental results and literature correlations

The drag coefficient of the octan-1-ol droplets in the water is higher than the drag coefficient of the toluene droplets; hence the toluene droplets of the same size rise faster than the octan-1-ol droplets. Furthermore, this diagram (figure 4) shows the correlations of the drag coefficients for bubbles [13] and for rigid spheres [12]. For a high flexible interface the drag coefficient will be lower than for a less mobile interface; thus bubbles rise faster than droplets with a rigid interface. The octan-1-ol droplets have almost the same characteristics as a rigid sphere; hence the mobility of the interface is limited compared to the mobility of the toluene/water interface. Therefore the occurring velocity oscillations of the toluene droplets are more distinctive than those of the octan-1-ol droplets.

While a droplet is rising in a surfactant solution the characteristics of its interface will change due to the adsorption of the surfactant molecules. This can be observed in figure 5. This diagram shows the transient drop rise velocity of a 2 mm octan-1-ol droplet in different SDS solutions with different concentrations. With an increase of the SDS concentration the interface will be covered with SDS molecules, which influence the interfacial tension as well as the mobility of the droplet. The drop rise velocity will

decrease due to the decrease of the interfacial mobility and the increase of the drag coefficient. Figure 5 shows also the calculated value for the drop rise velocity of a drop with a rigid sphere. For a SDS concentration of 10^{-3} mol/L the droplet behaves like a rigid sphere. Due to the low interfacial tension the range of the droplet's diameter was limited.

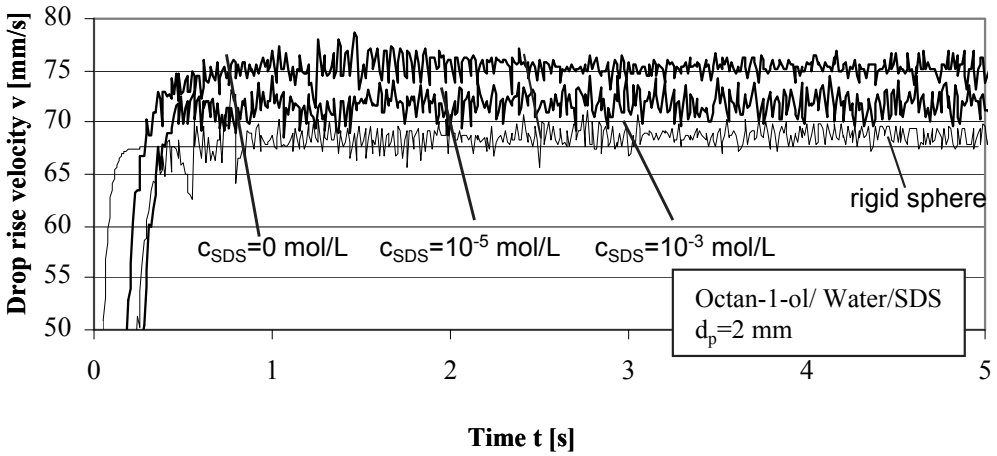

Fig. 5. transient drop rise velocity for a droplet diameter of 2 mm for different surfactant concentrations (0, 10^{-7}, 10^{-5}, 10^{-3}) and for the calculated value of a droplet with a rigid sphere [14]

Figure 6 shows the average terminal drop rise velocity in dependence of the interface's coverage with surfactants molecules for three different diameters.

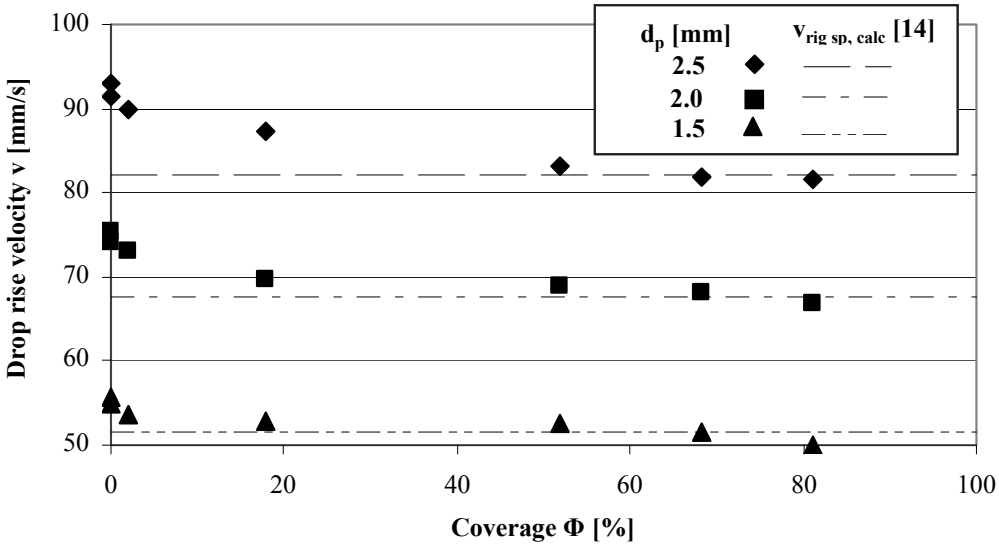

Fig. 6. Terminal drop rise velocity in dependency of the interface's coverage with surfactant molecules for different diameters and values of the rigid sphere for the corresponding diameter [14].

The results of section 3.1 were used to calculate the coverage of the surfactant molecules at the interface at a certain surfactant concentration. With increasing the surfactant concentration the coverage of the interface with surfactant molecules will increase, this causes a decrease in the mobility and will lead to a reduced terminal velocity. This can be observed for all three droplet diameters shown in this diagram. Furthermore, this diagram shows the drop rise velocities of the corresponding diameters for a rigid sphere. For a coverage of almost 50 percent the drop rise velocities of all three droplet diameters are reduced to the values of the corresponding rigid spheres.

Both phenomena shown in this diagram (figure 6); the influence on the fluid dynamics as well as the adsorption layer of surfactant molecules will influence the mass transfer.

3.3. Mass transfer

There are several approaches describing the influences of surfactants on the mass transfer as mentioned in section 1. Mostly a decrease of the mass transfer is described in the literature while increasing the surfactant concentration. Figure 7 shows the dye concentration as a function of time for different surfactant concentrations. The transport direction was chosen from the continuous phase to the dispersed phase.

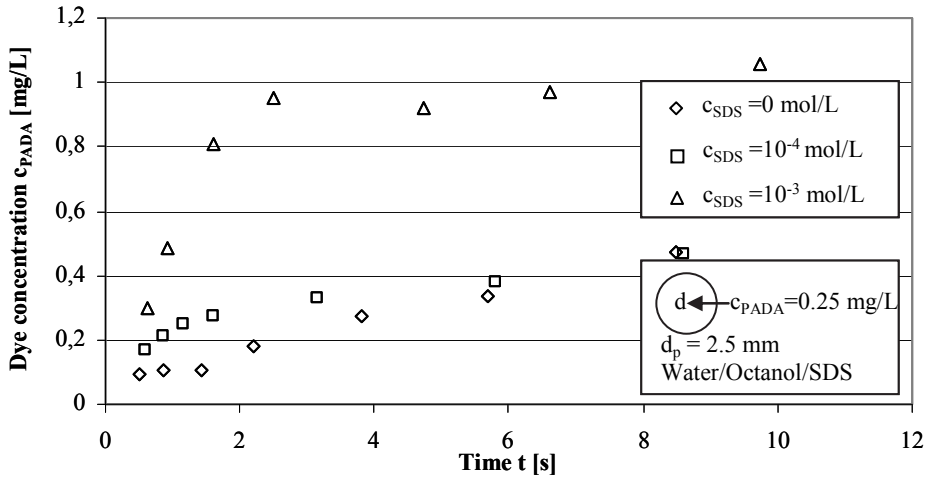

Fig. 7. dye concentration as a function of time for different surfactant concentrations

This diagram shows; PADA was transported from the continuous phase into the droplet, the longer the contact time of the droplet has been, the higher was the dye concentration of the droplet. With increasing the SDS concentration the dye concentration in the droplet was increased. As mentioned above, a decrease in the mass transfer was expected. While a droplet is rising in a surfactant solution the surfactants will be adsorbed at the interface and gather at the rear end of the droplet creating an interfacial tension gradient [3]. This Marangoni convection is able to improve the mass transfer, but improving the mass transfer that much is probably caused by the determination method of the mass transfer. Due to the

high coverage of surfactant molecules at the interface (see figure 6) the coalescence is hindered; thus the contact time is increased. Therefore the contact time given in this diagram is not the real contact time and the results are distorted.

4. Conclusion

The interfacial tension of the system water/octan-1-ol for different SDS concentrations was measured. Out of these measurements the adsorption of the surfactant was calculated. The adsorption behavior was used to explain the decrease of the fluid dynamics, due to the reduction of the interface's mobility. Furthermore, the accumulation of the surfactants at the liquid/liquid interface should be used to explain the influence of the mass transfer. The expected results were not obtained, due to the measurement method. The contact time couldn't be determined appropriately, due to the reduction of the coalescence. Improvements in the measurement method need to be made, to determine the mass transfer.

Acknowledgement

This work is part of the Collaborative Research Centre "Integrated Chemical Processes in Liquid Multiphase Systems" coordinated by the Technische Universität Berlin. Financial support by the Deutsche Forschungsgemeinschaft (DFG) is gratefully acknowledged (TRR 63).

Symbols

Notation

c= concentration, mol/L or mg/L
d= diameter, mm
ID= inner diameter, mm
n= number of ions
N= Nozzle
OD= outer diameter, mm
R= Gas constant
t= time, s
T= temperature, °C
v= drop rise velocity, mm/s

Greek letters

γ= interfacial tension, mN/m
Φ= coverage at the interface, %
ζ= drag coefficient

Dimensionsless numbers

Eo= Eötvös number = $\frac{d_p^2 \Delta\rho g}{\gamma}$

Mo= Morton number = $\frac{\eta^2 \Delta\rho g}{\rho\gamma^3}$

Re= Reynolds number = $\frac{d v \rho}{\eta}$

We= Weber number = $\frac{v^2 d\rho}{\gamma}$

Subscripts

0= no surfactant
cs= surfactant concetration
Max= maximal
p= particle
s= surfactant
calc= calculated
rig sp= rigid sphere

Literature

[1] Dwars T., Paetzold E., Oehme G.: Angewandte Chemie , 117 (2005), 7338– 7364
[2] Behr A., Westfechtel A.: Chemie Ingenieur Technik, 79 (2007), 621-636
[3] Chen J. et al.: Journal of Colloid and interface science, 178 (1996), 144-155
[4] Dehkodi A. et al: Industrial & Engineering Chemical Research, 46 (2007), 1563-1561
[5] Wegener M., et al: Chemical Engineering Science, 62 (2007), 2967-2978
[6] Wegener M, Paschedag A. R., Kraume M. : AIChE J, 56 (2010), 2-10
[7] Villers D, Platten K.J.: Journal of Physical Chemistry, 92 (1988), 4023-4024
[8] Paula et al: Journal of Physical Chemistry, 99 (1995), 11742-11751
[9] Saien J., Akbari, S.: Journal of Chemical & Engineering Data, 53 (2008), 525-530
[10] Chen L.-H., Lee Y.-L.: AIChE J, 46 (2000), 160-168
[11] Schwurger M., Findenegg G. et al: Lehrbuch der Grenzflächenchemie, Georg Thieme Verlag, Stuttgart 1996.
[12] Brauer H.: Fortschritt in der Verfahrenstechnik, 17 (1979), 61-99
[13] Brauer H.: Chemie Ingenieur Technik, 45(1973), 1099-1103
[14] Martin H.: Chemie Ingenieur Technik, 52 (1980), 199-209

18th International Conference Process Engineering and Chemical Plant Design
Günter Wozny and Łukasz Hady, Editors

JAN TALAGA*

UNTERSUCHUNGEN ZUR FLUIDDYNAMIK VON EIN- UND ZWEIPHASIGEN RÜHRWERKSSTRÖMUNGEN

Zusammenfassung

In der Arbeit wurden die Ergebnisse der experimentellen Untersuchung ausgewählter Größen, die die Fluiddynamik der Rührwerksströmung charakterisieren, dargestellt. Es wurden die momentanen Geschwindigkeiten der gerührten Flüssigkeit gemessen. Diese Messungen wurden unter Anwendung eines Laser-Doppler-Anemometers durchgeführt. Die ermittelten momentanen Geschwindigkeiten erlaubten die Mittel- und Schwankungsgeschwindigkeiten der flüssigen Phase zu bestimmen. Anhand von den Meßergebnissen wurden die Geschwindigkeitsprofile im Rührerausströmbereich ermittelt und im Form von Korrelationsgleichungen dargestellt.

Die experimentellen Untersuchungen zu den zweiphasigen Rührwerksströmungen wurden für das Feststoff-Flüssigkeits-System durchgeführt. Ziel dieser Untersuchungen war es, den Einfluß von den dispergierten festen Partikeln auf die fluiddynamischen Parameter der gerührten kontinuierlichen Phase zu bestimmen. Im untersuchten Größenbereich der Feststoffpartikeln und der Feststoffkonzentration wurde eine Anfachung der Turbulenz im Rührerausströmbereich gegenüber der einphasigen Strömung festgestellt.

Keywords: Rühren, Rührwerk, Turbulenz, LDA

1. Einleitung und Zielsetzung

Obwohl das Mischen zu weit in der Industrie verbreiteten Grundoperationen gehört, sind noch viele theoretische und technische Probleme nicht zu Ende gelöst. Die Ursachen dafür liegen einerseits in der komplexen Natur der industriellen Anwendungen des Mischens und andererseits in steigenden Qualitätsansprüchen bezüglich der Mischprodukte [1]. Infolgedessen nimmt die Bedeutung der Mischtechnik immer zu.

Eine Vielzahl von verfahrenstechnischen Apparate wird in der industriellen Praxis zwei- oder mehrphasig betrieben. Darin spielen fest-flüssig betriebene Rührreaktoren eine bedeutende Rolle. Um solche Apparate möglich optimal gestalten zu können, sind detaillierte Kenntnisse der Fluiddynamik der gerührten Feststoff-Flüssigkeits-Systeme erforderlich. In Hinsicht auf die praktische Anwendung von zweiphasig betriebenen

* Politechnika Krakowska, Al. Jana Pawła II 37, 30-838 Kraków, Polska

Rührbehältern kommt dabei den turbulenten Strömungsvorgänge im Apparat eine besondere Bedeutung zu. Die Interaktionen turbulenter Strömungen mit einer dispersen Phase, bestehend aus festen Partikeln, sowie deren Rückwirkungen auf das Trägerfluid sind heutzutage weitestgehend ungeklärt. Es ist darum notwendig, experimentellen Untersuchungen durchzuführen, um erweiterte Kenntnisse zu diesem Problem zu gewinnen.

In diesem Zusammenhang war ein Ziel der vorliegenden Arbeit, den Einfluß von suspendierten Feststoffpartikeln auf die turbulente Strömung der gerührten Flüssigkeit experimentell zu ermitteln. Dazu wurden Mittel- und Schwankungsgeschwindigkeiten zuerst in einer reinen Flüssigkeit und später in der Flüssigkeit mit der gleichzeitigen Suspendierung der Feststoffpartikel gemessen. Eine besondere Aufmerksamkeit wurde dabei einer Rührerausströmzone gewidmet. Die Messungen momentaner Geschwindigkeiten in einer Rührwerksströmung wurden mit einer berührungslosen Messmethode unter Anwendung der Laser-Doppler-Anemometrie durchgeführt.

2. Versuchsanlage

Die experimentellen Untersuchungen wurden in einer Versuchsanlage, die schematisch in Abb. 1 dargestellt wird, durchgeführt. Der zylindrische Rührbehälter aus Glas mit dem Durchmesser von D = 286 mm wurde mit 4 Stromstörern und mit einem 6-Blatt-Scheibenrührer (mit Durchmesser d = 1/3 D und mit den anderen Standardabmessungen [2]) ausgerüstet. Um einen Brechungsindex (n_D = 1,473) im ganzen gemessenen System anzupassen, kam das Dimethylo-sulfo-oxyd (DMS, Dichte ρ_{Fl} = 1100 kg/m^3, dynamische Viskosität η_{Fl} = 2,3 mPas.) als gerührte Flüssigkeit zum Einsatz. Die Rührerdrehzahlen wurden im Bereich n = 200 ÷ 550 1/min variiert, wodurch eine vollentwickelte turbulente Strömung im Rührbehälter gewährleistet wurde. Als disperse feste Phase wurden kugelförmige transparente Glaspartikel mit einem Durchmesser d_p = 1 ÷ 3 mm aus hochreinem Borosilikatglas verwendet.

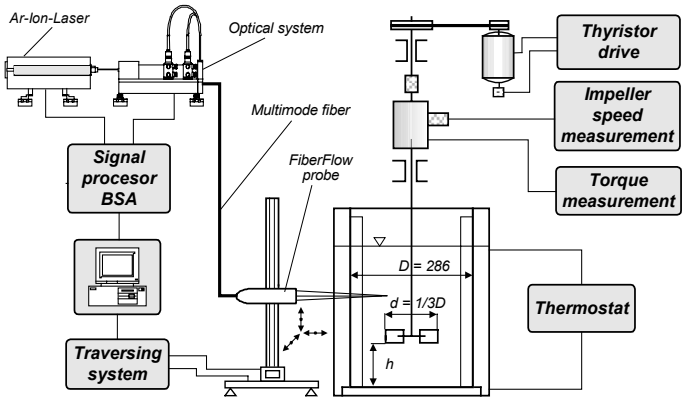

Abb. 1. Schema der Versuchsanlage.

Zur Erfassung der lokalen Strömungsgeschwindigkeiten kam eine Zweikanal-Laser-Doppler-Anemometrie-Anlage (Ar-Ion-Gaslaser) der F-ma *Dantec* im Rückwärtsstreuung

zum Einsatz. Der Schnittpunkt der zwei Lichtstrahlen (blau und grün) wurde anhand der speziell dazu entwickelten Meßmethode, die in einer früheren Arbeit [3] beschrieben wurde, eingestellt. Als Streuteilchen wurden in LDA-Messungen mit Silber beschichtete Hohlglaskugeln (S-HGS) mit einem mittleren Durchmesser von 10 μm verwendet. Die Meßdatenerfassung und Auswertung wurde mit Hilfe der BSA-Flow-Software v.4. [4] von *Dantec* durchgeführt.

3. Geschwindigkeitsprofile für einphasige Rührwerksströmung

Für die vollständige Aufwirbelung von Feststoffpartikeln im Rührbehälter werden nicht nur bevorzugte dazu axial fördernde Rührer (wie z.B. Propeller- Schrägblattrührer) [5,] aber auch radiale Rührer (Scheibenrührer) verwendet. In diesem letzten Fall hat ein Rührerbodenabstand h die große Bedeutung für die erforderliche kritische Rührerdrehzahl.

Meistens werden für die Erzeugung der vollständigen Suspension die Werte h/d=0,5 empfohlen [6,7]. Weil für die Gestaltung einer turbulenten Großraumströmung in einem Rührkessel der Rührerausstrom bedeutsam ist, wurden detaillierte Messungen der Geschwindigkeitsverteilungen im Rührerausströmbereich für die Rühreranordnung h/d=0,5 durchgeführt. In der Literatur gibt es dazu wenige Daten im Gegensatz zu dem Fall, wenn der Rührerbodenabstand den Standardwert h/d=1 annimmt. In Abb. 2 ist die Anordnung der Meßpunkte vorgestellt. Die Größe r* = 2r/d stellt einen dimensionslosen Radius im Behälter und z* = 2z/b eine dimensionslose Rührerblatthöhe dar.

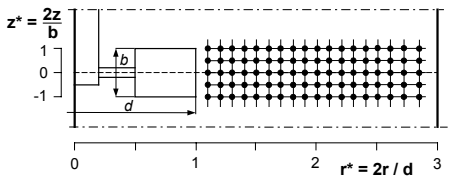

Abb. 2. Anordnung der Meßpunkte in der Ausströmzone des Scheibenrührers.

3.1. Mittelgeschwindigkeiten der einphasigen Strömung im Rührerausströmbereich für den Rührerbodenabstand h/d=0,5.

Anhand der Meßergebnisse der momentanen Geschwindigkeiten in allen drei Raumrichtungen (radiale, axiale und tangentiale Geschwindigkeiten: u_r, u_z, u_t) wurden sowohl die Mittelgeschwindigkeiten ($\overline{U}$) der Flüssigkeit als auch die Geschwindigkeitsschwankungen (u') gemäß der Reynolds-Hypothese ermittelt. Die gemessenen Geschwindigkeitswerte wurden mit der Rührerumfangsgeschwindigkeit $u_{tip} = \pi dn$ normiert, was sowohl für einphasige als auch für zweiphasige Strömungen sinnvoll ist [8] und einen späteren Vergleich mit anderen Versuchsergebnissen ermöglicht.

Zur Verdeutlichung der einphasigen Strömung in der Ausströmzone des Scheibenrührers für kleinen Bodenabstand h/d=0,5 sind in Abb. 3 die radialen und axialen Geschwindigkeitsverteilungen der normierten Mittelgeschwindigkeiten als Vektordiagramme wiedergegeben.

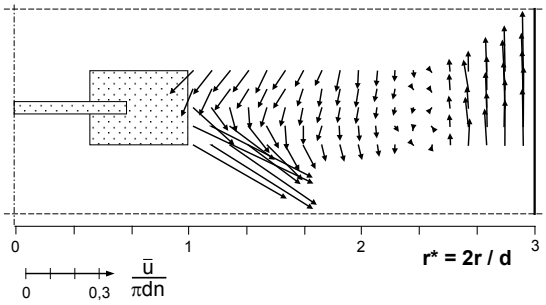

Abb. 3. Vektordiagramm der normierten radial/axialen Mittelgeschwindigkeiten im Rührerausströmbereich für einphasige Strömung (h/d=0,5).

Aus Abb. 3 geht deutlich hervor, daß eine Näherung des Scheibenrührers zu einem Behälterboden die Strömungsverhältnisse im Rührerausströmbereich signifikant ändert. Die typische radiale Strömung für Standardbodenabstand h/d=1 wird in die vorwiegende axiale Richtung umgelenkt, was für die Aufwirbelung fester Partikeln günstig ist.

In der Abb. 4 sind die gemessenen Änderungen der einzelnen Geschwindigkeitskomponenten entlang des Behälterradius in der horizontalen Achse des Rührers (die Hälfte der Rührerblatthöhe d.h. für z* = 0 –siehe Abb. 2) dargestellt.

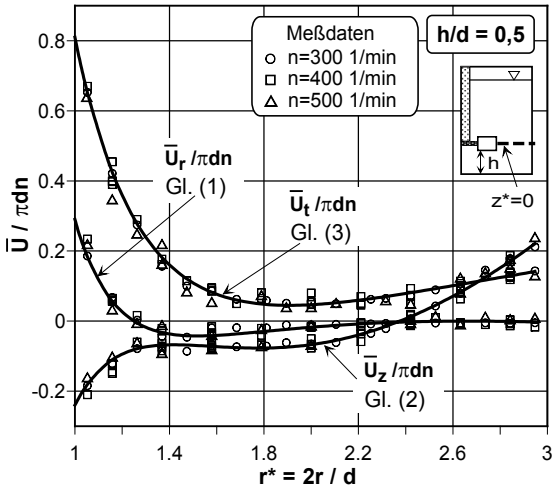

Abb. 4. Verlauf der radialen, axialen und tangentialen Mittelgeschwindigkeiten im Rührerausströmbereich als die Funktion des Behälterradius für einphasige Strömung (h/d=0,5).

Um den Verlauf der Geschwindigkeiten mathematisch zu beschreiben, wurden die entsprechenden Korrelationsgleichungen, die die quantitativen Änderungen der radialen, axialen und tangentialen Geschwindigkeit als folgende Funktionen:

$$\frac{\overline{U}_r}{\pi dn} = -0{,}42 + 2{,}76\left(\frac{2r}{d}\right)^{-1} - 5{,}77\left(\frac{2r}{d}\right)^{-2} + 3{,}72\left(\frac{2r}{d}\right)^{-3} \qquad (1)$$

$$\frac{\overline{U}_z}{\pi dn} = -10{,}20 + 1{,}40\left(\frac{2r}{d}\right) + 11{,}36\left(\frac{2r}{d}\right)^{-0{,}5} - 2{,}80\left(\frac{2r}{d}\right)^{-2} \qquad (2)$$

$$\frac{\overline{U}_t}{\pi dn} = 0{,}60 - 5{,}85\left(\frac{2r}{d}\right)^{-1{,}5} + 6{,}06\left(\frac{2r}{d}\right)^{-2}. \qquad (3)$$

des dimensionslosen Behälterradius umfassen, aufgestellt.

Der Einfluss der Rührereinbauhöhe auf das Geschwindigkeitsprofil in der Rührerebene ist deutlicher ersichtlich nach einem Vergleich der dargestellten Ergebnissen mit Versuchsergebnissen für den Standardbodenabstand h/d=1, die in der Abb. 5 wiedergegeben sind. Die entsprechenden Korrelationsgleichungen für die einzelnen Geschwindigkeitskomponenten werden wie folgt:

$$\frac{\overline{U}_r}{\pi dn} = 0{,}71\left(\frac{2r}{d}\right)^{-1{,}02} - 5{,}55\cdot 10^{-5}\left(\frac{2r}{d}\right)^{7{,}58} \qquad (4)$$

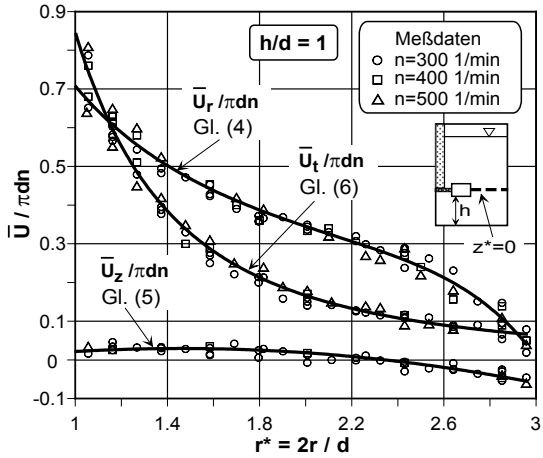

Abb. 5. Verlauf der radialen, axialen und tangentialen Mittelgeschwindigkeiten im Rühreraustrombereich als die Funktion des Behälterradius für einphasige Strömung (h/d=1).

$$\frac{\overline{U}_z}{\pi dn} = 0{,}052 - 0{,}011\left(\frac{2r}{d}\right)^{2{,}18} \qquad (5)$$

$$\frac{\overline{U}_t}{\pi dn} = 0{,}84\left(\frac{2r}{d}\right)^{-2{,}35} \tag{6}$$

ermittelt.

Aus den in Abb. 4 und 5 dargestellten Mittelgeschwindigkeiten geht hervor, daß die Abnahme der Rührereinbauhöhe der radialen und axialen Geschwindigkeitskomponente in der Rührerausströmzone deutlich ändert. Bemerkenswert sind die Änderungen der axialen Geschwindigkeit, die für die Aufwirbelung des Feststoffes vom Boden bei h/d=0,5 günstiger sind.

In Abb. 6 werden die Meßergebnisse zum Geschwindigkeitsprofil der radialen Komponente in der Abhängigkeit von der dimensionslosen Rührerblatthöhe (z*=2z/b) und von dem dimensionslosen Behälterradius (r*=2r/d) d.h. von einem Abstand vom Ende der Rührerblätter dargestellt. Die gewonnen Meßergebnisse wurden in Form einer folgenden Korrelationsgleichung

$$\frac{\overline{U}_r}{\pi dn} = A_2 + B_2 z^* + C_2 z^{*2} + D_2 \exp(-z^*) \tag{7}$$

umgefaßt. Die einzelnen Beiwerte A_2, B_2, C_2 und D_2 in Gleichung (7) sind die Funktion des Behälterradius und können mit folgenden Gleichungen

$$A_2 = -1{,}92 + 14{,}21 r^{*-1} - 33{,}16 r^{*-2} + 24{,}08 r^{*-3} \tag{8}$$

$$B_2 = 1{,}25 - 10{,}88 r^{*-1} + 28{,}30 r^{*-2} - 22{,}41 r^{*-3} \tag{9}$$

$$C_2 = -0{,}12 + 2{,}27 r^{*-1} - 7{,}80 r^{*-2} + 7{,}14 r^{*-3} \tag{10}$$

$$D_2 = 1{,}62 - 12{,}32 r^{*-1} + 29{,}13 r^{*-2} - 21{,}36 r^{*-3} \tag{11}$$

ausgedrückt werden. Die im Diagramm (Abb. 6) dargestellten Geschwindigkeitsverläufe wurden anhand der ermittelten Gleichung (7) berechnet und aufgezeichnet. Aus Abb. 6 geht hervor, daß im Fall h/d=0,5 das Profil der radialen Mittelgeschwindigkeit im Rührerausströmbereich im Vergleich mit symmetrischen Verlauf dieser Geschwindigkeit für den Standardbodenabstand [9] geändert wird. Die größten Werte der Geschwindigkeit treten in der unteren Hälfte der Rührerblätter. In der Nähe der Bähelterwand die radialen Geschwindigkeiten nehmen praktisch zum Null ab.

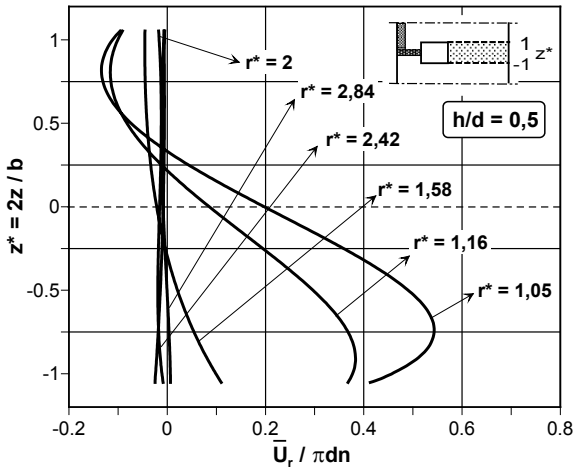

Abb. 6. Verlauf der radialen Mittelgeschwindigkeiten im Rührerausströmbereich als die Funktion der Rührerblatthöhe; einphasige Strömung (h/d=0,5).

3.2. Schwankungsgeschwindigkeiten der einphasigen Strömung im Rührerausströmbereich für den Rührerbodenabstand h/d=0,5.

Turbulente Strömungen zeichnen sich durch Auftreten von Schwankungsgeschwindigkeiten, die zur quantitativen Bestimmung des Turbulenzgrades verwendet werden können, aus. Als Maß der momentanen Schwankungswerte der Geschwindigkeit wird der Effektivwert (RMS-Wert) der turbulenten Schwankungsgeschwindigkeiten benutzt. In Abb. 7 werden die Ergebnisse der Untersuchungen zur Schwankungsgeschwin-

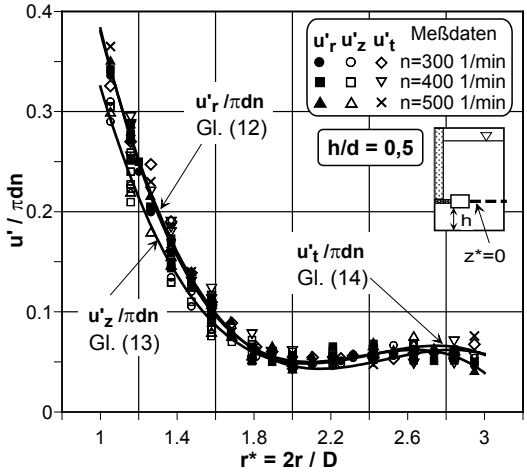

Abb. 7. Schwankungsgeschwindigkeiten im Rührerausströmbereich als die Funktion der Entfernung vom Rührerende; einphasige Strömung (h/d=0,5).

digkeitsverteilung im Rührerausströmbereich für den Rührerbodenabstand h/d=0,5 in normierter Form ($u'/\pi dn$) dargestellt. Die ermittelten folgenden Korrelationsgleichungen

$$\frac{u'_r}{\pi dn} = -1{,}917 - 2{,}429\left(\frac{2r}{d}\right) + 1{,}042\left(\frac{2r}{d}\right)^2 - 0{,}147\left(\frac{2r}{d}\right)^3 \qquad (12)$$

$$\frac{u'_z}{\pi dn} = 1{,}575 - 1{,}967\left(\frac{2r}{d}\right) + 0{,}83242\left(\frac{2r}{d}\right)^2 - 0{,}115\left(\frac{2r}{d}\right)^3 \qquad (13)$$

$$\frac{u'_t}{\pi dn} = 1{,}768 - 2{,}151\left(\frac{2r}{d}\right) + 0{,}881\left(\frac{2r}{d}\right)^2 - 0{,}118\left(\frac{2r}{d}\right)^3 \qquad (14)$$

beschreiben den Verlauf der normierten turbulenten Schwankungsgeschwindigkeiten in der Funktion der Entfernung vom Rührer (dimensionsloser Behälterradius).

4. Geschwindigkeitsprofile für zweiphasige Rührwerksströmung

In Abb. 8 wird das Vektordiagramm der normierten radial/axialen Mittelgeschwindigkeiten der kontinuierlichen Phase im Rührerausströmbereich für gerührtes Feststoff-Flüssigkeits-System (Massenkonzentration des Feststoffes c_m = 2%, Partikeldurchmesser d_p = 1,5 mm) dargestellt. Aus Abb. 3 (einphasige Strömung) und Abb. 8 geht deutlich hervor, dass die Feststoffteilchen die Strömung der kontinuierlichen Phase sowohl qualitativ als auch quantitativ deutlich ändern. Im Fall der zweiphasigen Systeme kann eine überwiegend radiale Strömung im Rührerausströmbereich festgestellt werden. Diese Änderungen in der Bewegung der kontinuierlichen Phase sind auf die relativ große Partikelträgheit im Gegensatz zur Trägheit der Fluidelemente zurückzuführen.

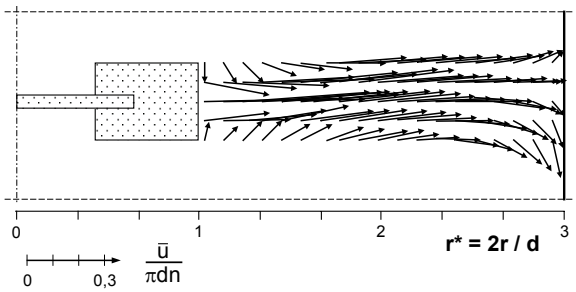

Abb. 8. Vektordiagramm der normierten radial/axialen Mittelgeschwindigkeiten der Flüssigkeit im Rührerausströmbereich für zweiphasige Strömung (h/d=0,5).

Es kann festgestellt werden, dass im Rührerausströmbereich die Bewegung der festen Phase die Bewegung der kontinuierlichen Phase erzwingt und determiniert.

Der Einfluss der Feststoffpartikeln auf die Strömung der Flüssigkeit im gerührten Zweiphasensystem ist noch deutlicher bei einer Analyse des Verlaufs der radialen Geschwindigkeitskomponente entlang der ganzen Rührerblatthöhe (Abb. 9) ausgeprägt.

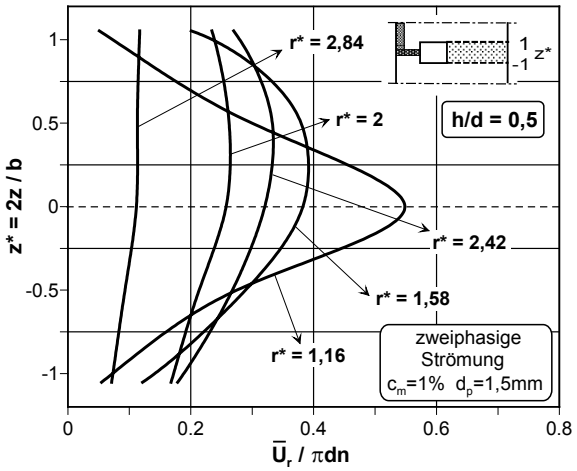

Abb. 9. Verlauf der radialen Mittelgeschwindigkeiten der Flüssigkeit im Rührerausströmbereich als die Funktion der Rührerblatthöhe; zweiphasige Strömung (h/d=0,5).

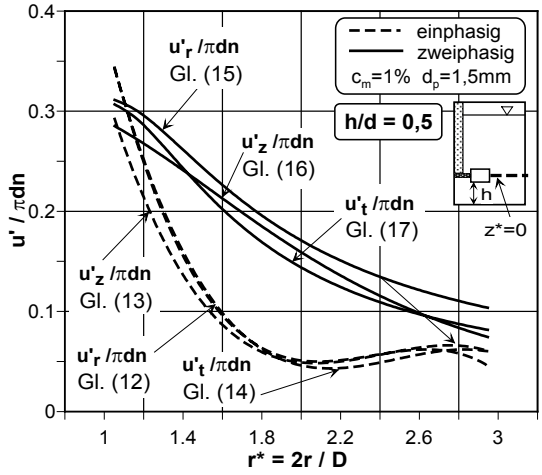

Abb. 10. Vergleich der Schwankungsgeschwindigkeiten im Rührerausströmbereich für ein- und zweiphasige Strömung im Rührwerk.

In Abb. 10 sind die turbulenten Schwankungsgeschwindigkeiten der kontinuierlichen Phase in einer Suspension (c_m = 1%, d_p = 1,5 mm) in aller drei Richtungen in normierter Form dargestellt. Zum Vergleich sind auch die Schwankungsgeschwindigkeiten in gerührten einphasigen Systemen (gestrichelte Linie) gezeichnet.

Der Verlauf der normierten radial/axial/tangentialen turbulenten Schwankungsgeschwindigkeiten in der Abhängigkeit von der Entfernung vom Rührer (dimensionsloser Radius r*) und von der Feststoffmassenkonzentration c_m wurde anhand der Versuchsergebnisse in Form der folgenden Korrelationsgleichungen

$$\left(\frac{u'_r}{\pi dn}\right)^{-1} = 3{,}238 - 38{,}85 \cdot c_m{}^{1{,}5} + 5{,}52 \cdot \ln^2\left(\frac{2r}{d}\right) \qquad (15)$$

$$\left(\frac{u'_z}{\pi dn}\right)^{-1} = 2{,}68 + 3{,}53 \cdot 10^{-4} \cdot c_m{}^{-1{,}5} + \left(0{,}412 - 5{,}397 \cdot c_m{}^{1{,}5}\right) \cdot \left(\frac{2r}{d}\right)^3 \qquad (16)$$

$$\left(\frac{u'_t}{\pi dn}\right)^{-1} = 3{,}299 - 59{,}56 \cdot c_m{}^{1{,}5} + 7{,}72 \cdot \ln^2\left(\frac{2r}{d}\right) \qquad (17)$$

erfasst. Es kann festgestellt werden, dass die suspendierten Feststoffteilchen die turbulenten Schwankungsgeschwindigkeiten im Rührerausströmbereich signifikant erhöhen.

Die ermittelten turbulenten Schwankungsgeschwindigkeiten im gerührten Ein- und Zweiphasensystem erlaubten die Turbulenzintensität in Form eines Turbulenzgrades Tu gemäß der Gleichung [10]:

$$Tu = \frac{\sqrt{1/3 \cdot (u'^2_r + u'^2_z + u'^2_t)}}{\pi dn} \qquad (18)$$

zu bestimmen.

Zur quantitativen Beurteilung des Einflusses der festen Teilchen auf die Turbulenz der kontinuierlichen Phase wird oft ein Modulationsgrad [11]:

$$M = \frac{Tu^* - Tu}{Tu} \qquad (19)$$

verwendet. (Tu*, Tu –Turbulenzgrad für Zwei- und Einphasensystem).

In Abb. 11 ist auf Grund der ermittelten Korrelationsgleichungen (12)÷(17) das Modulationsgrad der Turbulenz in der Rührerausströmzone dargestellt. Es kann festgestellt werden, dass die festen Partikel (mit dem Durchmesser von d_p = 1,5mm) im untersuchten Größenbereich der Feststoffkonzentration (1%÷5%) eine Anfachung der Turbulenz der kontinuierlichen Phase verursachen. Mit einer Zunahme der Feststoffkonzentration nimmt auch der Modulationsgrad zu.

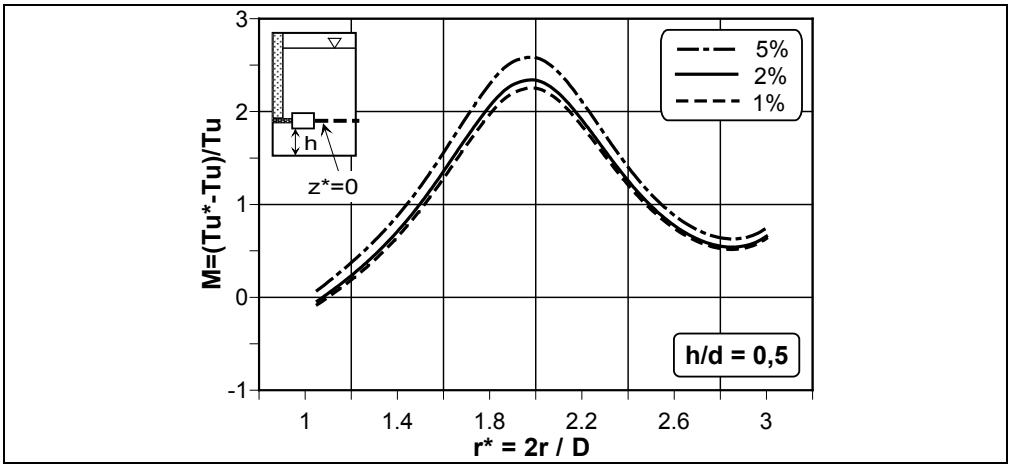

Abb. 11. Modulationsgrad der Turbulenz im Rührerausströmbereich.

Literatur

[1] Kraume M.: Chem. Ing. Techn., **79**, (2007), 923.
[2] Kraume M., Zehner P.: Trans IChemE, **79**, Part A, (2001), 811-818.
[3] Talaga J., Duda A.: Czasopismo Techniczne, z. 4-M, (2004), 267-275.
[4] Dantec Dynamics A/S: BSA Flow Software, Version 4, Installation & User's Guide, Skovlunde 2005.
[5] Kasat G. R., Pandit A. B.: Canad. Journ. Chem. Eng., **83**, (2005), 618-643.
[6] Armenante P. M., Nagamine E. U.: Chem. Eng. Sci., **53**, (1998), 1757-1775.
[7] Kamieński J., Mieszanie układów wielofazowych, WNT, Warszawa 2004.
[8] Geisler R. T.: Dissertation, TU München 1991.
[9] Dyster K. N., Koutsakos E., Jaworski Z., Nienow A. W.: Trans. Inst. Chem. Eng. **71**, Part A, (1993), 11-21.
[10] Talaga J., Wojtowicz R.: Inż. Ap. Chem. nr 4, (2010), 80-82.
[11] Brennen C. E.: Fundamentals of Multiphase Flow, Cambridge Univ. Press 2005.

18th International Conference Process Engineering and Chemical Plant Design
Günter Wozny and Łukasz Hady, Editors

PHILIPP SCHRADER*, UDO DORN*, ANDRES KULAGUIN – CHICAROUX*, SABINE ENDERS*

PHASE EQUILIBRIA OF SURFACTANT CONTAINING SYSTEMS

Abstract

The knowledge of the complex phase behavior of the ternary system composed of water, oil (dodecene) and surfactant ($C_{12}E_8$) is an essential condition for the use of microemulsions as media for chemical reactions, for instance the hydroformylation of long-chain alkenes. The paper deals with the experimental investigation of the ternary and the corresponding binary subsystems. Two binary subsystems, namely $C_{12}H_{24}$ + water and $C_{12}E_8$ + water, exhibit demixing gaps. In contrast, the binary subsystem $C_{12}H_{24}$ + $C_{12}E_8$ shows no demixing above the melting point of surfactant. The essential feature of this ternary phase behavior is the so-called "Kahlweit fish" appearing at a constant water-oil ratio as function of temperature. Additionally, an activity coefficient model was used to calculate the binary and ternary phase diagrams. Comparison of the theoretical predictions of the ternary phase diagram based on the binary data with the experimental data shows a limited agreement.

Keywords: Liquid-liquid phase equilibria, Surfactant systems, Microemulsions, Experimental data and modeling

1. Introduction

Hydroformylation, also known as oxo synthesis, is an important industrial process for the production of aldehydes from alkenes, because the resulting aldehydes are easily converted into many secondary products. The hydroformylation of alkenes with a low carbon number using a hydrophilic rhodium catalyst is one of the most important chemical reactions in the chemical industry [1]. However, the use of hydroformylation for production of long-chain aldehydes causes several problems, for instance the extreme low solubility of the educts in a hydrophilic environment. Haubach et al. [2] succeeded the preparation of long chain aldehydes (i.e. C_{13}) from long-chain alkenes (C_{12}) hydroformylation applying a rhodium catalyst in laboratory scale. The problem of the very limited water solubility of alkenes (i.e. $C_{12}H_{24}$) can be overcome, if the chemical reaction is

* Chair of Thermodynamics, Technical University Berlin, D-10623 Berlin, TK7, Germany

performed in a microemulsion forming system [2], in doing so the microemulsion is prepared from non-ionic surfactant, water and oil.

The microemulsion can be of the droplet type, either with oil droplets dispersed in water or water droplets dispersed in oil. The droplet-type microemulsions can be either a single-phase system or part of a two-phase system wherein the microemulsion phase coexists with the excess dispersed phase. There are also non-droplet-type microemulsions, referred to as middle-phase microemulsion. In this case, the middle-phase microemulsion is a part of a three-phase system with the microemulsion phase in the middle coexisting with an upper phase of excess oil and a lower phase of excess water [e.g. 3,4,5,6,7]. A convenient procedure for determining the position and extension of the three-phase body is to establish a vertical section though the phase prism at constant oil-water ratio. Several experimental data related to this three-phase body for the systems made from nonionic surfactant belong to the class n-alkyl polyglycol ethers, abbreviated as C_iE_j, + n-alkane + water are available in the literature [e.g. 3,5,6,8]. In this contribution we focus our attention on the phase diagrams of the ternary and the corresponding binary sub-systems, where the oily component is dodecene ($C_{12}H_{24}$).

For the binary subsystem $C_{12}E_8$ + water several data related to the cloud-point curve occurring in the diluted concentration range exist [9,10,11,12]; however, these data show a relatively large scatter. The liquid crystalline phases occurring at lower temperatures and higher surfactant concentration were investigated by Zheng et al. [13]. In contrast, for the binary subsystem $C_{12}H_{24}$ + water no experimental data could be found in the literature. In this contribution we present new experimental data related to miscibility gap of the system $C_{12}E_8$ + water showing a LCST-behavior, of the system $C_{12}H_{24}$ + water showing a UCST-behavior and finally of the ternary system $C_{12}E_8$ + $C_{12}H_{24}$+water.

To the best of our knowledge no equation of state or activity coefficient model, which can be used for the calculation of the phase diagram of the ternary microemulsion forming system in quantitative agreement with experimental data, especially for high values of i and j, is available in the literature, although several attempts were made [e.g.6,14,15,16,17,18,19,20,21]. In this contribution we try to predict the ternary phase behavior applying the Koningsveld-Kleintjens model [22], where the model parameters were fitted to the demixing curves of the binary subsystems water + surfactant and water + oil. For the binary subsystem oil + surfactant an ideal athermic behavior was assumed.

2. Experiments

The phase equilibrium measurements were carried out using $C_{12}E_8$ as surfactant, 1-dodecene ($C_{12}H_{24,}$) as oil and deionized water. Both chemicals ($C_{12}E_8$ and $C_{12}H_{24}$) were purchased by Sigma Aldrich. The chemicals were applied as received without further purification.

The binary subsystem water and $C_{12}H_{24}$ exhibits a large miscibility gap ranging from practical pure water to practical pure oil. For this reason the measurement of the solubility is challenging when highly insoluble substances are considered, exceeding the sensitivity of the analytical method such as spectroscopy or chromatography. Classical approaches for measuring solubility are based on the saturation shake-flask method. In brief, accurately known masses of both components were weighted out directly into tightly sealed vials and stirred in a thermostat at the desired temperature. After establishing equilibrium the

composition of each phase can be estimated. The water content of the organic phase at different temperatures can estimated with the help of Karl-Fischer titration (AE 260, Mettler-Toledo, Germany). The estimation of the oil content in the water-rich phase is quite challenging, because the amount of $C_{12}H_{24}$ are considered that exceed the sensitivity of analytical methods such usual spectroscopy or chromatography. For this reason the amount of $C_{12}H_{24}$ was enriched by stripping via dry air and afterwards the concentration was measured using HPLC. The HPLC-apparatus is equipped with C18 column (ChromSa (250 x 4.6 mm)) filled with Zorbax Pro (10/60, 10 µ) purchased by Agilent, GmbH, Germany. For the detection the UV-VIS absorption at a wavelength of 200 nm is used. The obtained correlation coefficient of the calibration line was 0.999.

The cloud point temperatures of the binary subsystem water-$C_{12}E_8$ were measured by visual observation. In order to make sure that the equilibrium is found, first the solutions were heated very slowly and the demixing temperature was recorded. Subsequently, the solution was cooled and the temperature at which the second phase vanished was detected. Differences between both temperatures were below 1 K.

In the absence of external fields a ternary mixture at constant pressure has three independent thermodynamic variables, namely the temperature, and two composition variables. The phase behavior of a ternary mixture can then be represented exactly in an upright phase prism with the Gibbs triangle as the base and the temperature as the ordinate. The phase behavior of the ternary system arises from the interplay between the miscibility gaps of the corresponding three binary mixtures representing the sides of the phase prism. Commonly, the phase behavior of oil+water+surfactant systems at constant oil-to-water ratios is expressed a quasi-binary temperature-composition diagram, where the composition is the surfactant weight fraction:

$$\gamma = \frac{m_{surfactant}}{m_{oil} + m_{water} + m_{surfactant}} \tag{1}$$

At a constant oil-to-water ratio the phase boundaries between the three-phase and the two-phase regions have a shape of a “fish” [3,5,6]. This “fish” was measured by mixing equal masses of water and oil and then adding different amounts of surfactant and observing the number of phases as function of temperature. The experiments were performed via very slowly heating and cooling, where the phase transition temperatures between heating and cooling were within 1K.

3. Modeling approach

The essential feature of a surfactant in solution consists in the formation of aggregates. The aggregation behavior in aqueous solution can be predicted using a detailed micellar formation model developed by Nagarajan and Ruckenstein [14]. This model allows the calculation of the aggregation behavior (i.e. critical micelle concentration, geometrical properties of the formed aggregates) and in combination with an expression for the excess Gibbs energy of mixing the calculation of the demixing curve close to the experimental data [23, 24]. However, the calculation of the phase split in ternary system build up from $C_{12}E_8$ (A) + dodecene (B) and water (C) is quite challenging from the numerical point of view [25]. Therefore, a simple activity coefficient model, describing the derivation of a real

mixture to an ideal-athermic mixture is applied. For the calculation all molecules are divided in segments of equal size. The segment numbers are given by:

$$r_i = \frac{M_i}{M_C} \qquad i = A, B, C \tag{2}$$

where the water is selected as standard molecule. This fixing leads to the following segment numbers:

$$r_A = 29.905 \quad r_B = 9.343 \quad r_C = 1 \tag{3}$$

The used expression for the excess Gibbs energy reads [22]:

$$\frac{G^E}{RT} = \phi_A\phi_B \frac{\beta_{AB}(T)}{1-\phi_B p_{AB}} + \phi_B\phi_C \frac{\beta_{BC}(T)}{1-\phi_B p_{BC}} + \phi_A\phi_C \frac{\beta_{AC}(T)}{1-\phi_C p_{AC}} \tag{4}$$

where the concentration is measured in segment fractions. The Eq. 4 permits the parameter fitting procedure using the experimental data of the binary subsystems and the prediction of the phase behavior of the ternary systems.

4. Results and discussions

The binary system $C_{12}E_8$ + $C_{12}H_{24}$ was completely miscible in the concentration range of interest over the whole temperature range starting from the melting temperature of the surfactant (approximately 303 K). For this reason the interaction parameter occurring in Eq. 4 were set to zero (Table 1).

Table 1

Fitted parameters of Eq. 4

System	β_1	β_2 / K	p_{ij}
H_2O-$C_{12}H_{24}$	-1.396	1209.3	0.63
$C_{12}E_8$-H_2O	1.277	-384	0.85811
$C_{12}E_8$-$C_{12}H_{24}$	0	0	0

For the system $C_{12}H_{24}$ + water no experimental data could be found in the literature. Analyzing available data related to the water solubility in hydrocarbons [26,27,28,29] leads to the following conclusion: the water solubility of hexane [27] is very similar to the solubility in octene [26] and the water solubility of octane [27] is very similar to the solubility of decene [26]. For this reason we expected a similar solubility of decane [26] and dodecene. The experimental data taken from the literature [26] are plotted in

Fig. 1, together with the fitted phase diagram using Eq. 4. The obtained parameters are collected in (Table 1).

The experimental solubility of dodecene in water at room temperature is $w_{oil} = 1.54 \cdot 10^{-7}$. The model, where the parameter were fitted to decane + water, predicts a value of $w_{oil} = 6 \cdot 10^{-8}$.

The experimental estimated solubilities of water in dodecene using Karl-Fischer titration are depicted in Fig. 2. The line in Fig. 2 represents the predicted oil solubility based on the data given in

Fig. 1. From the results in Fig. 2 it can be concluded that the above approximation that the solubility of decane is very similar to the solubility in dodecene is proved.

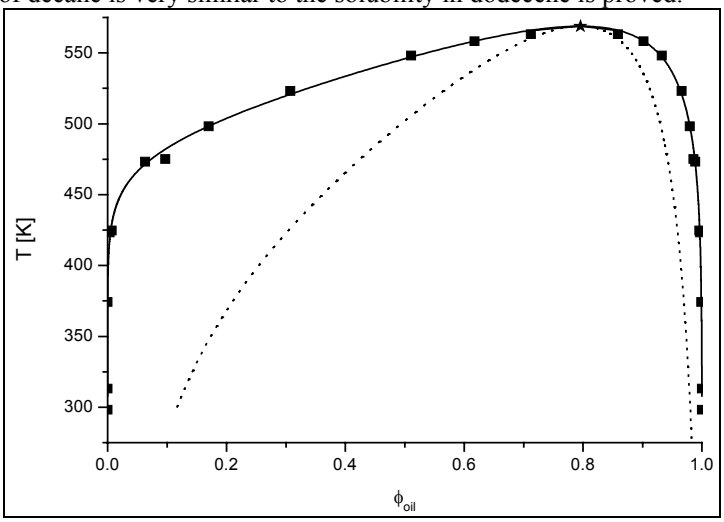

Fig. 1: Experimental [26] (squares) and calculated miscibility gap (solid line: binodale line; broken line: spinodale line, star: critical point) using Eq. 4 with parameters in Table 1 for the system decane + water.

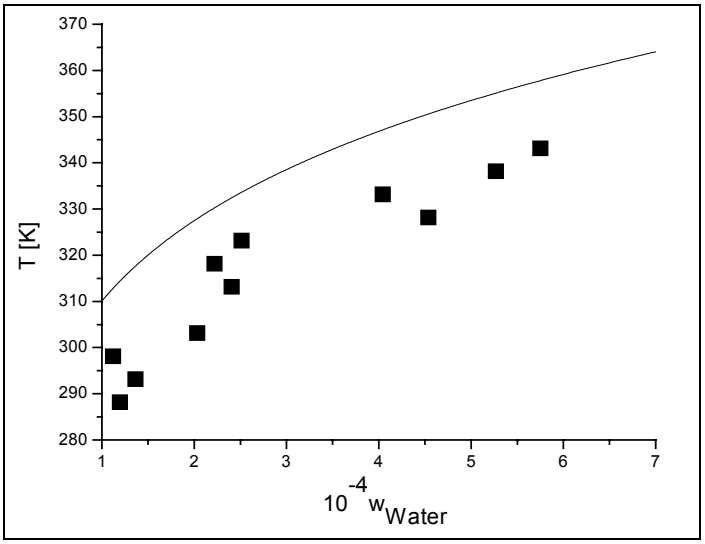

Fig. 2: Experimental (squares) and predicted (line) solubility of water in dodecene using Eq. 4 with parameters of Table 1.

Diluted aqueous solutions of nonionic amphiphiles usually exhibit a phase separation when the temperature is raised above a value which depends on the amphiphile

concentration. In the concentration-temperature plan, the single-phase micellar region is separated from the region in which two immiscible isotropic solutions are present by a cloud point curve (Fig. 3).

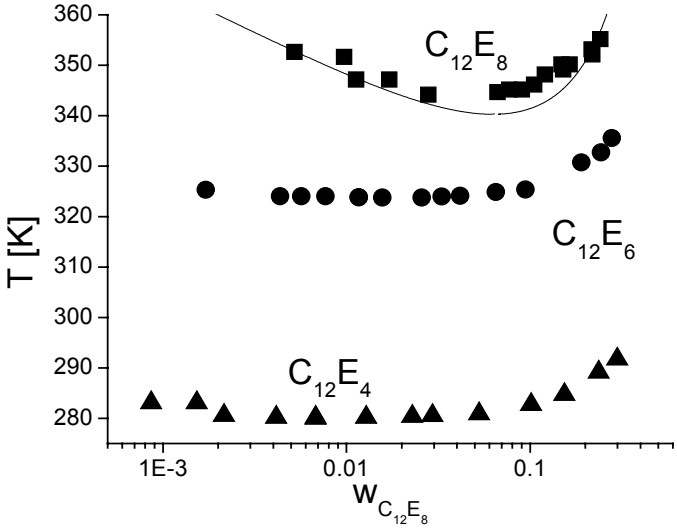

Fig. 3: LCST behavior of aqueous surfactant solutions (squares: $C_{12}E_8$ this work, circles: $C_{12}E_6$ [10], triangles: $C_{12}E_4$ [10], line calculated with Eq. 4 and parameters from Table 1).

The comparison of the phase diagram with those previously obtained for $C_{12}E_7$ and $C_{12}E_8$ demonstrates that with the decrease in the polyoxyethylene (POE) chain length, the region of L_α phase expands toward higher temperature, whereas the H_1 region shrinks toward lower temperatures [13]. This behavior is well explained in terms of the change in the critical packing parameter of the surfactant molecules associated with the change in the POE chain length. Corti et al. [30] measured the critical point using light scattering technique resulting in a critical point at T_C=348.65 K and w_C=0.032 g/g. The LCST behavior was also investigated by Shinoda [12]; however, the measured cloud point temperatures in the diluted concentration range are located approximately 10 K higher than the data in Fig. 3. Unfortunately, no further experimental information about the heating rate or the pureness of the used surfactant are given in the paper [12]. Fujimatsu et al. [10] measured the cloud point curve of this system with a surfactant purchased by Nikko Chemicals, where the samples were only heated with a constant heating rate of 1.3 K/min. The procedure leads also to demixing temperatures approximately 12K higher than the data given in Fig. 3. Our experimental data are close to the data presented in [9]. Unfortunately, the experimental data are given only via a line in a figure with a large scale. For this reason it is very hard to compare the exact data points. The line in Fig. 3 represents the modeling results, where the Eq. 4 was applied and the parameters given in Table 1 were fitted to our experimental data. Having in mind that our simple model contains no information of the

micelle formation it can be figured out that the model is able to describe the experimental data with a satisfactory accuracy.

Additionally, the cloud point curve could be modeled using a detailed micellar formation model developed by Nagarajan and Ruckenstein [14] in with an expression for the excess Gibbs energy of mixing [23,24,25].

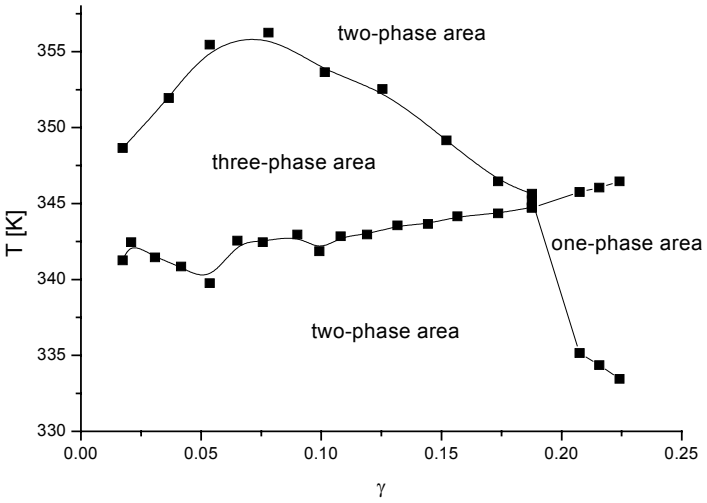

Fig. 4: Vertical section through the phase prism for the system water+dodecene+$C_{12}E_8$, where the squares are the experimental data and the lines are drawn to guide the eye.

Fig. 4 demonstrates the phase behavior at constant water-to-oil ratio in the mixture of 0.5. The point where one finds a direct transition from the three-phase to the one-phase region represents a measure for the efficiency of the surfactant, namely the minimum amount of amphiphile required for completely homogenizing equal masses of water and oil. In the central part of the multiphase region, the system actually separates into three phases, which are a microemulsion middle phase containing a large amount of the surfactant and large amounts of solubilized oil and water, and two excess phases, which are essentially pure oil and pure water.

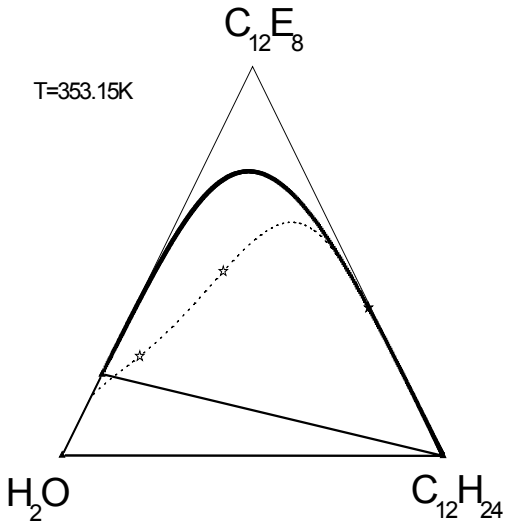

Fig. 5: Predicted phase diagram (filled star: stabile critical point; open star: instable critical point; dotted line: spinodale line; solid line: binodale line; triangle: three phase equilibrium) for the system water+dodecene+$C_{12}E_8$ at T=353.15K.

Using the parameters given in Table 1 the phase diagram of the ternary system at constant temperature can be predicted and plotted in a triangle diagram (Fig. 5). The three-phase equilibrium consists of two excess phases, namely practical pure water and pure oil, and the middle phase microemulsion. The simple model is not able to predict the composition of the middle phase microemulsion. According to the experiment this phase should be able to solubilize a remarkable amount of oil. However, the model predicts an aqueous surfactant solution with a very small amount of oil. The reason for this situation lies in the bicontinuous structure of this phase leading to a large entropy effect [31]. The three-phase region, symbolized as triangle in Fig. 5, is surrounded by three two-phase zones. Two of them arise from the corresponding miscibility gaps of the binary subsystems.

5. Conclusion

The paper presents new experimental data of the binary subsystems and the ternary system. The surfactant oil mixture does not exhibit a miscibility gap in the investigated temperature range. The behavior of dodecene in water is very similar to the behavior of decane in water. For the first time the solubility of water in dodecene as function of temperature and the solubility of dodecene in water were measured. The new cloud-point curve of the surfactant solution with a lower critical solution temperature is located at somewhat lower temperatures than the data given in literature. The phase behavior of the ternary systems was studied experimentally by the usual procedure, namely the construction of the Kahlweit fish. The simple activity coefficient model can describe the binary subsystems

and predict the general phase behavior of the ternary system. However; using the simple model we was not able to predict the composition of the middle-phase microemulsion close to the experimental data. Maybe, this problem can be solve, if a model were applied, taking the aggregation behavior into account [24,25,31].

6. Acknowledgements

The authors thank the German Science Foundation DFG for financial support related to the Collaborative Research Centre "Integrated Chemical Processes in Liquid Multiphase Systems" (SFB/TR 63/TPA5).

7. Literature

[1] Evans, D., Osborn, J.A., Wilkinson, G.: J. Chem. Soc., 33, (1968), 3133–3142.
[2] Haumann, M., Koch, H., Hugo, P., Schomäker, R.: Applied Catalysis A: General, 225, (2002), 239.
[3] Sottmann, T., Strey, R.: Fundamentals Interf. Coll. Sci., 5, (2005), 1-96.
[4] Kilpatrick, P.K., Gorman, C.A., Davis, H.T., Scriven, L.E., Miller, W.G.: J. Phys. Chem., 90, (1986), 5292-5299.
[5] Kahlweit, M., Strey, R., Busse, G.: J. Chem. Phys., 94, (1990), 3881-3894.
[6] Rudolph, E.S.J., Cacao Pedrosso, M.A., de Loos, T.W., De Swaan Arons, J.: J. Phys. Chem. B, 101, (1997), 3914-3918.
[7] Strey, R.: Curr. Opi. Coll. Interf. Sci., 1, (1996), 402-10.
[8] Dong, R., Hao, J.: Chem. Rev. 110, (2010), 4978-5022.
[9] Degiorgio, V., Piazza, R., Corti, M., Minero, C.: J. Chem. Phys., 82, (1982), 1025-31.
[10] Fujimatsu, H., Ogasawara, S., Kuroiwa, S.: Colloid Polym. Sci. 266, (1988), 594.
[11] Mitchell, D.J., Tiddy, G.J.T., Waring, L., Bostock, T., McDonald, M.P.: J. Chem. Soc., Faraday Trans. 1, 79, (1983), 975-1000.
[12] Shinoda, K.: J. Coll. Interf. Sci., 34, (1970), 278-282.
[13] Zheng, L.Q., Suzuki, M., Inoue, T., Lindman, B.: Langmuir, 18, (2002), 9204-9210.
[14] Nagarajan, R., Ruckenstein, E.: Langmuir, 16, (2000), 6400-15.
[15] Kahl, H., Quitzsch, K., Stenby, E.H.: Fluid Phase Equilibria, 139, (1997), 295-309.
[16] Riaz, M., Kontogeorgis, G.M., Stenby, E.H., Tan, W., Haugum, T., Christensen, K.O., Solbraa, E., Lokken, T.V.: Fluid Phase Equilibria, 300, (2011), 172-181.
[17] Browarzik, C., Browarzik, D., Winkelmann, J.: Fluid Phase Equilibria., 296, (2010), 82-87.
[18] Lin, B.J., Chen, L.J.: Fluid Phase Equilibria, 216, (2004), 13-20.
[19] Riazi, M.R., Moshfeghian, M.: J. Petrol. Sci. Eng. 67, (2009), 75–83
[20] Acosta, E.J.: Colloids Surfaces A: Physicochem. Eng. Aspects, 320, (2008), 193-204.
[21] García-Sánchez, F., Eliosa-Jiménez, G., Salas-Padrón, A., Hernández-Garduza, O., Ápam-Martínez, D.: Chem. Eng. J., 84, (2001), 257-274.
[22] Koningsveld, R., Kleintjens, L.A.: Macromolecules, 4, (1971), 637-41.
[23] Enders, S., Häntzschel, D.: Fluid Phase Equilibria, 153, (1998), 1-21.
[24] Dorn, U.: Diploma thesis, TU Berlin, 2011.
[25] Enders, S.: Habilitation thesis, University Leipzig, 2000.
[26] Economou, I.G., Heidman, J.L., Tsonopoulos, C., Wilson, G.M.: AIChE J., 43, (1997), 535-46.

[27] Maczynski, A., Wisniewska-Goclowska, B., Goral, M.: J. Phys. Chem. Ref. Data, 33, (2004), 549-577.
[28] Maczynski, A., Wisniewska-Goclowska, B., Goral, M.: J. Phys. Chem. Ref. Data, 33, (2004), 579-591.
[29] Shaw, D.G., Maczynski, A.: J. Phys. Chem. Ref. Data, 35, (2006), 154-203.
[30] Corti, M., Minero, C., Degiorgio, V.: J. Phys. Chem., 88, (1984), 309-317.
[31] Nagarajan, R., Ruckenstein, E.: Langmuir, 16, (2000), 6400-6415.

18th International Conference Process Engineering and Chemical Plant Design
Günter Wozny and Łukasz Hady, Editors

ZDZISŁAW JAWORSKI*, EUGENIUSZ CYDZIK

CUSTOMIZATION OF THERMODYNAMIC MODELS OF ELECTROLYTES FOR INCORPORATION IN CFD CODES

Abstract

In the presented study a procedure was developed to describe functional relationships between process parameters of crystallization at equilibrium in simple and direct form suitable for application in CFD codes. Development of appropriate correlations was based on numerical results of extensive simulations carried out for the Solvay soda system with a validated commercial code and on further analysis of polynomial regression for the simulated concentrations and temperature at thermodynamic equilibrium. Satisfactory level of accuracy and mathematical simplicity of the developed correlations for incorporation in used defined functions of CFD codes was concluded.

Keywords: Thermodynamic electrolyte models, customization, CFD codes.

1. Introduction

Majority of absorption or/and crystallization processes for inorganic chemicals are carried out in electrolyte environment. On the other hand, modern tools of engineering analysis, including multiscale modelling [1], usually involve computational fluid dynamics (CFD) codes in process optimization. However, currently available commercial CFD packages require adding external look-up tables for equilibrium conditions. The tables, prepared by the software users, are then used iteratively during CFD simulations, which makes the computing rather time-consuming. In this paper, an attempt is described to enable speeding up the computations by preparing own correlations of the equilibrium conditions, which can be further pre-compiled in user defined functions/subroutines incorporated in CFD codes modified in that way.

The typical approach to computing characteristic data for equilibrium of both gas – liquid electrolyte and/or electrolyte – crystal systems has been application of various models of thermodynamic equilibrium. Modern thermodynamic models of electrolyte solutions can be classified either as those using the excess Gibbs energy [2], fundamental and engineering models [3], empirical and molecular models [4] and those dependent on dissociation degree [5]. Several those models have significant limitations in their

* West Pomeranian University of Technology, Aleja Piastow 42, Szczecin 71-065, Poland

applicability to saturated conditions in gas-liquid-solid systems, which are usually important in process engineering. The preferred use of a commercial code for predicting equilibrium states in multi-component electrolyte solutions was one of the conclusions presented in [6]. In addition, our earlier studies for the Solvay soda system [7] clearly suggest the use of the Mixed-Solvent-Electrolyte (MSE) model as the most accurate one for predicting equilibrium conditions for the saturated electrolyte solutions in liquid phase.

2. Mixed-Solvent-Electrolyte model

The model was developed by Wang et al. [8] and it was dedicated to describing concentrated electrolyte solutions. The basic model equations, both for the excess Gibbs energy and activity coefficients, γ, encompass three components, which represent respectively long-range (LR), middle-range (MR) and short-range (SR) interactions.

$$\ln \gamma_i = \ln \gamma_i^{LR} + \ln \gamma_i^{MR} + \ln \gamma_i^{SR} \tag{1}$$

The part accounting for the long-range relations (LR) is defined in a similar way to that in the classic Debye–Hückel models, however it differs due to accounting for dependence of the dielectric constant on the composition of electrolyte solutions. It results in a complex relationship used in calculating the γ_i^{LR} value as published in [8].

Equation describing the long-range interactions can be presented in the following form:

$$\ln \gamma_i^{LR} = -A_x \left[\frac{2z_i^2}{\rho} \ln \left(\frac{1+\rho\sqrt{I_x}}{\sum_k x_k \left[1+\rho\sqrt{I_{x,k}^0}\right]} \right) + \frac{\sqrt{I_x}\left(z_i^2 - 2I_x\right)}{1+\rho\sqrt{I_{x,k}}} \right] + \\ - \frac{4A_x I_x}{\rho} \left\{ \ln \frac{1+\rho\sqrt{I_x}}{\sum_k x_k \left[1+\rho\sqrt{I_{x,k}^0}\right]} \left(\sum_l n_l \right) \left[\frac{1}{2\cdot d_s} \frac{\partial d_s}{\partial n_i} - \frac{3}{2\cdot \varepsilon_s} \frac{\partial \varepsilon_s}{\partial n_i} \right] - \frac{1+\rho\sqrt{I_{x,k}^0}}{\sum_k x_k \left[1+\rho\sqrt{I_{x,k}^0}\right]} + 1 \right\} \tag{2}$$

Equation (2) explains the LR activity coefficient depends on ionic charge, z, ionic strength, I, and on composition of a studied system by means of the dielectric constant, ε_s, molar concentration, d_s, and an empirical constant, ρ, which is characteristic for the system studied. The other interactions between ion-molecule or two ions, which were not explained by the γ_i^{LR} coefficient are described by a middle-range (MR) function.

The second component is of the middle-range type, MR, it includes binary coefficients, B, that are dependent on ionic strength and temperature and is expressed by Eq. (3) by means of virial coefficients.

$$\ln \gamma_i^{MR} = \sum_k \sum_j x_k x_j B_{kj}\left(I_x\right) - \left(\sum_i n_i \right) \sum_k \sum_j x_k x_j \frac{\partial B_{kj}\left(I_x\right)}{\partial n_i} - 2\sum_k x_k B_{ki}\left(I_x\right) \tag{3}$$

That part of the activity coefficient depends on composition and ionic charge. $B_{ij}(I_x)$ is a symmetrical parameter, i.e. $B_{ij}=B_{ji}$ and $B_{ii}=B_{jj}=0$. The parameter accounts for binary interactions, both ionic and molecular. The relationship is expressed by means of *a, b, c* model coefficients and on ionic strength, which is explained in detail in [8].

The third part is responsible for the short-range (SR) interactions and it is similar to that in the extended UNIQUAC model [9] since it consists of the combinatorial and residual terms.

It should also be mentioned that the two reference states, for ions and solvent, are different in the MSE model. The reference state for ions is for infinite dilution and for solvents it is related to pure solvent. Molality, *x*, is generally assumed as the concentration type for ions with molar ratio as that for solvents. The MSE model has significant advantage of full spectrum of its applicability ranging from solutions of infinite dilution up to saturated solution of salts. The model features are crucial in the case of simulating equilibrium conditions for the Solvay soda system. A commercial version of the model is available in OLI Analyzer Studio 3.0 – software delivered by OLI Systems Inc., which was employed in this study.

3. Software validation and data generation

A standard step to be performed before application of simulation software is its validation. In our study, it should include equilibrium predictions for four basic components that are involved in the Solvay soda system studied, i.e. NH_3, CO_2, NaCl and H_2O. The key reactor in the Solvay technology is a multi-stage carbonization column, where absorption of CO_2 in ammoniacal brine accompanied by crystallization of sodium bicarbonate, $NaHCO_3$, proceeds at elevated temperature and pressure. Thus, validation of the OLI code should be done in a broad range of process parameters met in the column.

Therefore, a broad validation was carried out with the use of experimental data published in 14 books/papers for two-, three- and four–component systems. Temperature variations in the experiments ranged from -10 to 120 ^{0}C and the total pressure varied between 0.07 to 30 bar. Three papers [10–12] reported results for four-component systems, however only one [11] used the basic components, which is shown in Fig. 1. Overall, for the full NH_3–CO_2–NaCl–H_2O system and its tested subsystems the predictions of solid phase type was almost ideal and the average error for estimating partial pressures by the MSE model was below 8% for all the conditions used in the tests. Therefore, the accuracy of the MSE model was assumed as satisfactory and the model was recognized as validated.

The next step was to simulate phase equilibrium, gas-liquid-solid, for reverse system of four salts in aqueous phase: $NaCl+NH_4HCO_3 \leftrightarrow NaHCO_3+NH_4Cl$. The modelling was performed with the help of the MSE model in OLI Analyzer Studio 3.0. Simulations were carried out for 6 temperature levels, from 15 till 65 ^{o}C, and 2 pressure levels; 1 and 3 bar. In addition, the pressure level of 2 bar was also used for the two extreme temperature levels resulting in 14 different pairs of temperature-pressure conditions.

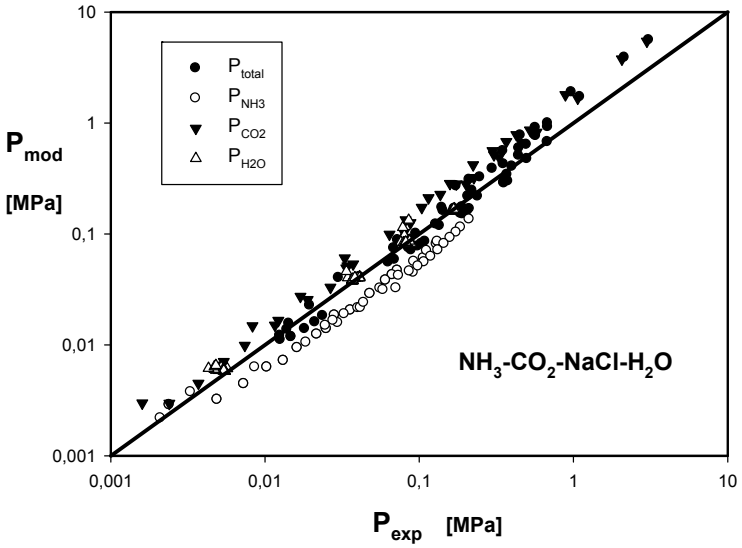

Fig. 1. Comparison of experimental (exp) and modelled (mod) pressure values

The input data stream for each point included temperature, pressure and number of moles of three salts, either NaCl, $NaHCO_3$ and NH_4HCO_3 or NaCl, NH_4Cl and NH_4HCO_3, depending on the target point in the square base of phase diagram of the Jänecke's type, cf. Fig. 2.

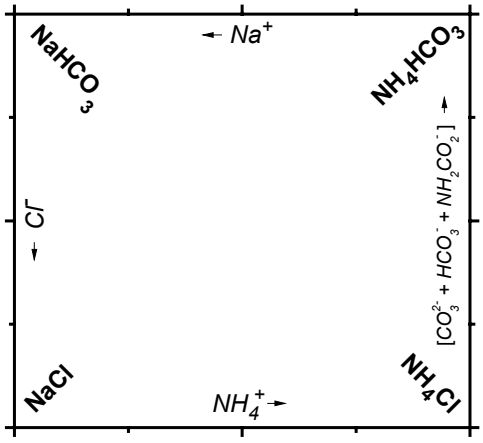

Fig. 2. Base of the phase diagram for the Solvay soda system

The base represents ion molar fractions, *x*, of dry components of the liquid phase, i.e. without water. Corners of the base stand for pure salts and border edges represent molar fraction of individual ions. The horizontal coordinate of the diagram base corresponds to cation fractions and the vertical to anion ones, however, with all anions stemming from CO_2 combined into one group placed opposite to chloride ions. The equivalent number of anion CO_2 moles, $n_{(CO2)-}$, was calculated from Eq. (4).

$$n_{(CO2)-} = n_{HCO3-} + 0.5n_{CO3=} + n_{NH2COO-} \tag{4}$$

The relative molar fraction of cations, x'_{NH3}, and that of anions, x''_{CO2}, were obtained from Eqs. (5) and (6), respectively.

$$x'_{NH3} = \frac{n_{NH4+}}{n_{NH4+} + n_{Na+}} \tag{5}$$

$$x''_{CO2} = \frac{n_{(CO2)-}}{n_{(CO2)-} + n_{Cl-}} \tag{6}$$

Water content in the liquid phase, x_{H2O}, is represented by vertical coordinate of the phase diagram, and it is perpendicular to the diagram base.

$$x_{H2O} = \frac{n_{H2O}}{n_{NH4+} + n_{Na+} + n_{(CO2)-} + n_{Cl-} + n_{H2O}} \tag{7}$$

For computing equilibrium concentrations in the gas and liquid phases at presence of either single or double salts in the solid phase, the "Precipitation Point" mode was applied in the software with water as the component added stepwise. However, the "Isothermal" mode was employed to determine concentration of liquid phase for two triple points. Appearance of the gas phase was forced by a minute addition of nitrogen, if required. For every set of temperature-pressure, 26x26=676 points evenly distributed over the diagram base were used in the simulations. The output data stream contained information on the predicted composition of the gas and liquid phase and on the type of solid phase present.

Ion concentrations computed for aqueous solutions in equilibrium with one, two or three salts were recalculated according to Eqs. (4) to (7) and then plotted in the phase diagram. Those points create four crystallization surfaces for the reverse four salts. The intersection points of two adjacent crystallization surfaces determined lines of double-salt crystallization. Two points of intersection of three crystallization surfaces corresponded to simultaneous crystallization of three different salts. Two examples of computed surfaces of liquid-solid equilibrium for the maximum and minimum temperature for identical pressure of 3 atm are shown in Fig. 3. It can be concluded that with increase in temperature the

solubility of the four salts also increases, however with different intensity and with the strongest influence on crystallization surface of NH_4HCO_3.

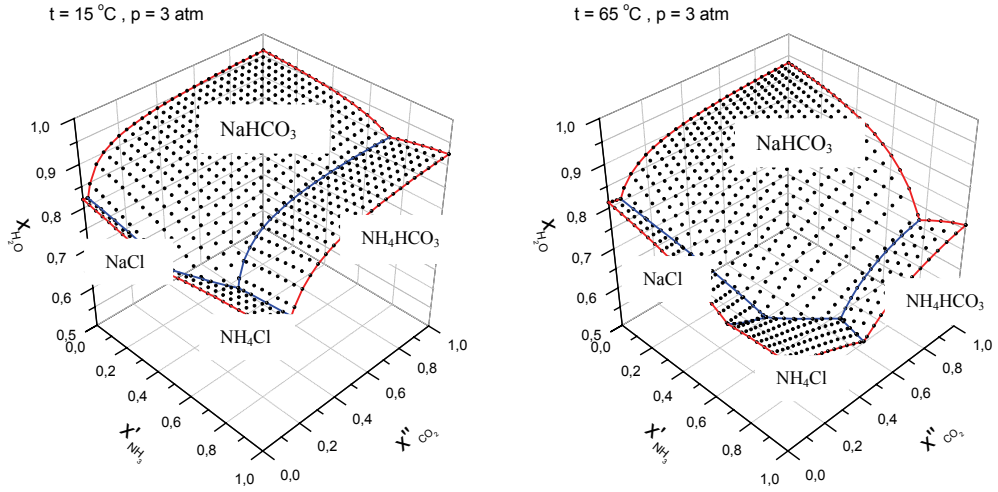

a) **b)**

Fig. 3. Computed crystallization surfaces for the Solvay soda system; a) at 15 °C, b) at 65 °C.

The simulated evolution of the crystallization surfaces can be summarized as follows:
- surface area of $NaHCO_3$ crystallization predominates in the whole temperature range,
- increase in temperature results in gradual shrinking of the crystallization area of NH_4HCO_3 followed by its disappearance at 65 °C and pressure of 1 atm due to decomposition of the salt,
- temperature rise reduces water concentration in liquid phase due to higher salt solubility,
- process pressure exerts small influence on the crystallization diagram.

4. Processing of equilibrium data

The broad simulation databank was then further processed to obtain correlation equations expressing mathematical relationship between water concentration, x_{H2O}, and molar fraction of "dry" cations, x'_{NH3}, and anions, x''_{CO2}. To simplify the functional records between those quantities their symbols were replaced by simpler ones: *x, y, z*.

$$x \equiv x'_{NH3} \;,\; y \equiv x''_{CO2} \;,\; z \equiv x_{H2O} \tag{8}$$

Preliminary trials with various functions $z=f(x,y)$ to adequately represent the four crystallization surfaces led to selection of polynomial of 4th degree presented in Eq. (9).

$$z = z_0 + a \cdot x + b \cdot y + c \cdot x^2 + d \cdot y^2 + e \cdot x^3 + g \cdot y^3 + h \cdot x^4 + i \cdot y^4 + \\ + j \cdot x \cdot y + k \cdot x^2 \cdot y + l \cdot x^3 \cdot y + m \cdot x \cdot y^2 + n \cdot x^2 \cdot y^2 + p \cdot x \cdot y^3 \quad (9)$$

The next step was regression processing of data, separately for 4 crystallization surfaces, to evaluate 15 coefficients of Eq. (9), i.e. z_0 to p, together with deriving the standard deviations of the coefficients. It was done for 14 sets of data for constant temperature and pressure. Values of the regression coefficients along with their confidence intervals were analysed against values of temperature and pressure. The analysis allowed to remove the expression "$k \cdot x^2 \cdot y$" from all correlations, and also 3, 4, 7 and 7 other elements of Eq. (9) for the $NaHCO_3$, NH_4HCO_3, NaCl and NH_4Cl surfaces, respectively. In addition, functional relationships $z=f(x,y)$ for the crystallization surfaces of NaCl and NH_4Cl were practically independent of pressure conversely to the surfaces for $NaHCO_3$ and NH_4HCO_3. Hence, the correlation (9) was developed only for the pressure level of 3 atm for the two latter salts – bicarbonates of sodium and ammonium.

The first term of Eq. (9) depended non-linearly on temperature, t, thus correlation (9) was further expanded to include the relationship of Eq. (10).

$$z_0 = z_{00} + z_1 \cdot t + z_2 \cdot t^2 \quad (10)$$

It should be mentioned that some regression coefficients of Eq. (9) were found statistically independent of temperature. Other coefficients of regression, which demonstrated statistical significance, were assumed to depend linearly on temperature, e.g. Eq. (11) represents that function for the a coefficient.

$$a = a_0 + a_1 \cdot t \quad (11)$$

Table 1 contains selected results in form of basic measures and validity ranges of the final correlations for the four crystallization surfaces.

T a b l e 1

Characteristic measures of correlations (9) for crystallization surfaces

Salt / Quantity	$NaHCO_3$ (3atm)	NaCl	NH_4HCO_3 (3atm)	NH_4Cl
Number of coefficients	23	13	10	12
Valid for x ∈	[0.00 ; 0.83]	[0.00 ; 0.70]	[0.68 ; 1.00]	[0.45 ; 1.00]
Valid for y ∈	[0.02 ; 1.00]	[0.00 ; 0.30]	[0.14 ; 1.00]	[0.00 ; 0.62]
Stand. deviation of z	0.0056	0.0003	0.0050	0.0038

Depending on complexity of the correlations they comprised from 10 to 23 terms. It should also be emphasized that the accuracy of correlating functional relationships

z=f(x,y,t) was better than 0.006, which also means only around 1% deviation from the values simulated by the OLI Anlyzer Studio package. The accuracy was regarded sufficient for the purpose of incorporating the correlations in CFD codes for predicting equilibrium conditions of crystallization in the Solvay soda system.

5. Concluding remarks

An extensive validation procedure for the Mixed-Solvent-Electrolyte model of thermodynamic equilibrium for saturated electrolyte solutions was performed. Positive results of the validation were obtained based on broad experimental literature data for gas-liquid-solid phase equilibrium of the NH_3–CO_2–NaCl–H_2O system. The literature sources covered wider ranges of temperature and pressure than those met in the Solvay soda technology.

An effective attempt was undertaken to transform simulated data for crystallization equilibrium of the soda system into polynomial correlations using the Jänecke's set of concentrations. The correlations represent with high accuracy the functional relationship of the four crystallization surfaces in dependence on ion concentrations and temperature. The obtained correlations are recognized as appropriate for including in pre-compiled user defined functions and then incorporated in CFD codes for predicting equilibrium conditions of crystallization.

Acknowledgement

This work was part of a research and development project financed by the Polish government funds for science in years 2007-2010.

Literature

[1] Jaworski Z., Zakrzewska B.: Computers and Chemical Engineering, **35**, (2011), 434-445.
[2] Liu Y., Watanasiri S.: Chemical Engineering Progress, **10**, (1999), 25–42.
[3] Loehe J.R., Donohue, M.D.: AIChE Journal, **43**, (1997), 180–195.
[4] Renon H.: Fluid Phase Equilibria, **30**, (1986), 181–195.
[5] Anderko A., Wang P., Rafal M.: Fluid Phase Equilibria, **194–197**, (2002), 123–142.
[6] Jaworski Z., Czernuszewicz M., Gralla Ł.: Chemical and Process Engineering, **31**, (2010), 789-811.
[7] Jaworski Z., Czernuszewicz M., Gralla Ł.:Chemical and Process Engineering, **32**, (2011), accepted for publication.
[8] Wang P., Anderko A., Young R.D.: Fluid Phase Equilibria, **203**, (2002), 141–176.
[9] Thomsen K., Rasmussen P., Gani R.: Chemical Engineering Science, **51**, (1996), 3675–3683.
[10] Koneczny H., Trypuć M.: Chemia Stosowana **XVIII**, 1, (1974), 15-21.
[11] Kurz F., Rumpf B., Sing R., Maurer G.: Industrial and Engineering Chemistry Research, **35**, (1996), 3795-3802.
[12] Kamps A., Sing R., Rumpf B., Maurer G.: Journal of Chemical Engineering Data **45**, (2000), 796-809.

18th International Conference Process Engineering and Chemical Plant Design
Günter Wozny and Łukasz Hady, Editors

KAI LANGENBACH[*, **], SABINE ENDERS[*]

CROSS-ASSOCIATION OF MULTI-COMPONENT SYSTEMS

Abstract

For the design of apparatus in chemical industry (e.g. heat exchanger) and process simulations the physical properties of mixtures, for instance the involved phase equilibria, must be known. For this purpose the perturbed-chain statistical associating theory (PC-SAFT) can be applied. For mixtures containing components able to associate or moreover to form cross associates the modeling of these mixtures is quite challenging.

This paper is dedicated to the suitable generalization of the self- and cross association models useful for process simulation. Special attention is paid to the safe solution procedure. This generalization allows a stable, always convergent and fast numerical procedure in order to calculate the monomer mole fractions.

The new method is applied to the calculation of phase equilibria, i.e. vapor-liquid equilibria, enthalpies and second order derivatives of the Helmholtz energy for mixtures and pure compounds. Especially for the calculation of several first and second order derivatives the new method shows advances in computational performance.

Keywords: Multi-component, PC-SAFT, second derivative properties, self- and cross-association, Wertheim theory.

1. Introduction

Chemical engineering applications typically involve the knowledge of several physical properties such as phase equilibria, heat capacities or enthalpies of vaporization. As the experimental database for these properties is far from completion, particularly for mixtures, and tedious to fill, a prediction of these properties is desirable. Such a prediction is possible via the use of an adequate equation of state (EOS). This EOS should be physically based, as it ought to be reliable for a wide range of substances with variable size and structure. Process simulations and the design of apparatus often involve associating species (e.g. water or alcohols) and thus the used EOS should be capable of describing the short ranged, highly directional intermolecular forces that are common to association bonds.

[*] TU Berlin, Chair of Thermodynamics and Thermal Separation Science, Straße des 17. Juni 135, 10623 Berlin, Germany, GSD Wärmetechnik GmbH, 57250 Netphen, Germany
[**] GSD Wärmetechnik GmbH, 57250 Netphen, Germany

The EOS called PC-SAFT, developed by Gross et al. [1,2], can be applied to the calculations of physical properties, including phase equilibria, of complex mixtures [e.g.3,4,5,6]. Besides this special EOS, many other from the SAFT family [7,8,9,10,11,12, 13,14,15,16] can also be used for this purpose. It has been shown, that PC-SAFT is applicable for many substances including associating ones, if the involved parameters are fitted to pure component vapor pressures and liquid densities [1,2]. Often it is possible to describe mixture properties with one binary parameter per species couple.

Using PC-SAFT [1,2] the self and cross association forces will be treated with the Wertheim first order perturbation theory [17,18,19,20,21], which was first applied to mixtures of hard spheres by Jackson et al. [22] and mixtures of hard sphere chains [23] by Chapman et al.. In order to include these association forces in the EOS an association model depending on the components of the considered mixture must be selected [24]. This situation leads to problems, if a general, substance independent algorithm should be developed. In the case of cross-association the monomer mole fractions must be calculated by means of solving a non-linear system of equations.

As PC-SAFT takes the association contribution to the Helmholtz energy into account using Wertheim first order perturbation theory [17,18,19,20,21], it has the intrinsic challenge of calculating the monomer mole fractions of associating species by means of solving a system of mass action equations [23] that are nonlinear (i.e. quadratic in the monomer mole fractions). As there is no known analytical solution, this system of equations needs to be solved numerically, which leads to substantial losses of computational performance. In addition simple strategies, such as Newton-Raphson iterations tend to fail if not properly constrained.

Michelsen et al. [25,26] and Tan et al. [27] have both suggested methods to solve the system of equations which involve either a constrained optimization procedure [25] or a recursive sequence [25,27]. In this paper the latter method is used in a modified way that increases performance by neglecting more linear dependent equations (i.e. equal monomer mole fractions) than in [27]. This is done by introducing a new characterization for associating compounds and modifying the indexing procedure for association sites.

2. Perturbed Chain Statistical Associating Theory (PC-SAFT)

2.1 Equation of State

PC-SAFT [1,2] is based on a perturbation theory of first order where the reference fluid is a hard chain fluid. Due to this the Helmholtz energy a is written as a sum of contributions.

$$a = a^{id} + a^{hc} + a^{disp} + a^{assoc} \tag{1}$$

The association contribution is generally written as

$$a^{assoc} = \sum_i x_i \sum_{A_i} \left(\ln\left(Y_{A_i}\right) - \frac{Y_{A_i}}{2} \right) + \frac{M_i}{2} \tag{2}$$

where Y_{A_i} is the fraction of nonbonded molecules at sites A_i of component i, x_i is the mole fraction of component i and M_i is the number of association sites of component i.

2.2 New Method for Calculating the Monomer Mole Fractions

The system of equations (see [23]), that has to be solved in order to calculate the contribution of association to the Helmholtz energy can be written in the form

$$Y_{A_i} = \frac{1}{1+\rho N_{AV} \sum_j \sum_{B_j} x_j Y_{B_j} \Delta_{A_i B_j}} \tag{3}$$

where i and j are component indices and A_i and B_j are association site indices. By introducing a bijective transformation $I \leftrightarrow (i, A_i)$ and $J \leftrightarrow (j, B_j)$ the association strength $\Delta_{A_i B_j}$, the monomer mole fractions Y_{A_i} and the mole fractions x_i can be rewritten, which results in an easier to read system of equations.

$$Y_{A_i} = Y_I \;;\; \Delta_{A_i B_j} = \Delta_{IJ} \;;\; x_{ij} \equiv x_{IJ} \tag{4}$$

$$Y_I + \rho N_{AV} \sum_J x_j \Delta_{IJ} Y_J Y_I - 1 = 0 \tag{5}$$

The entries of Δ_{IJ} are different from zero, if the association site $A_i \leftarrow I$ and the site $B_j \leftarrow J$ interact, which can be determined from their type. In this paper we propose the following possible types:

B – bivalent association site (interacts with B, P, N)
P – positive association site (interacts with B, N)
N – negative association site (interacts with B, P)

It is common practice to choose the association parameters such that the association strengths are equal for equal combinations of i and j (i.e. $\Delta_{IJ} = \Delta_{ij}$), if different from zero. From this, one can derive

$$Y_I + \rho N_{AV} \sum_J x_j \Delta_{ij} K_{IJ} Y_J Y_I - 1 = 0 \tag{6}$$

$$type(I) =: t(i) \tag{7}$$

$$K_{IJ} = \begin{cases} 0 & \forall I, J \mid t(I) = t(J) = P \vee t(I) = t(J) = N \\ 1 & else \end{cases} \tag{8}$$

Here K_{IJ} is a matrix that is zero, if the sites I and J cannot interact and unity, if they can. Denoting the type of association site I as Eq. (7), K_{IJ} can be written as Eq. (8).

This system of equations is only a different notation of Eq. (5). In order to reduce the number of equations, equal monomer mole fractions have to be identified. It can be shown that all Y_I with the same combination $(i, t(A_i))$ are equal. To identify conditions for $Y_{I_0} = Y_{I_1}$ the system of equations (8) can be used:

$$Y_{I_0} + \rho N_{AV} \sum_J x_j \Delta_{i_0 j} K_{I_0 J} Y_J Y_{I_0} - 1 = 0 \tag{9}$$

$$Y_{I_1} + \rho N_{AV} \sum_J x_j \Delta_{i_1 j} K_{I_1 J} Y_J Y_{I_1} - 1 = 0 \tag{10}$$

By subtracting one of these equations from the other under the condition, that $Y_{I_0} = Y_{I_1}$ holds it is possibly to simplify to:

$$\sum_J x_j Y_J \left(\Delta_{i_0 j} K_{I_0 J} Y_{I_0} - \Delta_{i_1 j} K_{I_1 J} Y_{I_1} \right) = 0 \tag{11}$$

This has to hold for all possible values of Y_J and x_j and thus it follows:

$$\Delta_{i_0 j} K_{I_0 J} = \Delta_{i_1 j} K_{I_1 J} \tag{12}$$

From Eq. (12) it is obvious that, if the two conditions

$$i_0 = i_1 \wedge K_{I_0 J} = K_{I_1 J} \tag{13}$$

are fulfilled, the monomer mole fractions Y_{I_0} and Y_{I_1} are indeed equal. This is similar to the statement, that the monomer mole fractions Y_{I_0} and Y_{I_1} are equal, if they belong to the same species i and to an association site of the same type. This means that the system of equations can be reduced, by characterizing components through the triple $(B, P, N)_i$ that counts the numbers of association sites of the different types on one species. The number of equations is g.

$$g = \begin{cases} 0 & \text{if no association occurs} \\ \sum_i \left(\operatorname{sgn}(B_i) + \operatorname{sgn}(P_i) + \operatorname{sgn}(N_i) \right) & \text{else} \end{cases} \tag{14}$$

This allows the use of a new index of smaller range.

$$I \leftrightarrow \left(i, t(B_i) \right); J \leftrightarrow \left(j, t(B_j) \right) \tag{15}$$

The system of equations can now be rewritten to the form

$$Y_I + \rho N_{AV} \sum_J x_j \Delta_{ij} D_{IJ} Y_J Y_I - 1 = 0 \tag{16}$$

which is of the size $g \times g$. This system of equations reminds of the system used by Tan et al. [27], but is smaller in some cases and uses only two indices instead of four due to the known transformation. This leads to some advantages from a computational point of view. The entries of the matrix D_{IJ} are the number of groups B_k interacting with the group A_i, where those groups are known from the index transformation (see Eq. 15).

Letting $(B)_j$, $(P)_j$ and $(N)_j$ denote the number of bivalent, positive and respectively negative association sites on molecules of the species j the matrix D_{IJ} has the form:

$$D_{IJ} = \begin{cases} (B)_j & \text{f.}t(B_j) = B \\ (P)_j & \text{f.}t(B_i) = P \wedge \left(\text{f.}t(B_j) = B \vee \text{f.}t(B_j) = N \right) \\ (N)_j & \text{f.}t(B_i) = N \wedge \left(\text{f.}t(B_j) = B \vee \text{f.}t(B_j) = P \right) \\ 0 & \text{else} \end{cases} \tag{17}$$

2.3 Example and Comparison to Other Methods

Considering a mixture of three components (i.e. (1,0,0)-(0,1,2)-(0,1,0)) the number of equations is $g = 4$ using the new method. The Matrix D_{IJ} together with the index transformation is

$$D_{IJ} = \begin{array}{c} i,t(I)/k,t(K) \\ 1,A \\ 2,P \\ 2,E \\ 3,P \end{array} \begin{array}{c} \begin{array}{cccc} 1,A & 2,P & 2,E & 3,P \end{array} \\ \begin{pmatrix} 1 & 1 & 2 & 1 \\ 1 & 0 & 2 & 0 \\ 1 & 1 & 0 & 1 \\ 1 & 0 & 2 & 0 \end{pmatrix} \end{array} \tag{18}$$

In contrast to this Tan et al. [27] give the number of equations as $g = s \cdot n$, where s is the number of site types in the mixture of n components which would mean $g = 9$, which is more than double the number of equations of the method developed in this contribution. Tan et al. [27] argue that this will not change the rate of convergence, which is apparently the case, as only zero entries are introduced to the matrix (staying in the notion of this contribution).

$$D_{IJ} = \begin{pmatrix} 1 & 0 & 0 & 0 & 1 & 2 & 0 & 1 & 0 \\ 0 & 0 & 0 & 0 & 0 & 0 & 0 & 0 & 0 \\ 0 & 0 & 0 & 0 & 0 & 0 & 0 & 0 & 0 \\ 0 & 0 & 0 & 0 & 0 & 0 & 0 & 0 & 0 \\ 1 & 0 & 0 & 0 & 0 & 2 & 0 & 0 & 0 \\ 1 & 0 & 0 & 0 & 1 & 0 & 0 & 1 & 0 \\ 0 & 0 & 0 & 0 & 0 & 0 & 0 & 0 & 0 \\ 1 & 0 & 0 & 0 & 0 & 2 & 0 & 0 & 0 \\ 0 & 0 & 0 & 0 & 0 & 0 & 0 & 0 & 0 \end{pmatrix} \tag{19}$$

Though this will not increase the number of iteration steps it will surely extend the computation time and memory usage for each iteration step. Especially for the treatment of polydisperse associating substances, modeled as pseudo-components, or when treating multi component mixtures this should prove a performance problem.

Michelsen et al. [25,26] used a different approach, i.e. maximizing an objective function Q, he showed to yield the solution to the system of equations (6) in the stationary point. This approach was not used here, because of the necessary matrix inversions involved. In terms of this contribution Michelsen's system of equations would be determined by

$$D_{IJ} = \begin{array}{c} i,t(I)/\,j,t(J) \\ 1,A \\ 2,P \\ 2,E_1 \\ 2,E_2 \\ 3,P \end{array} \begin{array}{c} \begin{array}{ccccc} 1,A & 2,P & 2,E_1 & 2,E_2 & 3,P \end{array} \\ \begin{pmatrix} 1 & 1 & 1 & 1 & 1 \\ 1 & 0 & 1 & 1 & 0 \\ 1 & 1 & 0 & 0 & 1 \\ 1 & 1 & 0 & 0 & 0 \\ 1 & 0 & 1 & 1 & 0 \end{pmatrix} \end{array} \tag{20}$$

Additionally the difference in matrix dimensions would grow the more association sites the mixture has, which is undesirable. The new method is applicable to multi component mixtures without previous knowledge about involved association models. The characterization of molecules by the number of association sites of the respective types together with the developed method for calculating the monomer mole fractions prove to minimize both the number of equations to be solved and the computational overhead due to the solution of trivial equations in the system of equations (6).

2.4 Derivatives of the Helmholtz Energy of Association

To calculate the contribution of association to first and second order derivative properties it is necessary to know the derivatives of the monomer mole fraction Y_J with respect to a variable τ out of the set of natural variables of the Helmholtz energy (i.e. $\tau \in \{\rho, T, x_i\}$, which can be calculated by differentiating Eq. (16) with respect to τ.

$$\frac{\partial Y_I}{\partial \tau} + \frac{\partial}{\partial \tau}\left(\rho N_{AV} \sum_J \mathsf{x}_j \Delta_{ij} D_{IJ} Y_J Y_I \right) = 0 \tag{21}$$

The result is a linear system of equations of the form

$$\frac{\partial Y_I}{\partial \tau} + \rho N_{AV} \sum_J \left(\mathsf{x}_j \Delta_{ij} D_{IJ} Y_I \frac{\partial Y_J}{\partial \tau} + \mathsf{x}_j \Delta_{ij} D_{IJ} Y_J \frac{\partial Y_I}{\partial \tau} \right) = -N_{AV} \sum_J \left(D_{IJ} \frac{\partial \left(\rho \mathsf{x}_j \Delta_{ij} \right)}{\partial \tau} Y_J Y_I \right) \tag{22}$$

that can be simplified by insertion of Eq. (16)

$$Y_I^{-2} \underbrace{\frac{\partial Y_I}{\partial \tau}}_{dY_I^\tau} + \sum_J \rho N_{AV} \mathsf{x}_j \Delta_{ij} D_{IJ} Y_I \underbrace{\frac{\partial Y_J}{\partial \tau}}_{dY_I^\tau} = \underbrace{-N_{AV} \sum_J \left(D_{IJ} \frac{\partial \left(\rho \mathsf{x}_j \Delta_{ij} \right)}{\partial \tau} Y_J \right)}_{b_I^\tau} \tag{23}$$

and written in matrix formulation

$$\underline{\underline{C}} \cdot \underline{dY^\tau} = \underline{b^\tau} \tag{24}$$

The left hand side matrix $\underline{\underline{C}}$ is independent of the variable with respect to which the equation is differentiated. As it always has positive entries on the diagonal and every entry is nonnegative it can be proven, with the help of Eq. (16), that the matrix is always strongly diagonally dominant. With the Levy-Desplanques theorem [28] it follows that it is always invertible, which allows to drop pivoting, when inverting or decomposing the matrix.

In order to obtain second derivatives of the monomer mole fractions Eq. (23) is differentiated with respect to a second variable φ out of the set of natural variables of the Helmholtz energy:

$$Y_I^{-2}\underbrace{\frac{\partial^2 Y_I}{\partial\tau\partial\varphi}}_{dY_I^{\tau,\varphi}}+\sum_J \rho N_{AV} x_J \Delta_{ij} D_{IJ} Y_I \underbrace{\frac{\partial^2 Y_J}{\partial\tau\partial\varphi}}_{dY_J^{\tau,\varphi}} = \underbrace{2Y_I^{-3}\frac{\partial Y_I}{\partial\tau}\frac{\partial Y_I}{\partial\varphi}-N_{AV}\sum_J D_{IJ}\frac{\partial\left(\frac{\partial\left(\rho x_J\Delta_{ij}\right)}{\partial\tau}Y_J\right)}{\partial\varphi}}_{b_I^{\tau,\varphi}} \quad (25)$$

$$\underline{\underline{C}}\cdot\underline{dY^{\tau,\varphi}}=\underline{b^{\tau,\varphi}} \quad (26)$$

where Eq. (26) is the matrix formulation. Again the left hand side matrix $\underline{\underline{C}}$ is independent of the variables with respect to which the equation is differentiated. Moreover $\underline{\underline{C}}$ is the exact matrix as in Eq. (24). This leads to numerical advantages, because the inverse, respectively the decomposition of the matrix, only has to be calculated once and can subsequently be used for any thermodynamic property as is the case for the procedure used by Tan et al. [27]. This is especially valuable for the design of apparatus (e.g. evaporators).

3. Calculation Results

To demonstrate the usefulness of the new method, some examples, ranging from liquid densities to the speeds of sound of ternary mixtures, are calculated and compared to experimental data. The results are obtained using the parameters in Table 1.

T a b l e 1

Pure component parameters

Component i	m_i	σ_i [Å]	$\frac{\varepsilon_i}{kT}$ [K]	κ_{A_i}	$\frac{\varepsilon_{A_i}}{kT}$ [K]	(B,P,E)	Ref.
Water	1.0656	3.0007	366.51	0.01	1800	(0,2,2)	[29]
Ethanol	2.3827	3.1771	198.24	0.032384	2653.4	(0,1,1)	[2]
1-Propanol	2.9997	3.237	233.4	0.015268	2276.8	(0,1,1)	[30]
1-Butanol	2.7515	3.6139	259.59	0.006692	2544.6	(0,1,1)	[2]

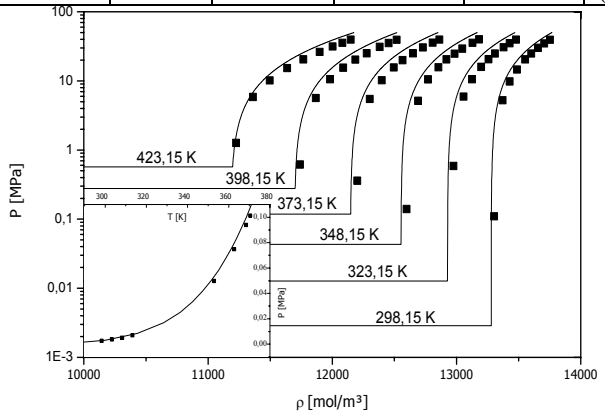

Fig.1: Pressure of 1-propanol for temperatures from 298.15K to 423.15K in steps of 25K against liquid densities. Symbols represent experimental data [31], solid lines represent PC-SAFT calculations. The insert is the vapor pressure curve of 1-propanol with experimental data from [32] (lower temperature) and [33] (higher temperature).

Figure 1 shows a comparison between calculation results and experimental data for the liquid densities of 1-propanol. The insert shows the calculated VLE compared to experimental data. The correlation results are excellent for both (relative standard deviation $RSD_\rho < 1\%$, $RSD_P \approx 3\%$) with a set of parameters fitted neglecting the high pressure VLE data. The critical regime is not taken into account, because it is not possible to describe near critical behavior with a mean field theory, as the critical fluctuations dominate at these conditions.

Figure 2 depicts the prediction of the vapor liquid equilibrium of the ternary system ethanol/1-propanol/1-butanol from pure component regression only, compared to experimental data. The agreement of the concentrations is again qualitatively and quantitatively good (absolute average deviation $AAD_{y_i} \approx 0.02$) except for the vapor fraction of one of the tie lines for the isopleths with liquid mole fraction of ethanol $x_{EtOH} = 0.2$. The fact that the equilibrium temperatures are predicted within an accuracy below one percent, as well as the irregularities in the equilibrium gas mole fractions for this isopleths, lead to the conclusion that, at least for this special case, the prediction may be better than the experiment.

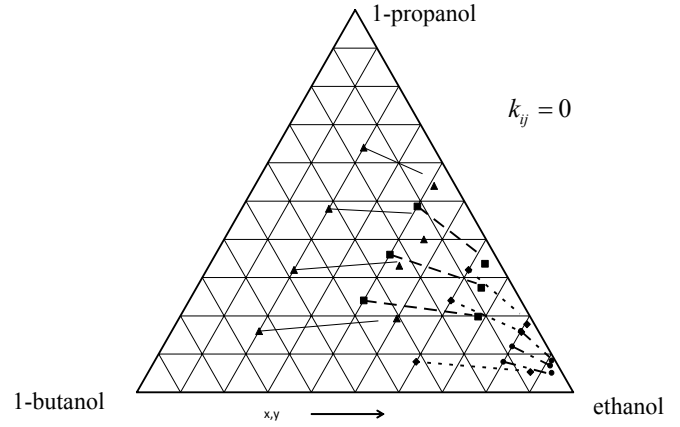

Fig.2: Predicted isobaric VLE at P=1.013bar of the mixture ethanol/1-propanol/1-butanol for four liquid isopleths (solid lines). Symbols represent experimental data [34].

Figure 3 shows the experimental and calculated heat capacities for water and 1-propanol. The agreement between calculated and experimental liquid isobaric heat capacity of 1-propanol very good except close to the two phase region (overall: $RSD_{c_P} \approx 6\%$, for $T < 300K$ $RSD_{c_P} \approx 4\%$). Also the isochoric and isobaric heat capacities of water show a good agreement (in the liquid: $RSD_{c_P} \approx 12\%$, $RSD_{c_V} \approx 7{,}5\%$, in the gas: $RSD_{c_P} \approx 7{,}5\%$, $RSD_{c_V} \approx 8\%$) between experimental data and calculations except for the trend of the liquid heat capacities with temperature. The ideal heat capacity is calculated from transitional and rotational degrees of freedom only.

$$c_V^{id} = \begin{cases} 1.5 \text{ for } m < 1.5 \\ 2.0 \text{ for } m < 2.5 \\ 2.5 \text{ for } m \geq 2.5 \end{cases} \tag{27}$$

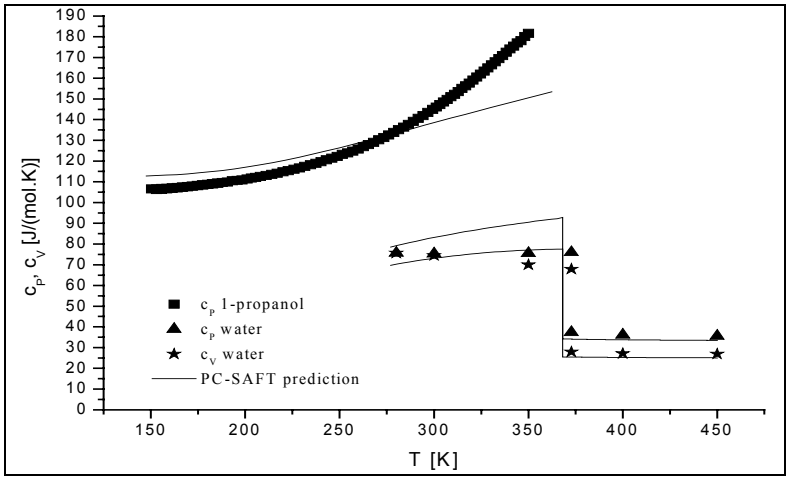

Fig.3: Comparison between predicted (solid lines) and experimental heat capacities of water and 1-propanol at 0.1MPa (c_P of 1-propanol [35]; c_P of water [36]; c_V of water [36]).

4. Conclusion

A general version of PC-SAFT has been implemented with special attention to the association contribution. The method used by Tan et al. [27] was modified in order to make it faster and hence more suitable for use in chemical engineering. The developed method exhibits some features that make it useful for the calculation of multiple properties at the same time. The advantage of the proposed method in terms of computing time in comparison with the method developed by Michelsen et al. [25,26] occurs especially, if second derivative properties of multi-component systems must be calculated. In the case of phase equilibria calculations both methods show similar performance. Both methods could gain strongly from parallelization, as they involve long summations and/or matrix inversions respectively decompositions. Finally, a new characterization for associating fluids is given, which eliminates the problems arising for general mixtures, if using the characterization of [24], which neglects the possibility of asymmetric association sites or induced association.

To demonstrate the new algorithm, PC-SAFT has been applied to the calculation of several physical properties for mixtures and pure components and it was shown that, while it captures the qualitative behavior of mixtures and pure components (associating and not associating), the theory needs some improvement to fully capture all of the calculated physical properties.

Ways to improve the behavior of the EOS might be, to include sound velocities in the parameter estimation, to use Wertheim's [17,18,19,20,21] TPT2 instead of TPT1 or, in the case of mixtures, to introduce a temperature dependent interaction parameter. The last alternative should be handled with care, as it leads to a loss of predictive power.

Literature

[1] Gross J., Sadowski G.: Ind. Eng. Chem. Res., **40**, (2001), 1244-60.
[2] Gross J., Sadowski G.: Ind. Eng. Chem. Res., **41**, (2002), 5510-15.
[3] Kouskoumvekaki I.A., Solms N. von, Lindvig T., Michelsen M.L., Kontogeorgis G.M.: Ind. Eng. Chem. Res., **43**, (2004), 2830-8.
[4] Kleiner M., Sadowski G.: J. Phys. Chem. C, **111**, (2007), 15544-53.
[5] Yarrison M., Chapman W.G.: Fluid Phase Equilib., **226**, (2004), 195-205.
[6] Solms N. von, Michelsen M.L., Kontogeorgis G.M.: Ind. Eng. Chem. Res., **42**, (2003), 1098-105.
[7] Paragand F., Feyzi F., Behzadi B.: Fluid Phase Equilib., **290**, (2010), 181-94.
[8] Gloor G.J., Jackson G., Blas F.J., Ro E. M. del, Miguel E.: J. Phys. Chem. C, **111**, (2007), 15513-22.
[9] Ramos M.C. dos, McCabe C.: Fluid Phase Equilib., **290,** (2010), 137-47.
[10] Khammar M., Shaw J.M.: Fluid Phase Equilib., **288**, (2010), 145-54.
[11] Vega L.F., Llovell F., Blas F.J.: J. Phys. Chem. B, **113**, (2009), 7621-30.
[12] Tan S.P., Adidharma H., Radozs M.: Ind. Eng. Chem. Res., **47**, (2008), 8063-82.
[13] Ramos M.C. dos, Blas F.J., Galindo A.: Fluid Phase Equilib., **261**, (2007), 359-65.
[14] Llovell F., Peters C.J., Vega L.F.: Fluid Phase Equilib., **248**, (2006), 115-22.
[15] Zhao H., McCabe C.: J. Chem. Phys., **125**, (2006), 104504.
[16] Clark G.N.I., Haslam A.J., Galindo A., Jackson G.: Mol. Phys., **104**, (2006), 3561-81.
[17] Wertheim M.S.: J. Stat. Phys., **35**, (1984), 19-34.
[18] Wertheim M.S.: J. Stat. Phys., **35**, (1984), 35-47.
[19] Wertheim M.S.: J. Stat. Phys., **42**, (1986), 459-476.
[20] Wertheim M.S.: J. Stat. Phys., **42**, (1986), 477-492.
[21] Wertheim M.S.: J. Chem. Phys., **87**, (1987), 7323-7331.
[22] Jackson G., Chapman W.G., Gubbins K.E.: Mol. Phys., **65**, (1988), 1-31.
[23] Chapman W.G., Jackson G., Gubbins K.E.: Mol. Phys., **65**, (1988), 1057-79.
[24] Huang S.H., Radosz M.: Ind. Eng. Chem. Res., **30**, (1991), 1994-2005.
[25] Michelsen M.L., Hendriks E.M.: Fluid Phase Equilib., **180**, (2001), 165-74.
[26] Michelsen, M.L., Ind. Eng. Chem. Res., 45, (2006), 8849-53.
[27] Tan S.O., Adidharma H., Radosz M.: Ind. Eng. Chem. Res., **43**, (2004), 203-08.
[28] Taussky O.: Am. Math. Mon., **56**, (1949), 672-76.
[29] Nino-Amezqitto G.O.: personal communications, TU Berlin, 2010.
[30] Langenbach, K., diploma thesis, TU Berlin, 2010.
[31] Abdulagatov I.M., Safarov J.T., Aliyev F.Sh., Talibov M.A., Shahverdiyev A.N., Hassel E.P.: Fluid Phase Equilib., **268**, (2008), 21-33.
[32] Safarov J., Verevkin S.P., Bich E., Heintz A.: J. Chem. Eng. Data, **51**, (2006), 518-25.
[33] Mejia A., Segura H., Cartes M., Bustos P.: Fluid Phase Equilib., 255, (2007), 121-130.
[34] Koshelkov V.A., Grudinina T.A., Pavlenko T.G., Timofeev V.S., Serafimov L.A.: Uch. Zap. Mosk. Inst. Tomkoi Khim. Tekhnol., **1**, (1971), 44-47.
[35] Miltenburg J.C. van, Berg G.J.K. van den: J. Chem. Eng. Data, **49**, (2004), 735-39.
[36] Wagner, W., Kretzschmar, H.-J.: International Steam Tables, Springer, Berlin 2007

18th International Conference Process Engineering and Chemical Plant Design
Günter Wozny and Łukasz Hady, Editors

ANETA GŁUSZEK*

ELECTRIC ENERGY USE AND ECOLOGICAL ANALYSIS FOR THE PRODUCTION OF FLAT-PLATE SOLAR COLLECTORS

Abstract

The Life Cycle Assessment (LCA) method has been applied to an evaluation of the environmental impacts generated during production of the flat-plate solar collector, weighing 39,17 kg including packaging. The mass and energy balances of the manufacturing process of this collector have been drawn up based on real data, collected by a direct interview in 2010. All stages of this process, including the black chromium electroplating for the selective coating on the absorber, the preparation and painting of the casing and the assembly of the properly cut collector parts, take place in the manufacturing plant in Poland. The analysis includes the environmental burden associated with the transport of the collector's components to the plant.
A summary report provides an assessment in relation to 7 environmental impacts: fossil energy depletion, water consumption, waste production, acidification, global warming, photochemical oxidation and eutrophication.

Keywords: ecological analysis, LCA analysis, production of flat-plate solar collectors.

1. Introduction

Concern about the condition of the surrounding environment, and the increased cost of heat production from traditional energy sources, stimulates the search for alternative energy sources. Photothermal conversion is one of the ways of getting thermal energy from renewable energy sources (RES). In practice, to use this kind of clean, free energy, there are necessary devices such as solar collectors, in which the heat of the solar radiation is collected through absorption and transferred to the solar liquid. This then heats up the water in the solar reservoir, which in turn can be used as domestic hot water or in a central heating system. It is a simple solution in technical terms, but contrary to popular opinion, the heat energy gained is not free from negative environmental impacts and causes the

* Ph.D. Eng., Cracow University of Technology, Institute of Chemical and Process Engineering, ul. Warszawska 24, 31-155 Kraków, Poland

depletion of natural resources. As a result of the manufacturing processes of solar collectors, their transportation and the exploitation follows the burden of the natural environment. To show the scale of the environmental impact of solar collectors, their electric power and ecological characteristics are drawn up, based on the classical Life Cycle Assessment (LCA). Standards ISO 14040 series allow the examination of the potential impact for a selected life cycle stage. Therefore the electric energy and ecological characteristics of a solar collector, usually refers to a range of "from cradle to gate" or "from gate to gate", depending on whether the investigation included the extraction of mineral resources. An expansion of the system boundaries allows us to find out hidden impacts, which are associated with phases of the collector life cycle, other than its operation phase. A few LCA studies on solar thermal collectors were carried out in the past [1, 2, 3], although existing literature does not cover collectors produced in Poland.

2. Life Cycle Assessment – goal and scope of the analysis

The LCA analysis was conducted to determine the environmental impact of the manufacturing process of the flat-plate solar collector with an absorption layer based on black chrome. The process assessment was made based on data from 2010. Any changes in the manufacturing process or changes in the distance or quantity of the delivery, would affect the results.

Electric power and the ecological characteristics of a solar collector describe a set of indicators of the environmental impact categories related to the functional unit (FU).

One flat-plate solar collector, having dimensions of 2018 × 1037 × 89 mm, 81,2% of optical efficiency, a total area of 2,09 m^2 and an absorber surface of 1,82 m^2, was accepted as a functional unit of LCA analysis. The commercial name of the studied collector cannot be specified, due to the privacy of data providers.

An average annual energy profit from 1 square meter of the collector active surface area, calculated on the basis of simulations made for all Polish provinces by using GetSolar computer programme, is about 460 kWh/(m^2·year).

The LCA analysis focuses on the production process of solar collectors without extracting the mineral resources. It means that this analysis includes a gate to gate system boundary where the starting gate is with the collection and transportation of the intermediate products and the output gate is the point of obtaining the final commercial product with the package. Environmental burdens associated with the transportation for delivering solar collectors components were included in the system boundary.

2.1. Mass and energy balances

The conducted analysis refers to the real product existing on the Polish and foreign market. The present collector is the product composed of intermediate products, with a total weight of 37,37 kg, which are both of domestic and foreign origin. The quantity of materials, distance for delivery and method of transportation, all need to be included in the LCA analysis of the transport of components to the manufacturing plant. The transportation can be carried out by: light-duty vehicles (LDV), heavy-duty vehicles (HDV) or cargo ships by sea. Table 1 contains results of the inventory and data characterising the transport [4].

T a b l e 1

Mass balance of the solar collector and data characterizing the transport [4]

No.	Components of the single collector	Weight [kg]	Distance delivery [km]	Number of deliveries per year
1	Aluminum Cover	7,08	300	24
2	Powder paint	0,3	15	12
3	Tempered glass	14	8000	17
4	Polymer-based adhesive	0,2	60	12
5	Mineral wool with a density of 60 kg/m3	6,2	400	24
6	Mineral wool with a density of 120 kg/m3	1,2	400	24
7	Aluminum sections (4 pieces)	2,5	8000	2
8	Glass veil	0,0776	700	4
9	Rubber seals (4 pieces)	0,0074	100	12
10	Brass Sleeve	0,055	15	12
11	Copper tape	3,2	950	9
12	Copper pipe with a diameter of $\phi 8 \times 0,5$ mm	1,65	900	6
13	Copper pipe with a diameter of $\phi 18 \times 1$ mm	0,9	50	90
TOTAL WEIGHT OF COLLECTOR:		**37,37**	-	-
14	Cardboard packaging	1,80	5	253
REAGENTS FOR GALVANIZING:		**0,242**	-	-
15	Chromic anhydride	0,050	60	3
16	Sulphuric acid (for pickling)	0,080	60	6
17	Nickel (II) sulphate	0,060	60	4
18	NPREP (Radical)	0,050	200	6
19	Nickel (II) Chloride	0,002	60	3

The manufacturing process of the solar collector, which is entirely done in Poland, can be divided into the following 4 stages:

1) **Preparation of the absorber in the galvanizing plant** – cut to suitable dimensions, the copper tape is degreased and washed to remove impurities. The chrome adheres well to the nickel, therefore the absorber is successively pickled with the sulphuric acid (H_2SO_4), then nickel plated and finally washed and covered with a layer of black chromium. The galvanizing processes are consuming about 8,15 kWh of electricity and 27 litres of water for each absorber. Wastewater is treated in an on-site sewage treatment plant causing additional electricity consumption, approx. 0,9 kWh per absorber. Water is not recycled to the process.
2) **Preparation of the heating pipes** – ready copper pipes are cut and laser welded in "harp" configuration and ultrasonically welded to the absorber sheet. The leak-tightness control and assembly of the sleeves are also being done at this stage. Electricity consumption per one finished element is approx. 0,9 kWh.

3) **Preparation and painting of the casing** – the aluminum sheet is cut and folded in such a way that it forms a tight structure. Approximately 0,2 kWh of electricity is needed for preparing one casing. Each casing is then powder coated, which additionally consumes 3,2 kWh of electricity.
4) **Assembly of the collector parts, packing and storage** – after preparing the casing and absorber, the remaining components of the collector are assembled, such as: glass wool insulation with two different degrees of hardness, glass veil, sections, seals and low iron tempered glass with high solar radiation flux covered by a metal profile. The finished collector is packed into a cardboard box. The electricity consumption estimated at this stage, per functional unit, is about 0,6 kWh and it includes the lighting of halls and stores.

The compressed air is used in all production stages of the solar collector. Approximately 2,1 kWh per functional unit is needed for the preparation of it. Total energy consumption for one solar collector is 16,05 kWh. The balance does not include the lighting of the office. Figure 1 shows the percentage of energy use in various stages of production.

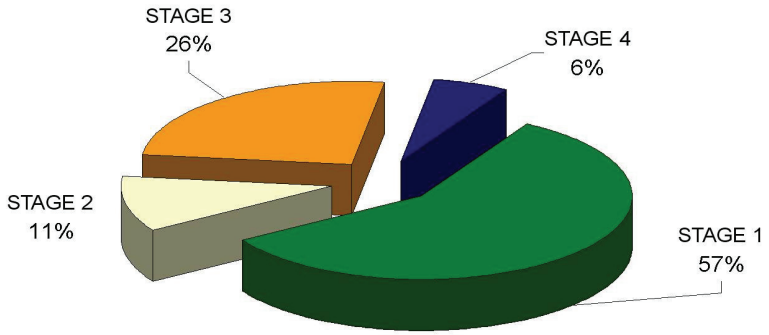

Fig. 1. The percent energy consumption during various stages of the solar collector production

2.2. Electric power and ecological characteristics

Assessment of the environmental burden quantity was estimated based on seven environmental impacts, counted on the defined functional unit (Tab. 2). By using relevant values of characteristic coefficients, different emissions collected during the inventory phase of LCA have been recalculated to have the same units. For example 1 g N_2O contributes as much to the global warming as 310 g CO_2 and therefore the 1 g N_2O is equal to 310 g CO_2-equivalents. The magnitude of the category indicator results is calculated relatively to the reference information [5]. The results depend not only on the quality of the input data obtained from the solar collector's manufacturer, but also on the reference values, because with the change of reference year the annual average per capita emissions are different.

Reference indicators of normalization which illustrate the average environmental impact for one capita of Poland in 2001 are presented in Table 2 [6].

The values of an environmental impact category indicator, which are the electric energy and ecological characteristics of a solar collector, were calculated according to:

– unpublished data on material and energy balances provided by the manufacturer of the solar collectors [4],
– equivalent loads for the emission related impact categories, mostly used in the LCA analysis for the evaluation of the potential impacts of a product on the environment [5].

The indicators of environmental burdens associated with the transport activities and 1 TJ of electric energy production in the Polish environment come from the GEMIS 4.6 database [7] and include the wider version of influence on the environment i.e. raw material extraction.

T a b l e 2

The electric energy and ecological characteristics of a solar collector

Lp.	Environmental impact categories	The impact category indicator results per 1 FU	Reference factors of normalization for one capita of Poland in 2001
1	Fossil energy depletion, GJ	2,483	78,28
2	Water consumption, m^3	0,125	292,00
3	Waste, Mg	0,029	3,22
4	Acidification, eq. kg SO_2	2,066	86,00
5	Global warming, eq. Mg CO_2	0,213	9,80
6	Photochemical oxidation, eq. kg C_2H_4	0,159	11,60
7	Eutrophication, eq. kg PO_4	0,226	65,62
1 FU = 1 flat-plate solar collector having dimensions 2018 × 1037 × 89 mm and absorber surface 1,82 m^2.			

The LCA method widened to the level of a normalised category indicator is presented in Fig. 2. The results of impact category indicators were related to reference factors of normalisation.

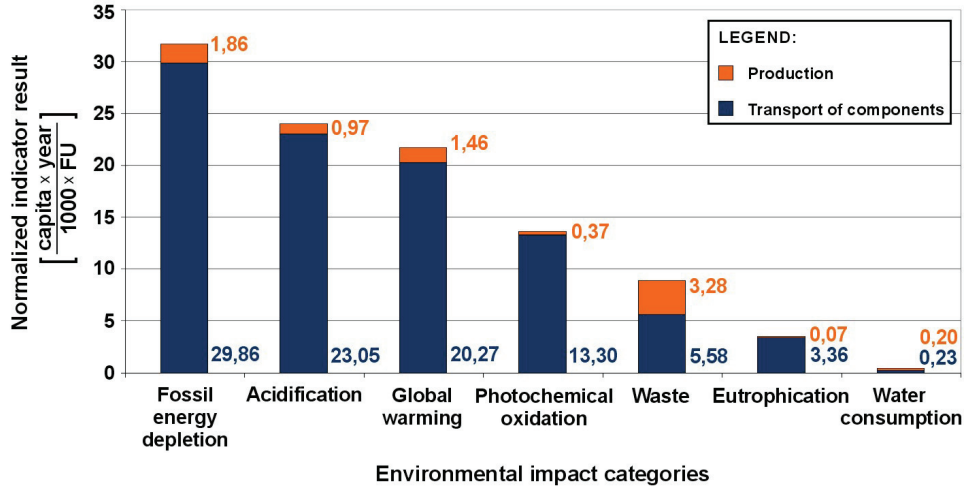

Fig. 2. The normalised category indicator results for the solar collector

The normalisation process makes for easy comparison, because various environmental influences are imported to the common unit. The results of normalised indicators are expressed by a general unit [capita × year × 10^{-3} / 1 FU] and they determine the size of the environmental impact. The bigger the impact value, the higher the potential negative influence on the environment [8]. Normalised indicators were calculated separately for obtaining the components of the solar collector and for the manufacturing process of the final product.

The analysis of Figure 2 shows that the share of primary energy in the transportation of the components is 16 times bigger than in the solar collector manufacturing process. Together with the flue gas coming from the transport vehicles into the atmosphere, are emitted: carbon monoxide, nitrogen oxides and hydrocarbons, which are the major components of photochemical smog. Therefore the photochemical oxidation indicator is 36 times bigger for transportation. A high indicator of soil and water acidification is also the result of combustion of the transportation fuels with sulphur content. During the combustion process inside a diesel engine, sulphur in the fuel is oxidized into SO_2. This is one of four main acid air pollutions. The indicator of acidification is 24 times bigger in the transport activities as compared to the manufacturing process.

3. Conclusions and future developments

The essential source of the environmental impact in solar collector production, are processes connected with the combustion of fuel in vehicle engines, which are transporting the intermediate products. The collector's manufacture has little influence on the environment. At this stage, the processes associated with the electric energy production bear the responsibility of the environmental burden.

Prepared in such a way this characteristic could be used in the future for comparison of the production processes of various types of the solar collectors. It can be also used to determine the electric energy and ecological characteristics of the full life cycle of the whole solar plant, in which the liquid flat-plate solar collector is applied. At present, the electric energy and ecological characteristics of collectors produced in Poland are not known.

The next research step will be performance of a sensitivity analysis to evaluate the reliability of the results.

Literature

[1] Ardente A., et al.: Renewable Energy, **30**, (2005), 109-130.
[2] Ardente A., et al.: Renewable Energy, **30**, (2005), 1031-1054.
[3] Battisti R., Corrido A.: Journal of Cleaner Production, **13**, (2005), 1295-1300.
[4] Świerkosz M.: Analiza cyklu życia płaskiego cieczowego kolektora słonecznego, Praca inżynierska, Politechnika Krakowska, WIiTCh, Kraków 2011.
[5] Guinée J. B. (Ed.): Handbook on Life Cycle Assessment, Kluwer Academic Publishers, Dordrecht 2002.
[6] Górzyński J.: Podstawy analizy środowiskowej wyrobów i obiektów, WNT, Warszawa 2007.
[7] Baza danych GEMIS 4.6, (21.05.2011): http://www.gemis.de/
[8] Głuszek A., Magiera J.: Czasopismo Techniczne PK, **2-M**, (2008), 87-94.

18th International Conference Process Engineering and Chemical Plant Design
Günter Wozny and Łukasz Hady, Editors

GEORGE TSATSARONIS *, TATIANA MOROSUK *

ADVANCED EXERGETIC ANALYSIS OF ENERGY-INTENSIVE PROCESSES

Abstract

An exergetic analysis identifies the location, magnitude and sources of thermodynamic inefficiencies in an energy-intensive process. This information is used for improving the thermodynamic performance and for comparing various processes. In addition, an exergetic analysis forms the basis for the other exergy-based analyses, i.e. the exergoeconomic and the exergoenvironmental analyses.

A conventional exergetic analysis does not consider the interactions among the components of a system nor the real potential for improving the system. These shortcomings of the conventional analysis are overcome and the quality of the conclusions obtained from an exergetic evaluation is improved, when for each important system component the value of the exergy destruction is split into endogenous/exogenous and avoidable/unavoidable parts. We call the analyses resulting from such a splitting *advanced exergetic analyses*.

The paper demonstrates how an advanced exergetic analysis provides the user with information on the formation processes of thermodynamic inefficiencies and on the ways through which these inefficiencies could be reduced. A refrigeration process is used as an example in this paper.

Keywords: irreversibility, exergy, exergy destruction, exergetic analysis, advanced exergetic analysis, refrigeration.

1. Introduction

Exergy-based methods is a general term that includes the conventional and advanced exergetic, exergoeconomic, and exergoenvironmental analyses and evaluations.

The exergy concept complements and enhances an energetic analysis by calculating (a) the true thermodynamic value of an energy carrier, (b) the real thermodynamic inefficiencies in a system, and (c) variables that unambiguously characterize the performance of a system (or one of its components) from the thermodynamic viewpoint.

* Technische Universität Berlin, Institut für Energietechnik, Marchstrasse 18, 10587 Berlin, Germany

The real thermodynamic inefficiencies in an energy conversion system are related to exergy destruction ($\dot{E}_D$) and exergy loss ($\dot{E}_L$). All real processes are irreversible due to effects such as chemical reaction, heat transfer through a finite temperature difference, mixing of matter at different compositions or states, unrestrained expansion, and friction. An exergy analysis identifies the system components with the highest contribution to the overall thermodynamic inefficiencies and the processes that cause them.

2. Conventional exergetic analysis

Exergy is defined as the maximum theoretical useful work (shaft work or electrical work) obtainable from an energy conversion system as this is brought into thermodynamic equilibrium with the thermodynamic environment while interacting only with this environment [1-3].

In an exergy analysis we calculate the exergy associated with each energy carrier (stream) in the overall system, the exergy destruction within each system component and process, and the *exergetic efficiency* (for each process, component, or system).

Central elements for the modern exergetic analysis are the general concepts of the *exergy of fuel* and the *exergy of product* introduced in [4]: The *exergy of product* is the desired result (expressed in exergy terms) achieved by the system being considered (e.g., the *k*th component), and the *exergy of fuel* represents the exergetic resources expended to generate the exergy of the product. The concepts of product and fuel are used in a consistent way not only in *exergetic analyses* but also in the *exergoeconomic* and *exergoenvironmental* analyses [1,5,6].

Using the exergy rates associated with fuel $\dot{E}_{F,k}$ and product $\dot{E}_{P,k}$, the exergetic balance for the *k*th component is

$$\dot{E}_{F,k} = \dot{E}_{P,k} + \dot{E}_{D,k} \quad (1)$$

and the exergetic balance for the overall system is

$$\dot{E}_{F,tot} = \dot{E}_{P,tot} + \sum_n \dot{E}_{D,k} + \dot{E}_{L,tot} \quad (2)$$

The following exergetic variables may be used for improving the overall effectiveness of the *k*th component in an iterative optimization [1,2]:

- Exergy destruction rate, $\dot{E}_{D,k}$
- Exergetic efficiency

$$\varepsilon_k = \frac{\dot{E}_{P,k}}{\dot{E}_{F,k}} = 1 - \frac{\dot{E}_{D,k}}{\dot{E}_{F,k}} \quad (3)$$

- Exergy destruction ratio

$$y_{D,k} = \frac{\dot{E}_{D,k}}{\dot{E}_{F,tot}} \quad (4)$$

3. Advanced exergetic analysis

The interactions among different components of the same system can be estimated and the quality of the conclusions obtained from an exergetic evaluation can be improved, when the exergy destruction in each (important) system component is split into endogenous/exogenous and avoidable/unavoidable parts [3,7-12].

We call the analyses based on these splittings *advanced exergetic analysis*.

Endogenous exergy destruction is the part of exergy destruction within a component obtained when all other components operate ideally and the component being considered operates with the same efficiency as in the real system. The *exogenous* part of the variable is the difference between the value of the variable within the component in the real system and the endogenous part:

$$\dot{E}_{D,k} = \dot{E}_{D,k}^{EN} + \dot{E}_{D,k}^{EX} \quad (5)$$

This splitting of the exergy destruction gives us an opportunity to estimate the interconnections among the components within the overall system. Another splitting of the exergy destruction (into unavoidable and avoidable parts) shows us the real potential for improving the *k*th component.

The *unavoidable* ($\dot{E}_{D,k}^{UN}$) exergy destruction cannot be further reduced due to technological limitations such as availability and cost of materials and manufacturing methods. The difference between total and unavoidable exergy destruction for a component is the *avoidable* exergy destruction ($\dot{E}_{D,k}^{AV}$) that should be considered during the improvement procedure

$$\dot{E}_{D,k} = \dot{E}_{D,k}^{UN} + \dot{E}_{D,k}^{AV} \quad (6)$$

Using the combination of the splittings we can calculate

- the *avoidable endogenous exergy destruction* ($\dot{E}_{D,k}^{AV,EN}$). This variable which can be reduced by improving the *k*th component from the exergetic point of view, and
- the *avoidable exogenous exergy destruction* ($\dot{E}_{D,k}^{AV,EX}$) that can be reduced by a structural improvement of the overall system, or by improving the efficiency of the remaining components, and always of course by improving the efficiency in the *k*th component.

To better understand the interactions among components, the exogenous exergy destruction (as well as the exogenous unavoidable and the exogenous avoidable exergy destructions) within the *k*th component are split further:

$$\dot{E}_{D,k}^{EX} = \sum_{\substack{r=1 \\ r\neq k}}^{n} \dot{E}_{D,k}^{EX,r} + \dot{E}_{D,k}^{mexo} \quad (7)$$

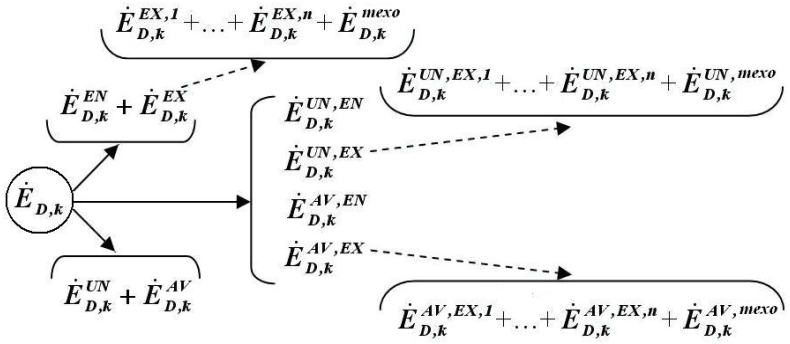

Fig. 1. Options for splitting the exergy destruction within the k th component in an advanced exergy analysis

The value of $\dot{E}^{EX,r}_{D,k}$ represents the part of the exogenous exergy destruction within the kth component that is caused by the irreversibilities occurring within the rth component. The remaining part $\dot{E}^{mexo}_{D,k}$ we call *mexogenous exergy destruction* within the kth component.

All approaches for splitting the exergy destruction can be shown using Figure 1. The methodology of splitting has been described in detail for a power system as well as for refrigeration machines in Refs. [7-13].

In order to identify priorities for improving components based on information obtained from an advanced exergetic analysis, the variable $\dot{E}^{AV,\Sigma}_{D,k}$ should be used. This variable presents the sum of the avoidable endogenous exergy destruction within the kth component and the avoidable exogenous exergy destructions within the remaining components caused by the kth component [11]

$$\dot{E}^{AV,\Sigma}_{D,k}=\dot{E}^{AV,EN}_{D,k}+\sum_{\substack{r=1\\ r\neq k}}^{n}\dot{E}^{AV,EX,k}_{D,r} \quad (8)$$

3. Example

A vapor-compression refrigeration machine with a closed compressor (Figure 2) is used as an example to demonstrate the application of the conventional and advanced exergy-based analyses. This machine consists of a compressor with electrical motor (CM), a condenser (CD), a throttling valve (TV) and an evaporator (EV). R 134a is the primary working fluid for the refrigeration machine, whereas water is used as the secondary working fluid in the condenser and the evaporator. The product from the overall system is the cold rate $\dot{Q}_{cold}$ =50kW, the exergy rate of which is kept constant in the analysis:

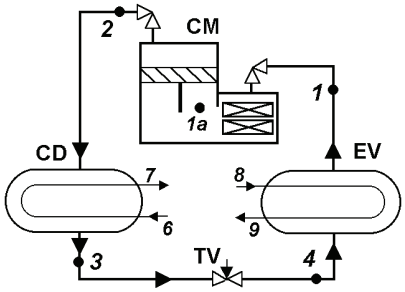

Fig. 2. Vapor-compression refrigeration machine with the closed compressor

$\dot{E}_{P,tot} = \dot{E}_9 - \dot{E}_8 = const$. The isentropic efficiency of the compressor is assumed to be $\eta_{CM} = 0.85$. For simplicity, pressure drops are neglected for the primary working fluid in the condenser and evaporator.

Table 1 shows the working fluid, mass flow rate, temperature, pressure and specific physical exergy (with the splitting into thermal and mechanical parts according to the methodology presented in [13]) of streams of matter shown in Figure 2. The exergy destruction within the components of the refrigeration machine is calculated as:

● Compressor

$$\dot{E}_{D,CM} = \dot{E}_{F,CM} - \dot{E}_{P,CM} = \dot{W}_{CM} - \left(\dot{E}_2 - \dot{E}_{1a}\right) \quad (9)$$

● Condenser

$$\dot{E}_{D,CD} = \dot{E}_{F,CD} - \dot{E}_{P,CD} = \left(\dot{E}_2 - \dot{E}_3\right) - \left(\dot{E}_7 - \dot{E}_6\right) \quad (10)$$

● Throttling valve

$$\dot{E}_{D,TV} = \dot{E}_{F,TV} - \dot{E}_{P,TV} = \left(\dot{E}_3^M - \dot{E}_4^M\right) - \left(\dot{E}_4^T - \dot{E}_3^T\right) \quad (11)$$

● Evaporator

$$\dot{E}_{D,EV} = \dot{E}_{F,EV} - \dot{E}_{P,EV} = \left(\dot{E}_4 - \dot{E}_1\right) - \left(\dot{E}_9 - \dot{E}_8\right) \quad (12)$$

Table 2 shows the exergy rates associated with fuel, product and exergy destruction as well as the exergetic efficiency and the exergy destruction ratio for each component. Note that the condenser is a dissipative component [1,5]; therefore, no exergetic efficiency is calculated for the condenser.

T a b l e 1

Thermodynamic and exergoeconomic data for the refrigeration machine shown in Figure 2

Stream	Working fluid	$\dot{m}$ [kg/s]	T [ºC]	p [bar]	e^T [kJ/kg]	e^M [kJ/kg]	e [kJ/kg]
1	R134a	0.3247	0	2.93	0.6	24.7	25.3
1a	R134a	0.3247	10	2.93	0.1	24.7	24.8
2	R134a	0.3247	49	8.16	7.9	39.6	47.5
3	R134a	0.3247	32	8.16	0	39.6	39.6
4	R134a	0.3247	0	2.93	11.9	24.7	36.6
6	Water	2.939	20	1.50	0	0.05	0.05
7	Water	2.939	25	1.42	0.18	0.04	0.22
8	Water	1.704	12	1.50	0.46	0.05	0.51
9	Water	1.704	5	1.42	1.67	0.04	1.71

Table 2

Conventional exergetic analysis of the refrigeration machine shown in Figure 1.

Component	$\dot{E}_{F,k}^{real}$ [W]	$\dot{E}_{P,k}^{real}$ [W]	$\dot{E}_{D,k}^{real}$ [W]	ε_k [%]	y_k [%]
CM	8 554	7 381	1 173	86.3	13.7
CD	2 573	0 496	2 077	–	24.3
TV	4 858	3 .864	0 994	79.5	11.6
EV	3 657	2 031	1 626	55.5	19.0

The results from the conventional exergetic analysis (Table 2) show that the highest exergy destruction occurs in the condenser and the evaporator. In this way during the improvement, the designer should focus on these two components; however the condenser has a higher priority for improvement than the evaporator.

In order to estimate the potential for improving each component from the thermodynamic point of view, the value of the exergy destruction should be split into unavoidable and avoidable parts. For this splitting we need to conduct the simulation of the refrigeration machine with so-called "unavoidable irreversibilities", that is taking into account the technological limitations (e.g., manufacturing methods) which cannot be overcome in future for heat exchangers having air as a secondary working fluid, and for reciprocating compressors. For the numerical analysis, we assumed the following parameter values in order to calculate the unavoidable inefficiencies: ΔT_{CD}^{UN} = 0.5 K, ΔT_{EV}^{UN} = 0.5 K, η_{CM}^{UN} = 95%. The value of the unavoidable exergy destruction $\dot{E}_{D,k}^{UN}$ should be calculated from [8-11]

$$\dot{E}_{D,k}^{UN} = \dot{E}_{P,k}^{real}\left(\frac{\dot{E}_D}{\dot{E}_P}\right)_k^{UN} \qquad (13)$$

where the term $\left(\frac{\dot{E}_D}{\dot{E}_P}\right)_k^{UN}$ is a ratio between exergy destruction and energy of product for the k th component at unavoidable operation conditions (from the simulation of the cycle with "unavoidable irreversibilities").

The values of $\dot{E}_{D,k}^{UN}$ and $\dot{E}_{D,k}^{AV}$ are given in Table 3. Only for the throttling valve we obtain $\dot{E}_{D,k}^{UN} > \dot{E}_{D,k}^{AV}$; for other components it is $\dot{E}_{D,k}^{UN} < \dot{E}_{D,k}^{AV}$. The condenser and the evaporator have the highest avoidable endogenous exergy destruction (Table 3) and the condenser is the component with the higher potential for improvement. Note that the compressor also has a high improvement potential, and $\dot{E}_{D,CM}^{AV}$ is comparable with $\dot{E}_{D,EV}^{AV}$.

The interconnections between the components within the system can be estimated through splitting the exergy destruction into endogenous and exogenous parts.

For this splitting, we need a set of special simulations of the system. The first step is to simulate a so-called "theoretical process". In this case the following assumptions should be valid for each component: $\dot{E}_{D,k}^{th} = 0$ (if it is possible, for example for the compressor with η_{CM}^{th}=1), or otherwise $\dot{E}_{D,k}^{th} = min$ (for heat exchangers with $\Delta T^{th} = 0$K). For the theoretical process the throttling valve should be replaced by a hypothetical expander (η_{EX}^{th}=1, therefore $\dot{E}_{D,EX}^{th} = 0$). For the theoretical process $T_{EV}^{th} = 5$ºC and $T_{EV}^{th} = 24.8$ºC. More detail explanations have been given in [7,12]. The second step is to simulate the so-called "hybrid processes 1": The number of these hybrid processes is equal to the number of components within the system. In the hybrid process only the component being considered is simulated with its real inefficiency, while all other components correspond to the theoretical process. The exergy destruction calculated for the k th component (with real irreversibility) is equal to the endogenous exergy destruction within this component.

The values of $\dot{E}_{D,k}^{EN}$ and $\dot{E}_{D,k}^{EX}$ are given in Table 3. For the compressor, the condenser and the evaporator, we have $\dot{E}_{D,k}^{EN} > \dot{E}_{D,k}^{EX}$. This means that the interconnections between the components are not very strong. For the evaporator, $\dot{E}_{D,EX}^{EX}$=0. This means, that the exergy destruction within the evaporator can be decreased only through improvement of the component itself and that the exergy destruction within this component is independent of the irreversibilities within the remaining components of the refrigeration machine. This conclusion is valid for all types of refrigeration machines [7-12]. For the throttling valve we have $\dot{E}_{D,k}^{EN} < \dot{E}_{D,k}^{EX}$, note that this relationship depends on the working fluid used for the refrigeration machine [12].

Subsequently the value of unavoidable endogenous exergy destruction $\dot{E}_{D,k}^{UN,EN}$ is calculated using the data from previous simulations

$$\dot{E}_{D,k}^{UN,EN} = \dot{E}_{P,k}^{EN}\left(\frac{\dot{E}_D}{\dot{E}_P}\right)_k^{UN} \qquad (14)$$

and the values of $\dot{E}_{D,k}^{UN,EX}$, $\dot{E}_{D,k}^{AV,EN}$ and $\dot{E}_{D,k}^{AV,EX}$ are easily estimated.

To understand how one component affects other components, we need to split the exogenous exergy destruction $\dot{E}_{D,k}^{EX}$ according to Eq.(7). For this splitting, we need again a new simulation, i.e. a set of so-called "hybrid processes 2": Two components are simulated with their real inefficiency while all other components correspond to the theoretical process. Not only the exogenous exergy destruction should be split, but also the terms $\dot{E}_{D,k}^{UN,EX}$ and $\dot{E}_{D,k}^{AV,EX}$. All data are given in Table 3.

The decision about the priority for improving the overall system through improvement of the k th component can be made based on the value of $\dot{E}_{D,k}^{AV,\Sigma}$ (Eq. (3)): $\dot{E}_{D,CM}^{AV,\Sigma}$ =524 W, $\dot{E}_{D,CD}^{AV,\Sigma}$ =1693 W, $\dot{E}_{D,TV}^{AV,\Sigma}$ =20 W, and $\dot{E}_{D,EV}^{AV,\Sigma}$ =1133 W. But also a detailed analysis is very informative. Based on the data obtained from the advanced exergetic analysis, we can conclude the following:

- The condenser and the evaporator can be improved through decreasing the irreversibilities within these components.
- An improvement of the condenser cannot affect the evaporator, but improving the evaporator will improve significantly the performance of all components of the refrigeration machine.
- An improvement of the condenser can decrease a part of the avoidable exogenous exergy destruction only within the compressor.
- The throttling valve can be improved only by decreasing the exergy destruction within the condenser and the evaporator.

4. Conclusions

With the aid of the *advanced exergy-based methods*

- the interactions among plant components are properly revealed, and
- the potentials for improving the most important components and the overall system are identified

as well as

- our understanding of what is really going on in an energy conversion process is greatly improved, and
- the knowledge, experience, creativity, and confidence (during the decision-making process) of an engineer are enhanced.

Table 3

Advanced exergetic analysis for the vapor-compression refrigeration machine (Figure 2)

Component	$\dot{E}^{EN}_{D,k}$ [W]	$\dot{E}^{EX}_{D,k}$ [W]			$\dot{E}^{UN}_{D,k}$ [W]	$\dot{E}^{AV}_{D,k}$ [W]
CM	677	496	**CD**	256	371	802
			TV	6		
			EV	208		
			mexo	26		
CD	1 799	278	**CM**	60	640	1 437
			TV	24		
			EV	150		
			mexo	44		
TV	373	621	**CD**	334	545	449
			CM	0		
			EV	202		
			mexo	85		
EV	1 626	0			756	870

Component	Splitting $\dot{E}^{real}_{D,k}$ [W]							
	$\dot{E}^{UN}_{D,k}$				$\dot{E}^{AV}_{D,k}$			
	$\dot{E}^{UN,EN}_{D,k}$	$\dot{E}^{UN,EX}_{D,k}$			$\dot{E}^{AV,EN}_{D,k}$	$\dot{E}^{AV,EX}_{D,k}$		
CM	203	168	**CD**	85	474	328	**CD**	171
			TV	2			**TV**	4
			EV	68			**EV**	140
			mexo	13			**mexo**	13
CD	588	52	**CM**	10	1 211	226	**CM**	50
			TV	8			**TV**	16
			EV	27			**EV**	123
			mexo	7			**mexo**	37
TV	373	172	**CD**	23	0	449	**CD**	311
			CM	0			**CM**	0
			EV	149			**EV**	53
			mexo	0			**mexo**	85
EV	756	0			870	0		

Symbols

E	exergy [J]
e	specific exergy [J/kg]
k	k th component [-]
m	mass [kg]
n	number of components [-]
p	pressure [Pa]
Q	heat [J]
r	r th component (different from the k th component) [-]
T	temperature [K]
W	work [J]
y	exergy destruction ratio [-]

Greek symbols

ε	exergetic efficiency [%]
η	isentropic efficiency [%]

Subscripts

D	refers to exergy destruction
F	fuel
P	product
tot	refers to the total system

Superscripts

$\bullet$	time rate
AV	avoidable
EN	endogenous
EX	exogenous
M	mechanical exergy
$real$	real operating conditions
T	thermal exergy
th	theoretical operating conditions
UN	unavoidable

Literature

[1] Bejan A., Tsatsaronis G., Moran M.: Thermal Design and Optimization, Wiley, New York, 1996.

[2] Tsatsaronis G.: Strengths and limitations of exergy analysis, Thermodynamic optimization of complex energy systems. Bejan A., Mamut E., eds., Dordrecht: Kluwer Academic Publishers (1999), 93–100.

[3] Tsatsaronis G.: Definitions and nomenclature in exergy analysis and exergoeconomics. Energy Int. J., **32** (2007)**,** 249-253.

[4] Tsatsaronis G.: Combination of Exergetic and Economic Analysis in Energy-Conversion Processes'. In: Energy Economics and Management in Industry, Proceedings of the European Congress. England, Oxford: Pergamon Press, **1** (1984), 151-157.

[5] Lazzaretto A., Tsatsaronis G.: SPECO: A systematic and general methodology for calculating efficiencies and costs in thermal systems, Energy Int. J., **31** (2006), 1257-1289.

[6] Meyer L., Tsatsaronis G., Buchgeister J., Schebek L.: Exergoenvironmental Analysis for Evaluation of the Environmental Impact of Energy Conversion Systems**,** Energy Int. J., **34** (2009), 75-89.

[7] Morosuk T., Tsatsaronis G.: New approach to the exergy analysis of absorption refrigeration machines', Energy Int. J., 33 (2008), 890-907.

[8] Tsatsaronis G., Morosuk T.: A general exergy-based method for combining a cost analysis with an environmental impact analysis. Proceedings of the ASME International Mechanical Engineering Congress and Exposition, Boston, Massachusetts, USA (2008), files IMECE2008-67218 and IMECE2008-67219.

[9] Tsatsaronis G., Park M.H.: On avoidable and unavoidable exergy destructions and investment costs in thermal systems, *Energy Conversion and Management*, **43** (2002), 1259–1270.

[10] Cziesla F., Tsatsaronis G., Gao Z.: Avoidable thermodynamic inefficiencies and costs in an externally fired combined cycle power plant, *Energy Int. J*., **31** (2006), 1472–1489.

[11] Morosuk T., Tsatsaronis G.: Advanced Exergy Analysis for Chemically Reacting Systems – Application to a Simple Open Gas-Turbine System, Int. J. of Thermodynamics, **12-3** (2009), 105-111.

[12] Morosuk T., Tsatsaronis G.: Advanced Exergetic Evaluation of Refrigeration Machines Using Different Working Fluids, *Energy Int. J*., 34 (2009), 2248-2258.

[13] Morosuk T., Tsatsaronis G.: Graphical models for splitting physical exergy. In: Kjelstrup S. et al. editors. Proceedings of the 18th International Conference on Efficiency, Cost, Optimization, Simulation, and Environmental Impact of Energy Systems; Trondheim, Norway. Tapir Academic Press (2005), 377–384.

18th International Conference Process Engineering and Chemical Plant Design
Günter Wozny and Łukasz Hady, Editors

M. N. CRUZ BOURNAZOU*, D. DOMASCHK*, T. BARZ*, G. WOZNY*,
H. ARELLANO-GARCIA*

EVALUATION OF INTEGRATION APPROACHES TO DAE SYSTEMS IN ENGINEERING APPLICATIONS

Abstract

Numerical integration of systems of Differential Algebraic Equations (DAE) is the core of process simulation and optimization. Many efforts have been made to develop methods in order to approximate the integration of DAE systems, and there now exists diverse approaches tailored to take advantage of particular systems characteristics. Unfortunately, the increased number of factors, which influence the performance of DAE- and ODE-solvers, makes it very difficult to establish the most efficient approach. Furthermore, a general approach to solve all different types of models applied in engineering cannot be established. Therefore, a comparison with "real life" engineering models is the most reliable way to test the performance between different methods.

Keywords: Orthogonal collocation, extrapolation method, DAE systems

1. Introduction

The solution of the system of Differential Algebraic Equations (DAE) is the core of process simulation and optimization. Many efforts have been made to develop methods to approximate the integration of DAE systems. Unfortunately, the increased number of factors, which influence the performance of DAE- and ODE-solvers, makes it very difficult to establish the most efficient approach. Furthermore, an overall approach to solve all different types of models applied in engineering cannot be established.

In this work we discuss the performance of Orthogonal Collocation on Finite Elements (OCFE). The analysis includes a comparison of methods commonly applied in real case studies. Various aspects of the different approaches are put under scrutiny, and finally a robust and efficient method for solving DAE systems with the common characteristics of engineering models is selected.

* Chair of Process Dynamics and Operation, Berlin Institute of Technology, Sekr.KWT-9 Str. des 17.Juni 135, D-10623 Berlin, Germany.

2. DAE Solver Selection

The first step in our analysis was to select a method for solving ODEs. The three methods compared were Runge-Kutta (RK), the backward differentiation formula (BDF), and OCFE. In order to compare the performance of these three methods independently of the residual measurement and step control method, different case studies were solved using an "optimal grid". To achieve this, a constrained optimization problem was formulated. The minimization of the number of intervals maintaining the real error under constraint was solved. The real error was obtained by comparing the numeric approximation with the analytical solution of the ODE system.

2.1. Runge-Kutta

Runge-Kutta (RK) is a single-step multi-stage method used to solve initial value problems. Matlab's ode45 solver uses a fifth order RK to estimate solutions [1]. The method uses six function evaluations, which generate a fourth and fifth order solution. The general form for this method is **(1)**

$$y_n + 1 = y_n + h(b_1k_1 + b_2k_2 + b_3k_3 + b_4k_4 + b_5k_5 + b_6k_6) \tag{1}$$

where

$$\begin{aligned}
k_1 &= f(t_n, y_n)\\
k_2 &= f(t_n + c_2h, y_n + a_{21}hk_1)\\
k_3 &= f(t_n + c_3h, y_n + a_{31}hk_1 + a_{32}hk_2)\\
k_4 &= f(t_n + c_4h, y_n + a_{41}hk_1 + a_{42}hk_2 + a_{42}hk_3)\\
k_5 &= f(t_n + c_5h, y_n + a_{51}hk_1 + a_{52}hk_2 + a_{53}hk_3 + a_{54}hk_4)\\
k_6 &= f(t_n + c_6h, y_n + a_{61}hk_1 + a_{62}hk_2 + a_{63}hk_3 + a_{64}hk_4 + a_{65}hk_5)
\end{aligned} \tag{2}$$

The coefficients are based on the Dormand Prince method. The difference between the fifth and fourth order solutions is used to estimate the local error.

The adaptive step size control of Matlab's ode45 solver functions as follows. After each step, successful or not, the step size is adjusted. If the error is too large, the step size is decreased. Conversely, if the error is too small, the step size is increased. The following equation **(3)** is used to calculate the new step size.

$$h_{new} = h_{present}\left(\frac{\Delta_{new}}{\Delta_{present}}\right)^{\alpha} \tag{3}$$

where

$$\alpha = \frac{1}{n+1}, \text{ if } \Delta_{new} > \Delta_{present} \text{ or } \alpha = \frac{1}{n}, \text{ if } \Delta_{new} < \Delta_{present} \tag{4}$$

and n is the order of the RK method. The error, $\Delta_{present,}$ is calculated by taking the difference between the solution of the fifth order RK and the fourth order. The variable Δ_{new} represents the maximum tolerable error.

While the goal of adaptive step size controllers is to select the largest possible step size, stability must also be taken into account. If a step size is chosen such that it generates a solution with an error at the maximum boundary condition, the error in the subsequent step will exceed the maximum error tolerance.

Matlab's ode45 solver accepts all steps with errors less than or equal to the relative error tolerance. The algorithm is designed such that the estimated step size yields an error close to the relative error without exceeding this value. However, this is not always the case. There are instances when the error is several orders of magnitude smaller than the error limit. In order to avoid such instances, the ode45 solver code was edited to reject such steps and obtain a close to optimal step size grid.

First, the differential equation is integrated analytically to be able to calculate the real error in each step. The edited step size control method uses an initial step size defined by the user. The error is calculated as the sum of the square of the difference between the RK approximation and the analytical solution. The step size is decreased linearly until the error is below but close to the tolerance. To avoid the maximum error issue mentioned above, the starting value at each new step is set equal to the value of the analytical solution.
By these means, the optimal grid shows the maximal possible step size of each interval independently of the past errors.

To ensure that the edited step size control takes the largest step possible, the errors at substeps within each step are calculated. The step size controller does optimize the step size such that the error is at or near the maximum tolerance in each step.

Editing the step size controller portion of the Matlab ode45 solver does increase the required computation time. However, the edited solver takes considerably fewer steps in reaching a final solution. The unedited Matlab ode45 solver to the edited step size control code for a damped oscillator initial value problem is compared against the edited algorithm. With the Unedited version, the solver needs 41 steps to complete the solution. The edited solver takes only 16 steps.

2.2. Backward Differentiation Formula (BDF)

The BDF is an implicit multistep method used to solve stiff initial value problems. The general formula for the BDF is **(5**)

$$\sum_{j=0}^{k} \alpha_j y_{n+j-k+1} = h\beta_k f_{n+1} \tag{5}$$

where k is the step number, h denotes the step size and αk = 1 [1]. It has been shown that BDF formulas are unstable for values of k ≥ 7 [2].

Matlab's ode15s solver uses a BDF to approximate solutions to differential equations. By default the ode15s uses the numerical differential formula (NDF); however, the user may change the Matlab option settings so that the BDF is used instead. The order of the BDF can be fixed to a maximum of five.

As with the ode45 solver, the step size control portion of the ode15s solver was modified to use the same control method. The user specifies an initial step size, and this value is decreased until the estimated solution is less than or equal to the maximum error tolerance.

2.3. Orthogonal Collocation

The Orthogonal Collocation on Finite Elements (OCFE) has been shown to be a valuable method for the numeric approximation of Differential Algebraic Equation (DAE) systems. OCFE has been successfully applied in the partial discretization approach for direct integration of general implicit and stiff DAE systems [3, 4].
The most important advantages of OCFE are:

1. self-starting in high orders
2. equivalent to particular implicit RK methods with highest order accuracy
3. excellent stability properties for index one and higher systems

For this study, the Radau orthogonal collocation with a third order was used to approximate solutions to initial value problems. The third through fifth order Radau collocation points are shown in Table 1 below [5]. The final solution is approximated using Lagrange polynomials after each step.

Table 2.Radau Collocation Points

	Third Order	Fourth Order	Fifth Order
x_1	0.1127016654	0.0694318442	0.0469100771
x_2	0.5000000000	0.3300094782	0.2307653450
x_3	0.8872983346	0.6699905217	0.5000000000
x_4		0.9305681557	0.7692346551
x_5			0.9530899230

In implementing the orthogonal collocation approximation, an initial step size was first defined. Matlab's fsolve function was then utilized to calculate optimal step sizes. Beginning with the initial step size, the fsolve function makes repeated calculations based on a constraint function and an error tolerance and adjusts the step until an acceptable solution is reached. The constraint function is the difference between the approximated solution using orthogonal collocation and the analytical solution. The fsolve function uses this difference to calculate a more accurate approximation to the solution. This approximation is compared with the analytical solution in order to calculate an error. Based

on the difference between this error and a user-defined error tolerance, the step is adjusted until an optimal step size is reached.

Two differential equations were used to test and compare the three ODE solver methods. The first was a damped oscillator with the equation (6).

$$\ddot{y} + 0.8\dot{y} + 2y = 0 \tag{6}$$

and initial values of $y1(0) = 1$ and $y2(0) = 0$.
The second initial value problem was a switching function (7)

$$\dot{y} = \frac{y}{0.01 + y}$$
$$\ddot{y} = \frac{3 - \dot{y} - 10y}{0.01 + y} \tag{7}$$

and initial values of $y(0) = 1$ and $\dot{y}(0) = 2$.

2.4. Comparison of Methods

The comparison of the optimal grids obtained with the three different methods under study allows an evaluation of the numerical approximation approachesindependently of the step size control.

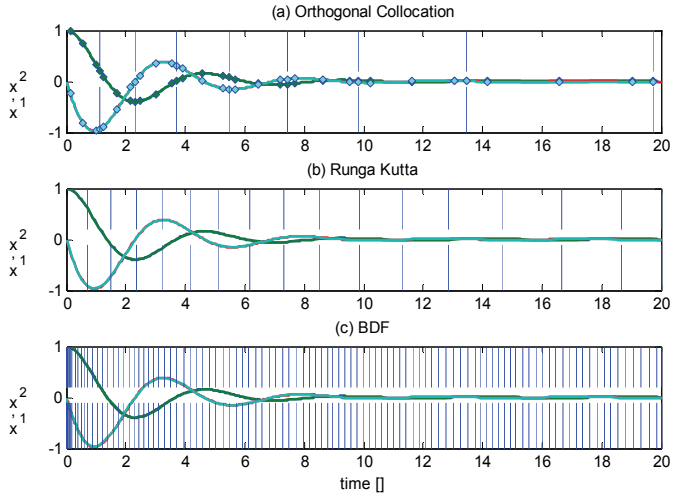

Figure 6: step size comparison for the oscillator model with the three methods proposed

The RK method is effective for calculating the solution to non-stiff differential equations. Because it is an explicit method, it is forced to reduce the step size drastically as

soon as the stiffness of the equation system increases. Another important drawback is the incapability to solve DAE systems.

Contrary to RK the BDF method is an implicit method. BDF is recommended for stiff problems and has been proven to be a very robust method. Nevertheless, the length of the discretization interval for highly nonlinear systems is hardly constrained. Moreover, the BDF is optimized to solve stiff initial value problems. With stiff initial value problems, the solution varies slowly, but there are rapidly varying solutions nearby. Therefore, the solver takes small steps in calculating a solution [5].

The Results obtained in this work confirm that OCFE is the most efficient method when the step size is optimal. The length of each interval is significantly larger when solved with third order OCFE. The method is numerically intensive and takes more computing time than Matlab's built-in solvers.However, the tradeoff between interval length and calculation costs shows positive results in the case where grid size is near to optimal. Based on this we assume the importance of an accurate grid selection in the solution of ODE systems with OCFE is demonstrated.

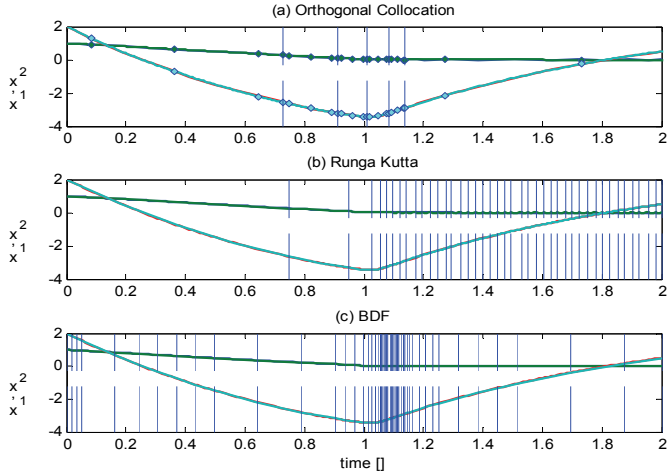

Figure 7: step size comparison for the oscillator model with the three methods proposed

3. Step Size and Error Estimation

The results of the optimal grid comparison suggest that an adequate step size selection is essential for the efficient implementation of OFCE methods. The step size control depends on two factors, the calculation of the error of the approximation, and the step size decision. The step size decision can be adopted from other methods, and the PID controller has been shown to be an efficient approach[6]. Contrarily, the evaluation of the error of the approximation depends on the method itself. Unfortunately, in order to calculate the exact error, the result of the analytical solution must be known. For this reason alternative methods to obtain a hint of the value of the real error have been developed for each approximation method. In our analysis, we evaluated two approaches to calculating the

approximation error: the collocation-based extrapolation method proposed by [7]and time derivative analysis, introduced by [8].

3.1. Extrapolation

In the extrapolation method, the approximation error is computed at a noncollocation point, which lies outside the collocation interval. The approach we consider is valid for problems of index 0 or 1. The index refers to the number of times the algebraic equations of the system must be differentiated in order to reach a standard ODE form. The error, also referred to as the residual, is the difference between the extrapolated derivative and the Lagrange polynomial basis function calculated at the end point of the collocation step (8).

$$\|e(t)\| = Cr(t_{nc})h + O(h^{k+1}) = O(h^k) \tag{8}$$

where h is the step length and $r(t_{nc})$ is the residual at the noncollocation point[7].

3.2. Time Derivative Analysis (TDA)

The TDA approach takes the time derivatives of the differential state variables at the collocation points and evaluates the degree of the nonlinearity to determine an appropriate step size [8].

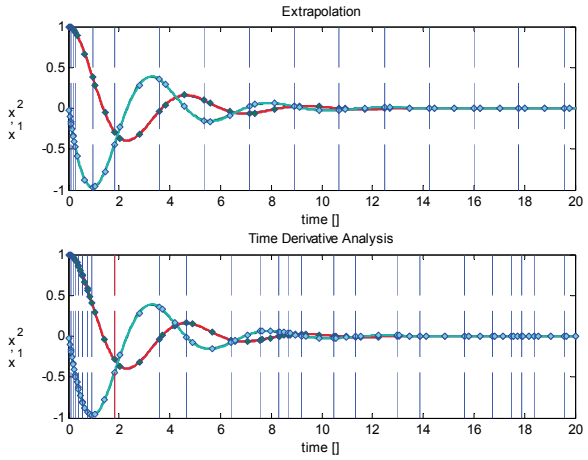

Figure 8: comparison between both methods for the oscillator case.

If the profiles at the collocation points are relatively linear, a larger step is taken. Conversely, if the degree of nonlinearity is relatively high, the step size is reduced.

The problem with this approach is that it only considers the gradients at the collocation points. A parabola offers a good example of the method's shortcomings. A solution to a simple parabolic equation can be estimated using a quadratic equation; however, the quasi-sequential approach considers only the gradients at the collocation points. This calculation will yield a high degree of nonlinearity, and unnecessarily small steps will be taken in reaching a solution.

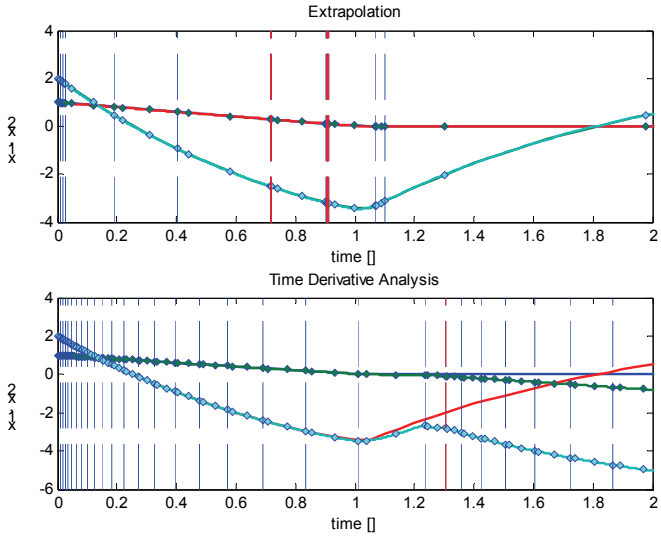

Figure 9: comparison between both methods for the switching function case.

3.3. Proportional Integral Differentiation (PID) Control

PID control is a common form of feedback used to control numerous types of applications. We used a PID controller for step size calculation. The input of the PID controller is the difference between the relative error tolerance and the estimated error, and the output is the new step size.

The algorithm that was used for the calculation of the step size is based on the ideas of [9], the equation is shown in (9).

$$h_{n+1} = h_n \frac{T}{e_n}^{\frac{\alpha}{k_n+1}} + \frac{e_{n-1}}{T}^{\frac{\beta}{k_{n-1}+1}} \frac{T}{e_{n-2}}^{\frac{\gamma}{k_{n-2}+1}} \tag{9}$$

where h is the new step size, e is the calculated error, k is the order, and

$$\alpha = k_I + k_P + k_D, \beta = k_P + 2k_D, \gamma = k_D \tag{10}$$

In selecting PID coefficients, the trade-off between stability and aggressiveness must be considered. With proportional control there is always steady state error. Adding integral control eliminates the steady state error but increases the settling time. The differentiation component decreases the settling time and overshoot but increases instability. A guideline for the selection of PID parameters is $\alpha > \beta > \gamma$. This places the greatest amount of weight on the most recent error value. Older error values have increasingly less influence on the calculation of the new step size.

3.4 Fed-batch fermentation model

Finally a model for the description of an E. *coli*fed-batch fermentation [10]served as case study to compare both error calculation methods with OCFE. Figure 10 shows the

comparison of both methods. It can be observed, that the extrapolation method offers a more sensitive error calculation although both methods enable the correct simulation of the model.

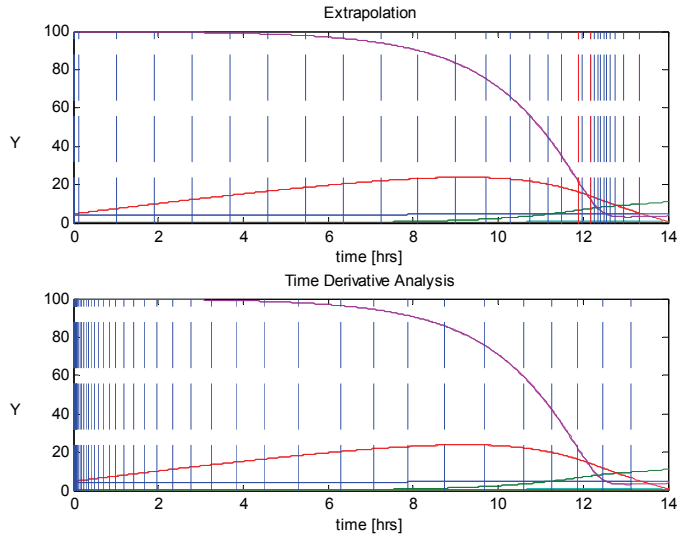

Figure 10: simulation of a fed-batch fermenation model

4. Conclusion

The first step in our analysis was to select a method for numeric approximation of differential equations. The three methods compared were RK, BDF and OCFE.

The results obtained suggest that OCFE is more robust than RK and more efficient for nonlinear problems than BDF. Based on this comparison it was determined that OCFE is the most robust method for solving initial value problems.

We then implemented a PID step size control in OCFE and compared various error estimation methods for use with the PID controller. Two approaches to calculating the approximation error were evaluated: time derivative analysis and the method proposed for the special case of collocation-based nonlinear programming (NLP) referred to as the extrapolation method.

This work shows the potential of OCFE as a general tool for solving DAE systems commonly applied in engineering. Finally, the urge of both, an accurate residual calculation and an efficient step-size control should motivate further research in the particular case of OCFE.

Literature

1. Ashino, R., M. Nagase, and R. Vaillancourt, Behind and beyond the MATLAB ODE suite. Computers and Mathematics with Applications, 2000. 40(4-5): p. 491-512.

2. Hairer, E. and G. Wanner, On the instability of the BDF formulas. SIAM journal on numerical analysis, 1983. 20(6): p. 1206-1209.
3. Li, P., et al., Optimization of a semibatch distillation process with model validation on the industrial site. Industrial & engineering chemistry research, 1998. 37(4): p. 1341-1350.
4. Wang, F.S., A modified collocation method for solving differential-algebraic equations. Applied mathematics and computation, 2000. 116(3): p. 257-278.
5. Moler, C.B., Numerical computing with MATLAB. 2004: Society for Industrial Mathematics.
6. Deuflhard, P. and F. Bornemann, Scientific computing with ordinary differential equations. Vol. 42. 2002: Springer Verlag.
7. Logsdon, J.S. and L.T. Biegler, Accurate solution of differential-algebraic optimization problems. Industrial & engineering chemistry research, 1989. 28(11): p. 1628-1639.
8. Bartl, M., P. Li, and L.T. Biegler, Improvement of State Profile Accuracy in Nonlinear Dynamic Optimization with the Quasi-Sequential Approach. AIChE Journal, 2010.
9. Brayton, R.K., F.G. Gustavson, and G.D. Hachtel, A new efficient algorithm for solving differential-algebraic systems using implicit backward differentiation formulas. Proceedings of the IEEE, 1972. 60(1): p. 98-108.
10. Lin, H.Y., et al., Determination of the maximum specific uptake capacities for glucose and oxygen in glucose-limited fed-batch cultivations of Escherichia coli. Biotechnol Bioeng, 2001. 73(5): p. 347-57.

18th International Conference Process Engineering and Chemical Plant Design
Günter Wozny and Łukasz Hady, Editors

WIESŁAW SZATKO[*], WALERIAN BLINICZEW[**], JANUSZ KRAWCZYK[*]

COMPARISON OF MATHEMATICAL MODELS DESCRIBING CHANGES OF THE SUSPENSION ABSORPTION CAPACITY AND THERMAL RESISTANCE OF THE SLUDGE

Abstract

The paper presents mathematical models of thermal resistance changes during formation of sediment layers on the surface of heat exchangers and changes in absorption capacity of dust particles under full re-circulation of liquids in wet scrubbing processes. Models are presented in the form proposed by Kern and Seaton. Asymptotic values of thermal resistance and particulate matter (dust) absorption by water and the process of reaching asymptotic states are driven by water flow velocity and speed of the gas and particulate spray impact on surface of the water.

Keywords: thermal resistance modelling**,** pipe-in-pipe" heat exchanger

1. Introduction

In the process of wet dust extraction under full liquid re-circulation conditions, concentration of solid particulate matter in the suspension increases with time. Along with the increase in concentration, efficiency of dust particle absorption may decrease, causing time-variation of the absorption capacity in the suspension.

Changes in absorption capacity are mainly driven by the velocity of the aerosol stream aimed at the surface of the liquid. Dust particles will only get absorbed by the suspension if they overcome the surface tension forces – in the case of high concentrations they will also have to overcome the internal structures of the suspension, which may cause the dust particles to bounce off.

Change in mass of absorbed and retained particulate matter may has an asymptotic character, so theoretically it is possible to determine such a concentration of the suspension, which will not allow further scrubbing of the gas (removal of particulate matter).

[*] Kraków University of Technology, Institute of Thermal and Process Engineering, Chair of Industrial Apparatus, 31-155 Kraków, Warszawska str. 24
[**] State University of Chemistry and Technology in Ivanovo, Ivanowo, Engels sq. 2

A similar phenomenon can be observed during the accumulation of sediment layers on surfaces of ducts and pipes by the flow-through of suspensions or solutions, precipitating crystalline deposits on the heat exchange surfaces.

Despite numerous publications [1,2,3 and 4] covering analysis of sediment precipitation on heat exchanger surfaces, the process has not yet been fully investigated and quantified due to the very complex mechanism of sediment formation.

Most of the theoretical models describing thermal resistance of sediment layers are simplified, as they are based on many assumptions, such as taking into account only one mechanism of sediment formation and neglecting the initial condition of the heat exchange surface. Such models are mainly focusing on the impacts of parameters such as time, velocity, temperature and concentration.

Especially significant discrepancies occur in the evaluation of the impact of scrubbing medium flow velocity on sediment layer formation effects and by the same token, on the heat resistance coefficient of the layer.

Along with partial obturation of the duct section, resulting from formation of a sediment layer, the dynamic impact of the stream on the layer increases, leading to asymptotic change of thickness in time.

Assuming that the thermal conductivity coefficient of the sediment layer remains constant, independently from its thickness and the changing conditions of its accumulation, change in thermal resistance of the forming layer may be used to measure the rate of the layer's thickness increase.

The mathematical model for both discussed cases may be derived from the following relationships:

$$\dot{m}_z = \dot{m}_d - \dot{m}_w \tag{1}$$

$\dot{m}_z$ - change in mass of retained dust in time, change in sediment mass in time,

$\dot{m}_d$ - change in mass of inflowing (supply) dust in time, change in mass of deposited particles,

$\dot{m}_w$ - change in mass of generated dust emission, removed from the sediment.

Assuming that:

$\dot{m}_d$ is constant in time

and that the mass stream of dust emission (mass stream of deposited particles) depends on the mass of dust retained in the system (mass of sediment)

$$\dot{m}_w = c \cdot m_z \tag{2}$$

From equations (1) and (2) and assuming that $m_z(0) = 0$ and

$$\lim_{t \to \infty} \dot{m}_z = m_d \cdot t_c \tag{3}$$

We obtain an equation expressing the mass of sediment deposited in time [5][6]:

$$m_z(t) = \dot{m}_d \cdot t_c \cdot \left(1 - \exp\left(-\frac{t}{t_c}\right)\right) \tag{4}$$

where t_c is a time constant, and from definition, describing the time needed for deposition of an amount of dust equal to m_z^*, if the dust is being retained with constant value of the inflow stream $\dot{m}_d$, without a particulate matter removal process ($\dot{m}_w$=0) and m_z^* is the asymptotic mass of retained dust

$$t_c = \frac{m_z^*}{\dot{m}_d} \tag{5}$$

where:

t_c – time constant,

$\dot{m}_d$ - inflow stream,

m_z^* - asymptotic value of retained dust mass.

After inserting relationship (5) into equation (4), we obtain

$$m_z(t) = m_z^*(1 - \exp(-\beta t)) \tag{6}$$

where β is the asymptotic state achievement rate and depends on the kinetic energy of dust particles, allowing them to overcome the forces of surface tension and break through the internal structures forming inside the liquid, and in the case of sediment formation, on the shear-tension of the sedimenting solid matter particles.

2. Mathematical model of thermal resistance changes in time

The thermal resistance coefficient of the sludge layer changes in time due to the gradual increase in the mass of removed dusts. However in frequent cases, after the initial period of rapid growth of the sludge layer, its thickness, and by the same token its thermal resistance remain practically constant. Therefore, there are favourable conditions for simultaneous removal of dusts from the surface.

Kern and Seaton [5] found that after the period of quick formation of the sludge layer, the thickness of the sediment and its thermal resistance remained practically constant. They have introduced a function of thermal resistance change in time, formulated as follows:

$$R_f = R_f^* [1 - exp(-\beta t)] \tag{7}$$

where R_f^* is the asymptotic value of thermal resistance in time $t \to \infty$ [5].

The Kern-Seaton model [5] became a base model describing variance of thermal resistance coefficient in time. Differences between the base model and all other models arise from different definitions of the sedimentation and removal streams.

The stream of removed particles almost always depends on the thickness of the sludge layer and by the same token, on the mass of sediment per unit of surface area.

Expressing change in mass of sediment in time as difference between the sedimentation and removal streams may cause doubts because growth of the sludge layer goes under conditions favouring removal of sedimented particles.

Pinheiro [2] proposed to express the change in thermal resistance of the sludge layer in time as a difference between sedimentation and removal functions

$$\frac{\mathrm{d}R_f}{\mathrm{d}t} = \phi_d - \phi_r \tag{8}$$

where ϕ_d - sedimentation function and ϕ_r - removal function.

Kern and Seaton [5] claimed that in the case of sludge formation through sedimentation of particles, the sedimentation function ϕ_d (8) is dependent, in a linear way, from the concentration of particulate pollutants in the stream of liquid and on the velocity of the liquid stream u:

$$\phi_d = k_1 c_b u \tag{9}$$

The removal function ϕ_r depends on the shear tension in the liquid stream at the sludge sediment layer and on the current thickness of the sediment x_f:

$$\phi_r = k_2 \tau x_f = k_3 u^2 R_f \tag{10}$$

Taking into account equation (8), we obtain an extended Kern-Seaton model of the following form:

$$R_f = \frac{k_1}{k_3}\frac{c_b}{u}\left[1 - \exp\left(-k_3 u^2 t\right)\right] \tag{11}$$

Comparing the base Kern-Seaton model (7) with model (11), one can notice that in the extended model, the sedimentation function ϕ_d, asymptotic value of thermal resistance of the sludge R_f^* and coefficient β depend on the flow velocity u in the following specific manner:

$$\Phi_d \sim \mathrm{u},\ R^*_f \sim 1/u,\ \beta \sim u^2 \tag{12}$$

Models developed by Watkinson [7], Gudmundson [2], Bohnet [1], Pinherio [2] and Cleaver&Yates [8] indicate an asymptotic increase in thermal resistance of the sludge. These models differ by the assumed impact of velocity on the course and parameters of the phenomenon. Analysing those models one could conclude that the asymptotic value of sludge thermal resistance R_f^* increases proportionally to the concentration of dust pollutants in stream c_b and decreases with increase in stream velocity u.

3. Experimental setup

The mathematical model has been verified using a test stand. The key element of the test apparatus is a "pipe-in-pipe" concentric heat exchanger of a length of 2 m and exchange surface of 0.1 m^2. The cooling media (source of sedimenting matter) used in the tests were:

- saturated water solution of $CaSO_4$,
- saturated water solution of $CaCO_3$,
- saturated water solution of $MgSO_4$.

The tests were carried out at cooling medium velocities of 0.1, 0.16 and 0.24 m/s.

Figure 1 shows an example of the $R_f = f(t)$ function for three sedimentation media at u = 0.16 [m/s] and T = 299 K.

The obtained values of the $R_f = f(t)$ function indicate that the change in thermal resistance coefficient is asymptotic, therefore the Kern-Seaton model was used to describe the process.

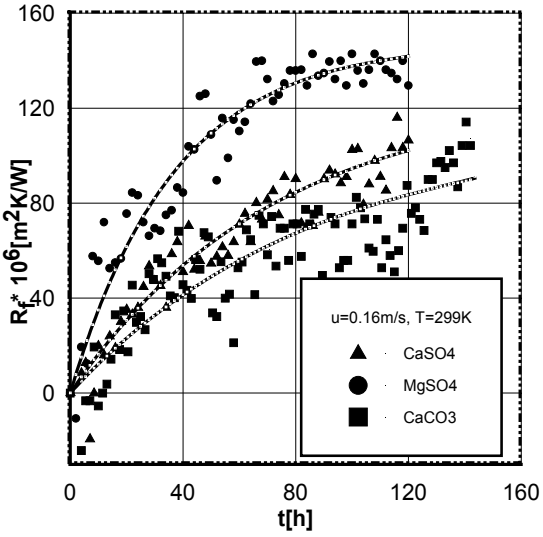

relative error	
$CaSO_4$	18 %
$MgSO_4$	22%
$CaCO_3$	16%

Fig. 1. The $R_f = f(t)$ function

Values of coefficients R_f^*, β and t_o in equation (11) were determined by finding the minimum value of the function being a sum of square deviations between experimental and theoretical points. Minimisation of the function values was made using gradient Marquardt method – the relative errors on Fig.1. The calculated values, for the three tested sludge media, are presented below.

T a b l e 1

Values of R_f, β and t_0 for u = 0.16 m/s and T = 299 K

		$CaSO_4$	**$CaCO_3$**	**$MgSO_4$**
$R_f^* \cdot 10^6$	$[m^2K/W]$	121,.2	116.5	144.6
β	[1/h]	0.0114	0.0117	0.0296
t_o	[h]	6	6	2,2

4. Mathematical model for changes in suspension absorption capacity in time

Having previously demonstrated in [10, 11, 12, 13 and 14] the effect of reduced scrubbing efficiency in the spray and barbotage zones and during impact against the surface of the liquid, further studies have been undertaken to describe and quantify the phenomenon. For that purpose, a test station has been designed and built, to allow analysis of changes in dust scrubbing efficiency in operation of the apparatus.

A scrubbing chamber with cross flows of the suspension versus the stream of dust-contaminated gas striking the surface of the liquid is a significant component of the test station. The apparatus was used in a series of tests in conditions of variable velocity of dust-contaminated air inflow stream striking the surface of the liquid and defined dosage of particulate matter (dust) to the system. Results of the analyses are shown in the table 2 below.

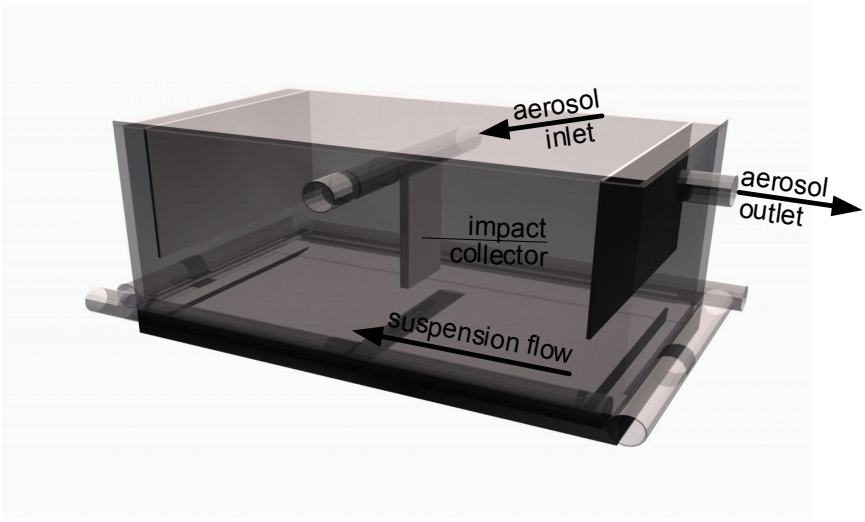

Fig. 2. Conceptual design of the test station for investigation of the scrubbing process using impact of contaminated gas on the surface of the liquid

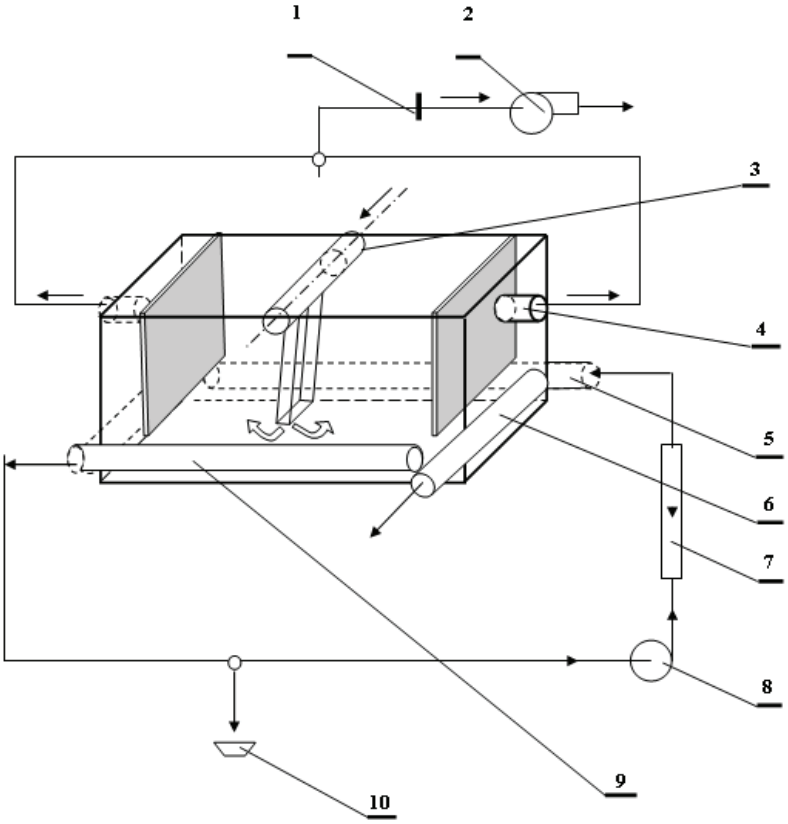

Fig. 3. Schematic diagram of the gas-to-liquid impact scrubbing test stand

1. square flange,
2. fan,
3. aerosol supply nozzle,
4. aerosol outlet,
7. rotameter,
8. pump,
9. suspension outflow piping,
10. suspension sample collection,

5. suspension supply piping,
6. backup suspension outflow piping,

5. Results of the impact chamber general efficiency analyses

Table 2 shows relationships between the mass of dust (particulate matter) retained in the system and the mass of dust applied at the input, at various aerosol flow velocities. The presented results were used as basis for calculation of current and cumulative scrubbing efficiency in function of applied mass of particulate matter.

T a b l e 2

Results of measurements for titanium oxide

m_z [kg]	Gas velocity [m/s]					
	u = 10	u = 14	u = 18	u = 22	u = 26	u = 30
Retained mass [kg]						
1.0	0.986	0.988	0.991	0.993	0.995	0.998
2.0	1.954	1.973	1.978	1.972	1.984	1.981
3.0	2.869	2.921	2.928	2.931	2.939	2.945
4.0	3.704	3.795	3.853	3.825	3.851	3.885
5.0	4.416	4.632	4.703	4.714	4.725	4.763
Cumulative efficiency [%]						
1.0	98.60	98.80	99.10	99.30	99.50	99.80
2.0	97.70	98.65	98.90	98.60	99.20	99.05
3.0	95.63	97.37	97.60	97.70	97.97	98.17
4.0	92.60	94.88	96.33	95.63	96.28	97.13
5.0	88.32	92.64	94.06	94.28	94.50	95.26
Current efficiency [%]						
1.0	99.20	98.80	99.20	99.20	99.60	99.80
2.0	96.60	97.40	97.80	97.40	98.40	97.60
3.0	88.60	92.60	94.20	93.60	93.60	94.20
4.0	81.20	84.20	92.80	87.60	90.40	93.80
5.0	66.40	82.20	78.40	89.60	86.40	86.20

Inserting the rate of achievement of asymptotic state in formula (13) to equation (6):

$$\beta = \dot{m}_d \, k_2 u^2 \tag{13}$$

and taking into account the fact that capacity of dust retention in the liquid and permanent penetration of particles into the liquid depend on the dynamic water adhesion to the dust particles [9] equation (13) has been written in the following form:

$$\beta = k_2 \dot{m}_d u^{2-\alpha} \tag{14}$$

A corrective factor D has been introduced taking into account variable conditions of dust supply to the system, arising from variable dispersion of the particulate matter at various aerosol velocities at the outlet of the nozzle. The stream of mass supplied to the system can be written in the following form:

$$\dot{m}_d = k_1 u^D \tag{15}$$

Inserting (14) and (15) into equation (6), we obtain a mathematical model for changes in mass of dust retained in the suspension, taking the following form:

$$m_z = A \cdot u^D \left[1 - \exp\left(- B \cdot u^{2-C} \cdot m_d\right)\right] \tag{16}$$

m_d – cumulative mass of supplied dust, directly proportional to the time of operation.

Verification of the model was performed on the laboratory test station, where the aerosol was directly streamed onto a perpendicular stream of liquid. The aerosol velocity was controlled in the range of 10 to 30 [m/s].
The regression coefficient of equation (16) was determined using the linear estimation method.

T a b l e 3

Values of regression coefficients for model /16/

A	**D**	**B**	**C**
38.257	0.020	0.020	1.950

The average correlation match relative error is 2.55%

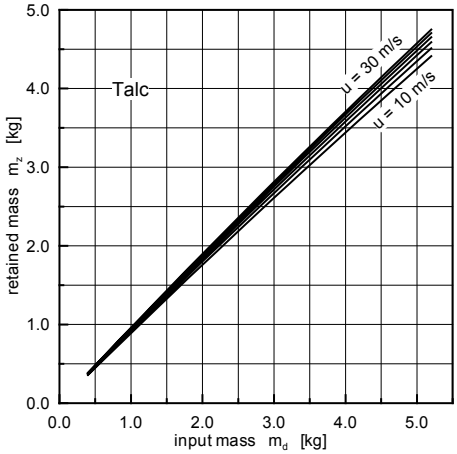

Fig. 4. Retained versus input mass

6. General remarks

He proposed model - eq. (16) - serves to description of phenomena, catching the particles in suspension, setting during the wet dust extraction. It using analog among this process and the process of deposit layering on the heat exchange surfaces the Kern - Seaton model was applied. Proposed solution is the quantitative problem description of increasing the particles concentration in suspension and changes of her absorption capacity in time.

Symbols

A, D, B, C	- rgression coefficients of equation /16/	
k_1, k_2, k_3	- coefficients in equations	
m_z	-mass of retained dust	kg
m_d	- mass of dust input to the system	kg
$\dot{m}_z$	– change in time of retained particulate mass	kg/s
$\dot{m}_d$	- change in time of input particulate mass	kg/s
$\dot{m}_w$	- change in time of particulate emission	kg/s
m_z^*	-asymptotic value of particulate (dust) mass	kg/s
R	- thermal resistance coefficient of the sludge layer	m^2K/W
R_f^*	-asymptotic value of thermal resistance in time $t \to \infty$	m^2K/W
S_w	– dust concentration	kg/m^3

t, τ	- time	s
t_o	- nucleation time	s
t_c	- time constant	s
V	– volume output capacity	m^3/s
u	– linear velocity	m/s
$\alpha., c$	- correction coefficient in the removal function	
Φ_d	- dust supply function	
Φ_w	- removal function	

Literature

[1] Bohnet M., Chem-Ing-Tech. 57, Nr 1 1985
[2] Pinheiro I de D.R.S., „Heat Exchangers" eds. Kakac, Bergles, Mayinge New York 1981
[3] Środulska-Krawczyk M., Mat. I Międz. Konf. Iwanowo - Plios 1993
[4] Kutiepow A.M.i inni, Obliczanie procesu powstawania osadów z wykorzystaniem modeli matematycznych, Chim. Prom. Nr 8, 1992
[5] Kern D.Q.,Seaton R.E., Britisch Chem.Eng., vol.4, 1959
[6] Butrymowicz D , Hajduk T., Technika Chłodnicza i Klimatyzacyjna, Nr 3/2006
[7] Watkinson A., Epstein N., Chem.Eng. Prog.Symp. Ser. 65., 1969
[8] Cleaver I.W., Yates B., Chem. Eng. Sci. 31., 1976
[9] Kabsch M., Metody badania zwilżalności pyłu, Monografia 7., Seria M. Politechnika Wrocławska, 1976.
[10] Krawczyk J., Maszek L., Mieszkowski A., Блиничев В., Теоретические и Экспериментальные Основы Создания Новых Высокоэффективных Процессов И оборудования, Iwanowo, 40-45, 2005
[11] Krawczyk J., Maszek L., H. Wisła. Теоретические и Экспериментальные Основы Создания Новых Высокоэффективных Процессов И оборудования Iwanowo, 46-52, 2005
[12] Krawczyk J., Roszak Z., H. Wisła, Inżynieria i Aparatura Chemiczna, 45 (37)., s. 99-101, 2006
[13] Krawczyk J., Roszak Z., Международная научная конференция Теоретические основы создания, оптимизации и управления энерго- и ресурсосберегающими процессами и оборудованием с.130-139, Ivanovo, 2007
[14] Krawczyk J., Maszek L., Mieszkowski A., Roszak Z., Czasopismo Techniczne, Mechanika, z.2-M/2008., s.143-145

18th International Conference Process Engineering and Chemical Plant Design
Günter Wozny and Łukasz Hady, Editors

V.A. MERCHAN RESTREPO, S. KUNTSCHE, H. ARELLANO-GARCIA, G. WOZNY*

SYMBOLIC GENERATION OF FIRST AND HIGHER-ORDER DERIVATIVES WITH MOSAIC

Abstract

Most numerical methods used in process engineering and chemical plant design require derivative information for the solution of equation based process models. Both the accuracy of the derivatives and the methods used for their determination can severely impact the efficiency of the performed calculations. Hence, proper and efficient methods for the generation of exact first and higher order derivatives can be crucial for the formulation and solution of complex problems and should be supported by modeling environments. This contribution describes the implementation of an automatic generation of first and higher order symbolic derivatives within the modeling environment called MOSAIC. Exploiting the ability of MOSAIC to generate code for diverse programming and modeling languages, it will be shown how the automatically generated derivative information can be used so as to increase the efficiency of some state of the art solvers.

Keywords: Code generation, higher-order derivatives, symbolic derivatives, MOSAIC.

1.Introduction

Numerical values of derivatives play a crucial role in the solution of model equations in process engineering and chemical plant design. Accurate values of the derivatives are required, among others, for the iterative solution of nonlinear problems and its respective sensitivity analysis [6], for the integration of DAEs (differential-algebraic equations) and stiff ODEs (ordinary differential equations) [3], for the solution of optimization problems [18], and the analysis of uncertainties [8]. The necessity for derivative information in process engineering and plant design is for example, shown by the fact that the current CAPE-OPEN standard does not only require the first derivative for all property calculations but also for user defined dynamic models[19]. But not only first order derivatives are of interest; in fields like optimal experimental design and robust optimization, which build an important part of the model based process development, exact

* Chair of Process Dynamics and Operation, Technical University of Berlin, Str. des 17. Juni 135, D-10623 Berlin, Germany

values (to within round off error) of higher order derivatives may be desired or required as well. Some examples on the applications of higher order derivatives are given in [13].

Although the evaluation or approximation of first and higher order derivative information provides obvious benefits for the solution of the types of problems listed above, it may also be associated with a relatively big[1], not always justifiable, computational effort. Hence proper differentiation methods need to be chosen in order to guarantee an efficient evaluation of derivative information [5]. According to the classification by Tolsma [20], 5 main methods for the calculation of derivatives are distinguished:

- Finite differences approximation
- symbolic differentiation
- algorithmic differentiation (AD)
- hand coded derivatives
- reverse polish notation evaluation (RPN).

In this contribution only results of the first three methods are considered and analyzed in detail. Hand coded derivatives are here not of interest, since we deal only with derivatives that can be automatically generated by a computer program. Given the fact that the derivative evaluation based on the RPN of an expression [9] can be considered as an alternative form of the classic symbolic differentiation described below, and that its implementation in the modeling environment MOSAIC is not planed, it will not be discussed further.

The finite differences approach, which only provides an approximation of the derivatives and is afflicted with truncation and round off errors, is the default method for derivative evaluation when no user information on the derivative is given. By symbolic differentiation is meant the application of differentiation rules on a computational tree representation of an equation resulting in another equation. The remaining method, algorithmic differentiation, defines a set of techniques, which create a computer program out of another computer program. Given a program for the evaluation of an arbitrary function, by using AD, a new program is created that returns the exact values of the function and its derivatives [17]. In contrast with symbolic differentiation, which applies the differentiation rules to transform equations for the function evaluation in equations for their derivatives, in AD the same rules are applied to the algorithmic definition of this evaluation, and the results are values of derivatives, not equations [15].

A look at the literature gives the impression that, AD, which has had a tremendous development in the last years, has significant advantages over the other methods of derivative evaluation [5,6,15]. However as Li et al [11] pointed out, AD is far from completely replacing the evaluation by finite differences and symbolic differentiation in the

[1] For example, Wolbert et al [21] recognized the evaluation of the Jacobians as the most time consuming step in flow sheet optimization.

field of process systems engineering. Rather, it is noted, that the available form of the evaluation procedures, the structure of the problem, as well as the kind of derivative information required by the solution algorithm (e.g. complete Jacobian or direction derivatives) are decisive factors for the election of an appropriate method for the evaluation of derivatives. Taking this into account, it is evident, that the strengths of code generation could be used for a problem tailored generation of derivative information. A general method for the exploitation of available symbolic expressions, as discussed in this contribution, is an important part towards the creation of problem tailored derivative information.

In this contribution a new approach for the generation of general derivative information of an arbitrary set of model equations is presented. Based on the concept of modeling in the documentation level and the automatic code generation techniques, as provided by new the web-based modeling environment MOSAIC [10], general expressions for symbolical derivative information of first and higher order can be generated, which can be exploited by different modeling environments or computer programs. It should be remarked, that the code generation offered by MOSAIC, also opens the possibility for the creation of tailored code for AD[2], but this contribution focuses on the exploitation of the available data structures for the generation of symbolic expressions. In section 2 some basics of the symbolic differentiation are presented. In section 3, the generation of symbolic derivatives in MOSAIC is explained together with an environment to check the rightness of the calculated derivatives. In Section 4 some numerical results are presented showing the positive effect of the consideration of the symbolical derivatives brought by MOSAIC.

2. Computational methods for symbolic differentiation and its applications in process engineering

According to [20] symbolic differentiation refers to application of differentiation rules on a tree representation of a mathematical expression. For equation 1

$$2^{2 \cdot x} - 4 \tag{1}$$

the equivalent binary tree representation is given by Fig. 1. Binary trees are very popular recursive data structures and an efficient way of representing mathematical expressions [14]. Exploiting the tree structure the evaluation and derivation of the expression can be achieved by applying very simple recursive algorithms. For instance the derivative of a sum equals the sum of the derivatives of the sub nodes. The derivatives of these sub nodes may further depend on some elemental operation on the sub nodes and its derivative.

But not only binary trees lead to simple algorithms for derivation and evaluation of mathematical expressions, so called n-ary trees [12], whose nodes may have an arbitrary number of children nodes may be used as well. While it is practical to generate a tree representation of derivatives out of a tree expression of the equations, there are several ways to evaluate the numerical values of the derivatives. Two main methods are

[2] See [1] for a discussion of a implementation of AD on XML-expressions

distinguished: The direct evaluation of the tree structure and the evaluation of code translated to specific programming language, like C/C++ or FORTRAN. This code is generated out of the tree representation and may be compiled before its execution.

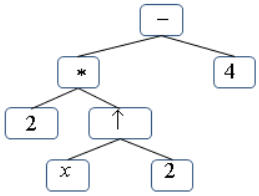

Fig. 1. Binary tree representation of equation 1

Popular equation oriented modeling environments in the field of process engineering like gPROMS or Aspen Custom Modeler apply the first method. Based on the binary tree representation they generate automatically the symbolic derivatives as further binary trees, which are optimized in order to guarantee a faster execution. An interesting comparison of the efficiency of the derivative evaluation between the symbolical derivatives of gPROMS and the derivatives calculate by the AD-tool Adol-C is discussed in [16]. The calculation with AD was found to be more efficient, but also partly due to the communication overhead between the Jacobian providing tool (gPROMS) and the optimizer.

Because of its faster execution, the second method, the evaluation of derivatives based on compiled code is more interesting for large problems. A possible application of this kind of derivative generation may require the usage of a computer algebra package as Maple and a further effort by the user for the integration of the respective codes to the own solver [7]. Since the most available computer algebra packages do not offer an open interface [12], this results in a difficult task and the implementations are normally restricted to a specific software tool, losing generality and flexibility.

3. Generation of symbolic derivatives in MOSAIC

3.1. Basics on the derivative generation with MOSAIC

Within MOSAIC the equations, which are normally written by the user as LaTeX code, are automatically translated to a well defined subset of MathML in the Presentation Markup. For example, the expression, (2)^{2 \cdot x} = 4, which represents the LaTeX representation of equation 2

$$(2)^{2 \cdot x} = 4 \tag{2}$$

is translated and saved by MOSAIC as the following MathML expression:

```
<math xmlns="http://www.w3.org/1998/Math/MathML">
  <msup>
    <mrow>
      <mo>(</mo>
      <mrow>
        <mn>2</mn>
```

```
        </mrow>
        <mo>)</mo>
      </mrow>
      <mrow>
        <mn>2</mn>
        <mo>&amp;amp;CenterDot;</mo>
        <mi>x</mi>
      </mrow>
    </msup>
   <mo>=</mo>
   <mn>0</mn>
</math>
```

While in this example, a very simple symbolic expression was chosen, MOSAIC also supports the usage of multiple indexed variables with several sub and superscripts [10].The stored MathML expression is mapped to a new data object of the class Equation. Through the interface for the Document Object Model (DOM), a Java API for XML processing, the original MathML structure, now a part of the Equation object, can be accessed.

This XML/MathML structure of the Equation objects is the fundament of further exploitation of the model equations. Among others, the code and documentation generation, or the generation of partial derivatives are based on the structural analysis of the XML/MathML representation. Within the structural analysis a equation is broken down to its elementary parts creating a tree representation as shown in Fig. 2. Though this representation seems to be a binary tree, MOSAIC decomposes the equations in n-ary trees.

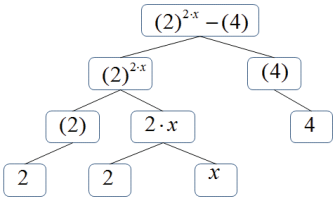

Fig. 2. MOSAIC's internal tree representation of equation 2[3]

The analysis for the generation of this tree is as recursive as the generated data structure. When the analysis of the tree expression has reached the leaf nodes, which are either variables or constants, and no further breakage of the expressions is possible, information about the derivative of the leaf nodes with respect to the desired variable (derivative is either one or zero) is gathered and a back propagation of the derivative information of the child nodes in direction to the root node takes place, leading to the production of derivative information of the respective parent nodes. After the information for the whole tree is gained, the derivative of the tree expression is built by a recursive calling of the derivative on the root node. The resulting derivative is assigned to a new data object of type Equation, which contains the MathML/XML structure of the derivative

[3] This tree representation shows a slightly different expression as found immediately before the code generation

expression as well. For the example in this section a part of this structure is shown in the next code excerpt:

```
<math xmlns="http://www.w3.org/1998/Math/MathML">
  <mrow>
    <mo>ln</mo>
    <mrow>
      <mo>(</mo>
      <mrow>
        <mrow>
   <mo>(</mo>
   <mrow>
     <mn>2</mn> …
```

As shown above, the derivative of an Equation object results in another Equation object which can be derived again by the same procedure. By using the defined Equation class and the methods for their analysis, derivatives of higher order can be generated. Further, because of the availability of the equations and its derivatives in neutral and tool independent MathML/XML format, tailored Jacobians, Hessians or other single derivative information can be generated for different modeling environments or solvers. Currently the generation of Jacobians has been implemented for the solution of nonlinear equation systems with MATLAB and a C solver of the GNU Scientific Library (CGSL), and the derivative for the right hand side of DAEs or stiff ODEs as solved by the integrator ode15s of MATLAB.

The prior description above shows how the tree representation of the equation is exploited for the generation of the derivatives. However, this tree structure is also used for other standard operation in MOSAIC, for example, for the generation of code and documentation, or for the evaluation of the model equations, as it is done for the evaluation of derivatives with finite differences, which is explained in the next section.

3.2. Test environment for partial derivatives and Jacobians

In order to proof the correctness of the generated symbolic derivatives, while evaluating discrepancies of these against approximations by finite differences, a test user interface was designed and programmed. The two main components of this interface are a component for the evaluation of single partial derivatives of a selected equation, shown in Fig. 3, and a component for the evaluation of complete Jacobians.

For a flexible evaluation of single partial derivatives the user interface offers the possibility to choose the respective equation and variable from different drop lists. Not only is a graphical representation of the resulting derivative given, but the actual numerical values of both, a direct evaluation of the symbolic equation and the approximation by finite differences. The numerical values result from the evaluation of the respective tree expression of the equations and its derivatives, analogous to the evaluation in interpretative environments as described in section 2. The interface for the evaluation of complete Jacobians works analogous to the previously explained interface but considering all equations and variables simultaneously. The partial derivatives with the biggest

discrepancies can be identified, giving an intuitive measure of the nonlinearities in the model at the point considered.

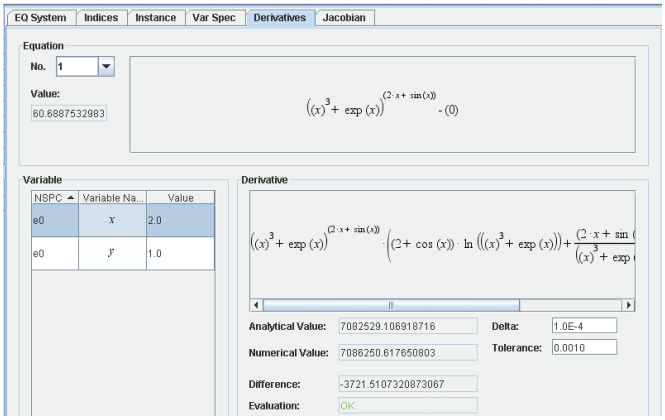

Fig. 3. User interface for the evaluation of symbolic derivatives against finite differences

4. Some numerical results

The following example gives insight into the influence of the chosen method of derivative evaluation on the calculation time for the solution of nonlinear equation systems. As a simple benchmark example, we consider a steady state model of a mixer with two input and one output stream, consisting of component balances and summation equations for the mol fractions, as given by the equation 3.

$$\begin{aligned} F_1 \cdot x_1 + F_2 \cdot x_{2j} - F_3 \cdot x_{3j} &= 0 \\ \sum_{j=1}^{NC} x_{3j} - 1 &= 0 \end{aligned} \tag{3}$$

The index of the F and the first index of the variables x are related to the respective stream, while the second index of the variables x represent the component. In order to register some measurable computational effort on the solution of the model, and to consider the influence of the sparsity of the Jacobian, two different realization of equation (3) are analyzed, considering 50 and 500 components respectively. The values of the chosen design variables and starting values are listed in Table 1.

Table 1: Chosen design and starting values

	Design values		Starting values	
Case 1 NC = 50	F_1, F_2	50 mol/h	F_3	50 mol/h
	x_{1i}, x_{2i}	0.02	x_{3i}	0.2
Case 2	F_1, F_2	50 mol/h	F_3	50 mol/h

NC = 500	x_{1i} , x_{2i}	0.002	x_{3i}	0.2

For the solution of the upper set of model equations, MOSAIC's generator for MATLAB code is used, which creates by default an implementation of the solver fsolve. In this comparison, three different methods for evaluation of the derivatives are considered, which are all supported by the code generation of MOSAIC, calculation with finite differences (FD), symbolic derivatives (SD) and AD fitted to the package TOMLAB/MAD [4]. Since the sparsity pattern of the Jacobian is not exploited by the standard solver using finite differences derivatives, no results are shown for this case. The sparsity considered for the TOMLAB/MAD calculation is characterized initializing the derivative with a sparse unity matrix

Since it was shown, that the different calculations led in all cases to the expected results after the same numbers of iteration steps, the differences on the calculation time are mainly caused by the evaluation of the derivation. For each problem the time of execution of the solver was recorded. The results are summarized in Fig. 4 and 5. All calculations were performed several times with MATLAB 2008b on a PC with Intel Core Duo CPU (3.00 GHz) and 2 GB RAM.

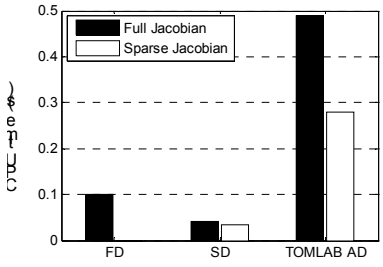

Fig. 4. CPU time for case 1 (NC=50)

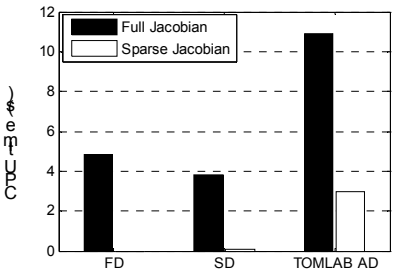

Fig. 5. CPU time for case 2 (NC=500)

For both, case 1 and case 2, a big dependency of the solution time with respect to the derivative evaluation method is found. For both cases, SD results in the fastest execution time, followed by FD and TOMLAB's AD forward mode. It is further shown how the exploitation of the sparsity of the problem results in a reduction the calculation time, which is more apparent for large sparse problems like case 2. In this case the evaluation time of SD with a sparse Jacobian took only around 1.5 % of the time needed with a full Jacobian. The shown superiority for SD in this example is related to the fact, that the derivatives of linear functions are best evaluated by symbolic derivatives, since its evaluation requires the smallest computational effort. Although these results are specific for the case above and therefore cannot be taken for general conclusion about the evaluation methods for derivative evaluation, they emphasize the central role of applying an appropriate derivative evaluation method for an efficient solution and show the strength of code generation techniques.

5. Conclusions and future work

In this contribution it was shown, how a language independent representation of model equations is used to generate general symbolical expression for the derivative information of first and higher order, which can be exploited by different solvers. The flexible code generation capabilities of MOSAIC are used here to generate solver code implementing different methods for the evaluation of derivatives. The given basic examples show the major role of the evaluation of the derivative information within the solution of numerical problems and hence emphasize the need of efficient methods for its generation and evaluation, as they can be provided automatically by MOSAIC.

Though the methods for the calculation of second and higher order derivatives are already available, no code generator implemented so far was designed to use this information. Since MOSAIC is currently being extended on the formulation and generation of optimization problems, a possible usage of the generated analytic Hessian, would be its application by the solution of constrained minimization problems. Further work result in the need to implement the support of models in form of external subroutines and thus proper methods for the calculation of their derivative information. In order to improve the evaluation of Jacobian and higher order derivatives the problem structure needs to be exploited. The implementation of a new strategy for a mixed generation of derivative information based on the specific problem structure would represent a further step in the generation of a problem tailored solution code.

Acknowledgements

The authors acknowledge the support from the Collaborative Research Centre SFB/TR 63 InPROMPT- Integrated Chemical Processes in Liquid Multiphase Systems coordinated by the Technical University of Berlin and funded by the German Research Foundation

Symbols

F_i	Molar flow of the stream i	mol/h
x_{ij}	Molar fraction of component j in stream i	-
NC	Number of components	-

Literature

[1] Bischof C.H., Bücker H.M., Marquardt W., Petera M., Wyes J.: Transforming Equation-Based Models in Process Engineering, In: Automatic Differentiation: Applications, Theory, and Implementations, Springer, Berlin, 2006.

[2] Braunschweig B.L., Pantelides C.C, Britt H.I., Sama S.: Chemical Engineering Progress, 96, (9), 65-76, 2000.
[3] Deuflhard P., Bornemann F.A.: Scientific computing with differential equations, Springer, New York, 2002.
[4] Forth S.A.: ACM Transaction on mathematical software, **32**, No 2, (2006), 195-222.
[5] Griewank A.: Complexity of Gradients, Jacobian and Hessians, In: Encyclopedia of Optimization, Springer, 2009.
[6] Griewank A., Walther A.: Evaluation Derivatives: Principles and Techniques of Algorithmic Differentiation, SIAM, Philadelphia 2002.
[7] Guay M., McLean D.D.: Computers & Chemical Engineering, **19**, No 12 (1995), 1271-1285.
[8] Helton J.C., Davis, F.J.: Reliability Engineering and System Safety, **81**, (2003), 23-69
[9] Krtolica P.V., Stanimirovi P.S.: Yugoslav Journal of Operations Research, **11**, No 1, 61-75
[10] Kuntsche S., Barz T., Kraus R., Arellano-Garcia H., Wozny G.: MOSAIC a web-based modeling environment for code generation, Computers & Chemical Engineering, In Press
[11] Li X., Zhijiang S., Qian J.: Computers and Chemical Engineering, **28**, (2004), 1551-1561
[12] Liberti L.: A Library for Symbolic Computation in C++ using n-ary Trees, techn report
[13] Marquardt W.: Higher-Order Derivatives in Computational Systems Engineering Problem Solving, 5th International Conference on Automatic Differentiation, Bonn, 2008.
[14] Pantelides C.C.: Symbolic and numerical techniques for the solution of large systems of nonlinear algebraic equations, London Imperial College, Phd thesis, London 1988 .
[15] Rall L.B., Corliss G.F.: Automatic Differentiation: Point and Interval, In: Encyclopedia of Optimization, Springer, 2009.
[16] Schäfer A.S.: Effiziente reduzierte Newton-ähnliche Verfahren zur Behandlung hochdimensionaler strukturierter Optimierungsprobleme mit Anwendung bei biologischen und chemischen Prozessen, Universität Heidelberg, Phd thesis, Heidelberg, 2004.
[17] Slawig T.: Algorithmisches Differenzieren in Simulation und Optimalsteuerung von Differentialgleichungen, Habilitationsschrift, TU Berlin, 2005.
[18] Thomas E., Himmelblau D.M.: Optimization of chemical processes, McGraw-Hill, Boston, 2001
[19] Tolsma J.E., Barton P.I.: European Symposium on Computer Aided Process Engineering, **11**, (2001), 309-314
[20] Tolsma J.E., Barton P.I.: Computers & Chemical Engineering, **22**,No 4/5, (1998), 475-490
[21] Wolbert D., Joulia X., Koehret B., Biegler L.T.: Computers & Chemical Engineering, **18**, 11-12, (1994), 1083-1095

18th International Conference Process Engineering and Chemical Plant Design
Günter Wozny and Łukasz Hady, Editors

RYSZARD WÓJTOWICZ*

THE VIBROMIXERS – A CURRENT STATE OF RESEARCH AND TRENDS OF FURTHER INVESTIGATIONS

Abstract

In the paper are described a state of research and trends of further investigations of an atypical mixing equipment – mixing vessels with a reciprocating agitator (the vibromixers). Against a background of a state of research are presented results of own investigations, devoted to the measurements of a power input for vibro-mixing and the numerical *CFD* simulations of the liquid flow in the vibromixer, obtained for selected disc position in the vessel.

Keywords: vibromixer, reciprocating agitator, multiphase systems, power input, *CFD* simulations

1. Introduction

Mechanical mixing of multiphase systems is a very popular unit operation in different kinds of tasks of a biological, chemical and process engineering. Preparation of gas – liquid, liquid – liquid or solid – liquid systems in industry is – so far – mainly carried out with the use of agitated vessels equipped with one or several (located on the same shaft) impellers. As impellers are used usually rotational, high speed ones with flat or pitched blades, generating a radial or axial flow circulation in the mixing vessel [1,2].

In recent years, aside from classical mixing vessels with rotational impellers, increasingly popular is also the other mixing equipment – the mixing vessels with solid or perforated, up-and-down moving (reciprocating) disc agitators - the vibromixers [3,4]. The mixers of this kind are shown in the offers of many concerns which are producing the industrial equipment [5,6]. The vibromixers – for the sake of many, essential advantages e.g. a generality of the application for various industrial processes or a simple mechanical design seem to be an interesting alternative for the classic mixing vessels, applied for mass and heat transfer processes and also in a very popular biotechnology.

* Cracow University of Technology, Al. Jana Pawła II 37, 31-864 Cracow, Poland.

2. The vibromixer – a principle of an operation

The vibro-mixing of the one of multi-phase systems can be carried out in many apparatuses, differing with a design. The circulation of a liquid in the mixing vessel can be generated with the use of various manners e.g. by means of the acoustic or ultrasound vibrations, the vessel vibrations as well as the vibration of a disc, reciprocating agitator inserted into the vessel. The last of those methods is the most popular in industry. The vibromixers with up-and-down agitators characterize a large efficiency and a simple design (Fig.1), and the broad possibilities of a choice of both mixing elements and drive systems extend additionally its applications.

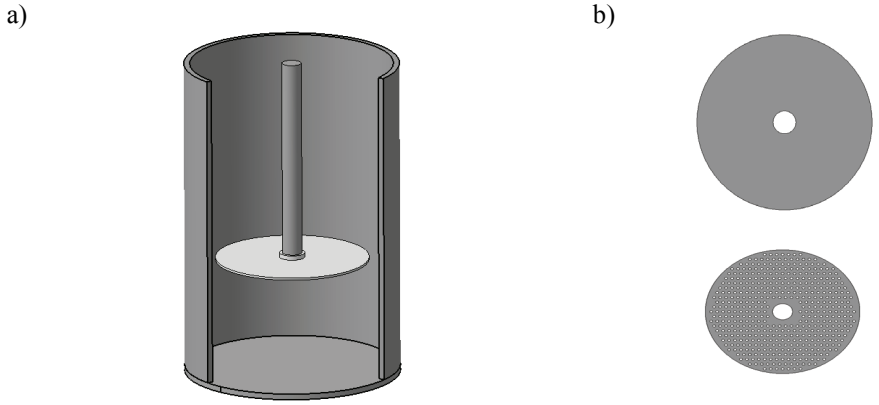

Fig.1. The vibromixer a) geometry of the mixing vessel b) a solid and perforated disc agitator

Inside of a cylindrical vessel with a flat bottom, on a movable shaft is located the solid or perforated, reciprocating disc agitator. The disc location in the vessel and its amplitude and frequency are changed depending on the kind of a process carried out. The up-and-down movement of the disc can be achieved with the use of two different methods (two alternative drive systems):

- a mechanical system - with a slider crank mechanism consisted of a variable speed motor, crank shaft, flywheel and vibrating-rod. When this kind of a drive system is used a disc moves with low frequencies (up to 6 Hz) and high amplitudes (even to 0,1 m).
- a electromagnetic one – with the electromagnetic vibrators. The frequencies of disc vibrations are high (even to 50 Hz) and amplitudes low (up to 0,01 m). For the use of this kind of the drive system a zone of a disc operation is very narrow and it is recommend to assemble two or more discs on the same shaft.

The selected vibromixers with reciprocating agitators used in the industry are shown in Fig.2, and its geometrical and operating parameters are listed in Tab.1.

It should be seen, that the mixing vessels with reciprocating agitators are able to operate in the broad range of amplitudes and frequencies, for low and high pressure and high

temperatures – therefore the mixers of this kind can be used for many, different industrial processes.

a) b) c)

Fig.2. The vibromixers: a) *Softmixer (Rutten Engineering* [5]), b) vibrating disk agitator (*Rutten Engineering*) [5], c) *Vibromix* (*B.Braun Biotech.*) [6]

T a b l e 1

The basic geometrical and operating parameters for the vibromixers [4]

Parameter	Dimension	Value
Volume of the vessel *(V)*	[m^3]	0,01÷20
Disc diameter *(D)*	[m]	0,02÷0,5
Vessel diameter to disc diameter *(T/D)* ratio	[-]	1,04÷3,33
Amplitude of vibration *(A)*	[m]	0,001÷0,3
Frequency of vibration *(f)*	[Hz]	0,001÷60
Degree of a disc perforation *(ϕ)* [4]	[-]	0÷0,5
Temperature *(t)*	[$^{\circ}$C]	to 700
Pressure *(p)*	[at]	to 500

[4] Degree of a disc perforation ϕ – the ratio of the area of holes to the total disc area.

3.The summary of a current stage of research

The investigations on the vibromixers were devoted to preparing of the multiphase systems first of all, mainly liquid-liquid and gas-liquid ones. During dispersion of two immiscible liquids in the apparatus with the up-and-down moving disc, the process was carried out fast and effectively, and - in comparison with classical mixing vessels - a shorter mixing time and less power input for system homogenization are required [3,7÷9]. The intensification of the process was observed also when the reciprocating discs were used as the mixing elements in extraction columns. Vibrations of liquid generated in a whole volume of a column additional vortices, that accelerate the rate of a diffusion process and caused the increase of an interfacial area. The intensity of a mass transfer for this kind of equipment is about several times grater than for e.g. packed columns [10].

Interesting results were obtained also when the vibromixers were used for solid dissolution processes. During mixing by reciprocating agitators - when the liquid in the vessel was brought into additional vibrations - dissolution of solid particles in the liquid took less time [11].

Similar benefits were observed while the vibromixers were used in a microbiological or biochemical technology. For the bioreactors equipped with reciprocating, perforated discs the biological process proceeded about two times faster [12].

For many industrial processes the mixing vessels are used also as the heat exchangers. Its main task – besides of heat transfer – is a homogenization of a temperature field in the whole volume of liquid. The experiments carried out showed that vibrations of liquid significantly intensify the thermal processes proceeding in the mixing vessels. Convective heat-transfer coefficients for vibromixers are several times greater than the ones obtained for both the double-pipe heat exchangers and the classical mixing vessels with high speed, propeller impellers [13].

Relatively, many papers were devoted to the measurements and calculating of a power input (power consumption) during vibro-mixing processes [14÷18]. The Authors as a result of their researches show power characteristics, mainly in the form of correlations between dimensionless *Reynolds* and *Newton* numbers. Unfortunately, there are not propose any uniform method for measurements and calculation of the power consumption in the literature. Some of the Authors [14,15] calculate the maximum value of the power input, the others [16÷18] the mean one, using the different defined dimensionless numbers often. It complicates considerably a description of the process and the comparison of the results makes impossible. Also, for many cases [14÷18], during the calculations the influence of inertial forces and the power consumption in the air (during an idle running) on the total power input are not taken into account.

Summing up, there are not many publications on the mixers with reciprocating agitators in the literature. The non-numerous communicates usually contain short reports on experimental investigations. In the literature lacks first of all the basic information concerning the model of liquid flow in the vibromixer. So far, it was not carried out any computer *CFD* simulations and e.g. laser anemometry *PIV/LDA* measurements, enabling to determine the values and maps of distribution of liquid velocities and turbulence parameters in the various zones of the vibromixer. The current state of research shows a need for further research work particularly for these problems.

4. The results of own investigations and a discussion

The power consumption and power characteristics for the vibromixer

The investigations were carried out for the vibromixer that geometry and a drive system is shown in Fig.3. The experimental system consisted of a cylindrical vessel (internal diameter T=0,286 m), closed at the top and a single, reciprocating agitator.

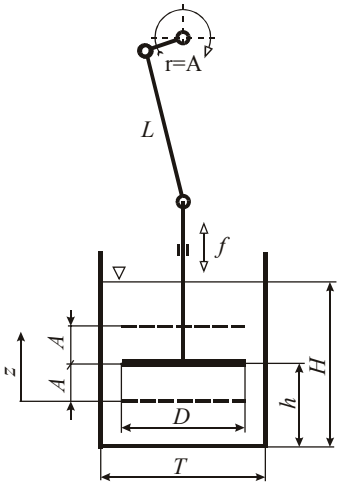

Fig. 3. Geometry of the vibromixer and drive system

The circular flat discs without perforations were used as a agitators, with the discs of D_1 = 0,260; D_2=0,238; D_3=0,220 and D_4=0,204 m in diameter. The agitator clearance (measured from the bottom of the vessel) varied depending on the selected experimental conditions h=(0,25÷0,50)H. The liquid height for all experiments was set at $H = T$. The four various liquids: water, ethylene glycol, glycerol and water solution of glycerol (90% wt.) were used as a model ones. The physical properties of liquids were different and it made possible to obtain the wide range of the power characteristics. The reciprocating movement of the disc was provided by mechanical system, from the top of the vessel by a variable speed motor, via a flywheel, connecting-rod and a vibrating-rod. Changing the position of the crankshaft on the flywheel could alter the amplitude of vibration.

Thus, a change of amplitude from A=0,02 to 0,05 m (at 0,01 intervals) could be achieved. The frequency of movement was altered by changing of the motor speed in the range of f=0,5÷3 Hz (at 0,25 Hz intervals).

The mean power input was calculated as a time integral of the product of the total force acting on the disc $F(t)$ and the instantaneous disc velocity $w(t)$, Eq.(1):

$$\overline{P} = f \int_0^{1/f} F(t) \cdot w(t)\ dt \tag{1}$$

The force function was determined using a piezoelectric sensor mounted in the vibrating rod, and data logger.

For description of instantaneous velocity of the disc the following equation was used:

$$w(t) \cong 2\pi A f \left[\sin(2\pi f t) + \frac{A}{2L} \sin(4\pi f t) \right] \tag{2}$$

where L is the total connecting-rod length.

The mean disc velocity is equal to: $\overline{w} = 4Af$ and the maximum one: $w_{max} = 2\pi Af$.

The mean power input $\overline{P}$ was determined for two cases: during mixing of liquid, and also – in order to estimate influence of inertial forces – in the air. The total value of mean power input for vibro-mixing process was always calculated as a difference between these two - in the water and in the air - mean values of power. The other details of the method of power input measurement are reported elsewhere [19].

Next, on the basis of mean power input, the dimensionless *Newton* number, defined for vibro-mixing as:

$$Ne_v = \frac{\overline{P}}{\overline{w}^3 D^2 \rho} \tag{3}$$

was determined.
Whereas the *Reynolds* number was calculated as:

$$Re_v = \frac{\overline{w} D \rho}{\eta} \tag{4}$$

The power characteristics $Ne_v=f(Re_v)$ obtained for selected two discs, minimum and maximum in diameter are shown in Fig. 4.

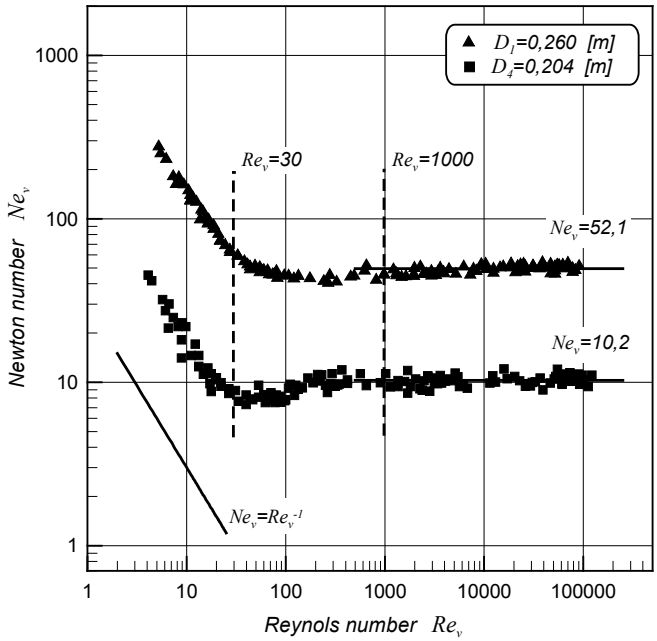

Fig. 4. Power characteristics for investigated discs
(D_1=0,260 m, D_4=0,204 m, h/H=0,50)

The power characteristics obtained for all investigated discs have a very similar shape. Similarly, as a traditional, rotational impellers for the up-and-down moving disc in the laminar range of flow ($Re_v \leq 30$):

$$Ne_v = C_1 \cdot Re_v^a \tag{5}$$

with the value of exponent on *Reynolds* number $a \approx -1$, but for the range of fully turbulent flow ($Re_v > 1000$) the *Newton* number is a constant value:

$$Ne_v = C_2 \tag{6}$$

The constants C_1 and C_2 for all discs used are in a range of C_1=168,8÷1477,5 and C_2=10,2÷52,1.

The numerical CFD simulations of the liquid flow in the vibromixer

The numerical *CFD* modelling of the vibromixer was carried out with the use of *FLUENT 6.3.26* [20] software as a solver and a popular preprocessor *GAMBIT 2.4.6* [21] as a grid generator. The simulations were performed for a vibromixer model shown in Fig.5 (internal tank diameter T=0,286 m, disc diameter D=0,220 m), with amplitude of vibration equal to A= 0,4 m and frequency f=2,5 Hz. For all simulations water as a model liquid filling the vessel was taken. For the sake of the use of a *Dynamic Mesh* mode for the modelling of disc motion, the mixing vessel was divided into three parts: the top zone – including upper part of the vessel, the bottom zone – including lower one, and the moving zone – including a middle of the vibromixer together with vibrating disc.

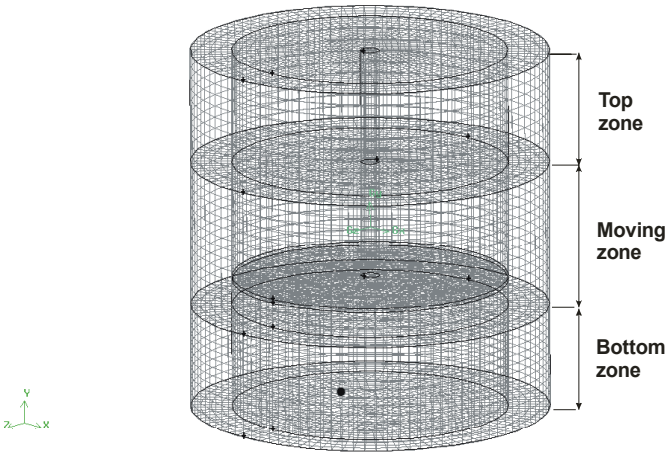

Fig.5. Geometry, mesh and zoning of the vibromixer

The reciprocating movement of the agitator and the moving zone was defined by inserted and compiled into the *FLUENT* an user defined function *(UDF)* **DEFINE_CG_MOTION,** describing a simple harmonic motion. The simulations were carried out for the *3D* case and k-ε turbulence model with the standard wall functions. The procedure of calculations was monitored on the basis of variations of residuals of calculated quantities (continuity, velocity components, turbulence parameters) during following iterations. For created numerical model of the vibromixer also the quality of the mesh was examined. The normalized criterion *EquiAngle Skew* [21] was used for the control of mesh elements degeneracy. The other details of the method of *CFD* modelling of the mixer with reciprocating agitator are reported elsewhere [22].

In the Fig.6 are shown the maps of the velocity vectors of flow, obtained for three selected disc locations in the vessel - the lowest (Fig.6.a), the middle (Fig.6.b) and the highest (Fig.6.c) disc positions. In the next figure are presented the contour maps of the turbulence kinetic energy (Fig.7).

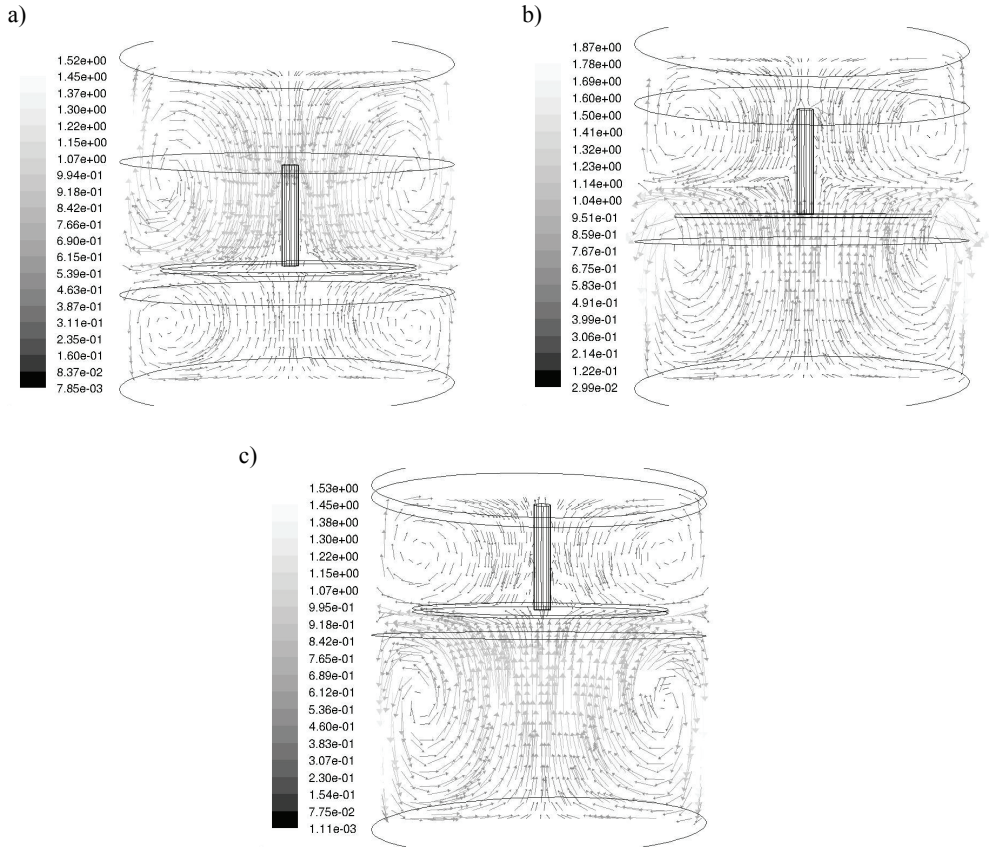

Fig. 6. Velocity vectors a) the lowest disc position, b) the middle disc position, c) the highest

disc position, (A=0,04 m, f=2,5 Hz)

Regardless of a disc movement direction (downward, upward), the maximum values of velocities are observed for the middle disc position (Fig.6.b), in the gap between the disc and the tank wall.

In the top and the bottom part of the vessel and also in the center (near to the axis of the vessel) the liquid flow weakens. Different velocity distributions are seen while the disc takes extreme - the lowest or the highest positions (Fig.6.a,c). In these cases the maximum velocities of flow are observed in the zones above or under the disc and in the gap the liquid flow decay.

The model of the liquid flow in the vibromixer described above, confirm also the maps of turbulence kinetic energy shown in Fig. 7. It is clearly seen that for the middle disc position (Fig.7.b), the most intensive liquid flow (the maximum kinetic energy of flow) occurs between tank wall and the disc, and for extreme (the lowest and the highest) disc positions the zones of the most turbulence energy is seen above and under the agitator, in the center of eddies and near to the tank wall (Fig.7.a.c).

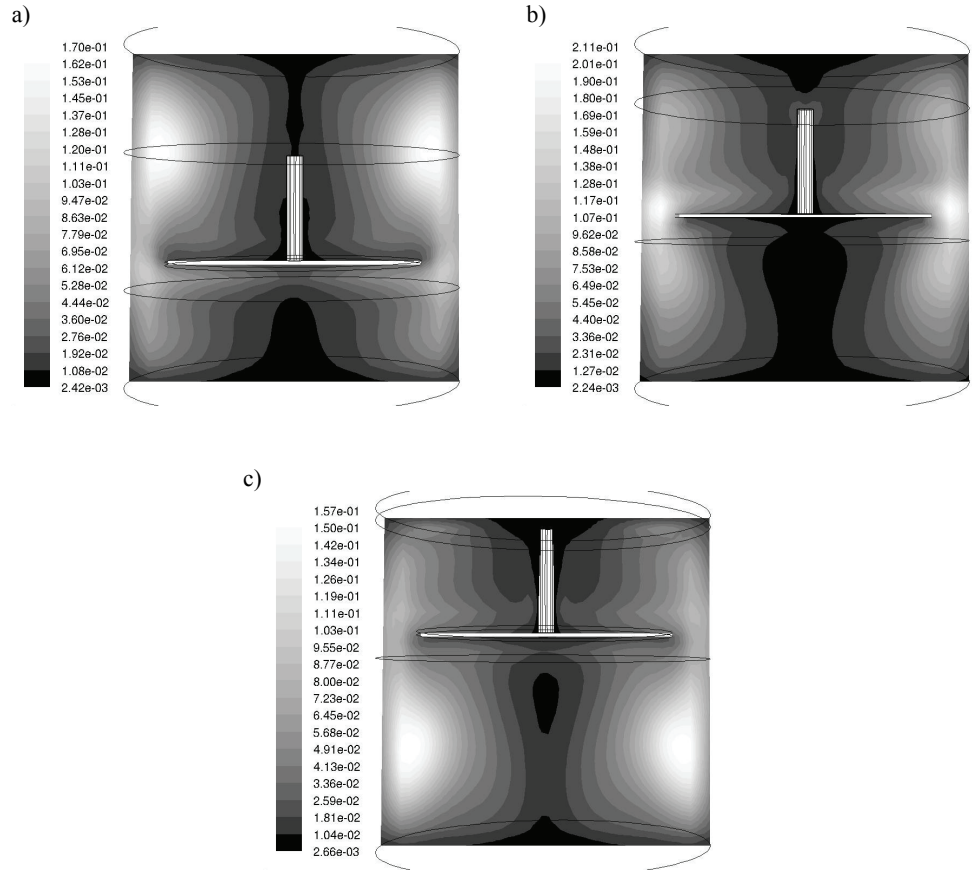

Fig. 7. Turbulence kinetic energy contours a) the lowest disc position, b) the middle disc position, c) the highest disc position (A=0,04m, f=2,5 Hz)

The large advantages of the using of *CFD* software for the numerical analysis of the vibromixer performance is also possibility of a creation of a computer animations and "live" analysis of the liquid movement in the vessel. We are able to do it not only on the basis of values of liquid velocities but - first of all - by determining the directions and senses of liquid flow vectors. Only with the vector maps we can show a formation, size and directions of the eddies relocation, the eddies dissipating the energy in the mixing vessel.

5. Conclusions

The vibromixers (mixers with reciprocating agitators) seem to be an interesting alternative for industrial mixing purposes. Mixing equipment of this kind can be used in many typical operations of chemical, physical and biological process. The interesting advantages were achieved when the vibromixers were use for preparation of multiphase systems (emulsions, gas – liquid dispersion, solids dissolution in the liquid) and also as the bioreactors, heat exchangers or extraction columns.

In spite of all those advantages the vibromixers are not popular in the industry. Also there are not many publications on the mixers with reciprocating agitators in the literature. First of all there are missing the basic information for the vibro-mixing process, concerning the liquid flow model. So far, it was not carried out any computer *CFD* simulations and anemometry measurements, enabling to determine values and maps of distribution of liquid velocities and turbulence parameters in various zones of the vibromixer. The current state of research shows a need for further research work particularly for these problems.

Symbols

A - amplitude of vibration, [m]
a - exponent in Eq.(5), [-]
$C_{1..2}$ - constants, [-]
$D_{1..4}$ - disc diameters, [m]
f - frequency of vibration , [Hz]
F - force acting on the disc, [N]
h - agitator clearance from the bottom of the vessel, [m]
H - liquid height, [m]
L - total connecting-rod length , [m]
t - time, [s] or temperature, [°C]
p - pressure, [at]
$\overline{P}$ - mean power input, [W]
T - internal tank diameter, [m]
T/D - vessel diameter to disc diameter ratio, [-]
V - volume of the vessel, [m^3]
w - disc velocity, [m/s]

Greek letters

η - liquid dynamic viscosity, [Pa·s]
ρ - liquid density, [kg/m^3]
ϕ - degree of a disc perforation, [-]

Indices

$_{max}$ - maximum value
$_{v}$ - denotes vibro-mixing

Dimensionless numbers

$Ne_v = \dfrac{\overline{P}}{\overline{w}^3 D^2 \rho}$ - *Newton* number for vibro-mixing

$Re_v = \dfrac{\overline{w} D \rho}{\eta}$ - *Reynolds* number for vibro-mixing

$\overline{w}$ - mean disc velocity, [m/s]

z - disc displacement, [m]

Literature

[1] Kamieński J.: Mixing of the multiphase systems, WNT, Warszawa 2004 (in Polish).
[2] Paul E.L., Atiemo-Obeng W.A., Kresta S.M.: Handbook of Industrial Mixing, J. Wiley & Sons Inc., New Jersey 2004.
[3] Kamieński J., Wójtowicz R.: Chem. Eng. Proc., **42**, (2003), 1007-1017.
[4] Masiuk S., Mudrak R.: Inż. Ap. Chem., **2**, (1996), 21-24 (in Polish).
[5] Rutten Eng. GmbH – available from: *http://www.rutten.com* (accessed: 9.04.2011).
[6] B. Braun Biotech. Inc. – available from: *http://bbraunbiotech.com* (accessed: 9.04.2011).
[7] Brauer H.: Inż. Chem. Proc., **15**, (1994), 15-36 (in German).
[8] Tojo K., Mitsui H., Miyanami K.: Chem. Eng. Commun., **6**, (1980), 305-311.
[9] Wójtowicz R.: The analysis of vibrating discs performance in two immiscible liquids systems, Ph.D. Thesis, Cracow University of Technology, Kraków 2000 (in Polish).
[10] Tojo K., Miyanami K.: J. Chem. Eng. Jap., **8**, (1975), 165-173.
[11] Khan O., Guszczin J.: Cwiet. Miet., **43**, (1990), 19-21 (in Russian).
[12] Brauer H., Annachhatre A.: Bioproc. Eng., **7**, (1992), 269-275
[13] Masiuk S.: Chem. Eng. J., **61**, (1996), 107-112.
[14] Masiuk S., Damra T.: Chem. Proc. Eng., **17**, (1996), 51-60.
[15] Masiuk S., Rakoczy R., Kordas M.: Chem. Eng. Process., **47**, (2008), 1258-1266.
[16] Komoda Y., Inoue Y., Hirata Y.: J. Chem. Eng. Japan, **33**, (2000), 879-885.
[17] Gierczycki A.T.: Chem. Biochem. Eng., **12**, (1998), 97-100.
[18] Gierczycki A.T., Dzido G., Kocurek J.: Inż. Ap. Chem., **4s**, (2002), 47-48 (in Polish).
[19] Kamieński J., Wójtowicz R.: Cz. Techn., **4-M**, (2004). 151-158.
[20] Fluent 6.2 - Documentation, Fluent Inc., Lebanon 2006.
[21] Gambit 2.4 - Documentation, Fluent Inc., Lebanon 2006.
[22] Wójtowicz R.: Cz. Techn., **2-M**, (2008), 371-384 (in Polish).

18th International Conference Process Engineering and Chemical Plant Design
Günter Wozny and Łukasz Hady, Editors

JERZY BAŁDYGA*, MAGDALENA JASIŃSKA*

REACTIVE MIXING AND DISPERSION PROCESSES IN ROTOR-STATOR DEVICES

Abstract

High shear rotor-stator devices are used in many technologies due to their ability to generate and control high shear stresses. In present work a Silverson double screen inline rotor-stator mixer was investigated both numerically and experimentally using CFD and applying the diazo-coupling homogeneous chemical test reactions. The expression for the rotor-stator power number consisting of two terms as proposed earlier by the authors was confirmed experimentally and predicted by CFD in present work. Results of application of the rotor-stator devices for dispersion of drops are presented as well.

Keywords: diazo coupling, drop breakup, effectiveness of mixing, high shear mixer.

1. Introduction

The rotor-stator devices are known from their ability to generate very high shear stresses and that is why they are used in many technologies in the chemical, pharmaceutical, biochemical, agricultural, cosmetic health care and food processing industries for homogenization, dispersion, emulsification, grinding, dissolving, performing chemical reactions with high selectivity, cell disruption and shear coagulation. Generation of very high stresses results from a high rotation speed and is related to high local values of the rate of energy dissipation, which requires of course high agitation power and focused delivery of energy. Hence, it is important to learn how effective for the process is dissipation of energy, and to design the rotor-stator device so that the energy will be dissipated effectively for any specific application. Design of such devices is usually performed based on engineering judgment, experience and intuition using trials and errors methodology, only recently with some support of CFD. As mentioned in ref.[1], "the current understanding of rotor-stator devices has almost no fundamental basis", which has obvious consequences for design methodology mentioned above.

* Warsaw University of Technology, Faculty of Chemical and Process Engineering,
ul. Waryńskiego 1, 00 645 Warsaw, Poland

In present work a Silverson double screen inline rotor-stator mixer is investigated using the multiple test chemical reactions and CFD; results of CFD predictions are compared with experimental data for the product distribution of test reactions and the agitation power that has been recalculated either from the measured torque or from the heat balance. In the second part of this work an application of the rotor-stator device for dispersion of droplets is presented. In the last case the population balances are applied together with CFD to simulate the process and interpret available experimental data.

2. Silverson rotor-stator high shear mixer – geometry and hydrodynamics

Figure 1 shows a Silverson double screen mixer 150/250/MS. The mixer is equipped with twin rotors that rotate together within close fitting screens.

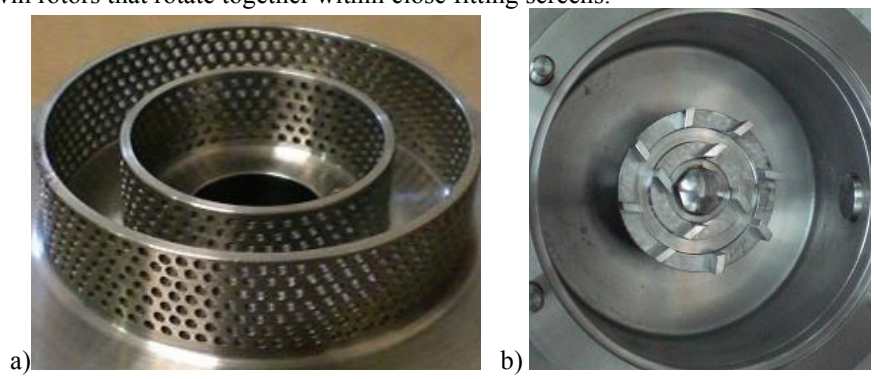

Fig. 1. Silverson 150/250 rotor-stator mixer a) Silverson screens (stator), b) Silverson blades (rotor)

The inner rotor is characterised by the inner diameter equal to $2.624 \cdot 10^{-2}$ m and outer diameter equal to $3.82 \cdot 10^{-2}$ m (1.5 in). The outer rotor diameters are equal to $4.99 \cdot 10^{-2}$ m and $6.34 \cdot 10^{-2}$ m (2.5 in) respectively. The inner stator screen has 6 rows of 50 circular holes each of diameter $1.59 \cdot 10^{-3}$ m (1/16 in) on a 0.100 in tri pitch. The outer screen has 7 rows of 80 circular holes each of diameter $1.59 \cdot 10^{-3}$ m on a 0.100 in tri pitch.

Simulations of the Silverson rotor-stator mixer hydrodynamics were carried out using the standard k-ε model of Fluent-Ansys and the multi-reference frame of reference. The 2D and 3D simulations were performed. An unstructured mesh consisting of 200 000 cells and 180 000 nodes was applied in 2D simulations; in 3D simulations the number of cells was equal to $4.6 \cdot 10^{6}$ with number of nodes equal to $4.8 \cdot 10^{6}$.

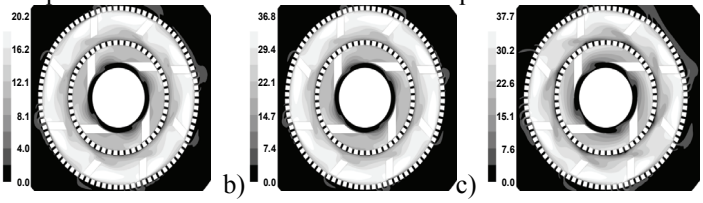

Fig. 2. Results of simulations of the flow in the rotor-stator mixer. Velocity [m/s] distribution for: a) $Q=1.67 \cdot 10^{-3}$ m^3/s, $N=100$ s^{-1} b) $Q=1.67 \cdot 10^{-3}$ m^3/s, $N=183$ s^{-1} c) $Q=6.67 \cdot 10^{-3}$ m^3/s, $N=183$ s^{-}

Fig.2 shows that velocity distributions are similar in considered case of well developed turbulence and that both the flow rate Q and the rotor speed N affect the flow field (see the maximum velocity values).

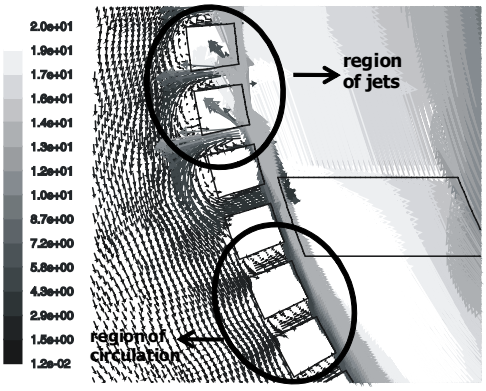

Fig. 3. Results of simulations of the flow in the rotor-stator mixer. Velocity [m/s] vectors for $Q=1.67\cdot10^{-3}$ m^3/s, $N=100$ s^{-1}. Outer screen.

Fig. 3 shows that within the holes placed behind the blade one can observe circulations, whereas in front of moving blade one can see that strong jests are emerging. This observation is important for interpretation of drop dispersion because a fast flow through the holes creates elongation, which is very effective for drop breakage, and jets create locally high values of the rate of energy dissipation and related turbulent stresses.

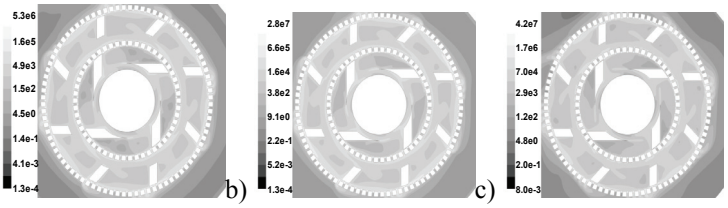

a) b) c)

Fig. 4. Results of simulations of the flow in the rotor-stator mixer. Rate of energy dissipation $[m^2/s^3]$ distribution for: a) $Q=1.67\cdot10^{-3}$ m^3/s, $N=100$ s^{-1} b) $Q=1.67\cdot10^{-3}$ m^3/s, $N=183$ s^{-1} c) $Q=6.67\cdot10^{-3}$ m^3/s, $N=183$ s^{-1}

Fig. 4 shows that the highest values of the rate of energy dissipation are observed close to the blades and in a vicinity of screens. One can also see that increasing of both rotor speed and flow rate increases significantly the rate of energy dissipation, so should increase as well required power input. More details regarding localization of regions of high rate of energy dissipation one can see on Fig.5, where increased dissipation of kinetic energy created by jets (Fig.3) is clearly observed.

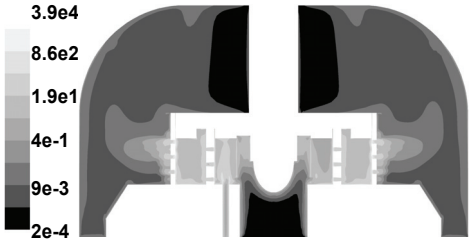

Fig. 5. Results of simulations of the flow in the rotor-stator mixer. Rate of energy dissipation [m^2/s^3] distribution for $Q=1.0\cdot10^{-4}$ m^3/s, $N=16.7$ s^{-1}

Based on presented results of computations it is possible to estimate the power number,

$$N_P = \frac{P}{\rho N^3 D^5} \tag{1}$$

where the power P was calculated either from 2D simulations or 3D simulations, either by integration of the rate of energy dissipation or from the torque. D in eq.(1) represents the outer rotor diameter. In the case of 3D simulations this procedure is straightforward, in the case of 2D simulations the active height of the outer stator was used ($h=1.3\cdot10^{-2}$ m). Results of simulations are shown in Fig.6 together with experimental data from ref. [2]. One can see that increase of the flow rate increases the power number for the same values of the rotor speed in agreement with Fig.4, where this effect is observed for the rate of energy dissipation. The same effect was observed in experiments for the power calculated either from measured torque or from the heat balance [2, 3]. To account for this effect a simple expression was derived in [2] and applied later in ref. [3] as well.

$$N_P = \frac{P}{\rho N^3 D^5} = N_{P1} + N_{P2}\frac{Q}{ND^3} = N_{P1} + N_{P2}N_Q \tag{2}$$

where N_Q represents the pumping or flow number.

The values fitted to 2D CFD results are [2]: for the power calculated from the rate of energy dissipation $N_{P1} = 0.47$, $N_{P2} = 0$ for $N_Q<0.013$, and $N_{P1}=0.20$, $N_{P2}=18.2$ for $N_Q>0.013$. For the power calculated from the torque $N_{P1} = 0.42$, $N_{P2} = 0$ for $N_Q<0.013$, and $N_{P1}=0.10$, $N_{P2}=18.4$ for $N_Q>0.013$.

In ref. [3] the single values for experimentally determined power number are given for the whole range of the pumping number: from torque $N_{P1}=0.197$, $N_{P2}=9.35$, from calorimetric data $N_{P1}=0.228$, $N_{P2}=8.1$. Comparing these with the values determined from 3D simulations we have obtained from torque $N_{P1}=0.32$, $N_{P2}=12.7$ and from the integrated rate of energy dissipation $N_{P1}=0.32$, $N_{P2}=5.6$.

Agreement between predicted and measured data is not perfect but good enough to conclude that the two-term expression (2) should be used instead of a single term expression applied usually to calculate the agitation power in stirred tanks.

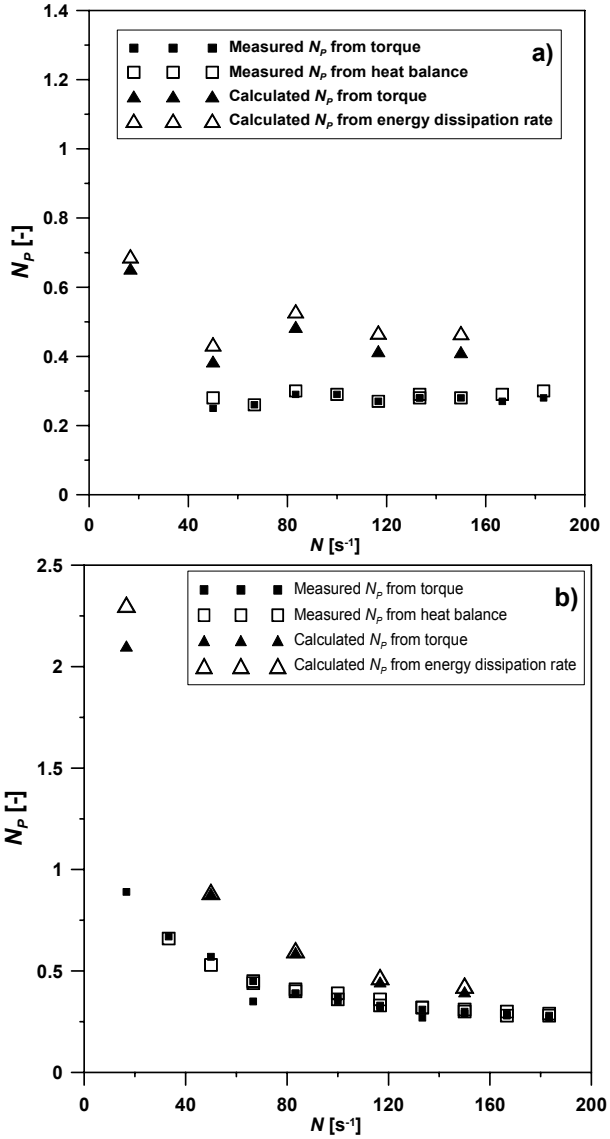

Fig. 6. Dependence of the power number, N_P, on the stirrer speed and flow rate a) $Q = 0.1 \cdot 10^{-3}$ m^3/s b) $Q = 0.5 \cdot 10^{-3}$ m^3/s.

3. Mixing in Silverson rotor-stator high shear mixer and application of test reactions

One of available methods to study mixer performance is application of fast homogeneous chemical reactions. Multiple chemical reactions offer the best way to test mixing models and characterize mixing in equipment of industrial importance. When choosing test reactions one should consider the system of reactions that are fast relative to mixing, so that the time constants of reaction and mixing are of comparable magnitude. Moreover all reactants and products should be soluble and reactions should be irreversible, so that the final product distribution stores the history of mixing [4]. Accurate quantitative analysis should be possible and all reactions' kinetics should be known. In present case a simultaneous diazo coupling between 1- and 2-naphtols and diazotized sulphanilic acid is considered. The reaction scheme contains parallel and consecutive second order reactions [4]:

$$A + B \xrightarrow{k_{1p}} p - R \tag{3}$$

$$A + B \xrightarrow{k_{1o}} o - R \tag{4}$$

$$p - R + B \xrightarrow{k_{20}} S \tag{5}$$

$$o - R + B \xrightarrow{k_{2p}} S \tag{6}$$

$$AA + B \xrightarrow{k_3} Q \tag{7}$$

where A denotes 1-naphtol, AA is 2-naphtol, B represents diazotized sulphanilic acid, o-R and p-R are two mono-substituted dyes (ortho and para), S represents a bisazo dye and Q is a single monoazo dye. At temperature equal to 298K, pH = 9.9 (with sodium carbonate and bicarbonate employed as buffers), for ionic strength $I = 444.4$ mol/m^3 the rate constants take following values:

$$k_{1p} = 12238 \pm 446 \text{ m}^3/\text{mol s}$$

$k_{1o} = 921 \pm 31$ m^3/mol s

$k_{2p} = 22.25 \pm 0.25$ m^3/mol s

$k_{2o} = 1.835 \pm 0.018$ m^3/mol s

$$k_3 = 124.5 \pm 1.0 \text{ m}^3/\text{mol s}$$

Extend of mixing is characterized by the product distribution. Two measures of product distribution can be employed, one concentrating on the yield of secondary product S and the other on the yield of the competitive product Q.

$$X_S = 2c_S \Big/ \left(c_{OR} + c_{pR} + c_Q + 2c_S\right) \tag{8}$$

$$X_Q = c_Q \Big/ \left(c_{oR} + c_{pR} + c_Q + 2c_S\right) \tag{9}$$

Both definitions express yields relative to the limiting reagent B.

Results of CFD simulations of passive scalar mixing are presented in Figures 7 and 8; Fig. 7 shows the mixture fraction, f, representing the mass fraction of the fluid injected as a tracer and Fig. 8 shows the variance of mixture fraction calculated using the turbulent

mixer model presented in detail in ref. [4]. One can see how the tracer is losing its identity due to mixing (Fig. 7) and how fluctuations of the passive tracer concentration are created and dissipated (Fig. 8). Both phenomena are observed close to the tracer feeding point.

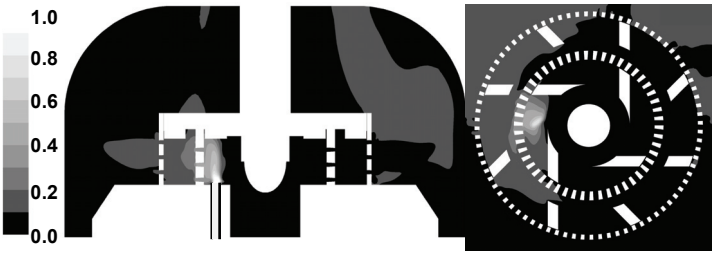

Fig. 7. Results of simulations of mixing in the rotor-stator mixer. Mixture fraction distribution for $Q=1.0\cdot10^{-4}$ m^3/s, N=16.7 s^{-1}

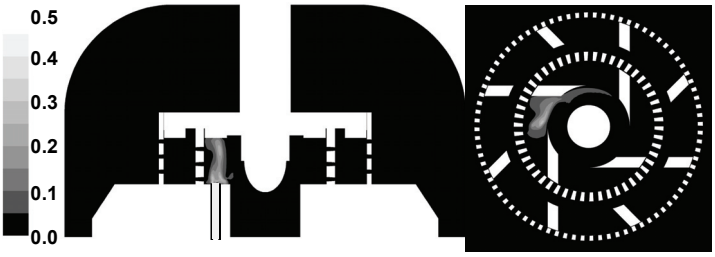

Fig. 8. Results of simulations of mixing in the rotor-stator mixer. Mixture fraction variance distribution for $Q=1.0\cdot10^{-4}$ m^3/s, N=16.7 s^{-1}

Finally Fig. 9 shows distribution of the product Q, which determines the product distribution X_Q.

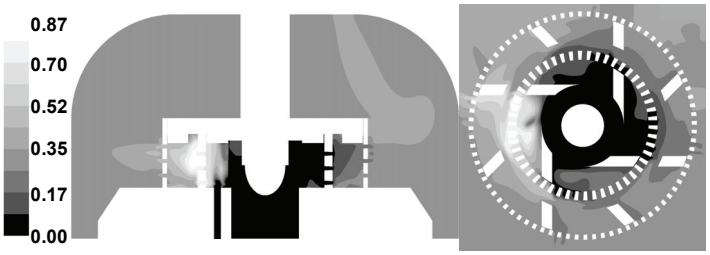

Fig. 9. Results of simulations of reactive mixing in the rotor-stator mixer. Concentration of product Q distribution [mol/m^3] for $Q=1.0\cdot10^{-4}$ m^3/s, N=16.7 s^{-1}

Experiments were carried out at $T=25^0$C, pH = 9.9, Q_A=360 kg/h, Q_B=24 kg/h, c_A= 1.2 mol/m^3, c_{AA}=1.2 mol/m^3, c_B=15 mol/m^3. When reactant B is injected into main stream containing A before the inner screen, then for $Q=1.0\cdot10^{-4}$ m^3/s, N=66.7 s^{-1} one gets in experiment X_Q=0.214, and for N=133.3 s^{-1} X_Q=0.139. For feeding between the screens

one gets X_Q=0.181 and X_Q=0.121 for N=66.7 s^{-1} and N=133.3 s^{-1} respectively. Such results show that mixing close to outer screen is more efficient than mixing close to inner screen; slower mixing close to inner screen enables creation of larger amount of product Q. Intensive mixing after creation of Q cannot change this anymore.. When the inner screen is removed one gets for the inner feeding point X_Q=0.199 and 0.139 for N=66.7 s^{-1} and N=133.3 s^{-1} respectively, and for outer feeding of B, X_Q=0.180 and 0.141 for N=66.7 s^{-1} and N=133.3s^{-1} respectively. One can see that presence of inner screen is not important for mixing. CFD predicts well effects observed in experiments. For Q=1.0·10^{-4} m^3/s, inner feeding and N=50s^{-1}, the value X_Q=0.272 has been predicted, whereas experimental value reads X_Q=0.244. When N is increased to 83.3s^{-1}, then predicted value reads X_Q=0.216 and experimental one X_Q=0.195.

4. Drop dispersion in Silverson rotor-stator high shear mixer

A drop, suspended in a continuous phase, breaks up when if the local instantaneous stresses generated by turbulent flow exceed the stabilizing forces due to interfacial tension and drop viscosity. To model drop dispersion in the rotor-stator mixer the breakage kernel based on the multifractal theory of turbulence is applied [4, 5].

The expression for the drop breakup frequency resulting from this theory can be presented as

$$g(d) = C_g \sqrt{\ln(L/d)}\, \varepsilon^{1/3} d^{-2/3} \int_{\alpha_{min}}^{\alpha_x} \left(\frac{d}{L}\right)^{\frac{(\alpha+2-3f(\alpha))}{3}} d\alpha \qquad (10)$$

where f(α) represents the multifractal spectrum, α is the multifractal exponent, which takes the values between the smallest one $\alpha_{min} = 0.12$ that is responsible for action of the most violent turbulent eddies and α_x characterizing the weakest eddies that still are able to break droplets. The value of α_x depends on the interfacial tension, viscosity of drops and continues phase, the rate of energy dissipation, and the integral scale of turbulence, L [4, 5]. This means that the drop breakup is scale dependent, with clear consequences for scaling up. Integral in eq.(10) means that all possible contributions from eddied characterized by α between $\alpha_{min} = 0.12$ and α_x are summed up. When α_x approaches $\alpha_{min} = 0.12$ then there is no breakage anymore and the maximum stable drop sizes are observed. In computations CFD is applied together with the quadrature method of moments (QMOM)[6].

Fig. 10 shows distribution of the integral scale in the mixer, which together with distribution of the rate of energy dissipation defines the breakage rate in the system. There is significant variation of the scale within the mixer, and results of simulations show that for well developed turbulence the scale distribution depends mainly on the system geometry.

Fig. 11 shows simulated results of the drop size distribution in the inline Silverson rotor-stator mixer. One can see that increasing the stirrer speed decreases the drop size, whereas increasing the flow rate, Q, decreases the size of drops although the power of agitation increases.

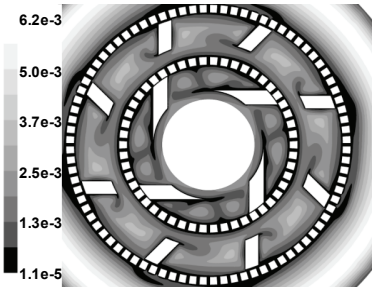

Fig. 10. Results of CFD simulations of the flow in the rotor-stator mixer.
Integral scale of turbulence, L [m] for Q=1.67·10^{-3} m^3/s, N=100 s^{-1}

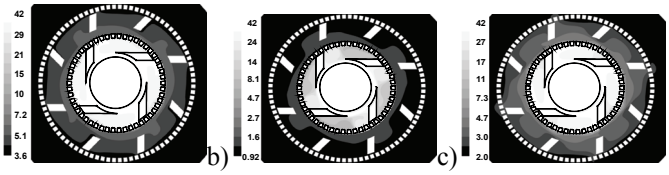

Fig. 11. Results of simulations of the drop breakup in the rotor-stator mixer. Distribution of d_{32} [μm]
a) Q=1.67·10^{-3} m^3/s, N=100 s^{-1} b) Q=1.67·10^{-3} m^3/s, N=183 s^{-1}c) Q=6.67·10^{-3} m^3/s, N=183 s^{-1}

The drops at the inlet to the mixer have the size characterized by d_{32}=42 μm; the size at the outlet for Q=1.67·10^{-3} m^3/s decreases from 3.6 μm to 0.92 μm when the rotor speed increases from N=100s^{-1} to N=183 s^{-1}; for N=183 s^{-1}increase of the flow rate Q from Q=1.67·10^{-3} m^3/s to Q=6.67·10^{-3} m^3/s increases the drop size at the outlet from 0.92 μm to 2 μm. Similar effect was observed in the process of dispersion of agglomerates as shown in Fig.15 of ref. [7]. Larger sizes of droplets or agglomerates after dispersion with increased flow rate result from decreased residence time, which means that the time available for breakage is then smaller. Another possible mechanism is bypassing; notice that not all fluids flow directly through the screen holes as strong, generating stresses jets, and such phenomena as recirculation and creation of weak jets are observed as well. Effect of agitation is much larger than effect of flow rate, which agrees qualitatively with observations reported in ref. [8].

5. Conclusions

Presented results show that the CFD modeling of mixing and dispersion processes in the Silverson type rotor-stator mixers gives results that agree qualitatively with experimental data. Taking into account that there is no fitting in methods applied in present work, reasonable quantitative agreement is observed as well.

In particular it has been shown that both experimental data and CFD predict the two term expression for power draw of an inline high shear mixer.

It has been also shown that developed earlier modeling methods to predict mixing of passive scalar and reactive mixing in stirred tanks and tubular reactors can be used to characterize mixing in the high shear mixers. Also experimental method to characterize

efficiency of mixing expressed by the product distribution X_Q has been applied with success.

The drop breakage kernel developed earlier to characterize drop breakup and validated experimentally for stirred tanks and jets has been applied to predict the course of drop breakup in high shear mixer, giving the trends consistent with experimental data.

Literature

[1] Atiemo-Obeng V.A., Calabrese R.V.: Rotor-stator mixing devices. in Handbook of Industrial Mixing, Science and Practice, Wiley, Hoboken, New Jersey 2004.
[2] Bałdyga J., Kowalski A., Cooke M., Jasińska M.: Chemical and Process Engineering, **28**, (2007), 867-877.
[3] Kowalski A.J., Cooke M., Hall S.: Chemical Engineering Science, **66**, (2011), 241-249.
[4] Bałdyga J., Bourne J.R., turbulent mixing and chemical reactions, Wiley, Chichester 1999.
[5] Bałdyga J., Podgórska W.: Can. J. Chem. Eng., **76**, (1998), 456-470.
[6] McGraw R.: Aerosol Sci. Technol., **27**, (1997), 255-265.
[7] Bałdyga J., Orciuch W., Makowski L., Malik K., Ozcan-Taskin G., Eagels W., Padron G.: Ind. Eng. Chem. Res., **47**, (2008), 3652-3663.
[8] Hall S., Cooke M., El-Hamouz A., Kowalski A.J.: Chemical Engineering Science, **10**, (2011), 2068-2079.

18th International Conference Process Engineering and Chemical Plant Design
Günter Wozny and Łukasz Hady, Editors

JERZY KAMIEŃSKI, ANDRZEJ DUDA*

THE DUAL IMPELLER CAPACITIES IN THE CONTEXT OF COMPARTMENT MODEL APPROACH

Abstract

The study was dedicated to the question of liquid flow rates in the dual mixing vessels. The pumping flow rate Q_p and the circulation flow rate Q_c are the basic magnitudes that characterise the liquid flow in the vessel. The pumping flow rate describes the liquid flow passing through the impellers' region, while the circulation flow rate determines the liquid flow in the total volume of the vessel.

When the two impellers in the dual mixing vessels have different geometries, one of them is always predominant, that imposes the structure and rate of the total liquid flow in the vessel. In case the liquid flow structure in dual mixing vessel consists of more than one circulation loop, the overall liquid flow is then evaluated from Q_c rate, increased by the additional Q_E rates, appearing between neighbouring loops. This feature can be described with usage of Compartment Model Approach (CMA).

Keywords: dual mixing vessel, flow rate, CMA model.

1. Introduction

The apparatuses equipped with two or more impellers i.e. dual or multi mixing vessels are often found in industrial installations. They seem to be an alternative versus standard constructions with single impeller, especially for mixing applications in bigger liquid volumes. The slender vessels, in which the height greatly exceeds their diameter and the shape factor is over unit, are then usually applied. Those vessels are equipped with two or more impellers assembled on the shaft.

The magnitudes describing liquid flow in the dual mixing vessels are ones of those technical key-issues that influence the selection of the impeller's geometry as well as the vessel itself. The intensity and structure of the flows relate to the mixing time required to gain the final effects of the process progressing within [1]. Those magnitudes depend on the geometry of used impellers, their position in vessel, as well as on the rotational speed and vessel's design. The liquid flow rate related to the mixing power determines efficiency,

* Cracow University of Technology, Faculty of Mechanical Engineering, Institute of Thermal and Process Engineering, Al. Jana Pawła II 37, 31-864 Cracow, Poland.

which is one of the basic criteria of the mixing vessel applicability [2,3,4]. Until recently, the pumping flow rate Q_p has been commonly recognised as a basic value used for description of the liquid flow in the mixing vessel [5]. However, it is believed for a few years that the flow rate should be evaluated in the total vessels' volume, as the additional flows entrained by the impellers' discharge and circling around the local centres of formed liquid loops are included in calculation [3,4,6]. Therefore, it was proposed to introduce the circulation flow rate Q_c as the basic magnitude characterising the impellers' functioning.

The flow structure in the dual mixing vessels can form one single circulation loop or be more complex and consist of the number of interacting loops. The exchange phenomena of the kinetic energy in the liquid occurs, as a result of the inter-stage flow rate Q_E, being induced by the fluctuation of an axial component of velocity [7,8]. In this case, the Q_c flow rate is understand as the sum of the flow rates evaluated in each loop, increased by the total value of the Q_E flows found on the all borders of the interaction between loops [9].

The inter-correlations of the magnitudes describing liquid flows in the mixing vessel, verified by the selected examples of the dual impeller configurations, were presented in the paper.

2. The experimental data and set-up

The liquid flow rates were evaluated by the integration of the mean and fluctuating velocity profiles in vessel, normal or parallel to its axis. The liquid velocity values were measured using laser anemometry technique LDA. The cylindrical vessel with diameter D=0.286 m was equipped with two impellers. The impellers that were used had different geometries and constant diameter d=0.095 m and were put together creating different configurations.

The geometry and dimensions of the impellers used were described in the paper [10]. The impeller spacing Δh was varied within the range of (0.5÷2) d however, the lower impeller clearance was constant, and was of 0.5 d. The measurements were carried out in the liquid with viscosity of 2.3 mPas and constant rotational speed, 5 s^{-1}. The liquid level H was of 1.5 D. The description of the experimental set-up as well as the measurement methods of the liquid velocities were presented in the papers [9,10]. Furthermore, the evaluation algorithm of the flow rates Q was described in [9,11,12].

3. The pumping flow rate

The pumping flow rate is commonly determined by the rate of the volumetric flow that enters Q_{in} or leaves Q_{out} the zone swept by rotating impeller, i.e. the flow rate passing across the planes established by rotating blades of the impeller, similarly as the rotating pump case [3,5]:

$$\left|Q_p\right| = \left|Q_{in}\right| = \left|Q_{out}\right| \tag{1}$$

, where each of the above flow rates is calculated on the base of mean velocity components, normal to the A_S plane established by rotating impeller:

$$Q_{in\,(out)} = \int_{A_S} \bar{u}_{n,\,in\,(out)}\, dA_S \tag{2}$$

In practice, more universal and often used is the dimensionless pumping flow number K_p [1-8]:

$$K_p = \frac{Q_p}{n \cdot d^3} \tag{3}$$

dependent only on the impeller's geometry in fully developed turbulent flow. The Q_p flow rate in the dual mixing vessels is the sum of the flows induced both by the upper ($Q_{p\ up}$) and the lower ($Q_{p\ low}$) impeller, regardless of their position in vessel [12]:

$$Q_{p\ sum} = Q_{p\ up} + Q_{p\ low} \tag{4}$$

Thus, the dimensionless pumping flow number K_p for the dual impeller with constant diameter assembled on common shaft, takes form:

$$K_{p\ sum} = K_{p\ up} + K_{p\ low} \tag{5}$$

The K_p numbers for upper and lower impeller as well as its total values, versus impeller spacing Δh was shown on the following figures, exemplified by the case of two Rushton turbines RT-6 (figure 1) and two Pitched Blade Turbines PBT-6/45° (figure 2). Moreover, the K_p values were collected in table 1 and 2. It can be concluded from the graphs that for the investigated dual impellers with identical geometries, the $K_{p\ up}$ and $K_{p\ low}$ number values take nearly similar values, independently the Δh spacing value. It is evident especially for two PBT-6 turbines (figure 2). For two RT-6 turbines, the 8 % decrease of the K_{plow} values occurs at $\Delta h = 1d$ (figure 1). It can be caused by the lower impeller having dumping effect on the flow, occurring at above spacing and correlated to the structure of the circulating liquid. The dual impeller sets with identical geometries operate the same way, i.e. yield proportional variations of the induced flow rates. The K_p values reach local extrema at $\Delta h = 1.5d$. It would point on either mutual damping of the induced flows (for two PBT-6 turbines) or an intensification of those flows, for the two RT-6 turbines case.

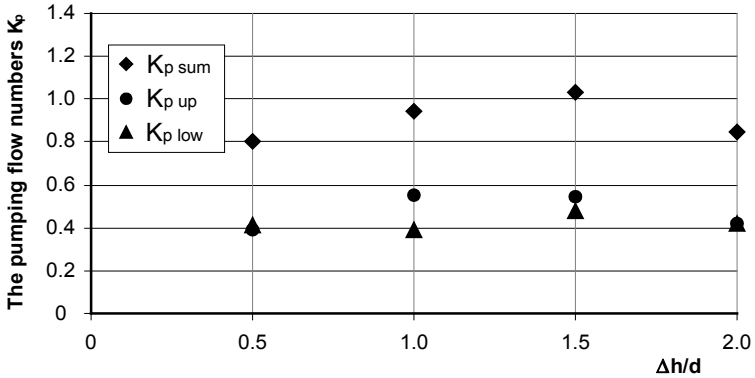

Figure 1. The pumping flow numbers K_p for the set of two RT-6 turbines.

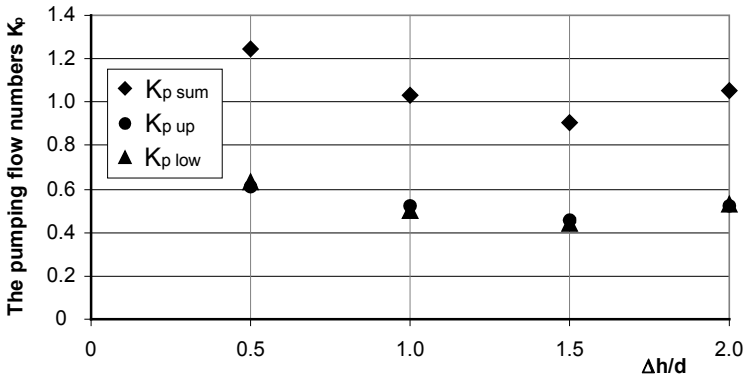

Figure 2. The pumping flow numbers K_p for the set of two PBT-6/45° turbines.

T a b l e 1

The $K_{p\ sum}$, $K_{p\ up}$ and $K_{p\ low}$ values for the set of two RT-6 turbines.

The pumping flow number	Δh /d			
	0.5	**1.0**	**1.5**	**2.0**
$K_{p\ sum}$	0.80	0.94	1.03	0.84
$K_{p\ up}$	0.39	0.55	0.55	0.42
$K_{p\ low}$	0.41	0.39	0.48	0.42

If the dual set consists of impellers with different geometries, one of them is always predominant. Thus, this impeller generates usually higher flow rates - yielding in higher K_p values, which has an influence on the $K_{p\ sum}$ number variations versus impeller spacing Δh and has strong effect on the final structure of the flow field in the vessel. This dependence

T a b l e 2

The $K_{p\ sum}$, $K_{p\ up}$ and $K_{p\ low}$ values for the set of two PBT-6/45° turbines.

The pumping flow number	Δh /d			
	0.5	**1.0**	**1.5**	**2.0**
$K_{p\ sum}$	1.25	1.02	0.90	1.05
$K_{p\ up}$	0.61	0.52	0.46	0.52
$K_{p\ low}$	0.64	0.50	0.44	0.53

is described on the graph, figure 3. It shows the dependence of the K_p numbers on the impeller spacing Δh, for the dual set: upper impeller - PBT-6/45° turbine, lower - RT-6 turbine. In this case the lower impeller is the predominant. The exact values of K_p numbers were collected in table 3.

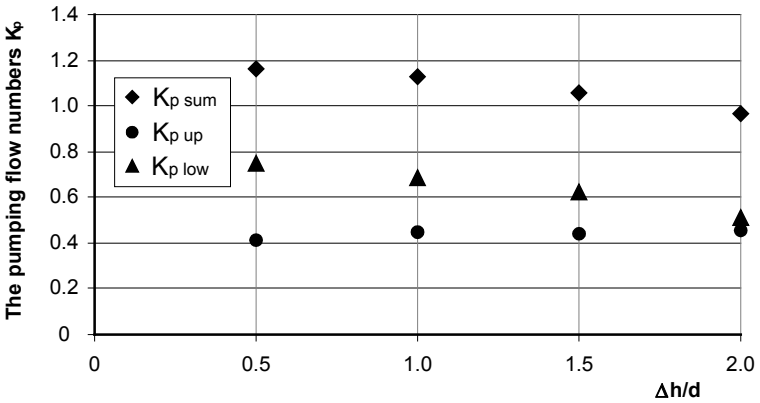

Figure 3. The pumping flow numbers K_p for the impeller set: lower - RT-6 turbine, upper - PBT-6/45° turbine.

T a b l e 3

The $K_{p\ sum}$, $K_{p\ up}$ and $K_{p\ low}$ values for the set of two turbines: lower - RT-6, upper – PBT-6/45°.

The pumping flow number	Δh /d			
	0.5	**1.0**	**1.5**	**2.0**
$K_{p\ sum}$	1.17	1.13	1.06	0.97
$K_{p\ up}$	0.42	0.45	0.44	0.46
$K_{p\ low}$	0.75	0.68	0.62	0.51

4. The circulation flow rate

The circulation flow rate Q_c is defined as total value of the flow determined in any axial or radial profile of the vessel (r_i), (z_i) i.e. normal or parallel to its axis, on the base of mean velocity components ($\bar{u}_r$, $\bar{u}_z$) normal to the profile section (r_i, z_i) [3]:

$$Q_c = \max_r \left\{ |Q_r| \right\} = \max_z \left\{ |Q_z| \right\} \tag{6}$$

, where:

$$Q_r(r_i) = 2\pi\, r_i \int_{z_1}^{z_2} (\bar{u}_r)_{r_i}\, dz \tag{7}$$

$$Q_z(z_i) = 2\pi \int_{r_1}^{r_2} (\bar{u}_z)_{z_i}\, r\, dr \tag{8}$$

Similarly to the pumping flow rate, the circulation flow rate Q_c is in practice determined by the dimensionless circulation flow number [3]:

$$K_c = \frac{Q_c}{nd^3} \tag{9}$$

, which depends only on the impeller's geometry in fully developed turbulent flow. The mentioned geometry strongly corresponds to the structure of flow in the dual mixing vessel and can form one loop circulating along the liquid height or can be composed of a number of interacting loops, figure 4.

In first case, the Q_c flow rate is evaluated according to the equations (6), (7) i (8). However, when the complex structure of the flow is taken into consideration, the Q_c flow rate is the sum of the flow rates evaluated within borders of each of n-loops:

$$Q_c = \sum_{i=1}^{n} Q_{ci} \tag{10}$$

and thus:

$$K_c = \sum_{i=1}^{n} K_{ci} \tag{11}$$

In case of simple flow structure, consisting of the one single circulation loop, there is a lack of additional flows entrained by the impellers' discharge and circling around the local centres. As a result, the flow rate of liquid passing the impellers' region is nearly equal to the flow of liquid in the total volume of vessel. This correspondence was presented for the case of two PBT-6/45° turbines. Figure 5 shows the collected $K_{p\ sum}$ and K_c numbers versus four values of the impeller spacing Δh. The graphs depicted confirm the thesis mentioned above, with exception the spacing $\Delta h = 1.5d$. Probably, it is an evidence for local disturbances in the flow structure, occurring at spacing value 1.5d. The values of the $K_{p\ sum}$ and K_c numbers were confronted in table 4. The last right hand column includes proportional ratio of the K_c to $K_{p\ sum}$.

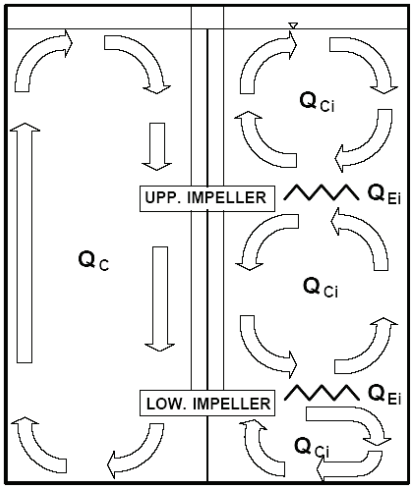

Figure 4. The liquid flow structure in the dual mixing vessel. Left hand side: one loop circulating along the liquid height. Right hand side: the case of several loops.

If the flow structure consists of two or more loops, the local disturbances cause dynamic increase of the liquid flow rate in the vessel related to the flow rate through the impeller region.

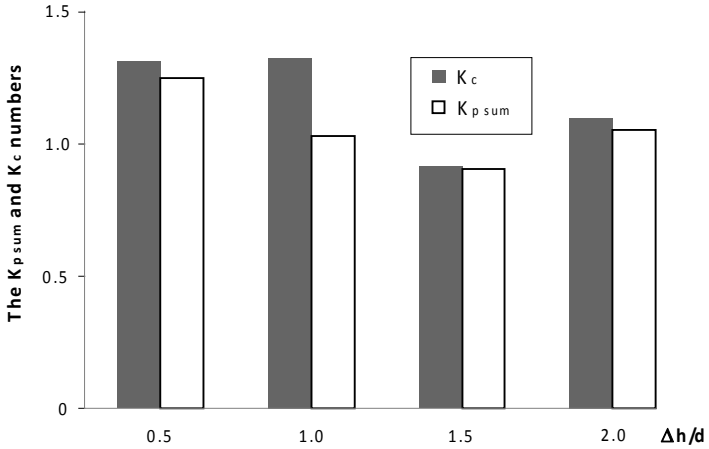

Figure 5. The comparison of the pumping flow number K_p and the circulation flow number K_c, for the dual set of two PBT-6/45° turbines.

T a b l e 4

The confrontation of the K_c and $K_{p\ sum}$ values for the set of two PBT-6/45° turbines.

Δh /d	Kc	$K_{p\ sum}$	$Kc/K_{p\ sum}$, (%)
0.5	1.31	1.25	105 %
1.0	1.33	1.03	129 %
1.5	0.92	0.90	102 %
2.0	1.10	1.05	104 %

It is reflected in the evident increase of the K_c number. The graph on figure 6 presents the impeller capacities expressed by the K_c and $K_{p\ sum}$ numbers, for three selected dual configurations and one constant spacing Δh=1d. For all three cases, the upper impeller was the RT-6 turbine of radial action, while the lower impellers generated typical axial flows in the vessel. The increase of the K_c values related to the $K_{p\ sum}$ is more than doubled and in one case (upper RT-6 and lower PBT-6 turbine) nearly tripled.

Also the impeller spacing Δh cannot be considered as negligible The graph on figure 7 shows variations of the correlation between the K_c and $K_{p\ sum}$ numbers versus impeller spacing Δh, exemplified by the dual set - RT-6 turbine (upper) and hydrofoil Chemineer HE-3. This configuration induced complex flow structure, just like the three sets mentioned above. From this graph it can be concluded that the intensity of induced flows is exceptionally closely related to the geometry of the dual impellers as well as to the vessel itself. At the small spacing Δh, the K_c number exceeds over double the $K_{p\ sum}$.

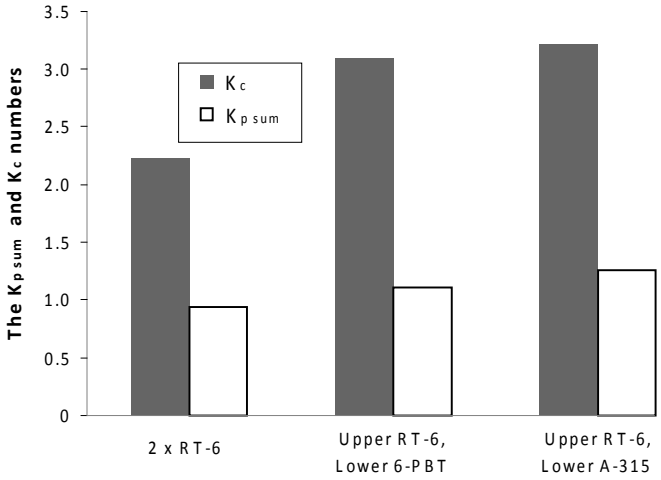

Figure 6. The comparison of the pumping flow number $K_{p\,sum}$ and the circulation flow number K_c, for the three dual sets: a) two RT-6 turbines, b) upper impeller: RT-6 turbine, lower impeller: PBT-6/45° turbine, c) upper impeller: RT-6 turbine, lower impeller: hydrofoil A-315.

As the spacing Δh is enlarged, the quotient of $K_c/ K_{p\,sum}$ increases dynamically, reaching its extrema at $\Delta h=1.5d$. Then, the liquid flow rate in the total vessel exceeds nearly four times the flow rate through the impellers' region. As a result, in the geometrical conditions of the vessel and dual impellers presented above, there are strong liquid flows induced, which circulate outside the impeller regions and reinforce themselves mutually.

5. The inter-stage flow rates Q_E. The CMA model

According to the state of the art, the exchange phenomena of the kinetic energy between respective liquid loops circulating in the vessel occurs as a result of the additional, inter-stage flow rate Q_E, [7,8,9,13]. The flow Q_E is situated at the point of contact of the two neighbouring loops and is thought to be induced by the fluctuation of an axial component of velocity. Similarly to the Q_c and Q_p flow rates, the inter-stage flow rate is expressed in the dimensionless form [7,13]:

$$K_E = \frac{Q_E}{nd^3} \tag{12}$$

If the flow structure in the vessel consists of a number of loops, the total inter-stage flow rate is then the sum of the Q_{Ei} flow rates, existing on the all interaction borders between respective loops. It also can be expressed as by the dimensionless criteria:

$$K_E = \sum_{i=1}^{n} K_{Ei} = \frac{\sum_{i=1}^{n} Q_{Ei}}{n \cdot d^3} \tag{13}$$

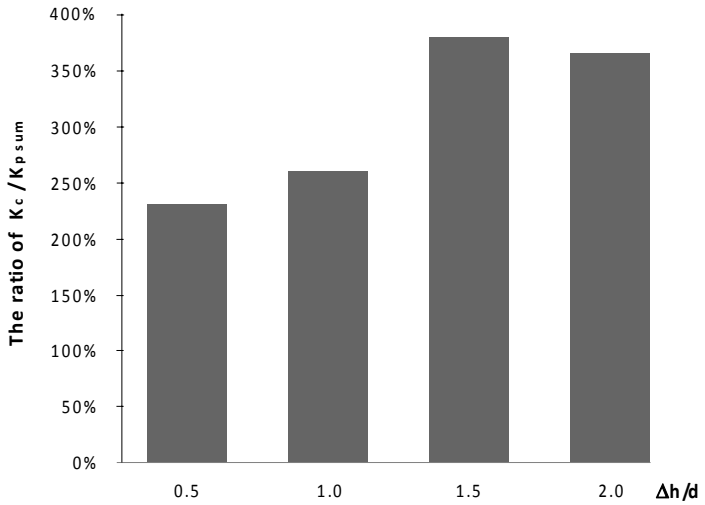

Figure 7. The proportional ratio of K_c / $K_{p\ sum}$ for the dual set: upper impeller: RT-6 turbine, lower impeller: hydrofoil HE-3, versus different values of Δh/d.

The total flow of the liquid in vessel is then caused both by the flows within each loop space, Q_{ci}, and the flows on the border, Q_{Ei}. The correlations between those magnitudes are described by the compartment model (approach), CMA [7,8,13]. The thorough study of the CMA model leads to the conclusion that the real total circulation flow rate Q_c in the dual mixing vessel, considering the equations (6)–(9), should be in fact defined by the corrected formula:

$$Q_{c\ KOR} = \sum_{i} Q_{ci} + \sum_{i} Q_{Ei} \tag{14}$$

and then:

$$K_{c\ KOR} = \sum_{i=1}^{n} K_{ci} + \sum_{i=1}^{n} K_{Ei} = \frac{Q_{c\ KOR}}{n \cdot d^3} \tag{15}$$

The corrected circulation flow rate $Q_{C\ KOR}$, evaluated as shown above, takes the values over $Q_{c,}$ and depends on the geometric parameters of the dual mixing vessel. As a result of the simple flow structure (one loop): $\Sigma Q_{Ei}=0$, and then $Q_{C\ KOR} = Q_c$. When the complex flow structures are taken into consideration, $Q_{C\ KOR} > Q_c$, as was presented in figure 8, exemplified by the two RT-6 turbines. In order to make a comparison, the magnitude of $K_{p\ sum}$ was added to the graph. The numerical values were collected in table 5. The following graph illustrates interchangeably the scale of a phenomenon – the difference between the $K_{C\ KOR}$ and $K_{p\ sum}$. It proofs, in the cases of the complex flow structure and the geometry of impellers, that the real flow rates in the vessel are many times higher than it seemed to result from the study of the pumping capacity exclusively for the impellers.

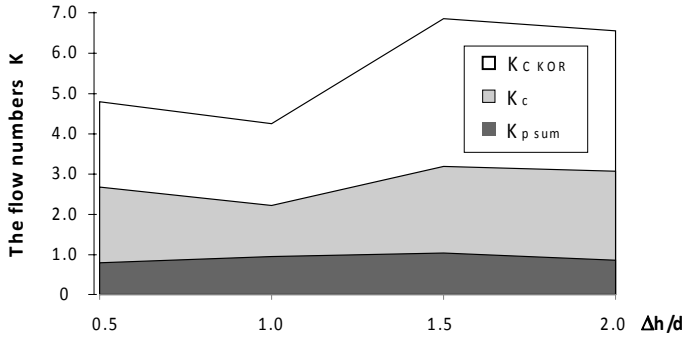

Figure 8. The confrontation of the $K_{p\,sum}$, K_c and $K_{C\,KOR}$ for the set of two RT-6 turbines, versus different values of Δh/d.

T a b l e 5

The confrontation of the $K_{p\,sum}$, K_c and $K_{C\,KOR}$ for the set of two RT-6 turbines.

Δh /d	$K_{p\,sum}$	K_c	$K_{C\,KOR}$
0.5	0.80	2.67	4.78
1.0	0.94	2.23	4.25
1.5	1.03	3.18	6.85
2.0	0.84	3.06	6.53

6. Resumé

The presented study draws attention to the aspect of the liquid flow rates in the dual mixing vessel. The knowledge of the flow structure and the flow rates is the key-issue, influencing the proper design of the vessel, impeller as well as the processes which are going to be conducted. The correct assumption of the flow rates, based on the corrected values of Q_{CKOR} and $K_{C\,KOR}$, assures the correct geometry and dimensions of the device, including the sufficient safety and reserve factor.

The list of more important symbols

D - tank diameter, [m]
d - impeller diameter, [m]
H - liquid height, [m]
Δh - impeller spacing, [m]
K - flow number, general, [-]
K_c - circulation flow number, [-]
$K_{C\,KOR}$ - corrected circulation flow number, [-]
K_E - inter-stage flow number, [-]
K_p - pumping flow number, [-]
$K_{p\,sum}$ - total pumping flow number for dual impeller, [-]
n - rotational speed, [s^{-1}]
Q - flow rate, general, [m^3/s]

Q_c - circulation flow rate, [m^3/s]
$Q_{C\ KOR}$ - corrected circulation flow rate, [m^3/s]
Q_E - inter-stage flow rate, [m^3/s]
Q_p - pumping flow rate, [m^3/s]
$Q_{p\ sum}$ - total pumping flow rate for dual impeller, [m^3/s]
Q_r - maximal flow rate in radial profile, [m^3/s]
Q_z - maximal flow rate in axial profile, [m^3/s]
r - vessel's radius, [m]
$\bar{u}_n$ - mean velocity component, normal to impeller plane, [m/s]
$\bar{u}_r$ - radial component of the mean velocity in vessel, [m/s]
$\bar{u}_z$ - axial component of the mean velocity in vessel, [m/s]
z - vessel's axis, [m]

Literature

[1] Nienow A.W.: Chemical Engineering Science, **52**, (1997), 2557-2565.
[2] Kamieński J.: Mieszanie układów wielofazowych, Wydawnictwa Naukowo-Techniczne, Warszawa 2004.
[3] Jaworski Z., Nienow A.W., Dyster K.W.: Canadian Journal of Chemical Engineering, **74**, (1996), 3-15.
[4] Jaworski Z., Nienow A.W., Koutsakos E., Dyster K.W., Bujalski W.: Trans IChemE, Part A, **69**, (1991), 313-320.
[5] Stręk F.: Mieszanie i mieszalniki, Wydawnictwa Naukowo-Techniczne, Warszawa 1981.
[6] Jaworski Z., Nienow A.W.: Eighth European Conference on Mixing, Cambridge, (1994), N^o 136.
[7] Vrábel P., van der Lans R.G.J.M., Luyben K.Ch.A.M., Boon L., Nienow A.W.: Chemical Engineering Science, **55**, (2000), 5881-5896.
[8] Vasconcelos J.M.T., Alves S.S., Barata J.M.: Chemical Engineering Science, **50**, (1995), 2343-2354.
[9] Duda A., Kamieński J., Talaga J.: Inżynieria i Aparatura Chemiczna, **Nr 2**, (2010), 27-28.
[10] Duda A., Talaga J.: 16th International Conference "Chemical Engineering and Plant Design", Berlin 2006, 159-168.
[11] Duda A., Kamieński J., Talaga J.: Czasopismo Techniczne, **5-M**, (2008), (105), 67-78.
[12] Duda A., Kamieński J., Talaga J.: Czasopismo Techniczne, **2-M**, (2008), (105), 67-74.
[13] Otomo N., Bujalski W., Nienow A.W.: The 1995 IchemE Research Event / First European Conference, (1995), 829-831.

18th International Conference Process Engineering and Chemical Plant Design
Günter Wozny and Łukasz Hady, Editors

R.M. GÜNTHER[*], J.C. SCHÖNEBERGER[**], H. ARELLANO-GARCIA[*],
H. THIELERT[**], G. WOZNY[*]

DESIGN AND MODELLING OF A NEW PERIODICAL STEADY-STATE PROCESS FOR THE OXIDATION OF SULFUR DIOXIDE IN THE CONTEXT OF AN EMISSION FREE SULFURIC ACID PLANT

Abstract

The oxidation of sulfur dioxide over vanadium pentoxide catalysts in a fixed bed represents a basic step in the sulfuric acid production process. In kinetic investigations, an effect in the dynamic operation of the catalyst was observed which leads to much higher reaction rates in a limited time period. The SMP (**S**aturated **M**etal **P**hase) effect can be observed by charging the catalyst with oxygen at the operating temperature and then exposing it to sulfur dioxide. This causes a reaction between the chemisorbt oxygen and the sulfur dioxide. This effect leads to several advantages in the sulfuric acid production process. In addition to a drastical increase in the efficiency of the whole process, possibilities for new process concepts can lead to an emission free sulfuric acid process in the context of coking plant gas treatment. Therefore, a mathematical model is used that can describe the dynamic effects and takes into account the varying active vanadium species. The developed approaches are based on experimental investigations in a miniplant for the oxidation of sulfur dioxide with commercial catalyst pellets.

Keywords: sulfur dioxide oxidation, unsteady state, sulfuric acid production

1. Introduction

Vanadium pentoxide based catalysts for the oxidation of sulfur dioxide to sulfur trioxide are some of the best investigated catalysts in heterogenous catalysis. Due to the fact that sulfuric acid is one of the most important chemicals and the sulfurdioxide oxidation is the basic step of the production process, research on the oxidation catalyst has

[*] Institut of Process Engineering, TU Berlin, Straße des 17. Juni 135, 10623 Berlin, Germany;
[**] Uhde GmbH Dortmund, Friedrich Uhde Straße 15, 44141 Dortmund, Germany;

been conducted for some 40 years [1,3,9,15,16]. Because of the equilibrium limited character of the reaction $SO_2 + ½ O_2 <-> SO_3$ it is imposible to reduce the SO_2 emissions down to zero at standard operating temperatures [9]. There have been great efforts to shift the equilibrium to the product side. On the one hand, there are air quenches or gas heat exchangers to reduce the reaction temperature of the higly exothermic reaction and increase the oxygen concentration between the reactor beds. Therefore, new vanadium based catalysts were invented to work in lower reaction temperatures down to 390°C with acceptable reaction rates. On the other hand, intermediate absorptions of SO_3 are installed to remove the product between the reactor beds.

Investigations about the dynamic behavior of the reaction by Boreskov and Matros [6] observed a change of the catalyst structure depending on the exposed gas mixture. Also, several authors observed different behavior of the reaction between dynamic and steady state operation [2,5-8,9,11-14,21-23]. In experimental kinetic studies, Schöneberger [17] observed a peak of the reaction rate if the catalyst is first exposed to oxygen and then to reaction mixture that contained oxygen and sulfur dioxide. A reaction network that describes the whole catalytic cycle can explain this behavior [2]. The usage of the additional dimension of time gives the possibility to achieve a super-equilibrium [10] which is limited by the equilibrium of one specific partial reaction in the catalytic cycle.

In the context of coking plant gas treatment, a new sulfuric acid process concept without any emissions is proposed. In this process, the sulfur dioxide in the sulfuric acid plant rest gas is hydrogenated to hydrogen sulfide and then recycled in the coking plant gas treatment. The usage of a transient working oxidation is a promising process alternative to meet the restrictions of sulfur dioxide and oxygen content in the hydrogenation reactor and the recycle gas.

2. Emission free sulfuric acid process

The sulfuric acid process in the context of coking plant conditions consists of three basic process steps. The H_2S containing feed gas stream is oxidized in a combustion unit to SO_2 under excess air conditions to decrease temperature and minimize NOx formation. In a second step, the SO_2 is oxidized to SO_3 over a vanadium pentoxide (V_2O_5) catalyst in a strongly exothermic reaction. The fixed bed reactor is divided into 4 or 5 beds and in each bed a defined temperature is set to maximize conversion. The temperature adjustment is realized with air quenches which, in addition to the temperature decrease, also lead to high oxygen content in the process gas. The last bed typically has the lowest temperature of all reactor beds to shift the reaction equilibrium to the product side and minimize the SO_2 content in the process gas stream. After the contact reactor, the gas passes through a sulfuric acid absorber, where the SO_3 is absorbed with water and converted to sulfuric acid. To prevent sulfuric acid mist, wire mesh filters are installed. After this last process step, the restgas is released out of a stack to the environment.

Due to the fact that the SO_2 oxidation is an equilibrium reaction, there are always SO_2 emissions. To prevent these emissions, a new process concept is recommended that recycles the sulfuric acid plant restgas back to the coking plant gas treatment. Thus, the SO_2 emissions can be reduced down to zero. A very low SO_2 and O_2 content is required to feed a gas stream into the coking plant gas treatment. These requirements are only met if the SO_2 content is reduced, for example, by the hydrogenation of SO_2 to H_2S

($3H_2+SO_2<->H_2S+2H_2O$) in an exothermal reaction with the equilibrium far to the product side. Therefore, a fixed bed with hydrogenation catalyst has to be installed behind the sulfuric acid absorber. To meet the requirements of the hydrogenation unit there has to be an oxygen content of less than x_{O2}=0.5 mol%. A transient working reactor using SMP could be used instead of the steady state contact reactor. The transient working reactor consists of

two fixed beds fed cyclically with oxygen and sulfur dioxide. SO_2 oxidation with a nearly oxygen free reactor outlet stream is possible with the temporarily shifted oxygen charging of the catalyst. In the oxygen charging step, an oxygen reduced stream can be used for combustion to reduce temperature and limit NOx production.

Figure 1 compares the process concepts of a conventional and an emission free sulfuric acid plant.

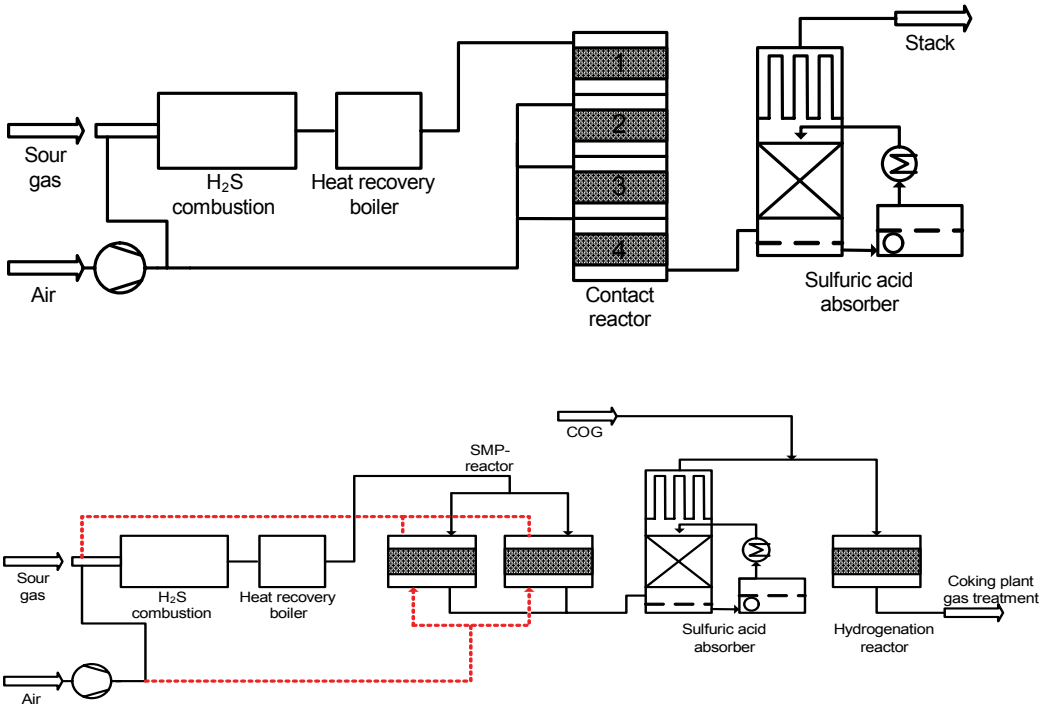

Fig. 1. Sulfuric acid plant and emission free sulfuric acid plant with SMP (**S**aturated **M**etal **P**hase)

3. Kinetic, model and numerical methods

For the simulation of the SMP process, the model needs to represent the dynamic behavior of the reaction. A model based on the overall reaction of the SO_2 oxidation (SO_2 + ½ O_2 <-> SO_3) does not consider the intermediate forms of the vanadium catalyst. The SO_2 oxidation takes place in a liquid metal phase [5] with the active species. Hence, besides mass transfer over the phase border, the reactions inside the metal phase have to be taken into account. Balzhinimaev [5] postulates the catalytic cycle (Eq. 1, 2, 3, 5) with vanadium intermediates as follows:

$$V_2^{5+}O_2^{2-} + SO_2 \leftrightarrow V_2^{5+}O^{2-} + SO_3 \qquad \Delta_R^h = 42\ kJ/mol \tag{1}$$

$$V_2^{5+}O^{2-} + SO_2 \leftrightarrow V_2^{5+}SO_3^{2-} \qquad \Delta_R^h = 80\ kJ/mol \tag{2}$$

$$V_2^{5+}SO_3^{2-} + O_2 \leftrightarrow V_2^{5+}O_2^{2-} + SO_3 \qquad \Delta_R^h = 63\ kJ/mol \tag{3}$$

$$2SO_2 + O_2 \leftrightarrow 2SO_3 \tag{4}$$

$$V_2^{5+}SO_3^{2-} \leftrightarrow V_2^{4+} + SO_3 \qquad \Delta_R^h = -42\ kJ/mol \tag{5}$$

The capacity for the absorption of SO_2, O_2 and SO_3 in the melt is described by Henry's Law because of the high adsorption velocity. The reaction rates are described by the mass action law recommended by Bunimovich [8].

The reactor model is realized as a heterogeneous and transient process model of a fixed bed reactor, which considers the gas phase and the catalyst phase separately. This modeling approach is necessary to display the components of the mobile phase (SO_2, O_2, SO_3) and of the immobile phase (SO_2, O_2, SO_3, $V_2^{5+}SO_3^{2-}$, $V_2^{5+}O_2^{2-}$, V_2^{4+}, $V_2^{5+}O^{2-}$).

Furthermore, it makes sense for dynamic simulation to consider the delaying effects of the interphase mass and energy transfer. According to changes in the steady state solution, they have great impact on the dynamic solution. The following assumptions were made:

1)No axial heat conduction of the catalyst phase
2)Plug flow. No radial heat or mass transport
3)No heat conductivity between catalyst and the wall (for calculation of heat losses)
4)No temperature dependence of the heat and mass transfer coefficients
5)No temperature and concentration gradients in the catalyst pellet
6)Reaction only in the catalyst phase

With the given assumptions, the partial differential equation system displayed in Eq. 6 – 10 results. It consists of an energy balance for the gas phase with a convective term for the gas flow, a heat transfer term between the phases and a heat transfer term that shows the heat losses to the environment.

$$\sum_{i=1}^{3} c_i \left(c_{p,i} - R\right)\frac{dT_g}{dt} = a\frac{1-\varepsilon}{\varepsilon}\alpha\left(T_k - T_g\right) - \frac{\dot{m}}{A\rho\varepsilon}\sum_{i=1}^{3} c_i c_{p,i}\frac{\partial T_g}{\partial z} - k_{RW}\frac{4}{D_r}\left(T_g - T_{RW}\right) \tag{6}$$

Additionally there is a mass balance for the gas phase, which has a term for axial dispersion, a convective mass transport term through the reactor and a term for interphase mass transfer.

$$\frac{dc_{g,i}}{dt} = D_{ax,i}\frac{\partial^2 c_{g,i}}{\partial z^2} - \frac{\dot{m}}{A\rho\varepsilon}\frac{\partial c_{g,i}}{\partial z} - a\beta\left(c_{k,i} - c_{g,i}\right) \tag{7}$$

The energy balance contains one term for the heat transfer between the phases and one term for the heat resulting from the sulfur trioxide absorption.

$$(1-\varepsilon)\rho_k c_{p,k}\frac{dT_k}{dt} = a\alpha\left(T_g - T_k\right) - C_V\varepsilon_L\sum_{i=1}^{4}\Delta h_R\dot{r}_i - \varepsilon_L Q_D\frac{\partial c_3^L}{\partial t} \tag{8}$$

The component balance of the catalyst (melt) contains the reaction term and the interphase mass transfer.

$$\varepsilon_L\frac{dc_i^L}{dt} = \varepsilon_L C_V\sum_{j=1}^{4}\nu_{i,j}\dot{r}_j + a\beta\left(c_{g,i} - c_{k,i}\right) \tag{9}$$

The component balance for the immobile components in the catalyst consider only the reaction term because the components stay in the melt and simply change from one species to another.

$$\frac{d\mu_m}{dt} = \sum_{j=1}^{4}\overline{\nu}_{m,j}\dot{r}_j \tag{10}$$

For the boundary and initial conditions

$$t=0:\quad c_i^L = c_{i,0}^L(z) \qquad z=0:\quad c_i = c_{i,in} \tag{11)(12}$$

$$c_i = c_{i,0} \qquad T_g = T_{g,in} \tag{13)(14}$$

$$\mu_m = \mu_{m,0}(z) \tag{15}$$

$$T_g = T_{g,0}(z) \tag{16}$$

$$T_k = T_{k,0}(z) \tag{17}$$

were implemented.

The parameters assumed by Balzhinimaev et al [5] could not be used because of working with real catalyst and not powdered catalyst like in common kinetic investigation. Transport limitations and modified catalyst compositions were assumed. Also different experimental conditions could lead to the deviation. The kinetic parameters are estimated with the measurement data from the miniplant as per description in [18]. This leads to results which can be used for simulations of industrial processes. The effort has to be made for each catalyst which is used for dynamic processes if reliable predictions shall be achieved.

For the numerical calculation the system is discretized with finite differences along the spatial coordinate. This discretization method has to be used because of the steep gradients in time and along the reactor. A discretization method like, the orthogonal collocation [4, 18], could not be used because of the affinity of the solution to oszillate. The temporal coordinate is solved by a multistep solver using Backward Differential Formulas (BDF). Because of the finite differences discretization in space the jacobian matrix is very sparse and has a bandstructur. Therefore the ODE solver works with a sparse jacobian matrix which makes it much more efficient.

3. Experimental setup

The experimental setup is a fixed bed reactor which can be used for the investigation of a variety of commercial catalyst pellets. It contains a gas mix section, a heating section and the reactor with several measurement points. It is displayed in Figure 2.

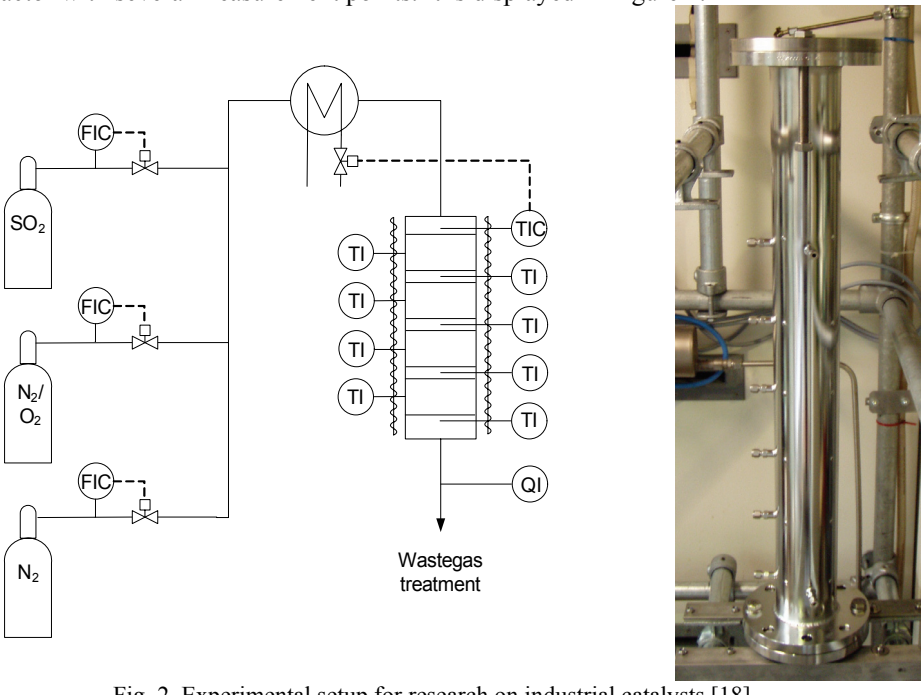

Fig. 2. Experimental setup for research on industrial catalysts [18]

The waste gas treatment is not shown in Figure 2. It contains a scrubber to remove SO_3 and SO_2 before process gas is released into the environment. The wall temperatures of the reactor are measured to quantify heat loss and the reactor has a heated jacket to reduce heat loss. The temperature measurement inside of the reactor show the temperature profile in the reactor and the quality indicator at the end of the reactor measures the oxygen content of the process gas.

4. Results and discussion

Figure 3 shows the comparison between the temperature measurement behind each reactor bed and the simulation results of the reactor. Each reactor bed has the same height so measurement points are equidistant distributed along the reactor. Figure 4 shows the relation of the temperature over reactor length from the simulation of the same experiment.

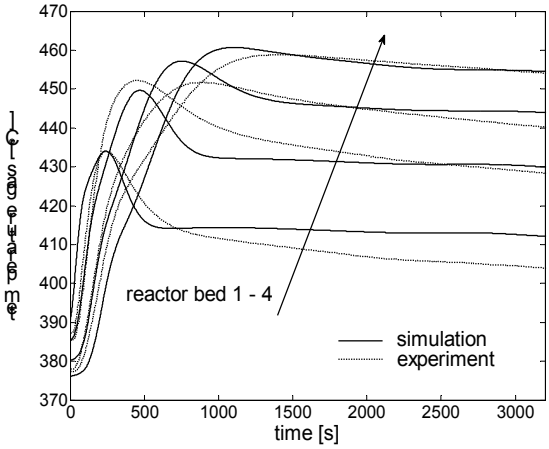

Fig. 3. Temperatures at four equidistant points in the reactor and simulation results of the model

Till t=0 the catalyst is heated with air to operating temperature and the heat loss leads to a decreasing temperature along the reactor. At t>=0 reaction mixture of SO_2, O_2 and inert gas N_2 is fed into the reactor. The reaction starts and high temperature gradients appear which lead to a strong increase in temperature along the reactor. At t=3000s a steady state has been established. During the accelerated reaction rate most of the SO_2 is converted to SO_3 so that a nearly SO_2 free reactor outlet stream can be achieved [23] which is in line with the simulation results in Figure 5.

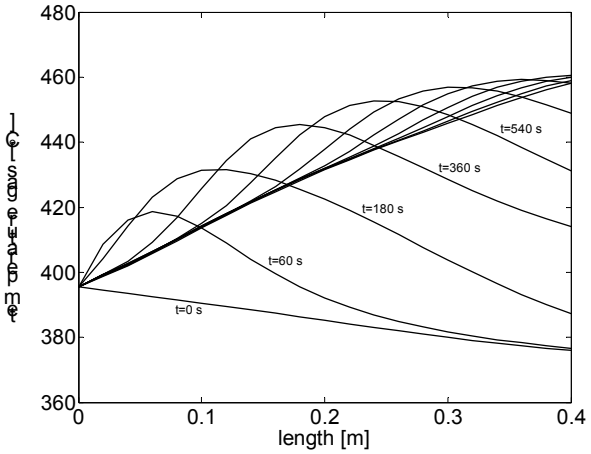

Fig. 4. Simulation results of the temperature profiles along the reactor

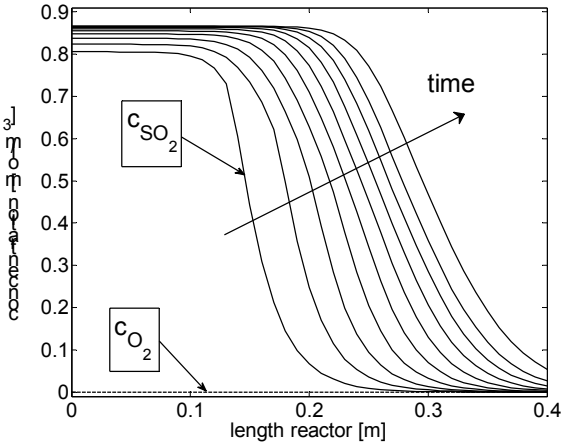

Fig. 5: SO_2 and O_2 along the reactor. Cyclic operation.

Considering that the SO_2 oxidation is an equilibrium limited reaction this is a great increase in efficiency.

If this effect is used in the proposed emission free sulfuric acid plant the SO_2 conversion is less important compared with the O_2 concentration in the off gas stream. In order to reach the required SO_2 concentrations together with the maximal allowed O_2 the amount of

catalyst required must be increased approximately by a factor of five if the conventional steady state process is choosen [18, 20].

Figure 5 shows simulation results with an oxygen free reactor inlet stream. Over time the SO_2 front shifts through the reactor until it reaches the reactor outlet. This is the point

where the reactor switch could take place. The oxygen amount at the reactor outlet is close to zero, because no oxygen is fed into the reactor. However, some oxygen might be generated in the gas phase by the reverse of reaction (Eq. 4). The fact that the oxygen is fed temporarily decoupled into reactor realizes this operation.

Figure 6 shows the distribution of the vanadium intermediates along the reactor in a periodical operated regime. In the adsorption half cycle the oxygen chemisorbs on $V_2^{5+}SO_3^{2-}$ and builds a reservoir of $V_2^{5+}O_2^{2-}$. Thus, the in the steady state process rate limiting step of the catalytic cycle is finished and the oxygen enriched vanadium intermediate is available for the much faster step of SO_2 conversion.

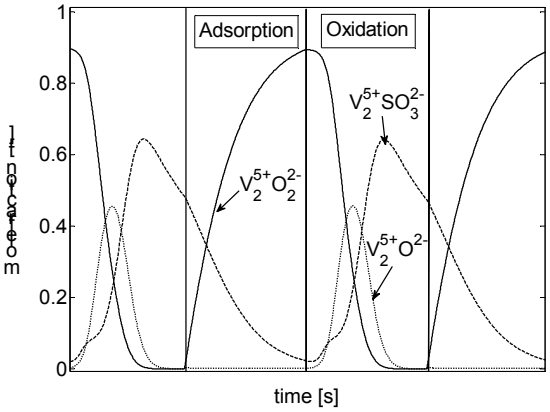

Fig. 6: Vanadium intermediates along the reactor. Periodical operation.

In the oxidation half cycle the vanadium species $V_2^{5+}O^{2-}$ and $V_2^{5+}SO_3^{2-}$ were produced sequentially in the reactions (Eq. 1) and (Eq. 2), each with one SO_2 molecule. When the oxygen carrier $V_2^{5+}O_2^{2-}$ is completely consumed the oxidation from SO_2 to SO_3 stops and the catalyst has to be recharged with oxygen.

5. Conclusions

A new process concept is shown, that can realize an emission free sulfuric acid plant in the context of coking plant wastegas treatment. With the use of this concept requirements of the sulfuric acid plant tailgas recycle in the coke oven gas are met. Moreover the efficiency of a sulfuric acid plant can be considerably increased. On one hand a smaller contact reactor can be built which leads to lower investment costs. On the other hand smaller downstream units can also be realized because of a decreased process gas stream. With the use of heat integration the efficiency could be further increased. With the oxygen reduced process gas stream an advantageous operation of the combustion is possible because of lower combustion temperatures which leads to lower NOx production. The process displayed in Figure 1 can be realized at new sulfuric acid plants in coking plant gas treatment. There is also the possibility to upgrade an existing sulfuric acid plant by

changing the operating conditions of the contact reactor an add as a last contact unit an SMP based reactor to realize a higher SO_2 conversion and remove oxygen from the process gas stream. If the process is used in the context of coking plant gas treatment the last process step is a hydrogenation unit that has to be installed to meet the reqirements for the recycle into the cokeoven gas treatment.

6. Acknowledgement

The present work was supported by the Max-Buchner-Reserch Foundation.

Symbols

A	Cross section area	m²
a	Catalyst solid surface	1/m
C_V	Total vanadium concentration	mol/m³
c_i	Concentration gasphase component i	mol/m³
c_i^L	Concentration melt component i	mol/m³
c_i^k	Concentration catalyst component i	mol/m³
$c_{p,i}$	Heat capacity gas component i	kJ/(kg K)
$c_{p,k}$	Heat capacity catalyst	kJ/(kg K)
$D_{ax,i}$	Axial dispersion coefficient	m²/s
D_r	Radius reactor	m
$\Delta h_{R,i}$	Heat of reaction	kJ/mol
k_{RW}	Thermal transmission coefficient	W/(K m²)
$\dot{m}$	Mass flow	kg/s
Q_D	Heat of SO_3 dissolution	J/mol
R	Gas constant	J/(mol K)
$\dot{r}_j$	Reaction rate	mol/(s kg_{cat})
T_k	Temperature catalyst	°C
T_g	Temperature gas	°C
T_W	Temperature wall	°C
t	Time	s
z	Length reactor	m
α	Heat transfer coefficient	W/(m² K)

β	Mass transfer coefficient	m/s
ε	Void fraction	-
ε_L	Void fraction liquid metal	-
$\mu_{m,i}$	Concentration vanadium species	-
ν_j	Stoichiometric coefficient	-
$\overline{\nu}_j$	Stoichiometric coefficient	-
ρ_k	Density of the catalyst	kg/m³
ρ	Density of the gas	kg/m³

Literature

book:
[1] Bartholomew C.H., Farrauto R.J.: Fundamentals of Industrial Catalytic Processes, Wiley-AIChE, 2 edition, 2005.
[2] Bunimovich G.A, Strots V.O., Goldman O.V.: Theory and industrial application of SO_2 oxidation reverse process for sulfuric acid production, Unsteady state process in catalysis, VNU Science Press, (1990), 7-24
[3] Näumann F., Schulz M.: Oxidation of sulfur dioxide, Handbook of heterogeneous catalysis, (2008), 2623-2635
[4] Finlayson, Bruce A.: Nonlinear analysis in chemical engineering, McGraw-Hill, New York, (1980), ISBN 0070209154

paper:
[5] Balzhinimaev B.S., Ivanov A.A., Lapina O.B., Mastikhin V.M., Zamaraev K.I.: Mechanism of sulfur dioxide oxidation over supported vanadium catalysts, Faraday Discuss. Chem. Soc., **87**, (1989), 133-147
[6] Boreskov G.K., Matros Yu.Sh.: Unsteady-state performance of heterogeneous catalytic reactions, Catalysis Reviews-Science and Engineering, **25**, (1983), 551-590
[7] Briggs J.P., Hudgins R.R., Silveston P.L.: Composition cycling of an SO_2 oxidation reactor, Chemical Engineering Science, **32**, (1977), 1087-1092
[8] Bunimovich G.A., Vernikovskaya N.V., Strots V.O., Balzhinimaev B.S.: SO_2 oxidation in a reverse- flow reactor: influence of a vanadium catalyst dynamic properties, Chemical Engineering Science, **50**, (1995), 565-580
[9] Dunn J.P., Stenger H.G., Wachs I.E.: Oxidation of sulfur dioxide over supported vanadia catalysts: molecular structure - reactivity relationships and reaction kinetics, Catalysis Today, **51**, (1999), 301-318
[10] Goldman, O.V., Bunimovich, G.A., Zagoruiko, A.N., Lakhmostov, V.S., Vernikovskaya, N.V., Noskov, A.S., Kostenko, O. V.: Sulphur dioxide oxidation method. RF Patent 2085481, C01B17/76, B, (1997), N21.
[11] Gosiewski K.: Dynamic modelling of industrial SO_2 oxidation reactors. Part II. Model of a reverse-flow reactor, Chemical Engineering and Processing, **32**, (1993), 233-244

[12] Holroyd F.P.B., Kenney C.N.: Sulphur dioxide oxidation kinetics: the absorption of oxygen in V_2O_5-potassium pyrosulphate melts, Chemical Engineering Science, **26**, (1971), 1971-1975
[13] Hong R., Li X., Li H., Yuan W.: Modeling and simulation of SO_2 oxidation in a fixed-bed reactor with periodic flow reversal, Catalysis Today, **38**, (1997), 47-58
[14] Ivanov A.A., Balzhinimaev B.S.: New data on kinetics and reaction mechanism for SO_2 oxidation over vanadium catalysts, React. Kinet. Catal. Lett., **35**, (1987), 413-424
[15] Mars P., Maessen J.G.H.: The mechanism and the kinetics of sulfur dioxide on catalysts containing vanadium and alkali oxides, Journal of Catalysis, **10**, (1968), 1-12
[16] Mezaki R., Kadlec B.: Remarks on the reduction-oxidation mechanism of sulfur dioxide on vanadium catalyst, Journal of Catalysis, **25**, 1972, 454-459
[17] Oruzheinikov A.I., Chumachenko V.A., Matros Yu.Sh.: Analysis of a nonsteady-state kinetic model for SO_2 oxidation, Reaction Kinetics and Catalysis Letters, **21**, 97-102
[18] Schöneberger J.C.: Entwicklung und Analyse katalytischer Abgasbehandlungs-prozesse am Beispiel der emissionsfreien Schwefelsäureanlage, Shaker Verlag Aachen, (2010)
[19] Schöneberger J.C., Arellano-Garcia H., Thielert H., Wozny G.: Identification of reaction mechanism with a dynamic PFR model, Advanced Control of Chemical Processes, **7**, (2009)
[20] Schöneberger J.C., Arellano-Garcia H., Thielert H., Wozny G.: Ein systematischer Ansatz zur Entwicklung und Analyse verfahrenstechnischer Prozesse am Beispiel einer Kohlenwertstoffanlage, Vortrag auf dem Jahrestreffen der Dechema Fachgemeinschaft Prozess-, Apparate- und Anlagentechnik (2009)
[21] Silveston P.L., Hudgins R.R., Bogdashev S., Vernikovskaya N.V., Matros Yu.Sh.: Modelling of a periodically operating packed-bed SO_2 oxidation reactor at high conversion, Cemical Engineering Science, **49**, (1994), 335-341
[22] Snyder J.D., Subramaniam B.: Numerical simulation of a periodic flow reversal reactor for sulfur dioxide oxidation, Chemical Engineering Science, **48**, (1993), 4051-4046
[23] Vernikovskaya N.V., Zagoruiko A.N., Noskov A.S.: SO_2 oxidation method. Mathematical modeling taking into account dynamic properties of the catalyst, Chemical Engineering Science, **54**, (1999), 4475-4482

18th International Conference Process Engineering and Chemical Plant Design
Günter Wozny and Łukasz Hady, Editors

JANUSZ MAGIERA*

ENERGIE – REALE MÖGLICHKEITEN ZUR GEWINNUNG SAUBERER ENERGIE FÜR WOHNHÄUSER

Allgemein

Der Beitrag stellt die derzeitige Struktur der Energienachfrage im Maßstab der Welt und der Länder der EU dar. Die Struktur der erzeugten und verbrauchten Energie in Polen und Deutschland wurde detailliert erklärt. Es wurden Hybridsysteme zur Wärmeerzeugung durch erneuerbare Energien gezeigt, die im Versuch in einer Produktionsanlage in Südpolen laufen. Es wurde ein neues Steuerungs-und Energiebilanzierungssystem vorgestellt, das auch online arbeiten kann.

Schlüsselwörter: Primärenergie, Solarenergie, Solarkollektor, Hybridanlage, Steuerungssystem

Energie wird immer knapper und immer teurer und damit gleichzeitig das kostbarste Allgemeingut für den statistischen Einwohner der Erde. Es gibt Schätzungen, die auf den letzten Konferenzen der UNESCO präsentiert wurden, dass die Preise für Energie und sauberes Wasser in diesem Jahrhundert am schnellsten von allen Gütern wachsen werden. Am Anfang des zwanzigsten Jahrhundert betrug die Bevölkerung der Erde rund 1,7 Milliarden Menschen. Bis zum Ende des Jahrhunderts im Jahr 2000 überschritt die Bevölkerung 6,0 Mrd. Das bedeutet einen 3,2-fachen Bevölkerungsanstieg. Gleichzeitig stieg der Energieverbrauch auf der Erde um mehr als das17-fache [1]. Es gibt Schätzungen, dass im letzten Jahrhundert, mehr Energie auf der Erde hergestellt und verwendet wurde als in der gesamten Dauer des menschlichen Lebens auf der Erde [2]. Derzeit ist die Wachstumsrate des Energieverbrauchs nicht so hoch wie im vergangenen Jahrhundert, aber der Verbrauch wächst weiter. Traditionelle Energieträger wie Kohle, Erdöl oder Erdgas werden in absehbarer Zeit erschöpft sein. Ihre derzeitige Nutzung ist mit erheblichen negativen Auswirkungen auf die Umwelt durch die Emission von CO2, SO2, NOx-und Partikelemissionen verbunden. Daher sucht man intensiv neue, saubere Energiequellen, möglichst ohne negative Umweltauswirkungen.

Obwohl Kernkraftwerke, per Saldo, als relativ "sauber" betrachtet werden, sind sie wegen der ungelösten Probleme der Endlagerung radioaktiver Abfälle noch immer nicht völlig akzeptabel. Man erinnert sich noch an die Reaktorkatastrophe von Tschernobyl in

* Technische Universität Krakau, 31-155 Krakau, Polen

der Ukraine, sowie die neuesten Ereignisse im März 2011 in Japan. Daher sucht man intensiv, sowohl in der Welt als auch in Europa nach neuen, sauberen Energiequellen, die die erneuerbaren Energien (RES), umfassen.

Derzeit überwiegen traditionelle Energiequellen in Form von Brennstoffen in der Struktur der Energieversorgung der Welt, wie in Abbildung 1 dargestellt.

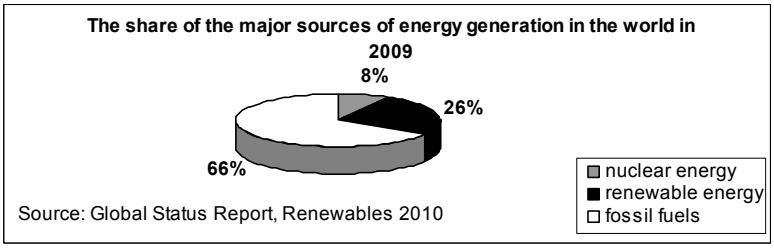

Abb.1. Anteil der wichtigsten Quellen der Primärenergieerzeugung in der Welt

Aus Abbildung Nr. 1 kann man erkennen, dass in der Welt die fossilen Brennstoffe noch etwa 66% der Primärenergie betragen. Eine interessante Information ist, dass der Anteil erneuerbarer Energien am Gesamtenergieverbrauch 26% beträgt. Das ist relativ viel, aber der größte Teil davon wird als Biomasse in Verbrennungsprozessen verwendet. Die größten Energieverbraucher der Welt im Jahr 2009 waren China und die USA, wie in Abb.2 dargestellt.

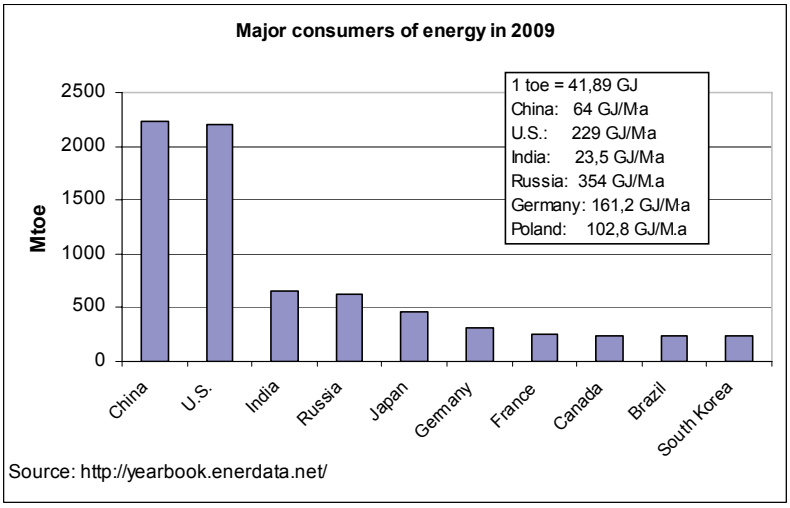

Abb.2. Die größten Energieverbraucher im Jahr 2009

Es ist erwähnenswert, dass der Verbrauch pro Person und Jahr sehr unterschiedlich ist, wie in der nächsten Abbildung angezeigt. Die Struktur des Energieverbrauchs in den Industrieländern ist etwa so, dass ca. 30% im Verkehr, etwa 30% in der Industrie und die restlichen 40% in Haushalten, Dienstleistungen, Landwirtschaft und anderen Bereichen anfallen.

Abb.3 zeigt den jährlichen Energieverbrauch in den 27 Ländern der Europäischen Union (EU) nach Bereichen. Im Jahr 2007 entfällt 32,6% der Energie der EU-Länder auf

den Verkehr, 27,9% auf die Industrie, 24,6% auf die Haushalte und 15% auf andere Bereiche.

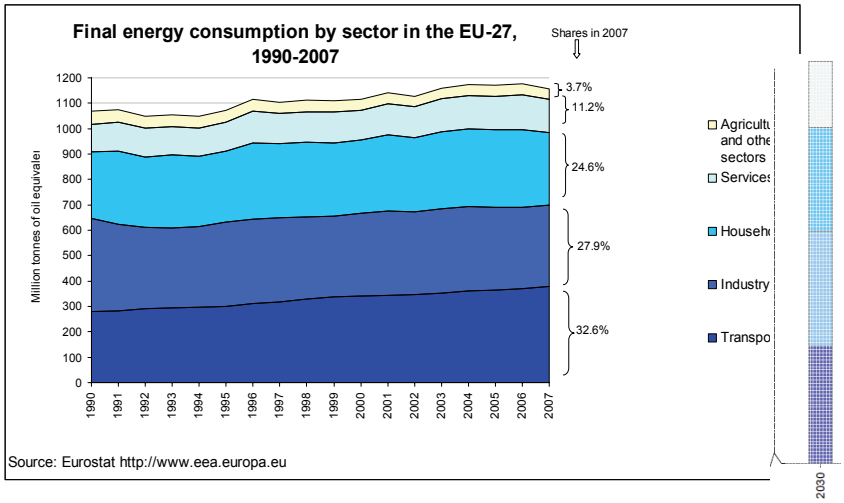

Abb.3. Der jährliche Energieverbrauch in der EU-27 nach Bereichen

Die bequemste Energieform im Einsatz (außer im Bereich des Verkehrs) ist die Elektroenergie, obwohl ihre Kosten die höchsten im Vergleich zu anderen Energieformen auf dem Markt sind. Abb.4 zeigt die Energiepreise für die Haushalte in den 22 Ländern der Europäischen Union und Abbildung 5 die geltenden Preise in der Industrie, ohne Steuer, in diesen Ländern.

Die Analyse dieser Daten zeigt, dass im Jahr 2010 die niedrigsten Strompreise, ohne Steuern, bei Haushalten in den 10 neuen EU-Ländern, die der EU am 01.05.2004 beigetreten sind, existierten. Die höchsten Preise wurden in Ländern wie Belgien, Irland, Zypern und Luxemburg erreicht.

In der Industrie hingegen sind die Preise am höchsten in Ländern wie Irland, Spanien, Zypern und in der Slowakei.

Für Endverbraucher werden die Strompreise inklusive Steuer interessant sein. Tabelle 1 zeigt dies. Die niedrigsten Preise für Strom findet man zurzeit in Bulgarien und Litauen. Die höchsten Preise für den Endverbraucher gibt es in Ländern wie Dänemark und Deutschland.

Tabelle 2 zeigt die Struktur der Primärenergie in zwei Ländern: in Deutschland und in Polen, sowie die Menge der erzeugten Energie unter Berücksichtigung seiner Quellen und der Bevölkerungszahl in diesen Ländern im Jahr 2010.

Tabelle 3 hingegen zeigt, wie viel Energie aus erneuerbaren Energiequellen in diesen Ländern erzeugt wird.

Aus Tabelle 2 und Tabelle 3 kann man erkennen, dass Deutschland eindeutig der Spitzenreiter beim Einsatz erneuerbarer Energiequellen ist. Es ist bekannt, dass

Deutschland, insbesondere bei der Nutzung von Wind- und Solarenergie, nicht nur in Europa führend ist, sondern auch eine führende Rolle im Weltmaßstab einnimmt.

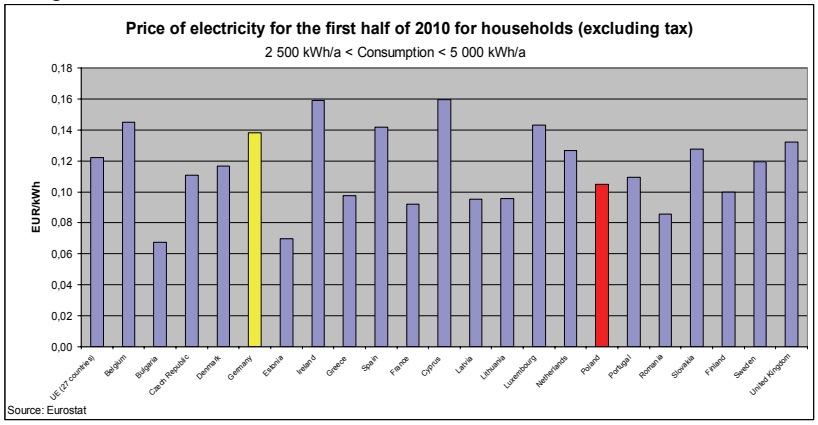

Abb.4. Die Strompreise für Haushalte in den EU-Ländern

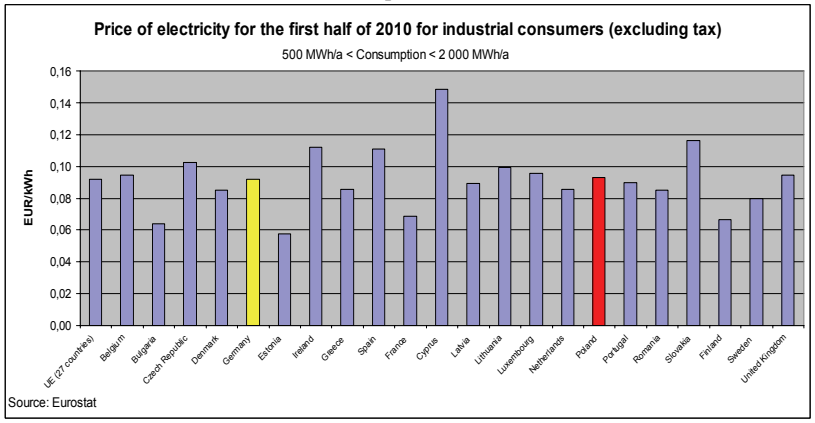

Abb.5. Die Strompreise für die Industrie in den EU-Ländern

Tabelle 1

Strompreise in der EU für Haushalte inklusive Steuer in € / kWh 2009

– ELECTRICITY RATES FOR HOUSEHOLDS– Average amount in euro per one kilowatt-hour of electricity for domestic consumers. Incl. energy taxes & VAT.			
Prices based on consumption of 3,500 kWh/year (30% during nighttime) Effective: September '10		Prices based on consumption of 7,500 kWh/year (30% during nighttime) Effective: September '10	
Austria	€ 0.1937	Austria	€ 0.1769
Belgium	€ 0.1896	Belgium	€ 0.1708
Bulgaria	€ 0.0865	Bulgaria	€ 0.0834
Cyprus	€ 0.1666	Cyprus	€ 0.1668
Czech Republic	€ 0.1455	Czech Republic	€ 0.1189
Denmark	€ 0.2462	Denmark	€ 0.2216
Estonia	€ 0.0928	Estonia	€ 0.0899
Finland	€ 0.1287	Finland	€ 0.1141
France	€ 0.1215	France	€ 0.1099
Germany	€ 0.2282	Germany	€ 0.2143
Greece	€ 0.1061	Greece	€ 0.1078
Hungary	€ 0.1697	Hungary	€ 0.1541
Ireland	€ 0.1714	Ireland	€ 0.1646
Italy	€ 0.1946	Italy	€ 0.2616
Latvia	€ 0.1089	Latvia	€ 0.1054
Lithuania	€ 0.0953	Lithuania	€ 0.0867
Luxembourg	€ 0.1852	Luxembourg	€ 0.1688
Malta	€ 0.1471	Malta	€ 0.1430
Netherlands	€ 0.1735	Netherlands	€ 0.2226
Poland	€ 0.1357	Poland	€ 0.1264
Portugal	€ 0.1668	Portugal	€ 0.1452
Romania	€ 0.1027	Romania	€ 0.0953
Slovakia	€ 0.1566	Slovakia	€ 0.1608
Slovenia	€ 0.1324	Slovenia	€ 0.1158
Spain	€ 0.1720	Spain	€ 0.1565
Sweden	€ 0.1450	Sweden	€ 0.1482
United Kingdom	€ 0.1347	United Kingdom	€ 0.1179

[Europe's Energy Portal http://www.energy.eu/#Domestic]

Tabelle 2

Primärenergie für Deutschland und Polen im Jahr 2008 und Bevölkerungszahl in diesen Ländern im Jahr 2010

ENERGY		
[ktoe]	POLEN	DEUTSCHLAND
Steinkohle und Braunkohle	6 036	50 040
Rohöl	762	3 087
Erdgas	3 690	11 314
Nukleare Energie	0	38 305
RES	5 457	29 744
GESAMT	15 945	132 490
Bevölkerung im Jahr 2010	38 186 860	81 742 000

Tabelle 3

Erneuerbare Energien in Deutschland und Polen

[ktoe]	POLEN	DEUTSCHLAND

Solarenergie	1	735
Biomasse	5186	23473
Geothermie	13	246
Wasserkraft	185	1801
Windenergie	72	3489
Source: Eurostat 2011		

Bei der Gewinnung erneuerbarer Energien schneidet Polen schlechter ab, als andere Länder der Europäischen Union, vor allem der Länder Westeuropas. Erst in den letzten Jahren erfolgte in dieser Hinsicht ein deutlicheres Handeln. Zur Erfüllung der im EU-Beitrittsvertrag unterzeichneten Verpflichtungen sollte in diese Maßnahmen wesentlich mehr investiert werden.

Die zuvor diskutierten Faktoren und das Bewusstsein, dass die Energie im Laufe des Jahrhunderts die größte Wachstumsdynamik zeigen wird, ermutigt uns zum Handeln sowie zum Entwerfen und Aufbauen von Anlagen zur Wärmeenergiegewinnung auf Grundlage der Nutzung erneuerbarer Energieträger. Eine dieser Anlagen arbeitet bereits seit dem Jahr 2004. Seitens der Energieerzeugung gibt es Solarkollektoren, einen Biomassekessel mit Wärmetauscher, einen Gaskessel und auch eine Fotovoltaikanlage [3].

Das Diagramm der Anlage ist in Abb.6 dargestellt.

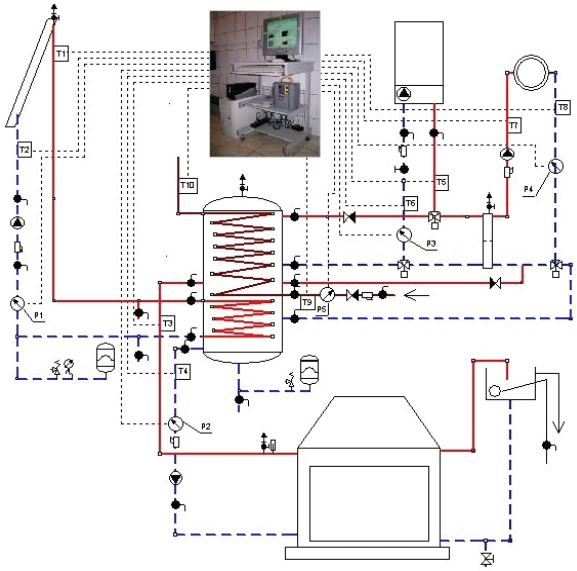

Abb.6. Schema der Hybridanlage für ein Zweifamilienhaus

Die erzeugte thermische Energie wird für Raumwärme und Warmwasserbereitung verbraucht. Die Solaranlage generiert Strom für die Notstromversorgung der Umwälzpumpen und für das Aufladen des Akkus mit einer Kapazität von 250 Ah. Die Anlage wurde auf einer kontinuierlichen Basis in den Jahren 2005 und 2006 betrieben. In Abb.7 werden in Form von einem Kurvenverlauf die im Gesamtjahr erzeugten Energiebilanzen und die thermische Energie, die verbraucht wurde, dargestellt.

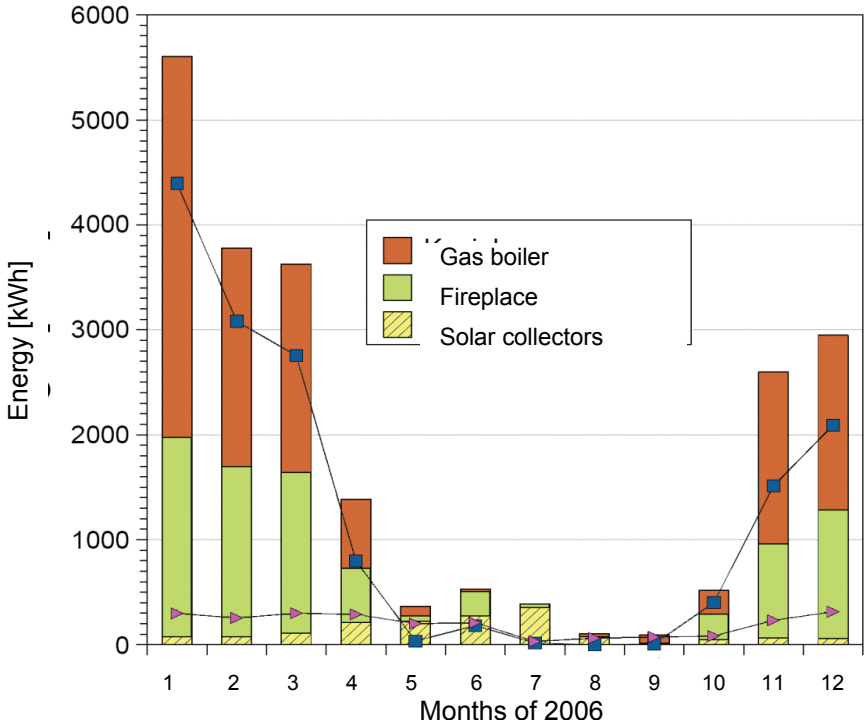

Abb.7. Energiebilanz der verbrauchten Energie eines Wohnhauses im Jahr 2006, das mit einer Anlage aus erneuerbarer Energiequellen ausgerüstet ist

Eine vergleichbare Anlage, die 50km südlich von Krakau in einer viel kleineren Ferienwohnung von ca. 110 m² montiert ist, ist in Abbildung 7 dargestellt. Für die Wärmeerzeugung wurden Solar-, Biomasse-Kessel und Elektroboiler installiert. Das Ferienhaus ist nicht in das Gasversorgungsnetz eingebunden. Zur Nutzung von Wärme und Warmwasser gibt es jedoch zwei Heizsysteme: Bodenheizung und Heizkörper, sowie Heizungsunterstützung des Swimmingpools. In diesem System werden aufgrund der periodischen Nutzung der Eigentümer keine kontinuierlichen Forschungen über erzeugte und verbrauchte Menge an Energie durchgeführt.

In diesem Fall ist die Installation einer Solar-Kollektorfläche von ca. 14 m² für den Energiebedarf im Sommer deutlich überdimensioniert. Aber in dieser Zeit sind die Kollektoren nicht durch übermäßige Hitze und Stagnation belastet, da die überschüssige Wärmeenergie in den Swimmingpool geleitet wird.

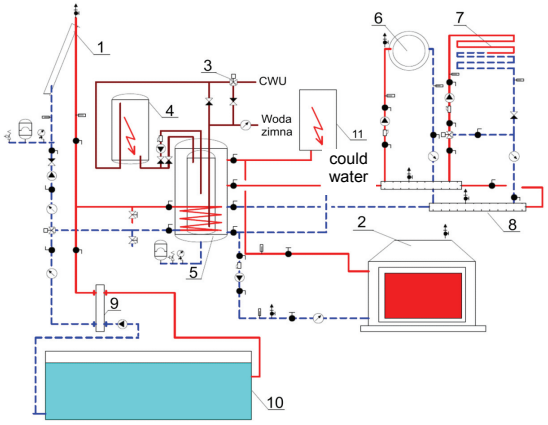

1 – solar collector
2 – fireplace with water jacket
3 – mixing thermostatic valve
4 – electric water heater
5 – buffer tank
6 – radiator heating
7 – floor heating
8 – divider
9 – plate heat exchanger
10 – swimming pool
11 – electric flow heater

Abb.8. Hybridanlage für Heizung und Erzeugung von Warmwa

In Abb.9 wurden teilweise die Ergebnisse der Arbeit der Anlage im Jahr 2010 sowie aktuelle Daten dargestellt. Beide Anlagen wurden im Jahr 2008 mit einem speziellen hybriden Steuer- und Energiebilanzsystem mit erneuerbaren Energien ausgestattet. [4].

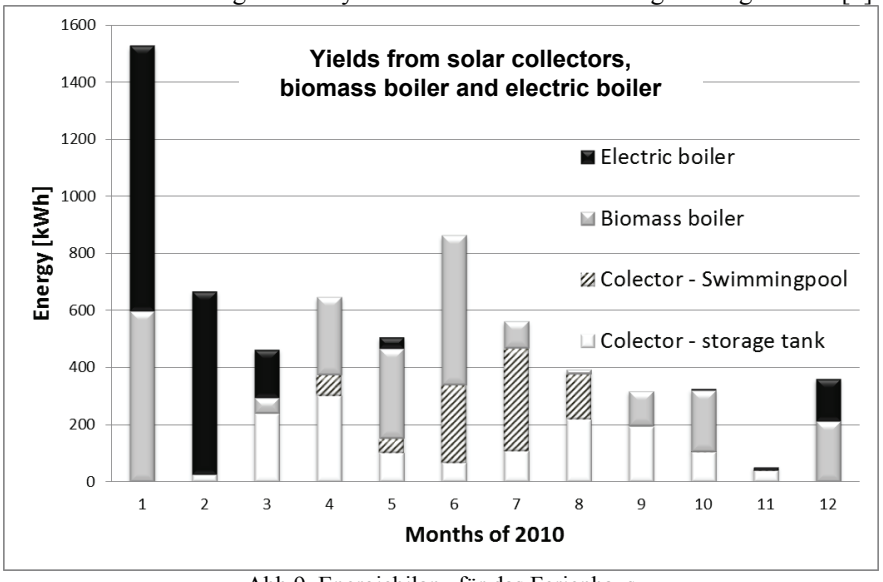

Abb.9. Energiebilanz für das Ferienhaus

Der Kern dieses Systems beruht darauf, einen kontinuierlichen Abgleich der Menge an Energie aus verschiedenen Quellen auf einen beliebigen Zeitraum zu ermöglichen. Es erlaubt ebenfalls die Darstellung einer Kostenbilanz unter Berücksichtigung der unterschiedlichen Kosten je Energieeinheit. Die Echtzeit-Grafiken sind sowohl Wärme-als auch Energieströmen, die aus verschiedenen Quellen generiert wurden, abgeleitet. Das System ermöglicht es, die gesamte Installation zu steuern, um eine wirtschaftliche Nutzung der thermischen Energie zu ermöglichen. Es besteht auch die Möglichkeit, die richtige

Arbeitsweise des Systems in Echtzeit über das Internet zu beobachten und zu steuern. Die Abb.10 zeigt die Veränderungen der erzeugten Energie im Jahr 2010.

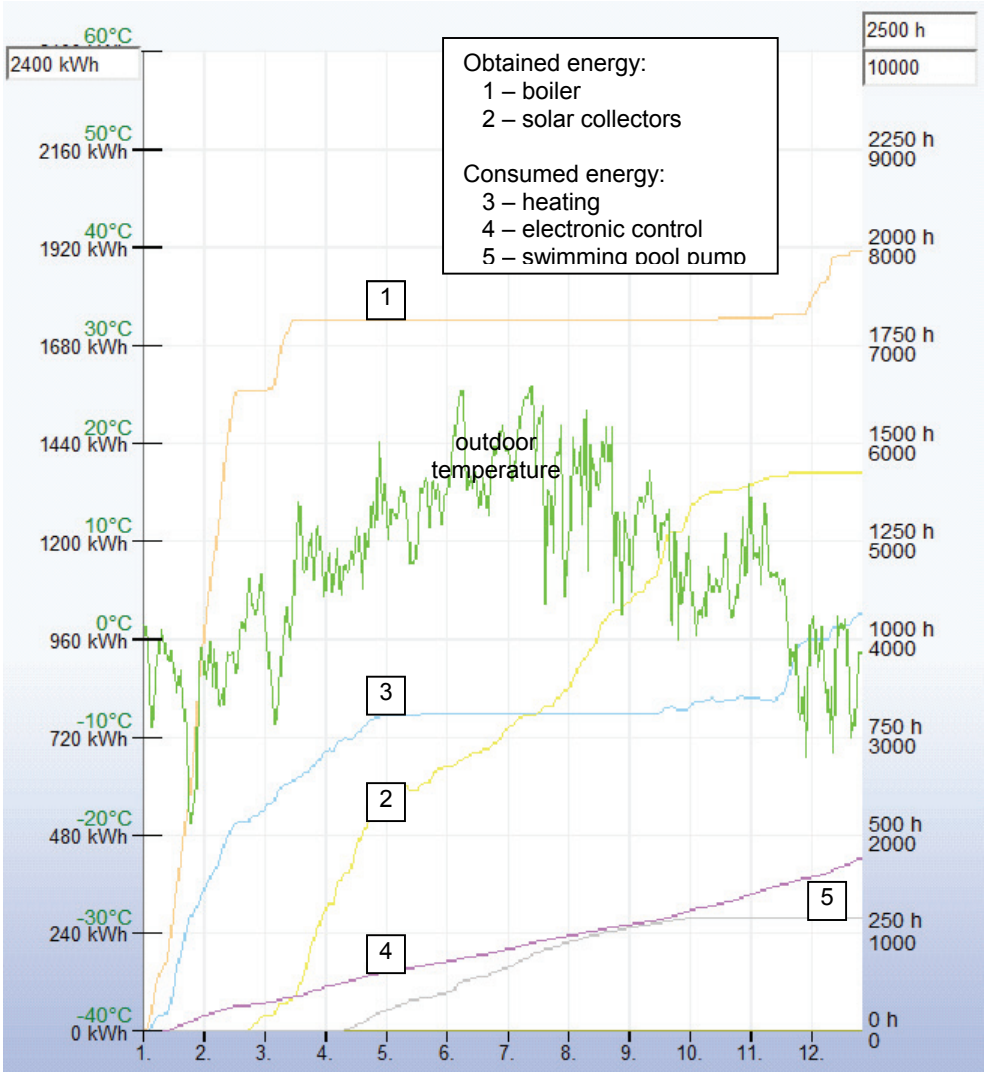

Abb.10. Verlauf der Veränderung von Energie und Außentemperatur des Ferienhauses fortlaufend im Jahr 2010

Schlussfolgerungen

1. Energie ist einer der wichtigsten Allgemeingüter für das menschliche Leben, jedoch werden die Kosten für ihre Herstellung und Nutzung in absehbarer Zeit trotz Bemühungen um Einsparung und Rationalisierung des Verbrauchs steigen.
2. Erneuerbare Energien können die Energienachfrage vermindern, wenn auch die Probleme der Energienachfrage der Welt und Europa in den kommenden Jahren nicht lösen.
3. Eine zur Wärmeerzeugung für Häuser und Wohnobjekte ausgelegte Anlage, die sich zur Wärmeenergieerzeugung mehr als einer Quelle bedient, einschließlich erneuerbarer Energiequellen hat den Praxistest gut bestanden. Mit einer Kostensenkung der Einrichtung wird eine weitere Verbreitung stattfinden.
4. Die Verwendung eines ausgebauten fernbedienbaren Systems der Energiebilanzierung und Steuerung, obwohl nicht in jeder Installation notwendig, ermöglicht jedoch eine wirksame Überwachung und Beaufsichtigung der Arbeit der Anlage durch das Internet. Anlagen dieses Typs, die auch als Fernlaboratorien dienen, erlauben, die Arbeit und energetisch erzielten Ergebnisse solcher Anlagen zu verfolgen.

Literaturverzeichnis

[1] Quaschning V.: Regenerative Energiesysteme, Carl Hauser Verlag , München Wien 1998.
[2] Magiera .: Efficiency of Solar Collectors and Air Heat Pump under Real Conditions, Polish Journal of Environmental Studies, **15**, (2004), 118-121.
[3] Magiera .J, Wojtaś K., Turoń M.: Renewable sources of energy for house heating and usable warm water production, Environmental Protection Engineering, **32**, (2006), 71-79.
[4] Neupauer K., Głuszek A., Magiera J.: Sterowanie nowego typu dla instalacji hybrydowych z odnawialnymi źródłami energii, Inżynieria i Aparatura Chemiczna, **49** (41), (2010), 87-88.

18th International Conference Process Engineering and Chemical Plant Design
Günter Wozny and Łukasz Hady, Editors

KRZYSZTOF NEUPAUER*

MÖGLICHKEIT DER BILANZIERUNG EINER HEIZUNGSANLAGE MIT DREI ENERGIEQUELLEN UND IHRE STEUERUNG IN DEM ONLINE-SYSTEM

Zusammenfassung

In die Arbeit wurden die Ergebnisse des Funktionierens von einer Hybrid-Heizungsanlage, in der die Quelle der Wärmeenergie für Heizung und Warmwassererzeugung Solarkollektoren, Biomasse-Kessel in Form eines Kamins mit einem Wassermantel und elektrischer Boiler mit modulierter Leistung präsentiert. Die Anlage wird von einem neuen Steuersystem gesteuert, die das Datenerhebung, Beobachtung aller gemessenen Parameter und Steuerung der Anlage mit verschiedenen Energiequellen und von mehreren unabhängigen Empfängern ermöglicht. Das dargestellte System erlaubt die Bilanzierung der Energieflüsse sowohl während ihrer Herstellung als auch ihrer Verwendung, was die Bestimmung des Wirkungsgrades und der Kosten der Energiegewinnung aus diesen Quellen ermöglicht.

Schlüsselwörter: Solarenergie, solarthermische Anlage, erneuerbare Energiequellen.

1. Einführung

In letzter Zeit erfreuen sich integrierte Systeme mit mehr als einer Energiequelle, einschließlich erneuerbarer Energiequellen wie Solarkollektor, Biomasse-Heizkessel oder Wärmepumpe großer Beliebtheit[1]. Diese Anlagen benötigen ein entsprechendes Steuerungssystem, welches sie so steuern könnte, dass erneuerbare Energiequelle an Energiegewinnung Vorrang hat und konventionelle Energiequellen als Reserve betrachtet werden. Es gibt schon solche Steuersysteme, die die Arbeit der einzelnen Geräte und Heizungsanlagen steuern und bilanzieren können[2,3,4]. Das beschriebene Steuersystem erlaubt als einziger das Steuern von einigen Energiequellen on-line durchzuführen und mehrere Zahlen von Geräten und Anlagen zu leiten. Ein zusätzlicher Vorteil dieses Systems ist die Möglichkeit der Kaskadenverbindung von einigen Steuergeräten, was unbegrenzte Möglichkeiten der Steuerung von Anlagen gibt.

*Technische Universität Krakau, Warszawska Str. 24, 31-155 Krakau, Polen

1.1. Heizungsanlage

Das erste Steuersystem, das in Polen auf der Basis von dem DigiENERGY Gerät arbeitet, wurde im Dezember 2009 in einem Rekreationsgebäude 60 km südlich von Krakau (49° 47′ 6″ N, 20° 10′ 49″ E) installiert. Es steuert die Hybridanlage (Abb. 1), die aus drei Wärmequellen besteht: Solarkollektoren mit der aktiven Gesamtfläche von zirka 14 m2, Biomasse-Kessel in Form eines Kamins mit Wassermantel mit der Heizleistung von 9 kW, der mit Holz beheizt wird und aus einem Elektro-Durchlaufwasserheizer mit der Leistung von 18 kW, mit einer flexiblen Steuerung der Heizleistung [5]. Jede Wärmequelle übergibt die Wärmeenergie an einen Pufferspeicher Typ „SISS"[5] mit dem Gesamtvolumen von 550 Liter, innerhalb dessen sich ein Gefäß mit dem Volumen von 150 l für die Erzeugung des warmen Nutzwassers befindet. In der Anlage befinden sich zwei Heizungskreisläufe: Fußbodenheizung im Erdgeschoß und Konvektionsheizung im Dachgeschoß. Außer der Fußbodenheizung wurde in den Badezimmern die Körperheizung für Badezimmer montiert. In der Urlaubszeit, wenn man kein warmes Nutzwasser braucht und die Solarenergie größer ist, ist der Überschuss von der Wärmeenergie in ein Schwimmbad mit der Größe von 3,15 x 6 x 1,5 m übergeben. Ein zusätzlicher Behälter des warmen Nutzwassers mit dem Volumen von 80 l und Heizleistung von 2 kW wurde in dem Kreislauf des warmen Nutzwassers installiert. Seine Aufgabe besteht in der Vorbereitung des warmen Nutzwassers ohne den Pufferspeicher zu heizen.

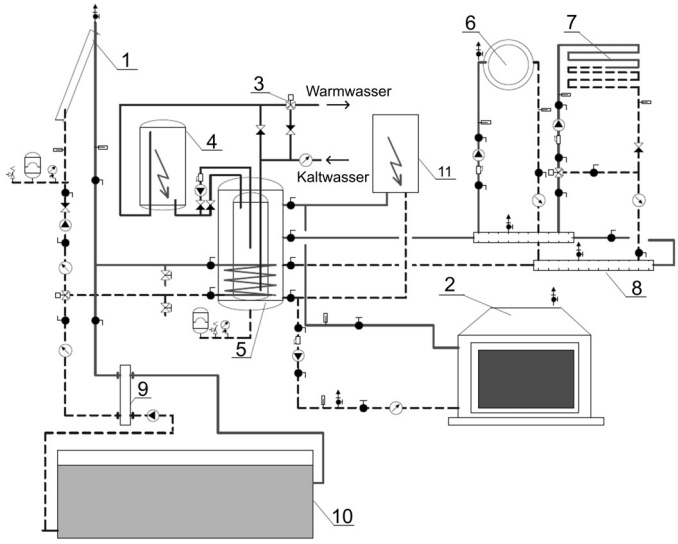

Abb. 1. Schema des Hybridsystems
von erneuerbaren Energiequellen mit der Anordnung von Meßpunkten
Elemente der Anlage: 1 – Solarkollektor, 2 – Kamin mit Wassermantel,
3 – mischendes thermostatisches Ventil, 4 – elektrischer Wassererhitzer, 5 – Pufferspeicher,
6 –Körperheizung, 7 – Fußbodenheizung, 8 – Verteiler,
9 – Plattenwärmetauscher, 10 – Schwimmbecken, 11 – Elektro-Durchlaufwasserheizer

[5] SISS – Speicher in Speicher System

2. Das DigiENERGY -Steuersystem

2.1. Hardware

Die Hardware des Steuersystems in seiner Grundversion besteht maximal aus 8 Meßmodulen und/oder Ausführungsmodulen. Die Modulmenge hängt von der Anzahl der Meßpunkte im System ab. Es besteht keine Möglichkeit der Modifizierung oder des Ausbaus von dem schon fertigen System. Das grundsätzliche und wichtigste Modul in jedem DigiENERGY System ist das Verwaltungsmodul mit dem Namen „Web Serwer". Es füllt zwei Funktionen aus: es verbindet alle anderen Module miteinander, sowie ermöglicht die Kommunikation des Systems von der Entfernung. Jedes Modul für die Temperaturmessung bedient maximal 9 Widerstandsfühler PT1000. Das Ablesen von den digitalen logischen Signalen z.B. Impulse aus dem Durchflussmesser erfolgt durch die Karte von Ein- und Ausgängen. Jeder Randstecker wird für das Ablesen oder Aufgeben von logischen Zuständen gebraucht (0-1), also zum Zusammenrechnen von Impulsen oder zum Steuern von anderen Anlagen mit Hilfe des +24V Signals. In solcher Karte befinden sich 8 Ein/Ausgänge. Das Modul mit analogen Ein/Ausgängen besitzt Randstecker in der Version mit der Spannung 0 – 10 V oder mit Strom 4 – 20 mA. Es dient der fließenden Steuerung z.B. von der Leistung des Kessels oder zum Ablesen der Werte von dem Pyranometer oder Hygrometer. Das Relaismodul besitzt 15 Halbleiterrelais für die Spannung von 230 V, die z.B. für das Einschalten der Pumpen, der Dreiwegeventile oder Elektroventile benutzt werden können. Der Durchsatz der Umlaufpumpen kann dadurch gesteuert werden, dass sich jedes Relais für die Arbeit im PWM –Modus (Pulse Width Modulation) eignet.

2.2. Software

Die Kommunikation mit dem DigiENERGY Steuersystem erfolgt durch einen Webbrowser [6]. Es ist der einzige Kommunikationsweg für die Aufsicht des Betriebs, für die Datenvisualisierung, Programmierung und Änderung der Daten. Das System verfügt über das Vierstufenmenu. In der Kartei „Informationen" - „Übersicht" befindet sich eine Ansicht der untersuchten Solaranlage (Abb. 2), die die Beobachtung der momentanen Temperaturwerte, Leistung, Volumen vom Durchsatz, Pumpendurchsatz sowie atmosphärische Bedingungen d.h. die Stärke der Sonnenbestrahlung sowie relative Feuchtigkeit ermöglicht. Das Schema wird abhängig von der Zahl der installierten Fühler und Empfänger durch das System automatisch modifiziert. Nicht alle programmierten Funktionen werden in der Visualisierung dargestellt. Das Symbol des Heizungskreislaufs wird zum Beispiel nur dann dargestellt, wenn mindestens ein Fühler diesem Kreislauf zugeordnet sein wird. Die Software des Steuersystems erlaubt Schema für beliebige Anlagen zu erstellen zu konfigurieren, was durch die Konfiguration von konkreten Anlagen wie: Kamin, Kessel, Wärmepumpe, Solarkollektor, Speicher erreicht wird.

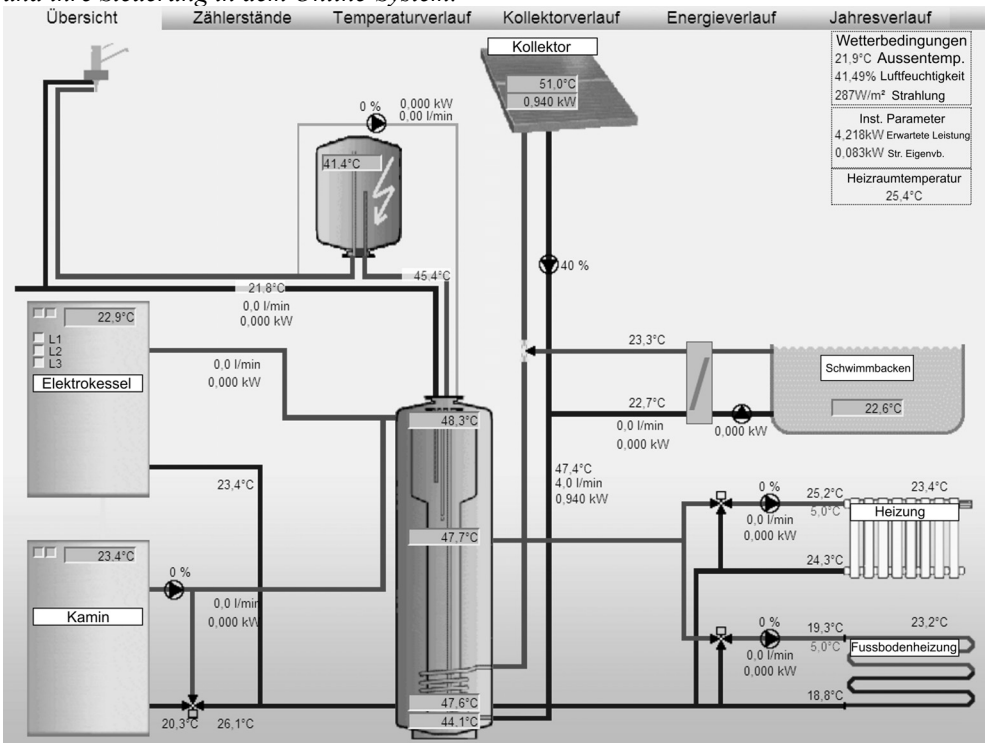

Abb. 2. Visualisierung der Betriebsdaten der Anlage, Zustand vom 23.05.2011. 11:26 Uhr

Das Steuersystem verfügt zusätzlich über die „Zählerstände" - Funktion (Abb. 3) für alle Heizungskreisläufe. Diese Funktion erlaubt aktuelle Wärmeleistung und elektrische Leistung für jeden Kreislauf sowie das Nutzwasservolumen zu verfolgen. Die energetische Bilanz wird nach dem Einstellen eines Zeitabschnittes generiert. Wenn die Einheitspreise für 1 kWh und 1 m3 des Wassers eingetragen werden, können Kostenbilanzen für den gewählten Zeitraum generiert werden.

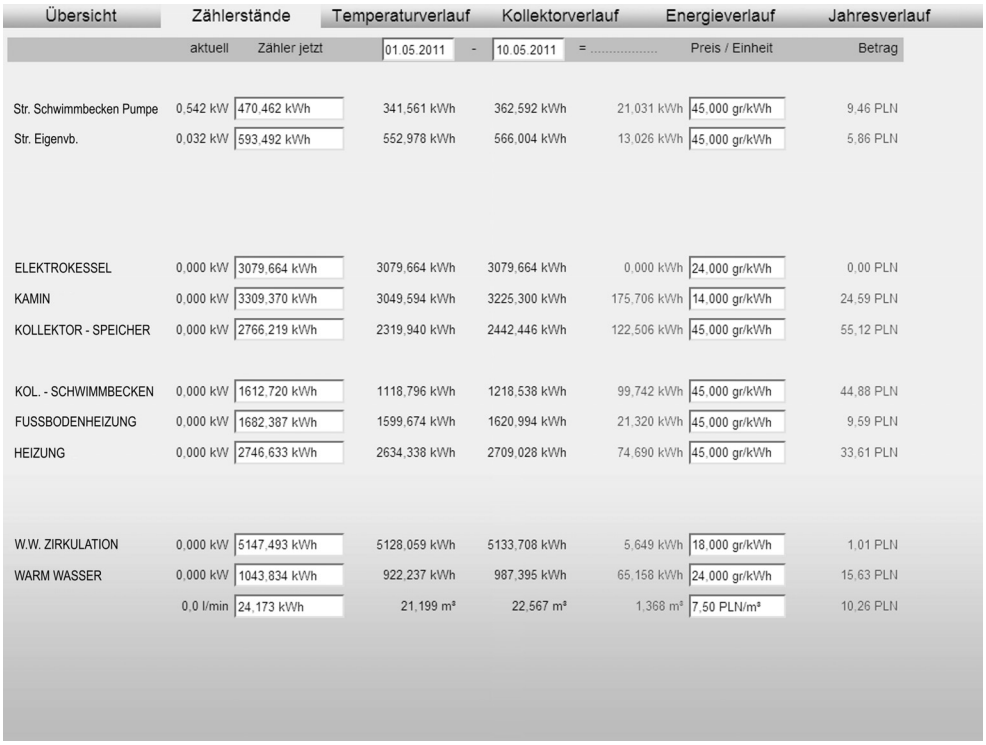

Abb. 3. Beispiel der energetischen und Kostenbilanz im Zeitraum vom 1.05.2011 bis zum 10.05.2011

In der Kartei „Temperaturverlauf" und „Kollektorverlauf" können Diagramme der Tagestemperatur gleichzeitig für einige Meßpunkte am Kollektor und Speicher generiert werden. Diese Diagramme sind dann nützlich, wenn Probleme mit dem Betrieb der Solaranlage auftauchen oder wenn er optimiert werden soll. Das Diagramm auf der Abb. 4 zeigt, dass die Umlaufpumpe des Kollektors (Kurve 4) zwischen 9:30 und 17:00 Uhr automatisch eingeschaltet wurde, denn die Temperatur des Kollektors (Kurve 1) größer als die Temperatur in dem Speicher (Kurve 2) war. In den Stunden 9:30 – 12:00 sowie 15:00 – 15:30 wurde das Dreiwegeventil (Kurve 5) geöffnet und die Wärme von dem Kollektor wurde zum Speicher (Puffer) und nicht zum Schwimmbecken weitergeleitet.

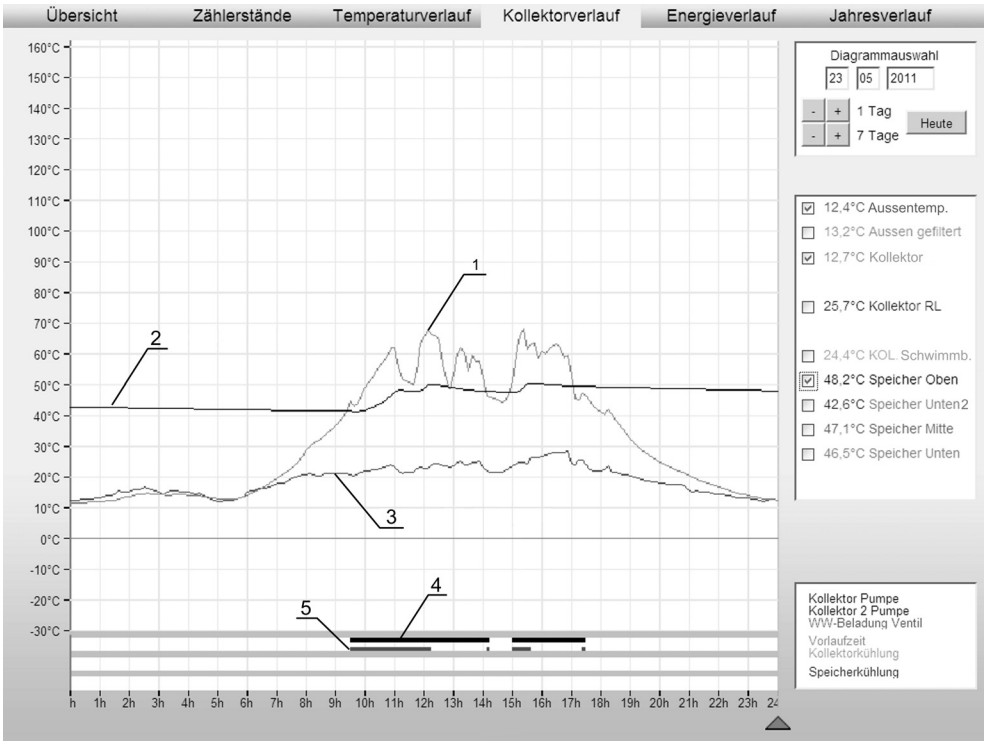

Abb. 4. Ausgewählter Tagestemperaturverlauf am 23.05.2011
Legende: 1 – Temp. beim Auslauf des Kollektors, 2 – Temp. im oberen Teil des Speichers, 3 – Aussentemp.,4 – Betriebszeit der Umlaufpumpe des Kollektors, 5 – Zeitraum der Öffnung von dem Dreiwegeventil (Durchfluss zum Speicher)

Die Diagramme der momentanen Leistungen in den einzelnen Kreisläufen sind in der Kartei „Energieverlauf" (Abb. 5) abrufbar. Aus dieser Abbildung lässt es sich ablesen, dass der Kamin die Wärmeströmung zum Speicher (Puffer) in der Zeit von 17:00 bis 24:00 übergeben hat. Die Wärmeströmung aus dem Kollektor wurde an diesem Tag sowohl zum Speicher als auch zum Schwimmbecken übergeben.

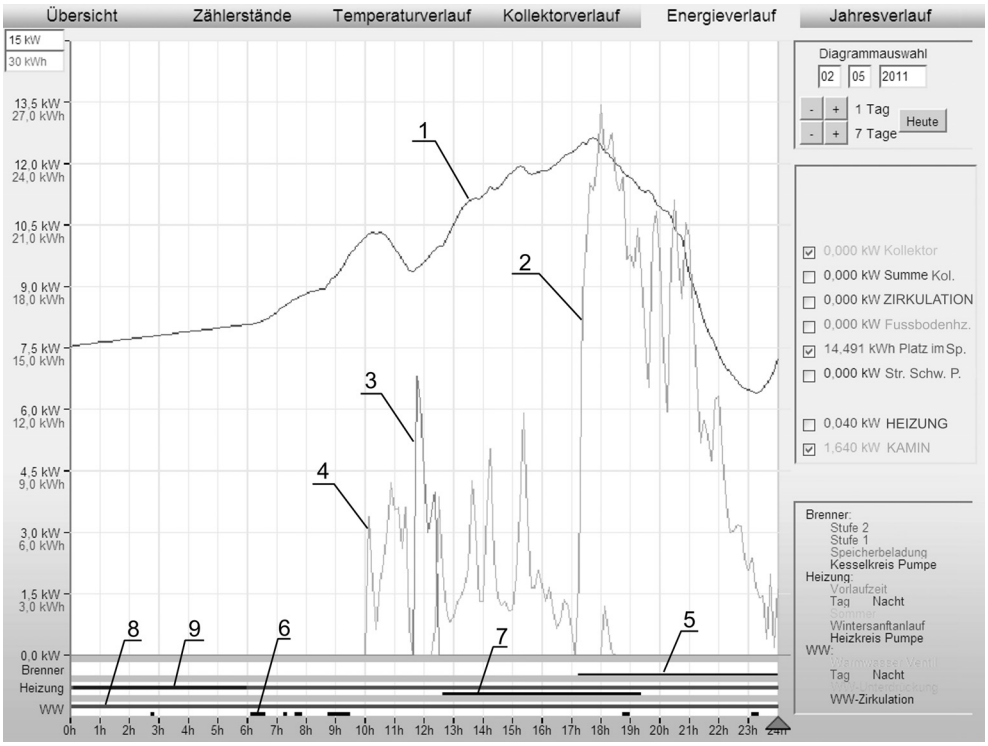

Abb. 5. Ausgewählte Tagesverläufe der Leistung am 2.05.2011
Legende: 1 – Wärmekapazität des Speichers, 2 – Wärmeleistung des Kamins, 3 – Wärmeleistung des Kollektors, die zum Schwimmbad übergeben wird, 4 – Wärmeleistung des Kollektors, die zum Speicher übergeben wird, 5 – Betriebszeit der Umlaufpumpe des Kamins, 6 – Betriebszeit der Umlaufpumpe im Kreislauf des warmen Nutzwassers, 7 – Betriebszeit der Pumpe im Heizungskreislauf, 8 – Verfügung über warmes Nutzwasser, 9 – Höhe der Innentemperatur – am Tag 20°C, in der Nacht 18°C

Die Software erlaubt Diagramme von einem Jahr zu generieren, wodurch der Verlauf von der Außentemperatur, Herstellung und Verbrauch der Energie für einzelne Kreisläufe sowie Daten aus den letzten zwei Jahren verglichen werden können. Diese Diagramme befinden sich in der Kartei „Jahresverlauf". Bei dem Vergleich der Kurven auf der Abb. 6 für das Jahr 2010 und 2011 sieht man, dass es im April und Mai 2010 schlechtere atmosphärische Bedingungen gab und dadurch zweimal kleinere Gewinne der Wärmeenergie aus dem Kollektor erhalten wurden.

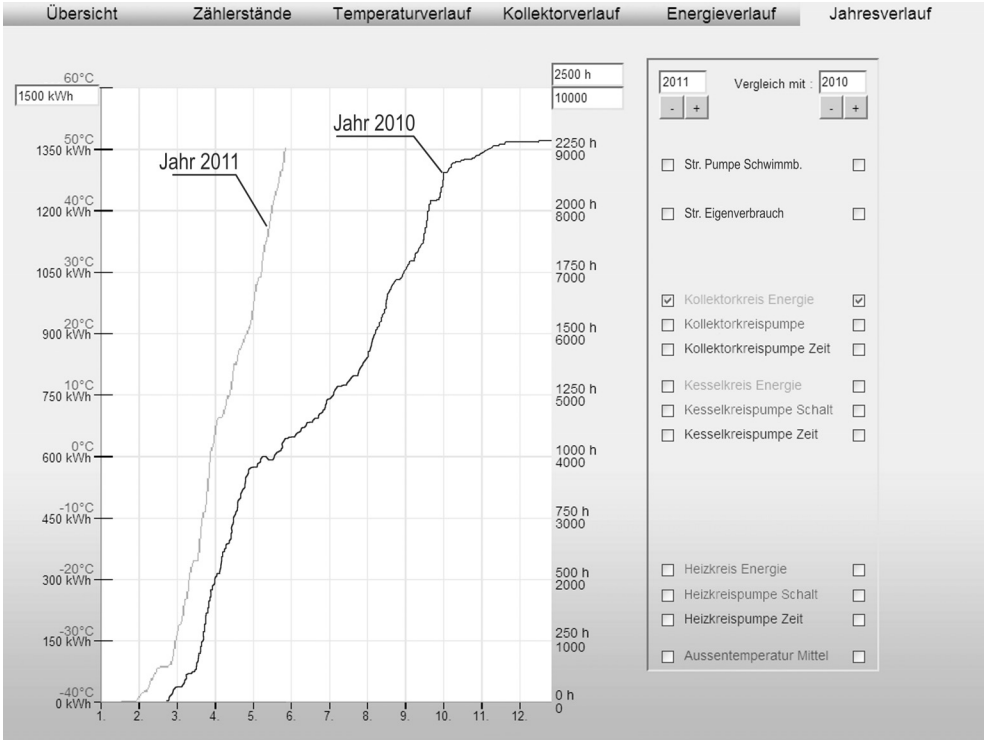

Abb. 6. Jährliches Diagramm der Wärmeenergie, die aus dem Solarkollektor erhalten wurde.

Das besprochene System erlaubt Zeiträume für die Heizung des Gebäudes zu definieren und die Menge des warmen Nutzwassers sowie die Priorität für den Energiegewinn aus ausgewählten Wärmequellen zu bestimmen.
In dem Zugangsmenu kann der Bediener in der Kartei „Konfiguration" Kenndaten für den Betrieb der Anlage einstellen, die Kalibration der Messgeräte durchzuführen sowie „manuellen" Betrieb jedes Systems und Geräts durchzuführen.
Das System gibt breite Möglichkeiten der Registrierung von Betriebsdaten der Solaranlage. Es ermöglicht nicht nur laufende Registrierung der Systemdaten, sonder auch Einführung von zusätzlichen Wechseldaten und Speichern dieser Daten in *.csv Dateien, die dann leicht z.B. in MS Excel zu bearbeiten sind.

3. Ergebnisse des Hybridbetriebs der Heizungsanlage

Auf der Abb. 7 wurden in Form eines Diagramms Beispielergebnisse des Hybridbetriebs im Monat Mai dargestellt. Die erzeugte Wärmeenergie stammte in 78% von dem Solarkollektor und in 22% aus dem Kamin. Dritte Reservequelle der Wärmenergie ist der elektrische Kessel, der in dem analysierten Monat nicht arbeitete. Gegen 2/3 der in

dieser Zeit erzeugten Energie wurde für die Heizung des Gebäudes und des Schwimmbads sowie für warmes Nutzwasser genutzt. Die Summen von Energiezufuhr und Abfuhr sind nicht gleich, weil der Speicherzustand am Anfang und Ende war verschieden.

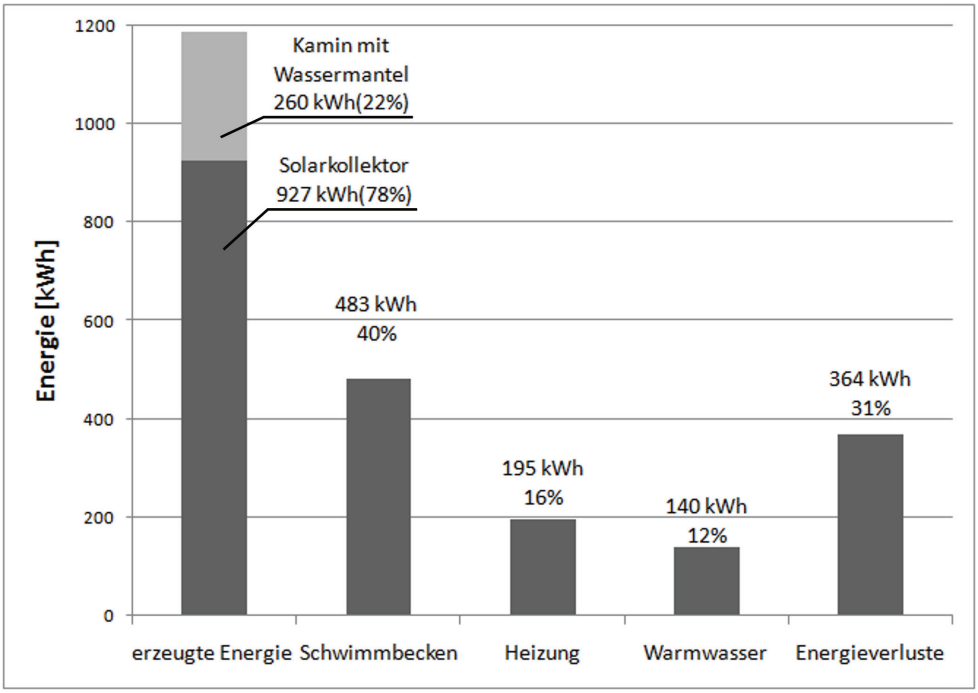

Abb. 7. Im Mai 2011 erzeugte und genutzte Wärmeenergie.

Das analysierte Wohnobjekt ist nicht typisch für konstantes Bewohnen und Benutzen der Energie. Die dargestellten Ergebnisse zeigen nur einen Teil der Möglichkeiten des besprochenen Steuer- und Bilanzierungssystems. Mit Hilfe von diesem System arbeiten zur Zeit in Polen auch andere außer der hier dargestellten Anlagen: ein Zweifamilienhaus in Mszana Dolna, großes Krankenhausgebäude in Krakau, eine Versuchsanlage mit Solarkollektoren in dem Labor der Solartechnik von Krakauer Technische Universität. Dieses System wird gerade auch in dem Zentrum für erneuerbare Energiequellen an der Bergbau und Hüttenakademie in Krakau – Miękinia sowie in Połtawska Wissenschaftsakademie in Ukraine montiert. Das System wird da Anlagen mit mehreren erneuerbaren Energiequellen steuern.

4. Zusammenfassung

Das dargestellte Steuersystem ist imstande, den Betrieb von jeder Heizungsanlage zu kontrollieren. Es kann auch die Hybridheizungsanlagen steuern, die aus mehreren Heizungskreisläufen bestehen und für die Energieerzeugung mehr als eine Energiequelle benutzen. Es gibt die Möglichkeit der Einstellung und der „on-line" – Kontrolle von den momentanen Betriebsdaten der ganzen Anlage. Dank der „Zahlerstände" Funktion kann der Bediener jederzeit kurz- und langzeitige energetische und Kostenbilanzen erstellen. Es gibt auch die Möglichkeit des graphischen Vergleichs der Werte mit den analogischen Werten vom letzten Jahr. Das System kann sehr schnell den Verlauf von ausgewählten Werten erstellen, was für den Benutzer für die Optimierung des Betriebs der Anlage und die Diagnostik von eventuellen Fehlern wichtig ist. Korrekt installiertes und eingestelltes System wird die Anlage rationell steuern, der Verbrauch der Energie wird optimaler sein, was in der Konsequenz Kostensparen für den Benutzer der Anlage bringen wird.

Literatur

[1] Dissertation, Michalak P. „Badania efektywności energetycznej budynku użyteczności publicznej wykorzystującego odnawialne źródła energii", Akademia Górniczo-Hutnicza Im. Stanisława Staszica w Krakowie, 2008.

[2] www.suntime.pl/innowacje.html, Zustand vom 14.07.2011

[3] Podlejski K., FELCENLOBEN Ł.: „Zastosowanie środowiska LabVIEW do sterowania pracą instalacji grzewczej z odnawialnymi źródłami energii", Prace Naukowe Instytutu Maszyn, Napędów i Pomiarów Elektrycznych Politechniki Wrocławskiej Nr63, Studia i Materiały Nr 29, 2009r.

[4] www.vaillant.de/Produkte/Gasheizung/Regelung/produkt_vaillant/vrnetDIALOG.html, Zustand vom 14.07.2011

[5] Neupauer K., Magiera J., Głuszek A.: „Efektywność wykorzystania kolektorów w konwersji energii słonecznej do energii cieplnej", Inżynieria procesowa w ochronie środowiska, Wydawnictwo i Drukarnia Świętego Krzyża, Opole 2009, 71-80.

[6] Neupauer K., Głuszek A., Magiera J.: Inżynieria i Aparatura Chemiczna, Nr 3/2010, (2010), 87-88.

18th International Conference Process Engineering and Chemical Plant Design
Günter Wozny and Łukasz Hady, Editors

STEFFEN STUENKEL, GUENTER WOZNY*

CO_2 CAPTURE FOR THE OXIDATIVE COUPLING OF METHANE PROCESS

Abstract

The gas treatment of reaction products is a crucial step in the process chain from the raw material to the product. CO_2 is produced by the oxidative coupling of methane (OCM) as an unwanted by-products or waste product and should be removed in an early stage. For the gas treatment are the energy requirement, the operation and investment cost a curial factor, that effect the overall process performance. Beside economic aspects, designing a sustainable process is the aim by utilization of CO_2 in a dry-reforming reactor. Due to the concurrent engineering procedure, the OCM process concept was developed and the process units were investigated parallel. The membrane reactor and the fluidized bed reactor concept were investigated for the oxidative coupling of methane and a C_{2+} yield of nearly 17% was achieved with standard catalysts. Beside the ethylene up to 25 mol% CO_2 were produced and could remove by a state of the art chemical absorption process using 5 MJ/kg_{CO2} specific thermal energy. This was halved by using a polyimide membrane for pre separation. In this article the technical feasibility of the general process concept for the OCM, including down streaming is discussed and presented.

Keywords: Oxidative Coupling of Methane, CO_2 capture, CO_2 utilization

1.Motivation Oxidative Coupling of Methane – Miniplant scale

In the wake of shortages and price rises for crude oil in recent decades also, the search for alternative raw materials in the chemical industry is of great importance. Hence opens the oxidative coupling of methane (OCM), a new route for the petrochemical industry in order to produce ethylene from methane natural gas or biogas [1]. Thus, this process forms the base to activate a large new feedstock for a variety of chemical products [2]. The OCM reaction is a heterogeneously catalyzed gas phase reaction at temperatures of up to 800° C, in which unwanted by-products such as carbon dioxide produced additionally to the desired product ethylene and must remove from the reaction product [3]. Although several alternatives can be found for OCM processes in the literature [4], an efficient OCM process

* TU Berlin, Straße des 17. Juni 135, Berlin 10623, Germany

is not installed in the industry yet. So far all proposed processes associated with high cost and energy demand, as well as cost-intensive gas processing part.

To overcome this limitation, in this work, the novel approach of the Concurrent Process Engineering is used to investigate the whole process from raw material to the product. After extensive preliminary investigations, a flexible mini-plant system was designed, built and operated. To evaluate effects of removal and the OCM catalyst life, the whole process is also being studied in a long time study. Due to the moderate ethylene yield for currently available OCM catalysts of 30% is the goal, besides the improving of the catalysts, the downstream gas conditioning process and make the process economical. This can only be achieved through the development of integrated process concepts that are based on energetically and economically enhanced processes and the usage of side products. The development process is part of the DFG Cluster of Excellence "Unifying Concepts in Catalysis" (UniCat).

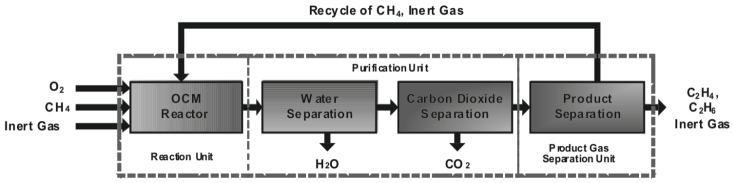

Figure 1 Process flow diagram of the OCM process, including processing

The challenge is to develop a flexible process in mini-plant scale to respond flexibly to changing one process requirements. As example here, the catalyst development is mentioned. By using different catalysts, a different amount of CO_2 is produced, which are separated in the downstream gas processing needs. Due to time savings in the process of development, the entire OCM process is set up in parallel in a mini-plant, and process synthesis for optimal OCM process is carried out in parallel. So the whole process for concurrent engineering has been divided into three units (see Figure 1): the reaction unit, the gas cleaning unit and the product separation unit, which are examined in parallel. Based on a holistic view and approach of the simultaneous process of development, the requirements relating to the separation task and purities for each unit process having regard to their interactions with each defined. Here were the CO_2 separation, the maximum limit for the CO_2 produced fixed at 25mol%, this border can be lowered down to 15mol% CO_2 by the latest developments. Therefore, the CO_2 separation is investigated in the concentration range of 15mol% to 25 mol%. Based on the process schematic of the flow chart in Figure 1 as well as studies on the macro-and micro-kinetics of the catalysts, the process conditions and process requirements for CO_2 separation were determined which are given in Table 1. Here, the maximum expected CO_2 concentration of 25 mol% is set as the basis for the design task.

Table 1 Process conditions and requirements for CO_2 separation

Gas temperature	F-Faktor	Raw gas pressure	CO_2	C_2H_4	CH_4	N_2	CO_2 removal
40 ° C	0.7Pa $^{0.5}$	32 bar	22mol%	15mol%	15mol%	48mol%	90 %

The removal of acid gas components from the reaction product stream is an important process step in the chain of gas processing, to achieve the goal in the purity of the product.

For the CO_2 capture process, several process concepts are available. The chemical absorption, however, preferred for selective amine scrubbing and washing are state of the art in this field [4]. Moreover, new detergents such as hyper branched polymers have a promising object of research and are examined parallel in a vapor-liquid equilibrium apparatus and later in the miniplant. Alternative separation methods such as membrane processes for CO_2 capture are also currently being investigated in parallel.

1.1. Design of a Miniplant for the OCM for technical feasibility demonstration

The miniplant technique is well-known in process synthesis, to obtain fundamental information experimentally in an early process synthesis stage. In this approach, a top-down process synthesis is applied and the process has been developed in miniplant scale to demonstrate its technical feasibility. Due to the concurrent engineering, the downstream requirements affect the reaction unit and the catalyst, especially the C_2 yield, the C_2- and CO_2 selectivity, the methane conversation and dilution concentration of the reaction gas. The reaction products that have to be separated in the downstream of the OCM process and their chemical families, properties and the feed conditions are given in Table 2, 3 and 4.

Table 2: Defined feed gas concentration (in mol%) for the process section

Unit	CH_4	O_2	C_2H_4	C_2H_6	CO_2	H_2O	N_2
Reaction	60 – 70	20	-	-	-	-	20 – 10
Purification	45	-	10	10	25	-	20 -10
Separation	60	-	13	13	-	-	14
Chemical family:	Alkan		Alken/ olefine	Alkan	Acid gas		
Treated	Raw material/ recycle	Raw material	Product	Byproduct	Remove	Remove	Inertgas

Table 3: Process conditions for each unit

Unit	Pressure range	Temperature range
Reaction	1 to 5 bar	30 to 900 °C
Purification	1 to 32 bar	30 to 100 °C
Separation	Up to 32 bar	Down to -100 °C

The defined ranges of the process- and stream conditions for the units are presented in Table 3. Those conditions are defined of a literature study for the state of the art processes for each unit operation for a starting value of the design procedure.

1.2. The downstream process

The reaction gases have to be conditioned in the downstream process, that consists of a phase separation unit, a carbon dioxide removal unit, and a product separation unit, as recommended by various authors [5] . Concerning the simultaneous design and construction in the miniplant, with the state of the art separation processes were started as a base case and was improved during the project. The base case purification unit consists of an amine based absorption process for the carbon dioxide separation. For the separation unit, a cryogenic distillation for the product separation was found to be the state of the art solution and is investigated only theoretically.

Table 4: Component properties [6]

Compo-nents	State 25°C, 1atm	Molar mass [g/mol]	Boiling Point 1atm[°C]	Melting Point 1atm[°C]	kinetic Diameter σ [A]	Critical Temperature T_c [K]	Critical Pressure P_c [bar]
Methane	vapour	16	-162	-182	3,8	191,1	45,8
Ethylene	vapour	28	-103,72	-169,18	4,228	282,4	50
Ethane	vapour	30	-89	-183	4,388	305,4	48,2
Nitrogen	vapour	28	-195	-210	3,667	126,2	33,5
Carbon Dioxide	vapour	44	Over critical		3,996	304,2	72,8

It shows that an increase of the downstream operating pressure up to the lowest critical pressure of the components (32 bar) results in a higher boiling point of the hydrocarbons and decreases the energy demand in the cryogenic distillation. The high operation pressure increases the absorption efficiency as well and is therefore applied in the purification unit too. Due to the high absorption pressure and a high CO_2 partial pressure a physical solvent could be used. Nevertheless, to improve the selectivity was a chemical solvent chosen for the base case and the state of the art absorbent Monoethanolamine is used. Optimal thermal energy demands of 3-4 MJ/kg_{CO2} of solvent rgeneration are reported for standard absorption processes using Monoethanolamine (MEA) [7]. As base case for the acid gas removal unit a chemical absorption process with 30 wt% of MEA was found and modeled with a detailed rate base model and an electrolyte NRTL approach, described below. Thermal energy for solvent regeneration was found with 3.6 MJ/kg_{CO2} for the design and base case and was improved by developing a hybrid separation process.

2.Process synthesis for alternative acid gas removal unit

The design task of this unit is to decreases the carbon dioxide concentration from the product stream by 90% from the initial CO_2 concentration as shown in Table 1.
Several strategies are known for process synthesis. In this research the Knowledge-Based Separation System Synthesis approach purposed by Barnicki and Fair [8] was followed. The general separation tasks can be classified by: 1. enrichment, 2. sharp separation and 3. Purification. The enrichment means the increase in one concentration of a species in one of the product stream [8]. Whereas in this context two high-purity product stream results by sharp separation. The classification of this design task is done with the ration of the key components in the product streams that has to be higher than 9 or less than 0.1 respectively. The key components in the acid gas removal part are the carbon dioxide (CO_2), that has to remove and the ethylene (C_2H_4) as the product. The separation ration for Carbon Dioxide results to:

$$S_{CO_2} = \frac{c_{CO_2}^{Rawgas}}{c_{CO_2}^{Puregas}} \quad (1)$$

Purification, in this context represents the separation task for the removal of low concentration of one component. For this case the removal of CO_2 of less then 10 mol%. For the OCM design case, the sharp separation has to be considered in general. The unit operation for the separation tasks applicable for all three kinds of separation tasks are presented in Table 5, and discussed in detail in the next following sections.

Table 5: Process alternatives and indicators for separation processes [8]

Process alternative	Indicator
Cryogenic Distillation	Relative volatility
Physical Absorption	Separation factor for gas solubility using Henry's approach
Molecular Sieve Adsorption	Difference in shape size and kinetic diameter
Equilibrium limited Adsorption	Ratio of the equilibrium loading for the key components
Membrane Separation	Separation factor, ration of the component permeability
Chemical Absorption	Chemical family of the components
Condensation	Difference in normal boiling point
Catalytically conversion	Product Worth

2.1. Cryogenic Distillation

The application of cryogenic distillation is economically only for high throughputs and a volatility for the key components higher than two [8]. The relative volatility for the key components at 32 bar is $\alpha_{CO2/C2H4} \approx 1$. For a system pressure of 1 bar results the relative volatility to $\alpha_{CO2/C2H4} \approx 3$. Therefore the low temperature range requires high-grade materials and high energy demand for the low temperature production, what makes the process uneconomically.

2.2. Physical Absorption

For the physical absorption a selectivity of the key components of $S_{abs\ CO2/C2H4} > 4$ is recommended [8]. The selectivity of the key components can be calculated using equation 2. For two common physical absorbents, methanol and water the Henry approach, equation 3 and 4 respectively can be used to obtain the selectivity. For methanol the selectivity results to $S_{absCO2/C2H4}=1.11$ and for water the selectivity results to $S_{absCO2/C2H4}=1.03$.

$$S^{abs}_{CO_2/C_2H_4} = \frac{X_{CO_2}}{X_{C_2H_4}} \quad (2)$$

$$X_{CO_2} He_{CO_2} = Y_{CO_2} P \quad (3)$$

$$X_{C_2H_4} He_{C_2H_4} = Y_{C_2H_4} P \quad (4)$$

2.3. Chemical absorption

Chemical absorption is favored for species that contains acid-based functional groups, like the Carbon Dioxide and for those components with low partial pressure in the gas stream.

2.3. Molecular sieve and equilibrium adsorption

To consider molecular sieve adsorption, the species have to classify by shape size and their kinetic diameters. The kinetic diameters of the components from Table 4 can be arranged according to size: $\sigma_{C2H6}>\sigma_{C2H4}>\sigma_{CO2}>\ \sigma_{CH4}>\sigma_{N2}$. The physical size properties of the commercial available adsorbents are listed in Table 6. It can be seen, that the kinetic

diameter of the Carbon Dioxide is in the middle of the components and all diameters are very close to each other.

Table 6: Commercial available adsorbents [9]

category	nominal aperture size [A°]	Zeolite Type
5	3	3A Linde 3ADavison
4	4	4A Linde, 4A Davison
3	5	5A Linde, 5A Davison
2	8	10X Linde
1	10	13 X Linde, 13X Davison

Equilibrium based adsorption is only suitable for species concentration less than 10 mol% and for a selectivity of the key components higher than 2. It was found, that the selectivity for equilibrium loading of the key components results to $S_{adsCO2/C2H4}$=1.74, for a 5A molecular sieve [9].

2.4. Membrane processes

Considering membrane as an economical feasible separation technique, the selectivity of the key components should be lager than 15 [8]. The selectivity for the key components can be obtained by the ratio of the permeability with equation 5.

$$S_{CO_2/C_2H_4} = \frac{P_{CO_2}}{P_{C_2H_4}} = \frac{D_{CO_2} S_{CO_2}}{D_{C_2H_4} S_{C_2H_4}} \quad (5)$$

The applications of membranes in gas processing are rare and therefore it is not astonishing, that no selectivity for the key components could be found in the literature. Provisionally the carbon dioxide/methane selectivity was taken into account, which was found to be higher than 15 [10]. Therefore, membrane separation was considered and new measurements were performed for the design specification by the Helmholtz – Zentrum Geehstacht, Germany.

2.6. Condensation and catalytically conversion

The separation by condensation should be considered when the difference in normal boiling points of the components is higher than 40 K. The separation by catalytic conversion is only suitable for impurities.

3. Alternative separation Process Synthesis

The recommended unit operations for sharp separation are physical separation, cryogenic distillation, molecular sieve and equilibrium adsorption. It shows that none of the process alternatives of Table 5 could fulfill the design task in a single step for sharp separation. Therefore, a two-step process was developed: An enrichment step for the reduction of the Carbon Dioxide down to 10 mol% and a purification step for last 10 mol%. The processes alternatives and their indicators for choosing the alternative are shown in Table 5 and discussed in section 2. It was found that the best process alternative is the design of a hybrid separation process, consists of a membrane and a chemical absorption unit, which is described and discussed in the next sections.

3.1. Absorption processes

The absorption technique for Carbon Dioxide separation is well developed and industrially available. Physical absorption processes like the UOP Selexol® Process or the Lurgi Rectisol® Process are known, which are using dimethyl ether and cold methanol, respectively. Those physical absorption processes cause high product losses of more than 30 %, due to a nearly similar solubility of the Ethylene and the Carbon Dioxide in the absorbent. Therefore, only chemical absorption liquids like Monoethanolamine (MEA), Diethanolamine (DEA) and Methyldiethanolamine (MDEA) or a mixture of them are applicable for the purpose of the OCM miniplant. Those chemicals are used in amine scrubbing processes like the aMDEA® Process in different concentration ranges. Stand-alone rigorous simulations for the absorption process of the miniplant were carried out in Aspen Plus®. The in-built ELECNRTL model, with activity coefficients of the electrolyte NRTL approach for the liquid phase was used and the Redlich-Kwong equation of state (EoS) was applied for the gas phase. Furthermore, concentration-based reaction kinetics was used and a rigorous rate-based model for absorption in packed column was applied.
Chemical absorption processes are high selective on the one hand, but suffer on the other hand on a high-energy rates, which is required for regeneration of the loaded solvent in the desorption part. A parameter study was done to evaluate the influence of solvent regeneration, reboiler duty, solvent flow rate and solvent concentration.

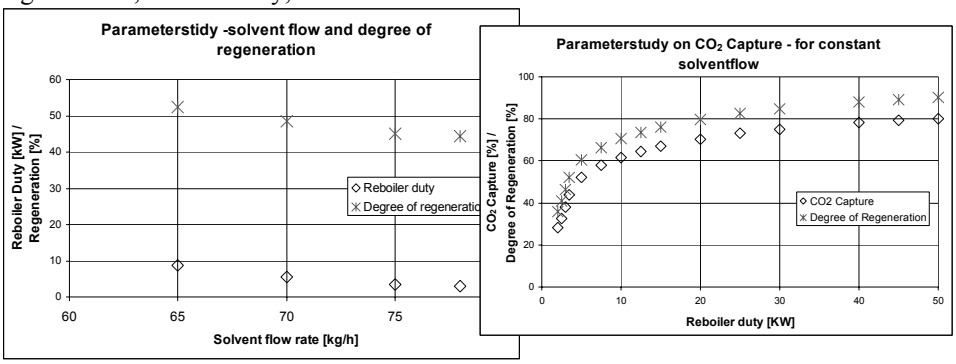

Figure 2: Parameter study – left: effect of flow rate for a constant design task, right: effect of reboiler duty of regeneration and carbon capture

At first, a simulation study with theoretical stages was carried out to investigate the effect of the flow rate on the energy demand. The range of the flow rate were varied and it was found, that increasing flow rate lowers the reboiler energy demand for absorbent regeneration. The influences of absorbent regeneration and reboiler duty on carbon capture were investigated with the more detailed model, including rate-based calculations with chemical reactions. It was found, that a regeneration of 50 to 60% is optimal to reach the an energy demand of 3.15 MJ/kg_{CO2} for 90 % carbon capture with 30 wt% MEA solution, which fulfill the design task of CO_2 reduction from 10 to 1 mol% for the process alternative.

3.2. Membrane unit

The advantages of a membrane unit are the easy operation and a short start up and shut down time caused by their small size. Those units are very flexible in use, due to the modular design. There is no solvent needed and no further treatment, if the selectivity is high enough. For vapor/gas membrane separation, different kinds of materials are available differs in physical mechanism:

- Polymeric membranes: Rubbery or glassy polymers, with different solubility and diffusion properties for carbon dioxide and hydrocarbons.
- Molecular sieves: Adsorption effects, separation by different molecule dimensions.

Glassy and rubbery polymeric membranes are preferred for the carbon dioxide separation and hydrocarbon recovery, but they are not used in olefin production. For the membrane unit, a glassy and a rubbery carbon dioxide selective membrane is investigated. The membrane unit was modeled with the solubility-diffusion model and an Aspen Custom Modeler® unit was developed for a one dimensional, dense membrane. The Peng-Robinson EoS is used for the fugacity, and the free-volume theory for the calculation of the permeability was applied. As further non-ideal effects, concentration polarization, the Joule-Thomson effect and pressure loss for low Reynolds numbers are considered. The membrane unit is calculated using geometry and free-volume parameter for an envelope type membrane module of the Helmholtz-Zentrum Geesthacht, Germany.
The carbon dioxide concentration could be reduced from 22 to 10 mol % with an one-stage membrane unit. The product losses are calculated as the ratio of the molar ethylene purge to the incoming ethylene mole flow. These losses were found in the range of 30 % for the rubbery membrane material and of 10% for the glassy membrane. While the glassy membrane has a higher carbon dioxide/ethylene selectivity, with a low trans-membrane flux. This causes higher membrane area, in comparison with the rubbery membrane material. The product loss has to be evaluated economical in comparison to the energy saving, when using an absorption process. The product loss can be reduced by a two-stage membrane process and is described in the next section.

3.3. The two stage membrane process

The application of a two-stage membrane unit can reduce the product loss, whereas the carbon dioxide reduction fulfills the design task for the alternative process design. The combination of rubbery and glassy membrane material was studied and it was found that using the rubbery membrane material in the first unit and the glassy material in the second unit could decrease the product loss. The results are presented in Table 7. Resulting by the simulation study, optimal feed temperature and operating pressure was found and the ethylene losses were reduced down to 2%. The electrical energy demand for the recompression unit of the second stage was found with 2.7 MJ/kg_{CO2}.

Table 7: Technical requirements of the two-stage membrane process

Membrane area 1st Stage	Feed Temperature 1st Stage	Membrane area 2nd stage	Feed Temperature 2nd stage	Feed Pressure 2nd stage	Product losses
1.75 m²	20 °C	1 m²	15°C	32 bar	2 vol%

Thus, the energy demand for the entire sharp separation increases, while the product loss decreases. The economical optimum of energy demand and product losses has to be found in this project.

4. Miniplant application

Simultaneously to the process synthesis, a miniplant was designed and builds for model validation and investigation of the entire process. The experimental studies showed long term effects like regeneration effects of the absorbent, deactivation of the catalyst and allows validating the theoretical models. The units are studied at first stand-alone, to optimize them. Table 8 summarizes the basic engineering details of the purification part, especially the absorption column design.

Table 8: Technical and hydrodynamic operation conditions of the absorption/desorption process

Packing height [m]	Column diameter [mm]	Max. F-factor [$Pa^{0,5}$]	Gas feed [kg/h]	Packing section [-]	Packing capacity [m^2/m^3]	Maximum liquid load [m^3/m^2h]	Top pressure [bar]
5	40	0.6	21	50	450	55	32

The simultaneous design and construction requires high flexible units, to handle the changes in carbon dioxide concentration. This target can be reached by using membrane units for enlargement or reduction the capacity easily. The miniplant is shown in figure 3, left side. The results of comparison of the concentration profile for the experiments with the simulation presented in figure 3 right side. This experiment is based on the reference absorbent 30 wt% Monoethanolamine.

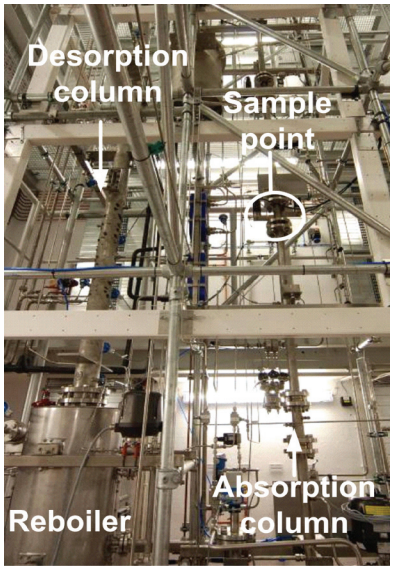

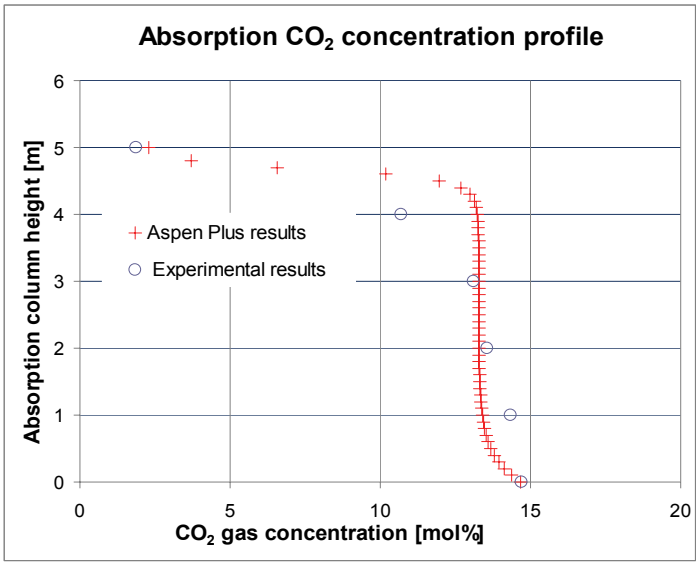

Figure 3: left side: Photo of the installed absorption and desorption process in a miniplant scale, right side: imulation results and comparison with experiments of the concentration profile

5. Conclusion – The hybrid separation process

Facing the required purity of the product stream and the lack of high thermal energy demand of 3.6 MJ/kg_{CO2} for the regeneration step in an absorption process, the use of a membrane unit for enrichment can reduce the overall thermal energy demand to 1.6 MJ/kg_{CO2} for the entire sharp separation of carbon dioxide from the OCM Product stream. To reduce the ethylene loss from 9 % down to 2%, a second membrane stage can be applied with different membrane materials. For the combination of a rubbery membrane and a glassy membrane with optimal process conditions of Table 7 an electrical energy demand of 2.7 MJ/kg_{CO2} can be reached. Carbon dioxide utilization alternatives are given and have to evaluate in further research.

Acknowledgements

The authors acknowledge the support from the Cluster of Excellence "Unifying Concepts in Catalysis", coordinated by the Berlin Institute of Technology and funded by the German Research Foundation (DFG).

Literature

[1] A. Behr, A. Kleyensteiber, U. Hartge, *Chem.Ing.-Tech*. **2010**, 82, 201. DOI: 10.1002/cite.200900122

[2] K. R. Hall, *Catalysis Today* **2005**, 106, 243. DOI: 10.1016/j.cattod.2005.01.176

[3] S. Jaso, H. R. Godini, H. Arellano-Garcia, G. Wozny, *Computer Aided Chemical Engineering* **2010**, 28, 781. DOI: 10.1016/S1570-7946(10)28131-2

[4] Kohl A. L., Nielsen R., „Gas Purification", Gulf Pub Co, 5th edition, 1997

[5] E.E. Wolf (Ed), Methane Conversion by Oxidative Processes, Fundamental and Engineering Aspects. Van Nostrand Reinhold, New York, 1992

[6]Bird, Stewart, Lightfoot, Transport Phenomena, 2. Edition, John Wiley&Son, 2006

[7] H. P. Mangalapally, R. Notz, S. Hoch, N. Asprion, G. Sieder, H. Garcia, H. Hasse, *Energy Procedia 1*, **2009**, 963-970, DOI: 10.1016/j.egypro.2009.01.128

[8] Barnicki and Fair, Separation System Synthesis: A Knowledge-Based Approach. 2. Gas/Vapor Mixtures, Ind. Eng. Chem. Res. 1992, 31, S. 1679-1694

[9] Pakseresht S., Equilibrium Isotherms for CO, CO_2, CH_4, C_2H_4 on the 5A molecular sieve by a simple volumetric apparatus, Separation and Purification Technology, 2002, Vol. 28, iss. 1, p. 53-60

[10] A. Car, Pebax®/polyethylene glycol blend thin film composite membranes for CO2 separation: Performance with mixed gases, 2008, Separation and Purification Technology, vol. 62, p. 110–117

[11] O. K. Varghese, M. Paulose, T. J. LaTempe, C.A. Grimes, High-rate solar photocatalytic conversion of CO_2 and water vapour to hydrocarbon fuel, 2009, Nanoletters, Vol. 9. No. 2. 731-737;

[12] V. Abidin, C. Bouallou, D. Clodic, Valorization of CO_2 Emissions into Ethanol by an Innovative Process, 2011, Proceeding for 14th conference on Process Integration, Modelling and Optimisation for Energy Saving and Pollution Reduction, Florence, Italien

[13] A. Egbedi, J.J. Spivey, Effect of H2/CO ratio and temperature on methane selectivity in the synthesis of ethanol on Rh-based catalysts, Catalysis Communications, 2008, (9)

18th International Conference Process Engineering and Chemical Plant Design
Günter Wozny and Łukasz Hady, Editors

WALTER MARTINI*, GÜNTER WOZNY*

HYPERBRANCHED POLYMERS FOR CO_2 CAPTURE: DATA ESTIMATION AND PROCESS SIMULATION

Abstract

The oxidative coupling of methane (OCM) is currently being intensively investigated at the Technical University of Berlin. However, during the process CO_2 is being produced, which then has to be separated in a downstreaming process. This is usually done by an absorption and desorption step using aqueous amine solutions and accompanied by high energy demands for regeneration. However, hyperbranched polymers have recently attracted attention as promising candidates for gas absorbents with a high capacity for CO_2 and with large selectivities. Though, only little physical data is available in literature. Therefore, missing parameters were estimated for the hyperbranched polymer Boltorn U3000 based on its structure only and used afterwards for the simulation of the CO_2 separation process within Aspen Plus.

Keywords: Hyperbranched Polymers, Carbon Capture, Absorption, Parameter Estimation

1. Introduction

As the main constituent of natural gas, the development of processes that allow the conversion of methane to more valued products is of strong economic interest. A chemical of particular importance is ethylene, which can be obtained via oxidative coupling of methane (OCM). It is a surface induced gas phase reaction and its overall yield is still limited up to 30%. Extensive research has resulted in a reasonable understanding of the elementary reactions that occur within OCM [1]. Besides ethylene, unwanted by-products such as carbon dioxide are produced and have to be cleaned in a downstreaming process subsequent to the reaction.

* Chair of Process Dynamics and Operation, Berlin Institute of Technology, Sekr.KWT-9, Str. des 17.Juni 135, D-10623 Berlin, Germany.

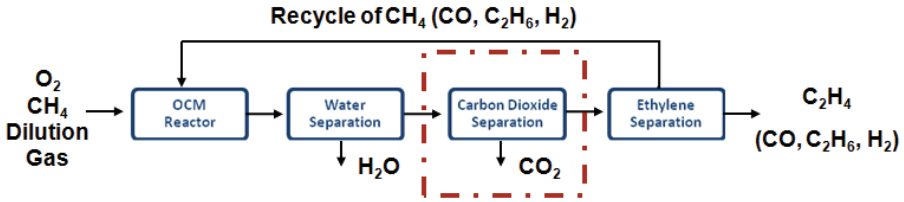

Fig. 1. Process flow diagram of the OCM process

Various alternatives for the OCM process have been proposed so far, such as the OXCO process, the UCC process, the ARCO process, the Suzuki process, the Turek-Schwittay process or the Co-Generation process [2]. All of them have in common that the product separation under high pressure and the recycling of unreacted methane is of most importance for the process economics [3]. Because of its current low yield and challenges for an efficient downstream process, OCM has not been applied in the industry yet and is currently being focused on by the German Cluster of Excellence UniCat [1]. Therefore, a miniplant has been built at the Chair of Process Dynamics and Operation of the Technical University of Berlin, where fundamental studies of process alternatives and the effect of recycles and efficiencies of each process unit are being investigated [4]. Figure 2 shows its generalized layout.

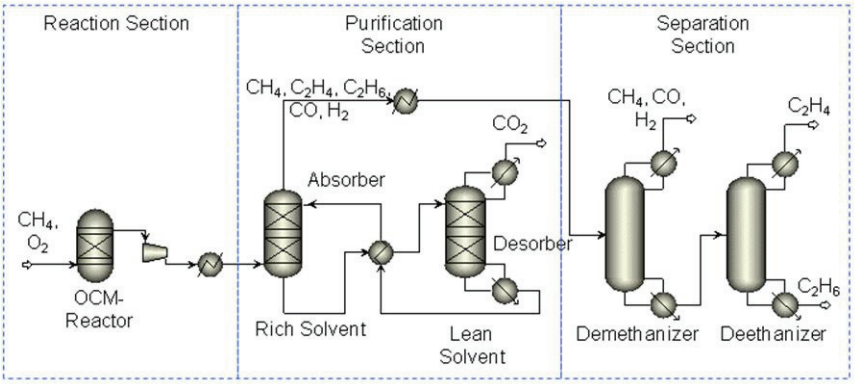

Fig. 2. Simplified process flow diagram of the OCM

The whole OCM process is divided into three general sections: subsequent to the reaction, a purification step takes place, where carbon dioxide has to be removed from the raw gas completely. Finally, in the separation section, the desired product, ethylene, is being separated from all other components, which may be recycled to the reaction section again.

The removal of carbon dioxide herein plays an important role for the economic efficiency of the overall process, and therefore, is being focused on in this work. The UOP Selexol ® or the Lurgi Rectisol ® processes are examples of known physical absorption processes, which use dimethyl ether and cold methanol, respectively. Due to a nearly

similar solubility of the product and the carbon dioxide in the liquid, those physical absorption processes cause high product losses of more than 30 vol%.

On the other hand, chemical absorption using aqueous amine solutions has been extensively used for the removal of CO_2 from gas streams in many industries and was therefore chosen for the miniplant. It involves one or more reversible chemical reactions between CO_2 and an amine (such as MEA) in an absorption column. Desorption of the absorbed carbon dioxide then proceeds via a thermal regeneration process, which is, in general, very energy intensive. The amine solution has a limited lifetime due to degradation through oxidation of the amine. In addition, corrosion problems are usually observed for the aqueous amine process. The high energy demand for regeneration and solvent losses are the main disadvantages of using aqueous amine solutions as washing fluids.

In this work, hyperbranched polymers are being investigated as an alternative for absorbents for carbon dioxide, since they have been shown to be promising candidates for gas absorbents with a high capacity for CO_2 and with large selectivities [5]. Thermodynamic data had to be generated to be able to model and simulate absorption and a desorption process to compare the use of hyperbranched polymers to MEA.

2. Hyperbranched Polymers

Currently, four major classes of polymers can be distinguished in accordance with their properties and polymeric architecture. Dendritic polymers herein represent the fourth class and are highly branched globular macromolecules. They can be subdivided into four subsets that are related to the degree of structural control, i.e. random hyperbranched polymers, dendrigraft polymers, dendrons, and dendrimers [6].

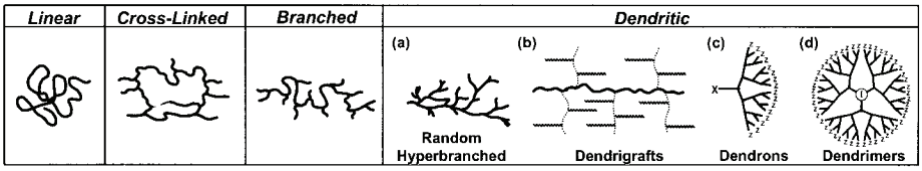

Fig. 3. Representation of the four major classes of macromolecular architectures [6]

Dendrimers show a well defined, monodisperse, perfectly branched structure and have a large number of functional end groups [7]. Their generation requires absolute control of all synthesis steps and makes large-scale production difficult and hence expensive. However, many applications do not require structural perfection. Therefore, using hyperbranched polymers can circumvent this major drawback of dendrimers [8].

Unlike dendrimers, randomly branched hyperbranched polymers with similar properties can be easily synthesized via one-step reactions and therefore represent economically promising products also for large-scale industrial applications. At room temperature, many branched polymers exhibit low viscosities in the pure state as well as in solution due to the absence of chain entanglement.

The structure of dendritic polymers resembles that of a treetop. They possess a core from which multiple branches are extended. Each branch can be source for more branches and hence different generations, thus giving exponential growth, in both end-group functionalities and molecular weights. The properties of dendritic polymers differ strongly from those of linear polymers of the same molar mass (less flexibility, lower entanglement degree, a significant chain-end effect, lower viscosity in solution and in the molten state, high solubility in common solvents, a different relationship between hydrodynamic volume and molar mass, and a different origin of the glass transition temperature) [9].

Potential applications of hyperbranched polymers range from the use as selective solvents in distillation of azeotropic mixtures or extraction to the control of flow characteristics, as well as the use as drug delivery system and many more.

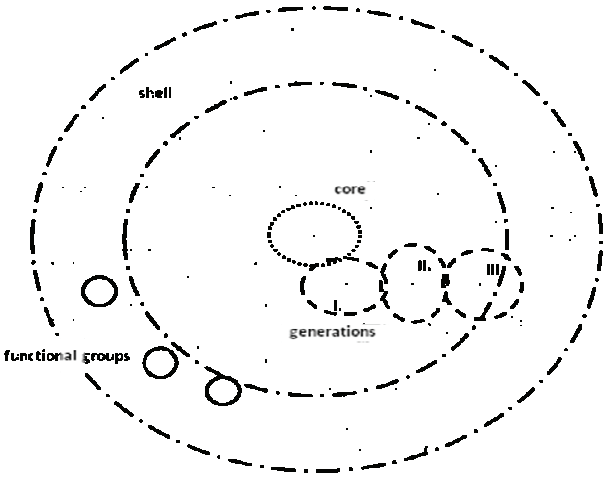

Fig. 4. Boltorn® U3000 molecule by Perstorp AB (Sweden)

In this work, the dendritic polymer Boltorn® U3000 by Perstorp AB was applied to carbon dioxide absorption. Because of its polydispersity, the molecular structure shown in Figure 4 is only one possible occurrence, which has been used for the simulation. The core consists of a polyalcohol, i.e. pentaerythritol (PE). The hyperbranched structure is built from 2,2-Dimethylol propionic acid (Bis-MPA), which has the unique functionality of one COOH-group and two OH-groups. The shell consists of a large number of OH-groups, which are possible locations for CO_2 to attach to. Previous measurements of Henry coefficients already have shown the potential of Boltorn U3000 for the absorption of carbon dioxide [10].

3. Estimation of Thermodynamic Data

In order to be able to simulate the absorption and desorption process using Aspen Plus, several physical and thermodynamic data is needed. Only very little data is available for

Boltorn U3000 in literature (such as density or viscosity at standard conditions). Therefore, a data estimation step had to be carried out first. To do this, several components that are part of the Boltorn molecule or consist of similar functional groups and where detailed data is available (see Figure 5), were chosen for a prior study of different estimation methods.

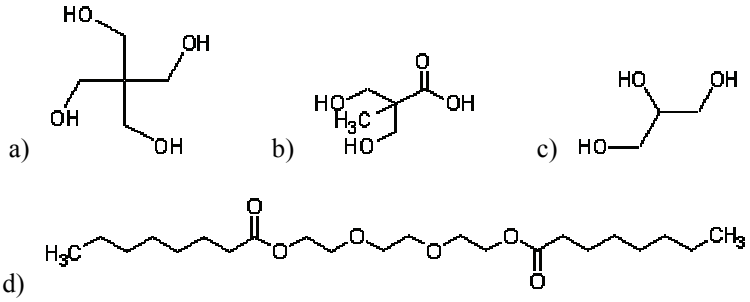

Fig. 5. Applied components: a) PE b) Bis-MPA c) Glycerol d) Triethylene-Glycol-Dioctanate

The results in Table 1 show the mean deviation for each parameter of all reference components between estimation and literature, based on the best method available.

T a b l e 1

Deviation of estimated thermodynamic data from literature

	Method	**mean deviation**
T_B	Gani [11]	-5,9%
T_C	Ambrose [12]	8,9%
p_C	Ambrose	14,6%
ν_C	Joback [13]	1,2%
Δh_{LV}	Gani	5,7%
Δh_f	Gani	0,6%
Δg_f	Gani	2,2%
ω	Definition	1,1%

This set of estimation methods was then applied to the parameter estimation for the hyperbranched polymer Boltorn® U3000. For parameters that are not included in Table 1, such as the relative van der Waals volumes and surface areas of the pure chemicals used for instance in UNIFAC, there was only one method available and hence no choice had to be taken. The vapor pressure was estimated based on the observation that, in general, it is very low or not existent for hyperbranched polymers. Additionally, molar liquid volumes and viscosities for a temperature range of 280 to 350 K were provided through earlier measurements [14].

To evaluate the quality of the estimations, Henry coefficients were then calculated based on the estimations and compared to measured values. As can be seen in Figure 6,

both agree rather well for both, methane and carbon dioxide in Boltorn U3000. Especially the latter is of most importance for the simulation of the absorption process.

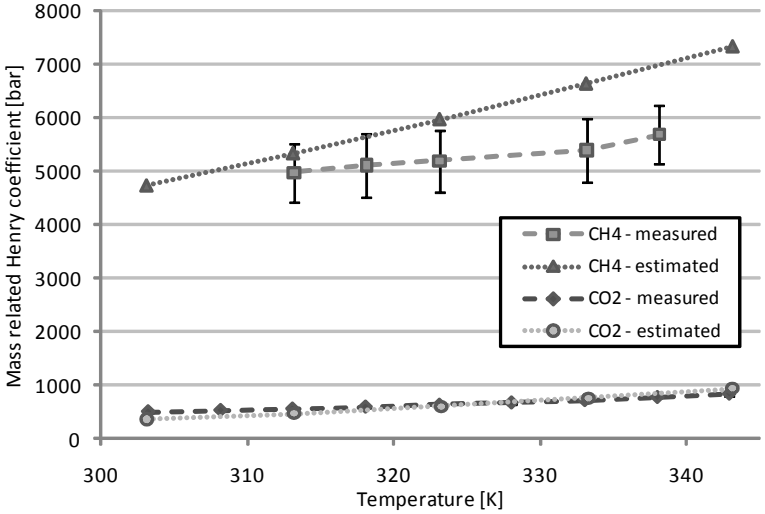

Fig. 6. Comparison of mass related Henry coefficients of CO_2 and CH_4 in Boltorn U3000 based on measurements and derived from data estimation

4. Simulation of the absorption and desorption process

A model for the simulation of the CO_2 separation was implemented in Aspen Plus as shown in Figure 7. The same conditions as in the miniplant were used with the same packings, 50 theoretical stages and a maximum pressure of 32 bar in the absorption column, 42 theoretical stages and 2 bar in the desorption column, respectively.

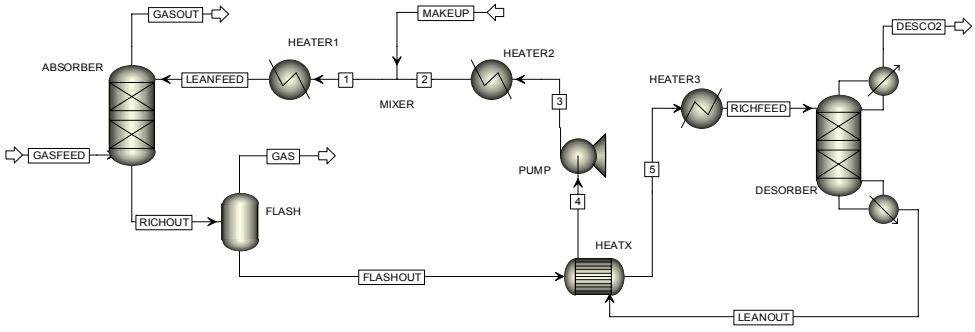

Fig. 7. Aspen Plus model of the absorption an desorption process

The gas feed with a flow of 10 kg/h consisted of 41.6% CO_2, 37.9% CH_4, 7.1% C_2H_6, 13.2% C_2H_4 and 0.2% H_2O. The aim of the absorption was to remove 90% of the carbon dioxide from the raw gas. As solvents, both the hyperbranched polymer Boltorn U3000 with small amounts of water as well as, for comparison, an aqueous solution of

monoethanolamine (MEA) was applied. For MEA, the built-in ELECNRTL model with the Redlich Kwong equation of state was used. Reactions were included in the Rate-Sep model by the MEA-REA package, where kinetic parameters were adjusted to literature [15]. For Boltorn U3000, the UNIFAC Dortmund model was used and no reaction was assumed.

The simulation results obtained show that for the polymer a mass flow of 220 kg/h was needed to meet the 90% CO_2 removal requirement compared to 55 kg/h of the chemical absorbent MEA. This is due to its lower capacity for carbon dioxide. Because of its relatively high viscosity and for an easier operation of the desorption column (strip-steam), small amounts of water were added to the solvent Boltorn U3000. The effects of this on the separation degree of different gases in the absorption column are shown in Table 2.

T a b l e 2

Separation degree of the gaseous components in the absorption column

Water content	none	1 weight%	5 weight%
CO_2	90.07%	90,13%	90,08%
CH_4	3.58%	3,80%	4,72%
C_2H_4	28.80%	32,58%	50,22%
C_2H_6	27.27%	29,38%	36,81%

Apparently, the added water has a negative effect especially on the selectivity concerning CO_2 and the main product ethylene. Therefore, it should be minimized to a degree, where operation of the desorption column is still feasible.

T a b l e 3

Heat duties per kg CO_2 required for the regeneration of the solvent

	MEA	Boltorn U3000
Heat Duty [kJ/kg CO_2]	2980	202
Pumping [W]	44	284

The main advantage of using a physical absorbent comes into play, when looking at the heat duty that is required for regeneration of the solvent, which usually accounts for the highest part of the whole energy demand. For chemical absorbents, typically absorption is exothermal and, hence, this energy has to be spent in the desorption column. In contrast to that, physical absorbents, such as the applied hyperbranched polymer, only need to be heated to a certain temperature for the CO_2 desorption process to take place. This effect can be seen in Table 3, where the energy requirement for Boltorn U3000 is a lot smaller than that for the aqueous amine solution. On the other hand, it has to be noted that, in case of hyperbranched polymers, for instance pumping requires more effort.

5. Conclusions

Thermodynamic and physical data of the hyperbranched polymer Boltorn U3000 were estimated based on its structure only. The results in terms of Henry coefficients regarding CO_2 and CH_4 showed good agreement with measured values. A model was built within Aspen Plus to simulate the absorption and desorption process on miniplant scale. The comparison of the physical absorbent Boltorn U3000 and the chemical absorbent MEA showed a very low energy demand for the former but some drawbacks concerning selectivities and operability because of its high viscosity. Therefore, further research is required to validate simulation results and to investigate additional hyperbranched polymers.

6. Acknowledgements

The authors acknowledge the support from the Cluster of Excellence „Unifying Concepts in Catalysis“ coordinated by the Technical University of Berlin (TU Berlin) and funded by the German research foundation – Deutsche Forschungsgesellschaft – DFG.

Symbols

T_B boiling point temperature
T_C critical temperature
p_C critical pressure
ν_C critical molar volume
Δh_{LV} heat of vaporization
Δh_f heat of formation at 298.15 K
Δg_f Gibbs free energy of formation at 298.15 K
ω Pitzer azentric factor

Literature

[1] Unifying Concepts in Catalysis, http://www.unicat.tu-berlin.de/.
[2] Wolf E.E., Methane conversion by oxidative processes, Van Nostrand Reinhold 1992.
[3] Salerno D., Arellano-Garcia H., Wozny G., AICHE Annual Meeting, Salt Lake City, USA, (2010).
[4] Stünkel S., Repke J.-U., Schomäcker R., Wozny G., Chemie Ingenieur Technik, **82**, (2010), 1416-1417.
[5] Rolker J., Seiler M., Mokrushina L., Arlt W., Ind. Eng. Chem. Res., **46**, (2007) 6572-6583.
[6] Tomalia D.A., Fréchet J.M.J., Journal of Polymer Science: Part A: Polymer Chemistry, **40**, (2002) 2719-2728.
[7] Tomalia D.A., Polymer Journal, **17**, (1985) 117-132.
[8] Seiler M., Fluid Phase Equilibria, **241**, (2006) 155-174.
[9] Zagar E., Zigon M., Macromolecules, **35**, (2002) 9913-9925.
[10] Martini W., Arellano-Garcia H., Wozny G., AIChE Annual Meeting, Salt Lake City, USA, (2010).
[11] Constantinou L., Gani R., O'Connel J.P., Fluid Phase Equilibria, **103**, (1995), 11-22.
[12] Ambrose D., Journal of Applied Chemistry and Biotechnology, **26**, (1976), 711-714.

[13] Joback K.G., Ph. D. dissertation, The Massachusetts Institute of Technology, Cambridge, Mass., (1984).
[14] Martini W., Arellano-Garcia H., Wozny G., Jahrestreffen Fachausschuss Fluidverfahrenstechnik, Fulda, Germany, (2011).
[15] Kuckaa L., Mueller I., Kenig E. Y., Gorak A., Chemical Engineering Science, **58**, (2003), 3571-3578.

18th International Conference Process Engineering and Chemical Plant Design
Günter Wozny and Łukasz Hady, Editors

VERENA LÖFFLER*, MATTHIAS KRAUME*

DEVELOPMENT OF MIXED-MATRIX MEMBRANES FOR SEPARATION OF GASEOUS HYDROCARBONS

Abstract

In this work mixed-matrix gas separation membranes were produced and tested for CH_4 / n-C_4H_{10} separation. The fundamental principle of mixed-matrix membranes is described on the basis of the Maxwell model to illustrate the requirements for membrane material selection. The rubbery polymer PDMS and a micro porous carbon adsorbent have been chosen as membrane components and mixed-matrix composite membranes of different phase fractions have been produced. The permeance and selectivity has been measured with a gas mixture of 95(vol.)% CH_4 methane and 5(vol.)% n-C_4H_{10}.

Keywords: gas permeation, mixed-matrix membranes, Maxwell model

1. Motivation

Membrane based gas separation is a fast growing area of separation technology, that has drawn a great deal of interest in research and industry in the past 25 years[1,2]. Applications for gas permeation are for example air separation, CO_2 removal, dew point adjustment or reclaiming of gasoline vapour. Gas permeation competes with conventional gas separation processes like pressure swing adsorption or gas scrubbing. In comparison to these techniques gas permeation plants offer advantageously small footprints, simple assembly, inherent steady state operation and absence of separation agents. In some applications, like e.g. air, H_2 or CO_2 separation, the technique is accepted as an alternative to conventional gas separation processes. In other applications further development of membrane material is desirable to reduce costs and energy demand of the plants and tap the full market potential of gas permeation[2]. Separation of hydrocarbons is one of these applications. In this work new mixed-matrix membrane material is produced and tested for separation of a methane-butane mixture.

State of the art for membrane separation of hydrocarbons from lighter gases is dense rubbery polymer membrane materials, where the separation mechanism works according to

*Technische Universität Berlin, Fachgebiet Verfahrenstechnik, Sekr. Ma 5-7, Straße des 17. Juni 136, 10623 Berlin, Germany

the solution-diffusion model[3,4]. This material features solution selectivity and high fluxes. In Fig. 1, a gas permeation plant for hydrocarbon dew point adjustment of natural gas with such membranes is illustrated: The feed contains methane and different higher hydrocarbons. It is compressed to high pressure and cooled down subsequently to separate condensed components. In the membrane unit higher hydrocarbons are enriched on the permeate side whilst the lighter ones like methane are concentrated in the retentate. The recycling of permeate prevents methane loss through the permeate flow. The main energy demand of such a plant is the compressor power, the cooling power of the condenser and the power of the vacuum pump. An increase of membrane permeability and selectivity would reduce both energy demand and material costs[3]: The pressure difference and membrane area required decreases with increasing permeability. An increase of membrane selectivity would decrease gas slip of the lighter components and reduce the recycled permeate flow. A decrease of the permeate flow would again reduce compressor power, cooling power and power of the vacuum pump.

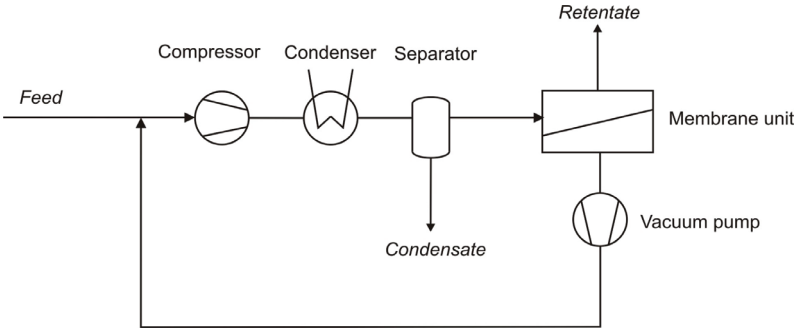

Fig. 1: Gas permeation process for dew point adjustment

However, further improvement of polymeric membranes is difficult, because the performance of polymeric membrane material is limited: The dependency of permeability and selectivity of all polymeric membrane materials underlies an upper bound, which depends on the components that are to be separated and is named Robeson Upper Bound after L.M. Robeson who first reported about this behavior in 1991. Fig. 2 shows the upper bound for CO_2/CH_4 separation[5]. It illustrates that rubbery polymers tend to have higher permeabilities with lower selectivities while glassy polymers use to have higher selectivities with lower permeabilities. But to reach the most attractive region of high selectivity and high permeability another membrane material is needed.

Accordingly inorganic materials were investigated as possible membrane material. In a number of research projects it was shown, that porous inorganic membranes, like zeolites or activated carbons, can have selectivities and permeabilities above the Robeson bound[6-8]. However these inorganic materials are difficult to produce, very brittle and expensive[9,10]. To our knowledge, no module with inorganic gas permeation membranes has come to market so far. The next generation of gas separation membranes could be some hybrid material combining the advantages of polymeric and inorganic materials.

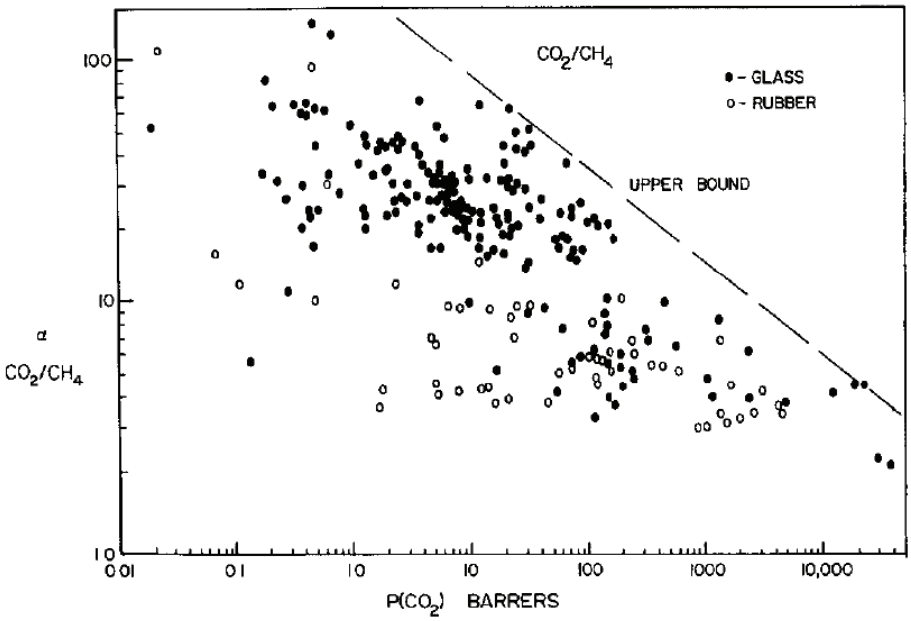

Fig. 2: Robeson Upper Bound for CO_2/CH_4 separation [5]

2. Mixed-matrix membranes

An innovative concept for membrane material is the combination of polymeric and inorganic materials in mixed-matrix membranes[2,11]. These consist of a dense polymeric matrix, in which inorganic solid material is dispersed. Accordingly mixed-matrix membranes are supposed to be easily produced and mechanically stable like polymeric membranes. They can also have separation properties close to or even above the Robeson Bound like inorganic membranes. Material selection is mostly important to produce a successful mixed-matrix membrane[7,8,11], because it is necessary that transport mechanisms through both phases prefer the same component.

Generally the total permeability P_{tot} depends on the ones of the single phases P_d and P_c and the dispersed phase volume fraction φ_d. To achieve an improvement in total permeability with respect to the pure polymer, it is necessary that the dispersed phase has got a higher permeability than the polymer. At the same time the dispersed phase needs to have a higher selectivity than the polymer to enhance total selectivity.

This fundamental character of mixed-matrix membranes can be described very clearly by the Maxwell model, which is a simple, but generally accepted model for mixed-matrix membranes[7,8]. It assumes an uniform film, in which a second phase is dispersed homogeneously, as shown in Fig. 3. Originally the model was developed to calculate the

conductivity of composite materials, but it is also usable to calculate gas permeation through mixed-matrix membranes even though it underlies some limitations.

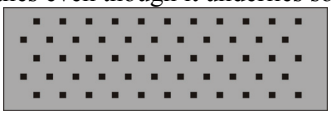

Fig. 3: Mixed-matrix membrane according to the Maxwell model

According to the Maxwell model the total permeability of a gas component A through a mixed matrix layer is

$$P_{tot}^{A} = P_{c}^{A} \frac{P_{d}^{A} + 2P_{c}^{A} - 2\varphi_{d}\left(P_{c}^{A} - P_{d}^{A}\right)}{P_{d}^{A} + 2P_{c}^{A} + \varphi_{d}\left(P_{c}^{A} - P_{d}^{A}\right)} \tag{1}$$

The total selectivity for a mixture of A and B can be calculated as follows:

$$S_{tot}^{AB} = \frac{P_{tot}^{A}}{P_{tot}^{B}} \tag{2}$$

As shown in Fig. 4 the Maxwell model predicts that highest selectivity improvements are possible, when the permeabilities of both phases are similar. In contrast, no selectivity improvement is seen when permeability in the dispersed phase is significantly higher or lower than in the polymer phase. Therefore, an adequate combination of polymer and solid material is crucial for successful preparation of mixed-matrix membranes.

Furthermore, the effect increases with the dispersed phase volume fraction. So it will be advantageous to realize high dispersed phase volume fractions as long as the membrane structure is not damaged.

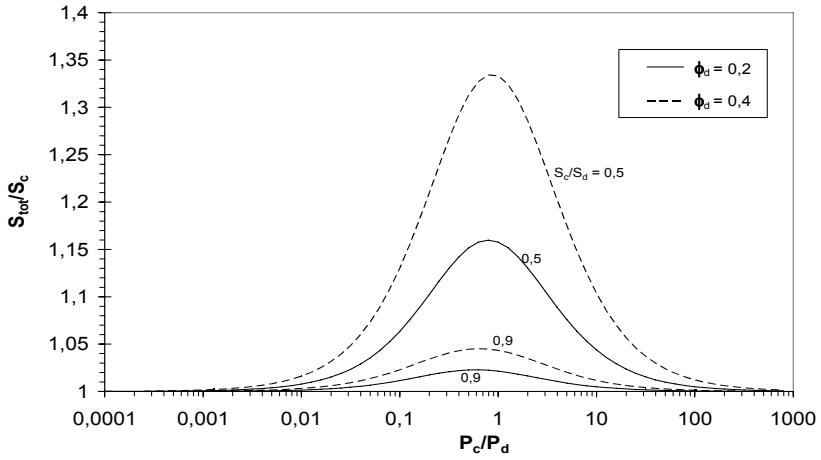

Fig. 4: Prediction of mixed-matrix membrane selectivity according to the Maxwell model

3. Material selection

Since rubbery polymeric membranes are state of the art for separation of hydrocarbons from lighter gases a rubbery polymer, Polydimethylsiloxan (PDMS), was chosen as continuous phase of the mixed-matrix membranes in this work. PDMS is one of the most common rubbery polymers used not only as membrane material but also in paper, food or cosmetic industry. Like other rubbery polymers PDMS is solubility selective, so higher hydrocarbons permeate better than lighter gases.

Accordingly, an inorganic phase with preferential adsorption and diffusion of higher hydrocarbons is needed. Fillers which are diffusion selective and prefer permeation of lighter gases are not suitable. Therefore, most molecular sieves are excluded. Some micro porous materials have been studied for solubility based separation in the last 15 years[12-15]. The transport mechanism is a selective surface flow of the adsorbed molecules where high selectivities are possible. If capillary condensation of the adsorbed species occurs, even higher selectivities are possible. In that case the other components are completely excluded from the pores. In this work a micro porous carbon adsorbent was chosen as dispersed phase, produced by the Blücher GmbH, Erkrath. The main characteristics of the chosen carbon are listed in Table 1.

However development of sorption selective mixed-matrix membranes does not only require a careful material selection but also an optimization of process parameters, because surface diffusion and capillary condensation depend on parameters like temperature, pressure and concentration.

T a b l e 1

Characteristic parameters of the carbon adsorbent

Average pore diameter	19	A
Total pore volume	0,64	cm^3/g
BET surface area	1361	m^2/g
Particle size distrubution	1 - 30	µm
Average particle size	9	µm

4. Membrane preparation

In this work mixed-matrix composite membranes were produced. The mixed-matrix separation layer was coated on a highly permeable support structure consisting of a polymeric non-woven with a microporous, polymeric toplayer. The coating solution was prepared by suspending a certain amount of carbon particles in polymer solution. The suspension was applied manually with a stainless steel roll. After preparation the membranes were dried.

In Fig. 5 the structure is illustrated schematically and two pictures taken with scanning electron microscopy (SEM) are shown. The pictures illustrate that particles are embedded completely in the polymer matrix. Further no gaps have been seen between polymer and carbon like they were found by other groups who produced mixed-matrix membranes with glassy polymers[9]. However, the membrane surface is not completely even.

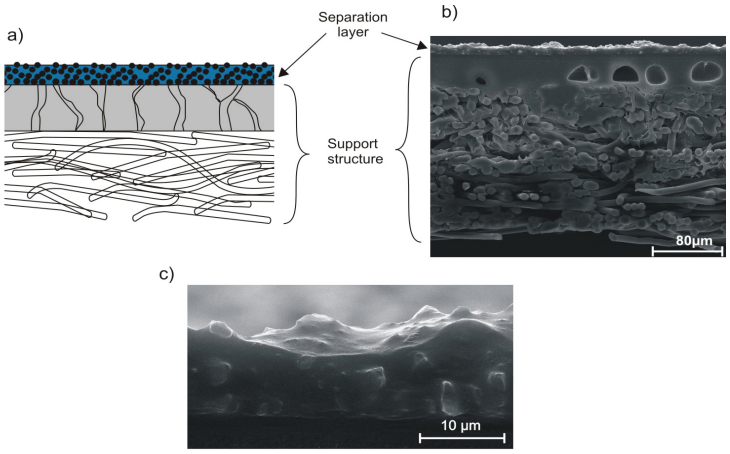

Fig. 5: Mixed-matrix composite membrane: a) schematic; b) SEM picture; c) magnification of separation layer

5. Measurement of permeance and selectivity

The separation properties of the mixed-matrix membranes were tested at the Helmholtz-Zentrum Geesthacht, Centre for Membranes and Structured Materials. A simplified flowchart of the setup is shown in Fig. 6.

The feed consisted of 95 (vol.)% methane and 5(vol.)% n-butane. Feed pressure was varied between 10 bar and 40 bar and permeate pressure was 1 bar. Composition of feed and permeate has been measured online by a gas chromatograph. The feed temperature was set to 25 °C.

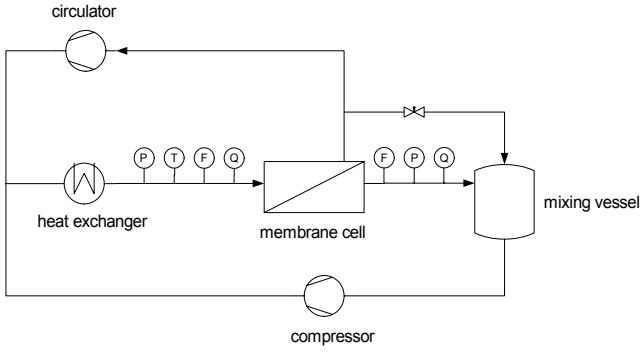

Fig. 6: Setup for permeability measurements

6. Results

The permeances L^i of both components methane and n-butane were calculated according to equation (3) from the detected values of permeate flow $\dot{V}_P$, feed pressure p_F, permeate pressure p_P, feed composition x_F^i, permeate composition x_P^i and membrane area A_M. Fugacity coefficients φ^i have been considered on the high pressure side.

$$L^i = \frac{\dot{V}_P \, x_P^i}{\left(\varphi^i \, p_F \, x_F^i - p_P \, x_F^i\right) A_M} \tag{3}$$

Selectivity S was calculated as the following ratio

$$S = \frac{L^{butane}}{L^{methane}} \tag{4}$$

For calculation of permeability the membrane thickness was measured with SEM.

$$P_i = L_i \, \delta \tag{5}$$

Dispersed phase volume fraction φ_d was calculated from the dispersed phase mass fraction in the coating suspension ξ_d, particle density and density of the cross-linked and dried polymer. Mean values of the results are given in Table 2.

T a b l e 2

Experimental results

	ϕ_δ %	ξ_δ %	δ µm	L_{butane} Nm³/(h bar m²)	P_{butane} 10^4 barrer	S [-]
PDMS	0	0	15,4	3,81 $^{-1,05}_{+1,12}$	1,41 $^{-0,39}_{+0,42}$	17,2 $^{-1,36}_{+1,18}$
MMM 1	31	3,8	15,1	2,80 $^{-0,59}_{+0,46}$	1,24 $^{-0,26}_{+0,21}$	18,3 $^{-0,59}_{+0,6}$
MMM 2	43	6,2	14,8	3,58 $^{-0,78}_{+0,49}$	1,59 $^{-0,34}_{+0,22}$	15,9 $^{-0,4}_{+0,7}$

The experimental values have been used to calculate the permeability of the dispersed phase according to the Maxwell model. Corresponding to equation (1) P_d of a component A is

$$P_d^A = P_{tot}^A \frac{P_c^A \cdot 2\left(1-\varphi_d\right) - P_{tot}^A \left(2+\varphi_d\right)}{\frac{P_{tot}^A}{P_c^A} \cdot \left(1-\varphi_d\right) - \left(1+2\varphi_d\right)} \tag{6}$$

The following two figures show the results for mixed-matrix membranes with dispersed phase fraction φ_d = 0,31 and φ_d = 0,43. Fig. 7 shows, that a slightly improvement in selectivity has been reached with respect to the pure PDMS. The experimental values scatter in the range of P_c/P_d = 10 and S_c/S_d = 0,7. Both values show, that material selection needs further improvement. A carbon with both higher permeability and selectivity is needed. On the other hand Fig. 8 shows, that improvement of phase fraction to φ_d = 0,43 did not improve selectivity as the Maxwell model predicts. Instead selectivity has decreased below the one of PDMS and permeability is around the value of PDMS. This behaviour can be explained by the microscopic structure of the membrane. The higher dispersed phase fraction led to a more irregular coating. The SEM analyses showed that thickness of the separation layer differed between 10 and 30 µm and that the surface was

very rough. Therefore it is possible, that the coating has got defects, which lower selectivity and enhance permeability with respect to the membrane with φ_d = 0,31. Moreover the determination of the mean thickness was most probably less exact for φ_d = 0,43.

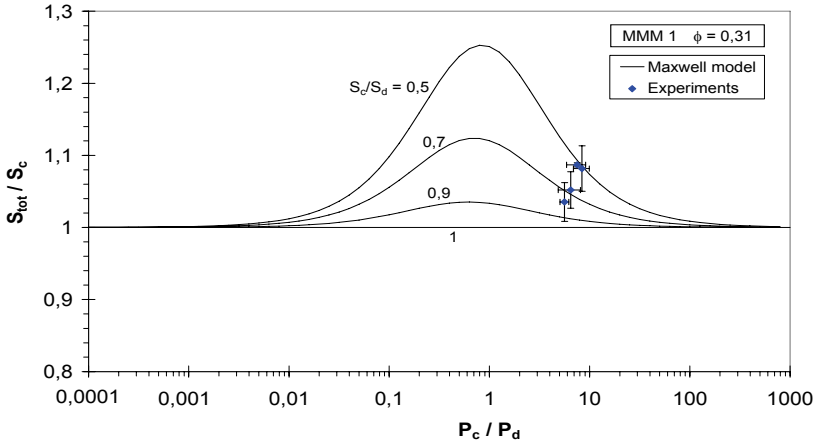

Fig. 7: Experimental results for φ_d = 0,31 and comparison with the Maxwell model

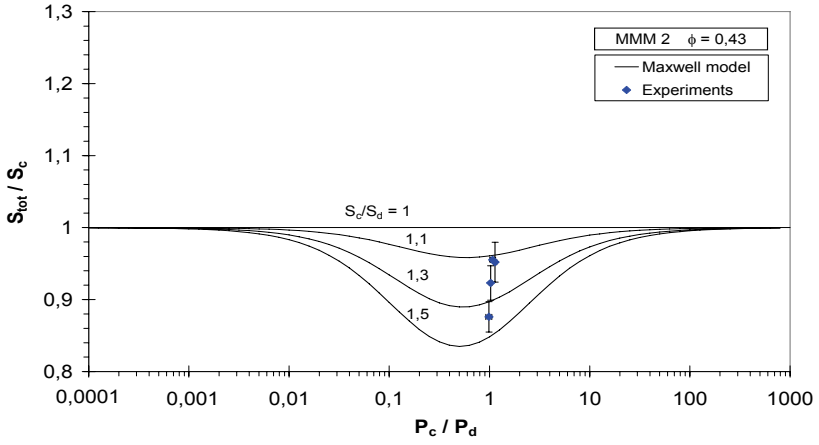

Fig. 8: Experimental results for φ_d = 0,43 and comparison with the Maxwell model

7. Conclusions

Preparation of mixed-matrix membranes and their optimization for a gas separation problem is a both promising and challenging task. It was shown that these hybrid membranes with an organic matrix and inorganic fillers could be the next generation of gas separation membranes because they combine the advantages of polymeric and inorganic

material. However, material selection is crucial for their separation performance. In this work mixed-matrix membranes of PDMS and carbon adsorbent were successfully produced and tested for CH_4/n-C_4H_{10} separation. Analysis of the experimental results with the Maxwell model showed, that further investigations and improvement of the dispersed phase is needed. But at the same time the process parameters at permeability measurement need to be varied and investigated carefully, because performance of solubility selective mixed-matrix membranes is not only depending on membrane material but also on process conditions as pressure, temperature and concentration.

8. Acknowledgements

The authors whish to thank their cooperation partners Helmholtz-Zentrum Geesthacht, Centre for Membranes and Structured Material, where permeability measurements have been carried out, and Blücher GmbH, who produced and supplied the carbon adsorbents.

Symbols

L	permeance
P	permeability
p	pressure
S	selectivity
x	molar fraction
δ	thickness of separation layer
φ^i	fugacity coefficient
φ_d	dispersed phase fraction
ξ_d	mass fraction of carbon in coating suspension

Indices:

A,B	any gaseous component
c	continuous phase
d	dispersed phase
F	feed
I	component (methane, n-butane)
P	permeate
tot	total

Literature

[1] Baker, R. W.: Membrane Technology and applications; 2. ed.; John Wiley and Sons: Hoboken, 2004.

[2] Baker, R. W.: Industrial & Engineering Chemistry Research, **41**, (2002), 1393-1411.

[3] Ohlrogge, K.; Wind, J.; Brinkmann, T. In Comprehensive membrane science and engineering; Drioli, E., Giorno, L., Eds.; Academic Press (Elsevier): Oxford, 2010; Vol. 2.

[4] Ohlrogge, K.; Wind, J.; Peinemann, K. V.; Stegger, J. In Membranen; 1 ed.; Ohlrogge, K., Ebert, K., Eds.; Wiley-VCH Verlag GmbH & Co. KGaA: Weinheim, 2006.

[5] Robeson, L. M.: Journal of Membrane Science, **62**, (1991), 165-185.

[6] Singh, A.; Koros, W. J.: Industrial & Engineering Chemistry Research, **35**, (1996), 1231-1234.

[7] Aroon, M. A.; Ismail, A. F.; Matsuura, T.; Montazer-Rahmati, M. M.: Separation and Purification Technology, **75**, (2010), 229-242.

[8] Chung, T. S.; Jiang, L. Y.; Li, Y.; Kulprathipanja, S.: Progress in Polymer Science, **32**, (2007), 483-507.

[9] Vu, D. Q.; Koros, W. J.; Miller, S. J.: Journal of Membrane Science, **211**, (2003), 311-334.

[10] Vu, D. Q.; Koros, W. J.; Miller, S. J.: Journal of Membrane Science, **211**, (2003), 335-348.
[11] Bernardo, P.; Drioli, E.; Golemme, G.: Industrial & Engineering Chemistry Research, **48**, (2009), 4638-4663.
[12] Javaid, A.: Chemical Engineering Journal, **112**, (2005), 219-226.
[13] Sircar, S.; Rao, M. B.; Thaeron, C. M. A.: Separation Science and Technology, **34**, (1999), 2081-2093.
[14] Anand, M.; Langsam, M.; Rao, M. B.; Sircar, S.: Journal of Membrane Science, **123**, (1997), 17-25.
[15] Rao, M. B.; Sircar, S.: Journal of Membrane Science, **110**, (1996), 109-118.

18th International Conference Process Engineering and Chemical Plant Design
Günter Wozny and Łukasz Hady, Editors

MATAN BEERY*, JI JUNG LEE**, JOON HA KIM**, JENS-UWE REPKE***, GÜNTER WOZNY*

NOVEL AND INTENSIFIED PROCESS DESIGN FOR SEAWATER RO DESALINATION PRE-TREATMENT

Abstract

In this work a combined theoretical-experimental approach was applied to improve the current state of the art of seawater reverse osmosis (SWRO) pre-treatment technologies. On the one hand, a new process design software tool was developed based on steady-state simulation and evaluation of all the common state-of-the-art pre-treatment process units such as media filtration, membrane filtration, coagulation, flotation, etc. On the other hand, experimental work was carried out in order to both calibrate and validate the models as well as to explore the feasibility of new solutions that specifically address the drawbacks of current technologies. Such solutions include process integration and intensification. A novel lab-scale experimental system was set up and tested for its feasibility as a SWRO pre-treatment. The results indicate that such an integrated approach to process design in SWRO pre-treatment show a positive potential in improving the sustainability of desalination technology.

Keywords: Desalination, pre-treatment, process design.

1. Introduction

Due to fast urbanization, population growth, increase in standard of living and climate change, water stress has become a major global cause for concern in recent years. As a result, securing new water sources, for example by means of seawater desalination, is becoming a common solution in many areas of the world. Seawater reverse osmosis (SWRO) has seen a great rise in popularity as the preferred method of choice for

* Chair of Process Dynamics and Operation, TU-Berlin, Strasse des 17 Juni 135, 10623, Berlin, Germany
** Department of Environmental Science and Engineering, Gwangju Institute of Science and Technology (GIST), Gwangju, 500-712, Republic of Korea
*** Institute of Thermal, Environmental and Natural Products Process Engineering, TU Bergakademie Freiberg, Leipziger Strasse 28, 09596 Freiberg, Germany

desalination technology recently reaching annual growth rates of 15-20% [1] and a record breaking 6.6 million m^3/d of new capacity (approx. 2700 olympic swimming pools) being brought online in 2010 alone [2]. Despite showing major technical and economical improvements in the last decade (especially in the area of membrane performance and energy recovery solutions), membrane based desalination still has a long way to go in order for it to be considered a sustainable technology. The reason for that being mostly its substantial energy consumption which makes it both expensive and less "green" compared to other water treatment processes. This was confirmed in a life-cycle based sustainability assessment of desalination processes [3]. The most major step in increasing SWRO's sustainability would therefore be a reduction of its carbon footprint.

RO membranes used for seawater desalination are highly susceptible to fouling due to organic/inorganic, biological and particulate matter often present in the sea. Fouling of the RO membranes has several negative effects which decrease the plant's economical and environmental efficiencies. Such effects include reduction in production rate, higher energy and chemical consumptions, frequent membrane cleanings and replacements, increase in the plant's downtime etc. An effective, location-specific pre-treatment of the seawater is therefore a key issue in maintaining long term operational success of an SWRO plant. As a result, the design of such systems can no longer be purely done in the traditional rule of thumb and trial and error methods (as is currently still the case). The assessment of the process sustainability aspects should be predicted in a systematic and analytical way. Reaching an optimal design thus requires a multidisciplinary approach which must be performed in the planning phase of the process and not during its operation. The goal of this work is to apply a systematic approach to the process design of SWRO pre-treatment which combines theory (in the form of modeling, simulation, evaluation) and practice (lab experiments for validation and testing of new process configurations).

2. Theoretical work

The introduction of system theories and methods to chemical engineering can be traced back to the 1960's in the UK and the US. It incorporates different methodologies which assist in decision making for the creation and operation of chemical supply chains [4]. In process design the common steps include process synthesis, simulation and evaluation, which are repeated iteratively until an optimal design is found. Dudley et al. [5] indicate that PSE, in the form of process simulators and flowsheeting tools, has seen very low to practically no acceptance in the drinking water community. They suggest that the reasons for that lay in the industry's misconception of water treatment models being not accurate enough (or hard to calibrate) and the fact that water treatment plants are traditionally designed with conservative rules-of-thumb aiming at water quality rather than economic efficiency. In seawater reverse osmosis on the other hand, the economic performance of the plant and the total cost of ownership play a major role in the design considerations. As a result, several major companies in the membrane desalination market (DOW, Hydronautics, Toray, ERI etc.) offer, often free-of-charge, process simulation tools to assist the engineer with the design, assessment and optimization of SWRO processes. These tools are stand-alone easy to use graphic user interfaces (GUI) based on steady state simulations which are helpful in achieving fast and basic design solutions for the RO and energy recovery systems. However, there are currently no such tools to carry out process design

for the pre-treatment system. Its design is left for the traditional rule-of-thumb approach, relying on past experience, pilot testings and over-design. This results in sub-optimal process designs which often negatively affect the performance of the RO stage and the sustainability of the entire desalination plant [6].

Using Matlab, a GUI process systems engineering design tool was created to help fill-in this gap in the pre-treatment process design stage. It follows the synthesis-simulation-evaluation concept and relies on basic steady-state models and process parameters found in literature or laboratory/pilot experiments (figure 1).

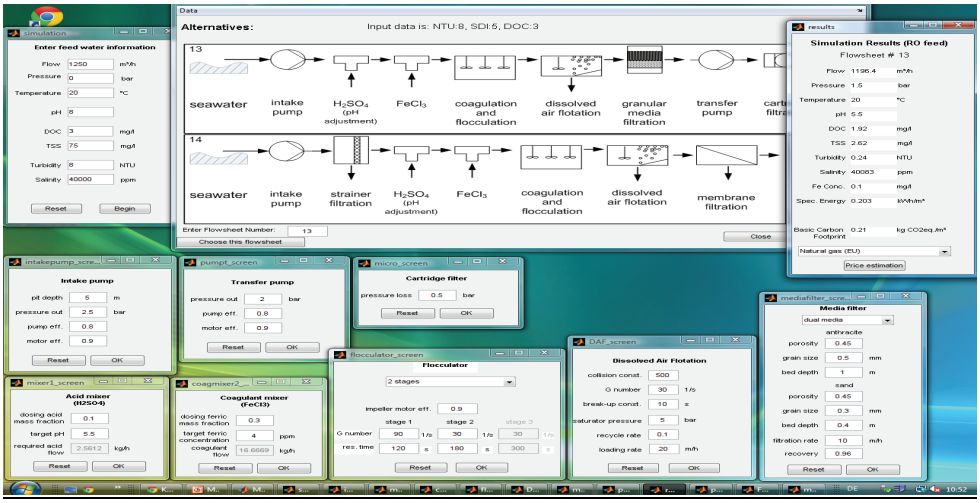

Fig. 1. Screen shot of the computer-based process design tool

The most common unit operations seen in SWRO pre-treatment are: Pumps, mixers, coagulators, sedimentation, flotation, strainers, media (carbon/sand) filtration, membrane (MF/UF) filtration and cartridge filtration. The question of which units to use and how to interconnect them corresponds to process synthesis and is highly depended on the feed seawater characteristics as well as on the desired product water specifications. The guidelines given by RO membrane manufacturers and practiced by SWRO plant operators are fairly clear: RO feed water should have silt density index (SDI) of less than 3, turbidity of less than 1NTU and total organic carbon (TOC) levels of less than 2mg/l. Using the tool, the user first gets several flowsheet suggestions that will meet these specifications based on industrial heuristics [7] and feed water quality.

Once one of the possible flowsheets has been selected, a steady state simulation takes place. Based on state of the art basic models which incorporate steady state mass and energy balances as well as physical separation mechanisms (such as sedimentation or flotation). The physical and chemical properties relevant to the models (most important are viscosity, density and particle size) are either calculated by correlations [8] or given as an input by the user. This level of modeling is sufficient in acquiring basic design information with relatively low computational effort. The model parameters are either literature based, experimentally identified or freely defined by the user. The user first defines an input vector describing the seawater intake feed (flow, pressure, temperature, pH, DOC,

suspended solids, turbidity, and salinity). The units then get solved one by one with the tool prompting the user to input some additional required parameters if necessary (like filtration flux, media depth, coagulant dose etc.).

After the flowsheet simulation is completed the processes can be analyzed. Following the principles of sustainability, the evaluation takes place in both economical and environmental forms. Economically, a net present value assessment is made on counts of the simulation sizing and operation results. Environmentally, a basic carbon footprint assessment is performed based on the forecasted process electricity and chemical consumptions. The user can then choose the best flowsheet and/or try to continue and improve the simulation and evaluation results until finally reaching an optimal process design which can then be taken into the next engineering step.

3. Experimental work

The experimental work performed in this project has two distinct goals. First, it must compliment the theoretical work in the form of parameter identification and model validation. Second, it should explore the technical feasibility of previously untested/undocumented new pre-treatment process configurations including new ideas for process integration and intensification.

One of the main challenges that current pre-treatment systems have a hard time of coping with is the removal of bio-fouling causing materials, namely organic fractions ranging from microalgae to small organic molecules (transparent exopolymer particles) [9]. Since coagulation tends to improve the removal of organics by causing them to flocculate into larger particles it is often used by plant operators in excess without substantial technical merits but with higher economic and environmental burdens (caused by the production of the coagulant as well as of that of the sludge). As a result, solutions which will eliminate the need for coagulation but still produce low bio-fouling RO-feed water are needed [10]. This was the motivation behind the experimental testing of a new, coagulant-free intensified filtration system for SWRO pre-treatment. The system was composed of a deep-bed rapid granular activated carbon (GAC) 50cm filtration column followed by dead-end membrane microfiltration. The system is depicted in figure 2. More information about the GAC and the membrane module is given in tables 1 and 2, accordingly. The water used was collected from the shore of Mokpo, at the shore of the Yellow Sea and the experiments took place at Gwangju, Korea. The water quality parameters are given in table 3. It should be pointed out that the water is rich in organics and suspended solids which pose a difficult task to a potential desalination plant.

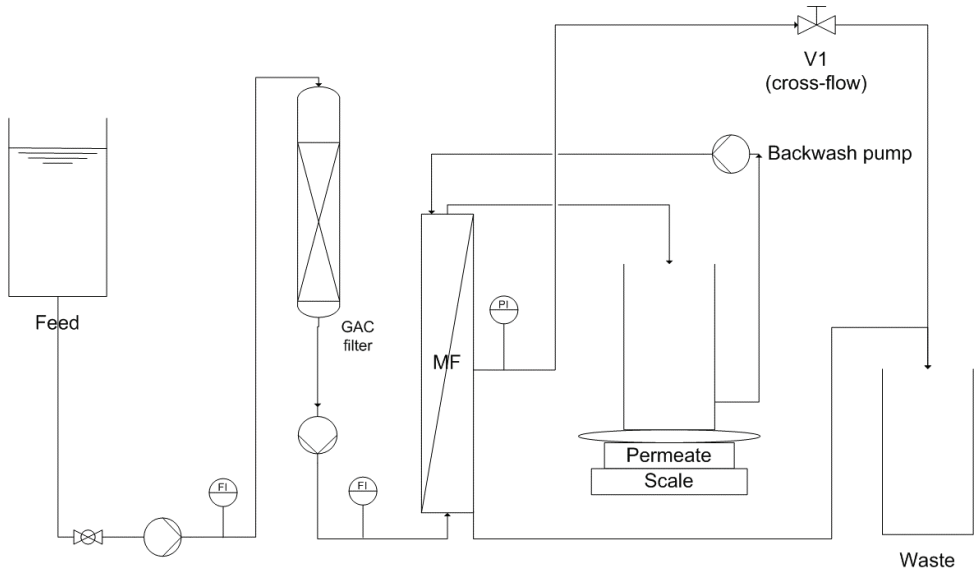

Fig. 2. The system used for the combined active carbon-microfiltration experiments

T a b l e 1

Granular activated carbon properties

Parameter	Value	Deviation
Particle size	12*30 Mesh	
Bulk density	0.51g/l	±0.03
Specific area	100m²/g	±0.5
Suspended solids reduction potential	92.9%	±0.5%
Turbidity reduction potential	93%	±5%
Fixed carbon	95%	±5%
Maximum ash content	7%	±3%

T a b l e 2

Technical data of the membrane module

Type	Pore size	Material	Fiber length	Diameter (in/out)	Fiber num.	Effective area	Mechanical strength	Operation
hollow fiber (Kolon)	0.1μ	PVDF	0.25m	0.8/2.0 mm	10	135cm²	>25kgf/fiber	Dead-end (const. flux)

T a b l e 3

Raw seawater quality parameters

Temp	pH	DO	Turbidity	TOC	TSS
18.5°C	7.86	5.97mg/l	4.78NTU	9.2mg/l	49mg/l

The GAC filter was operated at a moderate, common rapid filtration rate of 7m/h and the membrane was tested with different fluxes to determine which flux produces controllable fouling that can be sufficiently removed using backwashes (at 20 minutes intervals) with a minimal need for chemical cleanings. Each experiment was conducted using 20L samples and the water quality parameters were measured after the GAC and the MF membrane. Flows were measured before both filters and pressure was measured on the feed side of the membrane. The measured flux, J, was corrected for temperature, T, using equation 1 [11].

$$J_{corrected} = J \cdot \left(1.784 - 0.0575 \cdot T + 0.0011 \cdot T^2 - 10^{-5} \cdot T^3\right) \quad (1)$$

The water quality results are shown in figure 3. As it is seen in the figure, the active carbon was already very efficient in removing most of the turbidity and a large amount of the organic content. The values in the effluent stream were 0.51NTU and 4.34mg/l accordingly. Compared to the usual 10-20% TOC removal usually seen in pre-treatment systems (even with coagulation), the 53% removal of organics seen here can be considered very promising. The MF membrane has shown a further decrease in turbidity to levels of 0.19NTU. Unfortunately the TOC measurements of the membrane filtrate could not be performed due to technical contingencies, however it could be speculated that a further decrease took place.

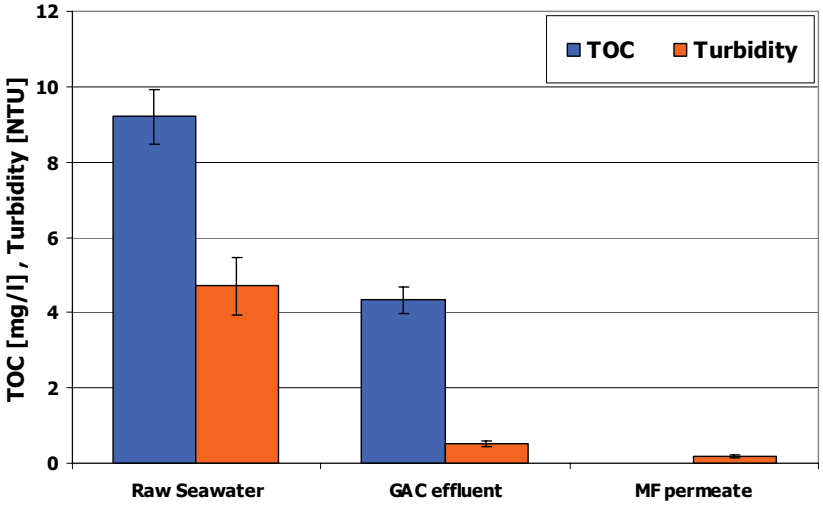

Fig. 3. Organic carbon content and turbidity of the seawater at different process points

The operation of the membrane filtration proved to be fairly stable when using fluxes of 300 L/m²h or lower. Under such conditions the increase in trans membrane pressure due to fouling was moderate and could be somewhat well controlled using backwashes. Higher fluxes resulted in fast increases in operating pressures and irreversible fouling (figure 4). It should be noted that even 300 L/m²h is a fairly high flux compared to the typical 60-120 L/m²h fluxes usually seen in SWRO pre-treatment. This could be explained by the high

quality water coming out of the GAC filter. After every experiment the permeability of the membrane could be completely restored by soaking the module in a 0.5% NaOCl solution overnight.

The parameters identified in these experiments were used in the process design tool GUI developed in the theoretical work. Such parameters include membrane resistance, cake resistance, carbon attachment efficiencies, permeabilities etc.

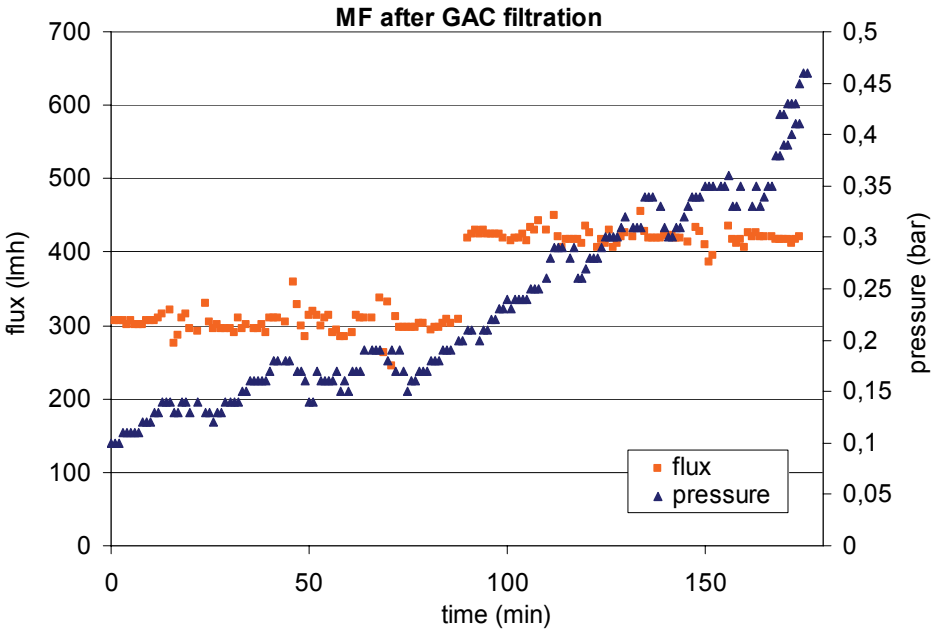

Fig. 4. Flux and pressure development during membrane filtration of GAC-filtered seawater

3. Conclusion and Outlook

In this work a combined theoretical-experimental approach was deployed in order to improve the sustainability of SWRO pre-treatment process design. An independent GUI flowsheeting tool was programmed to assist engineers in basic design of pre-treatment process including synthesis, simulation and evaluation concerning water costs and carbon emissions. Additionally, experimental work was done to both identify model parameters and test out new process configurations, for example a coagulation-free intensified GAC-MF filtration process. The results show that such a process both technically feasible as well as beneficial in waters containing a large organics fraction.

Literature

[1] Pankratz T.: Water Desalination Report, **44** (2008), 1.
[2] Gasson C.: International Desalination Association Newsletter 11-12 (2010), 7.

[3] Beery M., Repke J.-U.: Desalination and Water Treatment, **16** (2010), 218–228.
[4] Westerberg A.W.: Proc. Chemical Engineering Centennial Symposium (2004), 53-60.
[5] Dudley J., Dillon G., Rietveld L.C.: Journal of Water Supply: Research and Technology, **57** (2008), 13-21.
[6] Henthorne L.: International Desalination Association Journal, **3** (2010), 12-13.
[7] Beery M., Wozny, G., Repke J.-U.: Computer-Aided Chemical Engineering, **29** (2011), 1286-1290.
[8] El-Dessouky H.T., Ettouney H.M : Fundamentals of Salt Water Desalination, Elsevier 2002.
[9] Voutchkov N.: Pretreatment Technologies for Membrane Seawater Desalination, Australian Water Association, Sydney 2008.
[10] Busch M., Chu R., Rosenberg S.: International Desalination Association Journal, **2** (2010), 56–71.
[11] Allgeier S., Alspach B., Vickers J.: Membrane Filtration Guidance Manual, United States Environmental Protection Agency, 2005

18th International Conference Process Engineering and Chemical Plant Design
Günter Wozny and Łukasz Hady, Editors

MICHAŁ DYLĄG[*], JERZY ROSIŃSKI[**], JERZY KAMIEŃSKI[**]

ANWENDUNG DES MITTLEREN GESCHWINDIGKEITSGRADIENTEN AUF DIE MODELLIERUNG VON FLOCKUNGSPROZESSEN

Abstract

In der Arbeit ist das Ergebnis der Vergleichsrechungen zwischen einem als ideal durchmischt angenommenen Reaktor und einem ortsdiskret betrachteten Flockungsapparat dargestellt. Die Wiedergabe der realen Flockungsgrößenverteilungen ist in jedem Fall bei der Simulation eines ortsdiskreten Reaktors besser als für einen als ideal durchmischt angenommenen Flockungsapparat.

Keywords: Koagulation, Aggregation, Partikelwechselwirkungen, Populationsbilanzen, Primärpartikel und Flockengrößenverteilungen.

1. Einleitung

Die Modellierung und Simulation von Strömungsvorgängen in mehrphasigen Stoffsystemen war Gegenstand vieler Forschungsaktivitäten in den vergangenen Jahren. Zugängliche Methoden der Modellierung gaben keine Möglichkeit die Prozesse zu beschreiben, bei denen mit einer Veränderung von Partikeleigenschaftsverteilungen, z. B. Größenverteilungen, zu rechnen war.

Erst in den 60er Jahren wurde die so genannte Populationstheorie veröffentlicht [1] und nach Überwindung der „Kinderkrankheiten“ mit großem Erfolg angewandt [2, 3]. Obwohl der Einfluss der Hydrodynamik auf die Partikelwechselwirkungen jedoch nur sehr vereinfacht formuliert wurde, konnte ab der ersten Dekade des 21. Jahrhunderts ein erheblicher Fortschritt festgestellt werden [4, 5, 6, 7].

Ein aus wirtschaftlich und umwelttechnisch relevanten Gesichtspunkten wichtiger Prozess, bei dem Partikelwechselwirkungen durch Teilchenagglomeration, Bruch und Erosion auftreten, ist der Vorgang der Flockung. Der Anwendungsbereich zieht sich von der Bioverfahrenstechnik (Proteingewinnung) über die Lebensmitteltechnik bis vor allem in den Bereich der Abwasserreinigung hin.

[*] Institute of Advanced Manufacturing Technology, ul. Wrocławska 37a, 30-011 Kraków, Polska
[**] Cracow University of Technology, ul. Warszawska 24, 31-155 Kraków, Polska

2. Formulierung des Problems

Eine wichtige Rolle spielt der Einfluss der Hydrodynamik im Flockungsreaktor, die bisher bei der Berechnung von Flockungsprozessen gar nicht oder oft nur in einer sehr untergeordneten Weise berücksichtigt wurde.

Aufgrund des hohen Rechenaufwandes bei der numerischen Lösung der Populationsbilanzen wurden die Strömungs- und populationsdynamischen Simulationsrechnungen getrennt durchgeführt. Für den in dieser Arbeit betrachteten Rührkesselreaktor wurde zunächst in einer reinen Strömungssimulation das Strömungsfeld bestimmt [8, 9]. Die gewonnenen Ergebnisse dienten als Grundlage zur Berechung des Flockungsprozesses.

Die angenommenen Voraussetzungen nach Patankar, d. h. dass der Reaktor als ideal durchmischt angesehen werden kann, folgt die Anwendung des Camp und Stein Konzeptes [13] zur Lösung der Populationsbilanzen. Sowohl intuitiv als auch nach dem Stand des Wissens muss diese Vereinfachung mit großem Zweifel betrachtet werden. Dem Vergleich des ortsdiskret betrachteten Reaktors mit dem als ideal durchmischt angenommenen Reaktor wird in dieser Arbeit besondere Beachtung geschenkt.

Aufgrund der Komplexität der Modellgleichungen [5] hat sich gezeigt, dass in diesem Fall eine geschlossene Transformation der Populationsbilanzen zu Momentengleichungen nicht möglich ist. Stattdessen wird eine Art Hybrid-Verfahren angewandt, bei welchem ebenfalls nur noch die Momente der Partikelgrößenverteilungen von Primärpartikeln und Flocken als Unbekannte bestimmt werden, jedoch die kinetischen Ansätze der Partikelwechselwirkungen übernommen werden können, ohne die expliziete Durchführung der Integraltransformation.

Wie bei den Populationsbilanzen handelt es sich um Integro-Differentialgleichungen, aber der Vorteil liegt in der wesentlich geringeren Anzahl der Unbekannten. Diese Vorgehensweise erfordert während des Simulationsablaufes die ständige Rekonstruktion der Partikelgrößenverteilungen aus den Momenten. Hierzu hat sich die Methode der Rücktransformation über eine vorgegebene Verteilungsfunktion als praktikabel erwiesen. Dabei werden beispielsweise für eine Normalverteilung die relevanten Parameter der Verteilungsfunktion (Mittelwert, Standardabweichung,…) aus den berechneten Momenten bestimmt, sodass die Verteilungsfunktion eindeutig definiert ist.

Zur numerischen Behandlung der Populationsbilanzen in ihrer ursprünglichen Form sowie der Momentengleichungen wurde die Methode der Finiten Volumen angewandt. Auf dieser Basis erfolgte sowohl die Ortsdiskretisierung als auch die Eigenschaftsdiskretisierung der Bilanzgleichungen [6, 11, 12]. Dadurch konnte einer Simulationsrechnung jede beliebige Verteilung von Primärpartikeln und der Flocken als Startverteilung vorgegeben werden.

Weitere Simulationsrechnungen zeigten, dass die tatsächliche Flockungsgrößenverteilung näherungsweise bestimmt werden konnte. Für die Genauigkeit des Rechenmodells spielt von allem die Wahl der Verteilungsfunktion, die der Rekonstruktion der Flockengrößenverteilung zugrunde liegt, eine wichtige Rolle. Prinzipiell ist festzuhalten, dass die Anwendung der Momentenmethode eine schnelle Abschätzung der sich einstellenden Flockengrößenverteilung erlaubt, die Rechenzeit liegt um etwa einen Faktor Fünf niedriger als bei Verwendung von anderen Methoden. Es ist jedoch zu beachten, dass dieses sogenannte Hybrid-Verfahren bei niedrigen Primärpartikelkonzentrationen und

hohen Reynoldszahlen versagt, wenn die resultierenden Flockengrößenverteilung sehr eng sein wird.

3. Zielsetzung

Die praktische Auslegung von Flockungsreaktoren erfolgt auf der Basis des so genannten G-Wert-Konzepts, bei dem schweigend angenommen wird, dass ein Flockungsreaktor als ideal durchmischt betrachtet werden kann. Die getroffene Voraussetzung liegt trotz der nichtrealistischen Betrachtung weit vom realen Ablauf des Prozesses, bei dem zusätzlich ein Energieeintrag homogener gewährleistet werden soll.

Diese unreale Betrachtung begründet die Vergleichsuntersuchungen zwischen einem als ideal durchmischt angenommenen und einem ortsdiskret betrachteten Reaktor. Um dieser Zielsetzung entgegen zu kommen, werden sowohl experimentelle als auch numerische Prozeduren der Rechnungen verwendet.

4. Numerische Formulierung und Lösung

Die numerische Lösung der Populationsbilanzen und Momentengleichungen erfolgte mit Hilfe der Methode der Finiten Volumen. Zur vollständigen Diskretisierung von Populationsgleichungen wurde neben der Ortsdiskretisierung die Diskretisierung der Eigenschaftskoordinaten notwendig [6, 12].

4.1. Diskretisierung des Rührkesselreaktors

Betrachtet wurde ein Rührkesselreaktor mit 6-Blatt-Turbinenrührer mit vier Strombrechern. Dazu wird die Hälfte des Reaktorquerschnittes mit einem Rechengitter diskretisiert, welches sieben Bilanzelemente in axialer Richtung und fünf in radialer Richtung aufweist und damit wesentlich gröber ist, als das Rechengitter für die Strömungsberechnungen. Abb. 1 zeigt in der linken Hälfte den diskretisierten Reaktor, in den Abb. 2 und 3 das auf dem feinen Gitter berechnete [9] und gemessene [8] Strömungsfeld. Zusätzlich wurden die Ergebnisse der Strömungssimulationen [9] und LDE-Messungen [8] quantitativ verglichen.

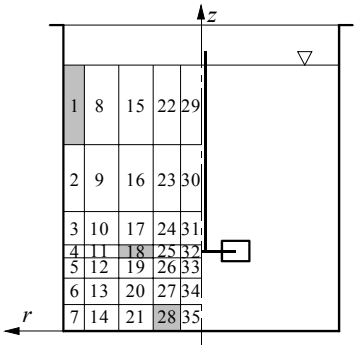

Abb. 1. Rührkesselreaktor mit diskreten Bilanzelementen zur Lösung der Populationsgleichungen

Die Ergebnisse der detalierten Strömungssimulationen wurden unter Berücksichtigung der turbulenten Dispersionsströme für die neu generierten Bilanzelemente interpoliert und zusammengefasst und in Form eines minimal notwendigen Datensatzes dargestellt, auf welchen das Simulationsprogramm mit den Populationsbilanzen zugreift. Dieser enthält

- die Elementkoordinaten in radialer und axialer Richtung,
- die in ein Element tatsächlich eintretenden Volumenströme über die Grenzflächen in bei den Richtungen,
- die über das Element gemittelten Werte der turbulenten kinetischen Energie κ und der turbulenten Energiedissipation ε sowie,
- den Druck in jedem Bilanzelement.

Für ein Bilanzelement, wie es in Abb. 1 dargestellt ist, werden in radialer und axialer Richtung Ein- und Austrittseiten definiert. Als Eintrittseite wird bezüglich jeder Koordinate die Seite bezeichnet, die in positiver Koordinatenrichtung als erste durchstoßen wird.

Die konvektiven Terme in den Bilanzgleichungen werden mit Hilfe der über die Elementgrenzen fließenden Volumenströme formuliert. Für jedes Element wird aus der Summe der eintretenden Volumenströme, unter der Voraussetzung einer inkompressiblen Strömung, der aus Kontinuitätsgründen insgesamt austretende Volumenström berechnet. Die austretenden Flocken und Primärpartikeln entsprechen in ihrer Konzentration und Größenverteilung den Partikeln im Bilanzelement selbst. Diese Vorstellung entstammt dem sogenannten UPWIND-Schema vom Patankar, bei welchem jedes Bilanzelement als ein ideal durchmischter kleiner Rührkessel angenommen wird [10].

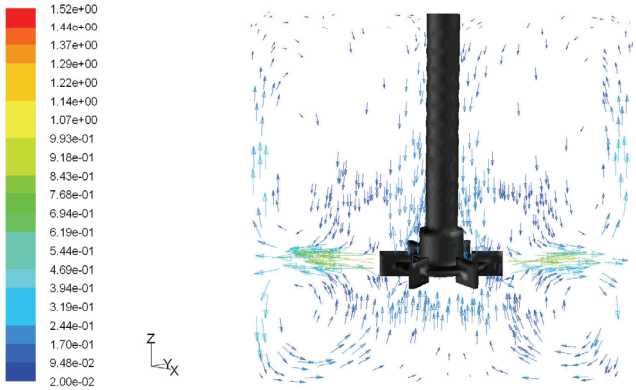

Abb. 2. Rührkesselreaktor – berechnetes Geschwindigkeitsfeld für Re = 10^4; der farbige Teil des Bildes beschreibt die berechnete Geschwindigkeitswerte (auch nach der Farbe erkennbar)

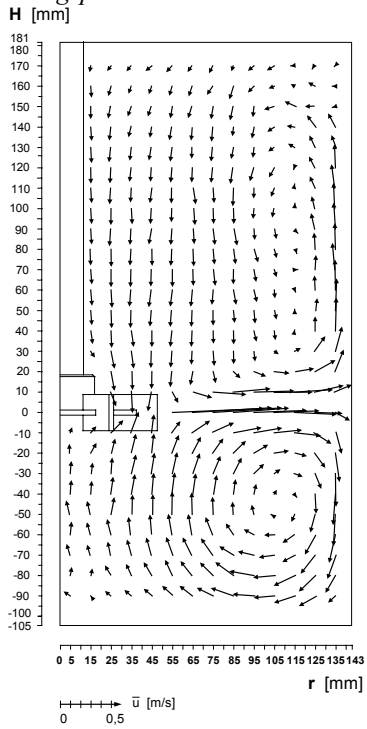

Abb. 3. Rührkesselreaktor – gemessenes Strömungsfeld für Re = 10^4

4.2. Eigenschaftsdiskretisierung

Die Diskretisierung der Eigenschaftskoordinate (Masse m) kann äquidistant oder nicht äquidistant erfolgen. Bei Diskretisierung wird aber der Bereich kleiner Partikeln nur durch wenige Intervalle beschrieben. Gerade in diesem Größenbereich liegen jedoch zumindest zu Beginn des Flockungsprozesses die meisten Partikeln vor. Diese Tatsache erzwingt eine weitgehende Umformung der Populationsgleichungen von Primärpartikeln und Flocken sowie Voraussetzung, dass die Eigenschaftsintervalle (Größenklassen) bei beiden Partikelarten im gemeinsamen Größenbereich jeweils identisch sind. Zusätzlich, da es sich aufgrund der Struktur der Quell- und Senkenterme um Integro-Differentialgleichungen handelt, müssen weiterhin die Integrationen durch entsprechende algebraische Formulierungen ersetzt werden. Leitgedanke und Problemlösung ist in der Arbeit [9] ausführlich dargestellt.

5. Experimentelle Untersuchungen

Zur Validierung der Simulationsergebnisse wurden experimentelle Untersuchungen zur Flockulation von Quarzpartikeln in einem Rührkesselreaktor durchgeführt. Die Untersuchung der entstehenden Flocken hinsichtlich ihrer Größenverteilung erfolgte mit einem rechnergestützten Bildanalysesystem.

Dieses Verfahren ist bezüglich der Flockenbeanspruchung wesentlich schonender als beispielsweise eine laserspektroskopische Untersuchung mit zusätzlichen Pump- und Rühreinrichtungen zur Aufwirbelung der Flocken in der Suspension. Der Versuchsaufbau, die Versuchsdurchführung und die Auswertung sind nachfolgend beschrieben.

5.1. Versuchsaufbau

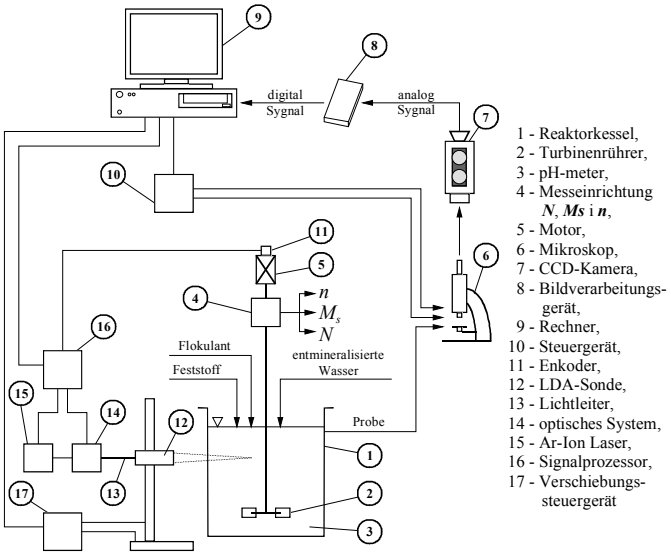

Abb. 4. Aufbau des Labor-Prüfstandes-Schema der Versuchsanlage

Die Koagulation der Quarzpartikeln wurde in einem Rührkesselreaktor aus Plexiglas mit dem Durchmesser ø300×6 und mit vier Strombrechern, welche jeweils um 90 Grad zueinander versetzt an der Reaktorwand angeordnet waren, untersucht. Die Strömung im Reaktor wurde durch einen 6-Blatt-Turbinenrühren mit einem Rührerdurchmesser $d_R = 1/3D_R$. Die angebrachte Messeinrichtung erlaubt sowohl die Drehzahl des Rührens als auch die eingebrachte Leistung online zu messen.

Die Anordnung ist mit der Rührkesselkonfiguration identisch, für welche die Simulationen des Strömungsfeldes durchgeführt wurden, die den populationsdynamischen Rechnungen zugrunde liegen. Damit ist eine direkte Vergleichbarkeit (Ähnlichkeit) von Rechen- und Messergebnissen gewährleistet.

5.2. Versuchsdurchführung

Zur Durchführung der Flockung wurde ein handelsüblicher Quarzstaub verwendet. Dessen Größenverteilung wurde mit einem Laserbeugungsspektroskop (Fa. Fritsch) bestimmt und bei den Simulationsrechnungen entsprechend als vorgegebene Primärpartikelverteilung angenommen. Zur Durchführung der Koagulation wurde dieser Quarz zunächst dem Reaktor zugegeben, der mit vollentsalztem Wasser gefüllt war. Mit

Hilfe des Rührers wurden die Quarzpartikeln ca. fünf Minuten dispergiert, sodass zu Beginn der Koagulation keine undefinierten Agglomerate vorlagen und eine gleichmäßige Verteilung der Quarzpartikeln in der Suspension sichergestellt war.

Anschließend wurden 40 g Calciumchlorid $CaCl_2$ und 40 g Natriumhydroxid NaOH in jeweils 2 l voll entsalztem Wasser gelöst, und die Lösungen wurden an zwei gegenüberliegenden Stellen an der Flüssigkeitsoberfläche nacheinander zugegeben. Danach wurde das entsalzte Wasser dem Behälter zugegeben, bis die Einfüllhöhe den Wert 288 mm erreicht hatte. Die notwendige Zeit bis zur vollständigen Vermischung der Salze mit der Suspension ließ sich aus Ähnlichkeitsgesetzen abschätzen und betrug einige Sekunden. Zusätzlich wurde die Grenze der Löslichkeit bestimmt und festgestellt, dass der Grenzwert nicht überschritten ist, sodass keine Fällungsflockung auftritt. Durch Chemikalienzugabe stellt sich ein pH-Wert 12,1 ein. Durch hohe Dosierung des Koagulationsmittels ist die vorher getroffene Modellannahme einer Agglomerationseffektivität $\alpha' = 1$ gerechtfertigt. Sonst müsste zusätzlich ein Modell zur Bestimmung der Agglomerationseffektivität in das Simulationsprogramm implementiert werden. Dem Flockungsreaktor wurde bei laufendem Rührer vorsichtig eine Suspensionsprobe von ca. 7 µl entnommen.

5.3. Versuchsauswertung

Das Funktionsschema der Bildanalyse zur Bestimmung von Partikelgrößenverteilungen ist aus Abb. 4 abzulesen. Das im Mikroskop Olympus sichtbare Probenbild wird von einer am Phototubus des Mikroskops angebrachten CCD Kamera (Sony) mit 256 Graustufen aufgenommen und in entsprechende Analogsignale umgesetzt. Diese werden von einer Bildverarbeitungskarte im angeschlossenen PC in digitale Signale umgewandelt und von einem Bildverarbeitungsprogramm eingelesen. Zur Vereinfachung des Analyseablaufs und zur besseren Reproduzierbarkeit der Messungen wurden ausgefeilte Bildauslesesysteme angewandt.

Um die teilweise porösen Flocken als jeweils einzelne Partikeln erfassen zu können, wird noch der Vorgang des „Schließens“ auf das binarisierte Bild angewandt. Dabei werden die Hohlräume innerhalb einer Flocke ausgefüllt, sodass einzelne Flocken eindeutig erkennbar sind und ausgewertet werden können. In Abb. 5 sind die unbearbeiteten Photos einer Flockenprobe zu sehen. Schließlich wird die Größenverteilung der Partikeln und Bezug in einem charakteristischer Durchmesser ermittelt.

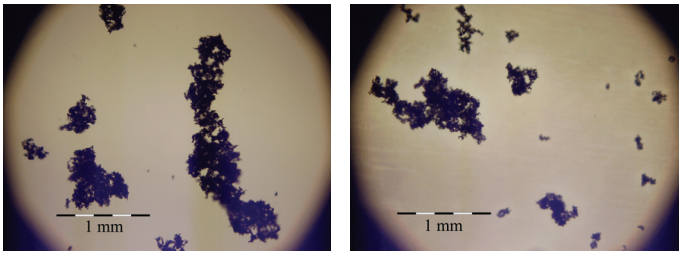

Abb. 5. Unbearbeitete Photographien einer Flockenprobe

6. Auswertung und Diskussion der Ergebnisse – Vergleich mit dem Modell des ideal durchmischten Reaktors

Simulationsrechungen wurden für einen Rührkesselreaktor bei Reynoldszahlen von Re = 10^4 und Re = $2{,}0 \cdot 10^4$ durchgeführt. Zur Lösung wurde die früher beschriebene Methode der Finiten Volumen angewandt.

Nachfolgend sind die Ergebnisse der berechneten und gemessenen Partikelgrößenverteilungen von Primärpartikeln und Flocken in Reaktor im stationären Zustand dargestellt. Die Partikelwechselverteilungen werden als massenbezogene Durchgangssumenwerte in Abhängigkeit eines kugeläquivalenten Partikeldurchmesser aufgetragen. Die Nummerierung der Bilanzelemente bezieht sich auf die in Abb. 1 dargestellte Reaktordiskretisierung.

Zur Auslegung von Flockungsreaktoren wird häufig das von Camp und Stein [13] vorgeschlagene G-Wert-Konzept angewandt. Die durch ein Rührwerk (oder eine Pumpe) in einem Flockungsreaktor eingebrachte Leistung P wird dabei durch den resultierenden mittleren Geschwindigkeitsgradienten G nach Gl. (1) charakterisiert, wobei $\varepsilon = P/m_R$ mit der Masse m_R des Reaktorinhalts ist.

$$G = \sqrt{\frac{\rho \cdot \varepsilon}{\eta}} \tag{1}$$

Dabei stellt G sowohl ein Maß für die Häufigkeit von Partikelkollisionen als auch für die Flockenzerstörung durch Erosion und Bruch dar. Der Reaktor wird auf dieser Grundlage als ideal durchmischt vorausgesetzt, obwohl in vielen Arbeiten [2, 6] auf die Bedeutung der im Flockungsreaktor vorliegenden unterschiedlichen lokalen Strömungsverhältnisse hingewiesen wird.

In Abb. 6 ist der Vergleich zweier Rechenergebnisse mit unterschiedlichen Modellvoraussetzungen dargestellt. Die durchgezogene Linie links zeigt die gemittelte Flockengrößenverteilung im Rührkesselreaktor wie in Abb. 4 der Literatur [15], unter der Berücksichtigung von 35 Bilanzelementen mit ihrem jeweiligen lokalen Energieeintrag und der anschließenden Mittelung der lokalen Flockengrößenverteilungen entsprechend der Volumenanteile der einzelnen Bilanzelemente.

Die gestrichelte Linie zeigt die mittlere Flockengrößenverteilung im Reaktor unter der Annahme idealer Durchmischung. Vor der Lösung der Populationsgleichungen wurden die lokalen Energieeinträge in den einzelnen Bilanzelementen entsprechend ihrer Volumenanteile zu einem für den gesamten Reaktor konstanten mittleren Energieeintrag gemittelt. Dieser liegt für Re = 10^4 bei $\varepsilon = 0{,}0225$ W/kg.

Die Rechnung zeigt, dass sich unter der Annahme des ideal durchmischten Reaktors eine Flockengrößenverteilung ergibt, die bei wesentlich größeren Flocken liegt. Ursache ist die Vernachlässigung des signifikanten Einflusses hoher Energiedissipationsraten in wenigen Elementen in Rührernähe. In diesen Bereichen ist die Zerstörung der Flocken so stark ausgeprägt, dass sich die Flockengrößenverteilung für den gesamten Reaktor bei wesentlich kleineren Werten einstellt, ein Ergebnis, welches auch durch die zuvor beschriebenen Experimente bestätigt wurde [15]. Diese lokal auftretende Zerkleinerung der Agglomerate wird unter der Voraussetzung des ideal durchmischten Reaktors nicht berücksichtigt. Insbesondere können bei dieser vereinfachten Betrachtungsweise auch lokale Unterschiede in der Flockungsgrößenverteilung, nicht wiedergegeben werden [14].

Dieses Ergebnis zeigt die Problematik bei der Anwendung des G-Wert-Konzepts, da Inhomogenitäten im (turbulenten) Strömungsfeld und deren Folgen durch diese empirische Gesetzmäßigkeit nicht berücksichtigt werden.

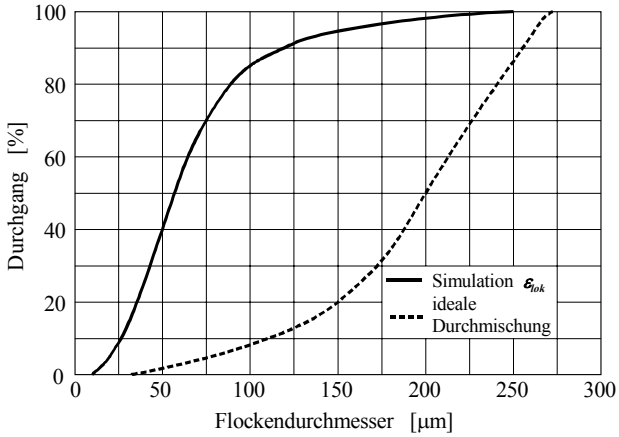

Abb. 6. Vergleich der über der Reaktor gemittelten stationären Flockungsgrößenverteilung bei ortsdiskreten und ideal durchmischt angenommenen Reaktor mit Re = 10^4, Primärpartikelkonzentration c_p = 1 g/l

Führt man denselben Vergleich bei einer geringeren Primärpartikelkonzentration durch (c_p = 0,25 g/l), so könnte unter Berücksichtigung der in Abb. 4 der Literatur [15] gezeigten Ergebnisse, dass Flockengrößenverteilung in den verschiedenen Elementen in stationären Zustand zusammenfällt, der Eindruck entstehen, dass der Reaktor für diesen Fall tatsächlich als ideal durchmischt betrachtet werden darf. Anhand des in Abb. 7 gezeigten Ergebnisses wird jedoch deutlich, dass dies nicht der Fall ist.

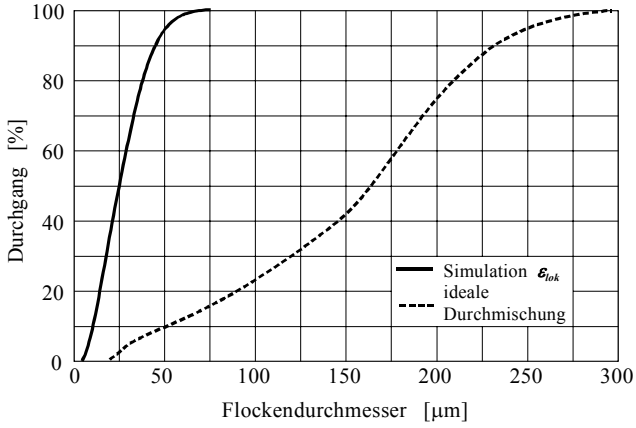

Abb. 7. Vergleich der über den Reaktor gemittelten stationären Flockengrößenverteilung bei ortsdiskreten und ideal durchmischt angenommenen Reaktor mit Re = 10^4; Primärpartikelkonzentration c_p = 0,25 g/l

Die durchgezogen dargestellte Durchgangssummenkurve zeigt die für den Reaktor berechnete mittlere Partikelgrößenverteilung, welche wieder durch Mittelung der Partikelgrößenverteilungen in den 35 diskreten Bilanzelementen bestimmt wurde. Die gestrichelte Kurve stellt die berechnete Flockengrößenverteilung unter der Annahme eines mittleren Energieeintrags im gesamten Reaktor dar. Auch für diesen zweiten vereinfachten Fall liegt die Flockengrößenverteilung insgesamt bei kleineren Flocken mit dem Ergebnis bei höherer Primärpartikelkonzentration nach Abb. 6. Ursache für die unterschiedlichen Ergebnisse ist nach wie vor die Annahme eines gemittelten Energieeintrags im Reaktor, sodass der Einfluss der hohen Energiedissipationsrate in einigen wenigen Elementen im Bereich des Rührers und die dort auftretende Flockenzerstörung nicht mehr berücksichtigt werden. Der Reaktor kann also nur unter der Voraussetzung als ideal durchmischt betrachtet werden, wenn auch die Turbulenzstruktur möglichst homogen ist!

Bei der Berechnung der Flockungsprozesse im Rührkesselreaktor bei Re = $2{,}2 \cdot 10^4$ wurde neben der Anwendbarkeit des Rechenmodells auf der Basis der Finite-Volumen-Methode wieder der Einfluss der Primärpartikelkonzentration sowie die Folge der Modellannahme eines ideal durchmischten Reaktors untersucht. In Abb. 8 sind die berechneten und gemessenen Primärpartikel- und Flockengrößenverteilungen im stationären Zustand dargestellt.

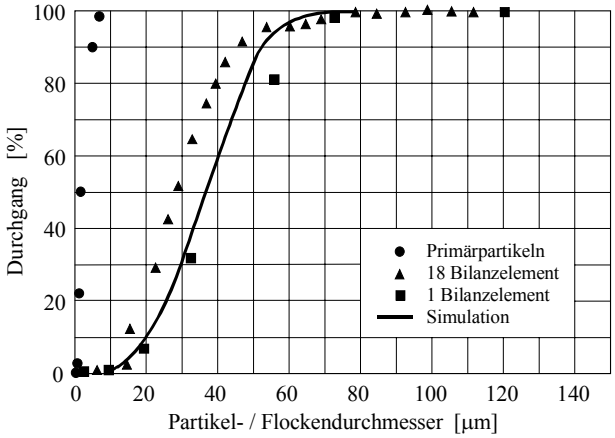

Abb. 8. Gemessene stationäre Flockengrößenverteilungen in dem Elementen 18 und 1 des Rührkesselreaktor bei Re = $2{,}2 \cdot 10^4$ im Vergleich mit der berechneten mittleren Flockengrößenverteilung im Reaktor; Primärpartikelkonzentration c_p = 1,0 g/l

Anhand der Messung ist festzustellen, dass bei den sich im stationären Zustand einstellenden Flockengrößenverteilungen im Reaktor ebenfalls lokale Unterschiede auftreten. Durch das Rechenmodell können diese lokalen Unterschiede nicht mehr wiedergegeben werden. Die berechneten Flockengrößenverteilungen sind für alle Bilanzelemente identisch, in Abb. 8 ist daher als Simulationsergebnis die für den gesamten Reaktor berechnete mittlere Flockengrößenverteilung dargestellt. Offensichtlich werden

vom Rechenmodell die Partikelwechselwirkungen als zu langsam beschrieben, so dass die Konzentrationsunterschiede durch die Konvektion vollständig ausgeglichen werden. Trotzdem ergibt sich durch die Simulationsrechnung eine mittlere Flockengrößenverteilung, die die realen Verhältnisse im Reaktor zufriedenstellend wiederspiegelt.

Insgesamt sind die Flocken kleiner als bei einer Reynoldszahl Re = 10^4 bei derselben Primärpartikelkonzentration. Durch den erhöhten Energieeintrag werden größere und damit instabilere Flocken in Strömungsfeld jetzt nicht nur in unmittelbarer Rührernähe, sondern im gesamten Reaktor schneller wieder zerstört.

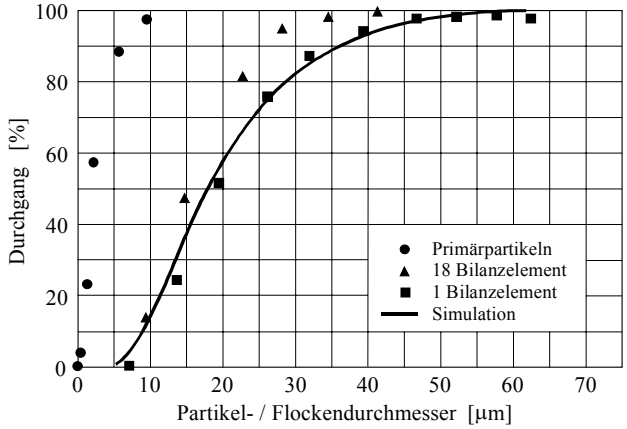

Abb. 9. Gemessene stationäre Flockungsgrößenverteilungen in den Elementen 18 und 1 des Rührkesselreaktors bei Re = $2{,}2 \cdot 10^4$ im Vergleich mit den beachteten mittleren Flockungsgrößenverteilung im Reaktor, Primärpartikelkonzentration c_p = 0,5 g/l

Ein entsprechendes Resultat erhält man wieder bei einer geringeren Primärpartikelkonzentration von 0,5 g/l, das in Abb. 9 aufgetragen ist.

Die Messung zeigt, dass die Flockungsgrößenverteilungen in den verschiedenen Bereichen des Reaktors eng beieinander liegen, die Ursuche wurde bereits bei Untersuchungen zur Re = 10^4 ausführlich diskutiert. Wie schon bei der höheren Primärpartikelkonzetrationen können auch hier mit dem Rechenmodell die lokalen Unterschiede nicht mehr wiedergegeben werden, für alle Bilanzelemente im Reaktor wird die gleiche Verteilung berechnet, welche jedoch die mittlere Größenverteilung wieder gut beschreibt.

Schließlich soll auch hier ein Vergleich mit dem Modell des ideal durchströmten Rührkesselreaktors erfolgen. Abb. 10 zeigt das entsprechende Ergebnis.

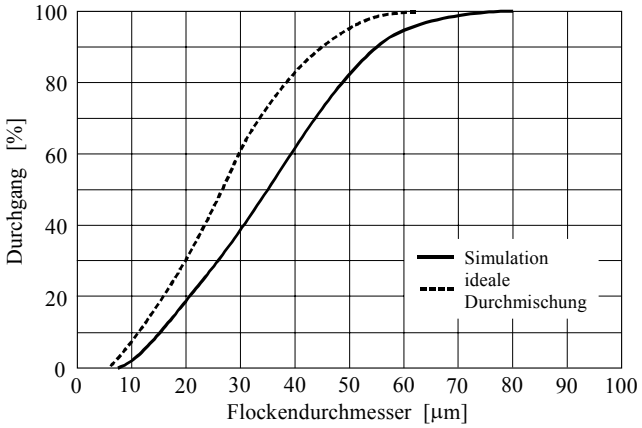

Abb. 10. Vergleich der über den Reaktor gemittelten stationären Flockungsgrößenverteilung bei ortsdiskreten und ideal durchmischt angenommenem Reaktor mit $Re = 2{,}2 \cdot 10^4$; Primärpartikelkonzentration $c_p = 1{,}0$ g/l

Überaschenderweise stellt sich durch diese Vereinfachung eine Flockengrößenverteilung ein, die von der mit dem ortsdiskreten Rechenmodell bestimmten zu kleineren Flocken hin abweicht. Die mittlere Energiedissipationsrate im Reaktor ist zu hoch, um die in Bilanzelementen geringerer lokaler Energiedissipation überwiegenden Koagulationsvorgänge ausreichend zu beschreiben. Die Annahme eines ideal durchmischten Reaktors erweist sich auch hier als eine zu starke Vereinfachung!

7. Zusammenfassung und Schlussfolgerungen

Ingesamt kann durch die Ergebnisse festgestellt werden, dass die Bildung enger Flockengrößenverteilungen bei Koagulationsvorgängen wie z. B. in einem Strömungsfeld mit höheren Reynoldszahlen auftreten, vom vorliegenden Rechenmodell nur noch näherungsweise wiedergegeben werden können.

Jedoch liegen in Flockungsreaktoren selten Strömungsbedingungen mit $Re > 2{,}0 \cdot 10^4$ vor, so dass die aufgezeigten Grenzen des Rechenmodells für praktische Anwendungsfälle kaum relevant sind.

Dagegen ist bei der Simulation von Flockulationsprozessen eine gute Wiedergabe der sich einstellenden Flockengrößenverteilungen zu erwarten, da bei der Flockung mit Polymeren erfahrungsgemäß deutlich größere Flocken und damit breitere Flockengrößenverteilungen entstehen als bei Koagulationsvorgängen.

Die Annahme eines ideal durchmischten Rührreaktors ist jedoch für alle hier besprochenen Anwendungen eine zu große Vereinfachung. Die Wiedergabe der realen Flockengrößenverteilungen ist in jedem Fall bei der Simulation eines ortsdiskreten Reaktors besser als für einem als ideal durchmischt angenommenen Reaktor.

Die praktische Auslegung von Flockungsreaktoren erfolgt seit vielen Jahren auf Basis des sogenannten G-Wert-Konzepts von Camp und Stein, bei dieser Vorstellung wird ein Flockungsreaktor als ideal durchmischt mit einem homogenen Energieeintrag betrachtet, beispielweise ein Rührwerk. Vergleichsrechnungen zwischen einem als ideal durchmischt

angenommen und einem ortdiskret betrachteten Rührkesselreaktor bei der Reynoldszahl $Re = 10^4$ zeigen jedoch, dass bei der Annahme idealer Durchmischung die entstehende Flockengrößenverteilung bei viel zu großen Flockendurchmessern liegen. Die tatsächlichen Größenverteilungen können nur unter Anwendung des ortsdiskreten Reaktorsmodells in Übereinstimung mit Messergebnissen gut wiedergegeben werden. Ursache ist die Vernachlässigung des hohen lokalen Energieeintrags im Nahbereich des Rührers, welche zu hohen lokalen Bruch- und Erosionsraten führt.

Eine Übertragung des Rechenmodells auf einen Rührkesselreaktor bei einer Reynoldszahl $Re = 2{,}2 \cdot 10^4$ zeigt dessen Extrapolierbarkeit. Die gemessenen lokalen Unterschiede der Flockengrößenverteilung im Reaktor zeigen aber wieder eine gute Übereinstimmung mit Messergebnissen, auch bei unterschiedlichen Feststoffkonzentrationen. Insbesondere stellt sich auch hier die Annahme eines ideal durchmischten Reaktors zur Auslegung des Flockenprozesses als ungeeignet heraus.

Literatur

[1] Hulburth H. M., Katz S.: Chem. Eng. Sci., **19**, (1964), 555-574.
[2] Bałdyga J., Boorne J. R.: Turbulent Mixing and Chemical Reactions, John Wiley & Sons, Chichester 1999.
[3] Bałdyga J., Orciuch W.: Chem. Eng. Sci., **56**, (2001), 2435-2444.
[4] Marchisio D. L.,Vigil R. D., Fox R. O.: Chem. Eng. Sci., 58, (2003), 3337-3351.
[5] Thomas D. N., Judd S. J., Fawcet N.: Wat. Res., **7**, (1999), 1579-1992.
[6] Jaworski Z.: Numeryczna mechanika płynów w inżynierii chemicznej i procesowej, Akademicka Oficyna Wydawnicza EXIT, Warszawa 2005.
[7] Gierczycki A.: Powstawanie i rozpad agregatów ciała stałego zawieszonych w cieczy, Zeszyty Naukowe Politechniki Śląskiej, Gliwice 2005.
[8] Talaga J., Wójtowicz R.: Inż. i Ap. Chem., **4**, (2010), 80-81.
[9] Wójtowicz R.: Inż. i Ap. Chem., **4**, (2010), 92-93.
[10] Patankar S. V.: Numerical Heat Transfer and Fluid Flow, New York, Hemispheres Publishing Corporation, 1980.
[11] Dyląg M., Kamieński J., Rosiński J.: Inż. i Ap. Chem., **2**, (2010), 35-36.
[12] Dyląg M., Kamieński J., Rosiński J., Szatko W.: Inż. i Ap. Chem., **4**, (2010), 22-23.
[13] Camp T. R., Stein R. C.: J. Boston Soc. Civ. Eng., **4**, (1943), 219-237.
[14] Dyląg M., J. Rosiński J., Kamieński J.: Czasopismo Techniczne, **5-M**, (2008), 89-96.
[15] Dyląg M., J. Rosiński J., Kamieński J.: Czasopismo Techniczne, 9-M, (2008), 3-18.

18th International Conference Process Engineering and Chemical Plant Design
Günter Wozny and Łukasz Hady, Editors

CONTENTS